



**HAL**  
open science

# Characterization of 3D thermomechanical properties of bituminous binders within the linear viscoelastic domain

Nuh Isa

► **To cite this version:**

Nuh Isa. Characterization of 3D thermomechanical properties of bituminous binders within the linear viscoelastic domain. Mechanics of materials [physics.class-ph]. École Nationale des Travaux Publics de l'État [ENTPE], 2023. English. NNT : 2023ENTP0017 . tel-04689529

**HAL Id: tel-04689529**

**<https://theses.hal.science/tel-04689529v1>**

Submitted on 5 Sep 2024

**HAL** is a multi-disciplinary open access archive for the deposit and dissemination of scientific research documents, whether they are published or not. The documents may come from teaching and research institutions in France or abroad, or from public or private research centers.

L'archive ouverte pluridisciplinaire **HAL**, est destinée au dépôt et à la diffusion de documents scientifiques de niveau recherche, publiés ou non, émanant des établissements d'enseignement et de recherche français ou étrangers, des laboratoires publics ou privés.



Thesis National Number : 2023ENTP0017

**A THESIS OF ENTPE  
Member of the Université de Lyon**

**Doctoral school N° 162  
Mécanique, Énergétique, Génie Civil et Acoustique (MEGA)**

To obtain the graduation of  
**PhD in civil engineering**

Defended on 21/12/2023 by:  
**Nuh Isa**

---

**Characterisation of 3D  
thermomechanical properties of  
bituminous binders within the linear  
viscoelastic domain**

---

In front of the following examination committee:

TEBALDI, Gabriele Professeur II classe Università degli Studi di Parma	Committee chair
HAMMOUM, Ferhat DR1 HDR Université Gustave Eiffel	Reviewer
TSANTILIS, Lucia Professeure associée Politecnico di Torino	Reviewer
TEBALDI, Gabriele Professeur II classe Università degli Studi di Parma	Examiner
BABADOPULOS, Lucas Professeur associé Universidade Federal do Ceará	Examiner
SAUZEAT, Cédric Docteur ITPE HDR ENTPE	Supervisor
MANGIAFICO, Salvatore CR ENTPE	Tutor
DI BENEDETTO, Hervé Professeur émérite ENTPE	Guest

Numéro national de thèse (NNT) : 2023ENTP0017

**THÈSE DE DOCTORAT DE L'ENTPE**  
**Membre de l'Université de Lyon**

**École Doctorale N° 162**  
**Mécanique, Énergétique, Génie Civil et Acoustique (MEGA)**  
**Spécialité: Génie Civil**

Soutenue publiquement le 21/12/2023, par :  
**Nuh Isa**

---

**Caractérisation des propriétés  
thermomécaniques 3D des liants  
bitumineux dans le domaine  
viscoélastique linéaire**

---

Devant le jury composé de :

TEBALDI, Gabriele	Professeur II classe Università degli Studi di Parma	Président
HAMMOUM, Ferhat	DR1 HDR Université Gustave Eiffel	Rapporteur
TSANTILIS, Lucia	Professeure associée Politecnico di Torino	Rapporteuse
TEBALDI, Gabriele	Professeur II classe Università degli Studi di Parma	Examineur
BABADOPULOS, Lucas	Professeur associé Universidade Federal do Ceará	Examineur
SAUZÉAT, Cédric	HDR, ENTPE	Directeur de thèse
MANGIAFICO, Salvatore	DR, ENTPE	Co-encadrant de thèse
DI BENEDETTO, Hervé	Professeur émérite ENTPE	Invité

## ABSTRACT

This doctoral thesis was developed at the Laboratory of Tribology and Dynamics of Systems (LTDS – Laboratoire de Tribologie et Dynamique des Systèmes) at the Ecole Nationale des Travaux Publics de l'Etat (ENTPE), France. Financed by the Petroleum Technology Development Fund (PTDF) in Nigeria and the LTDS Laboratory. The objective of this research is to characterise the thermomechanical properties of bitumen in three dimensions within the linear viscoelastic domain using a Dynamic Shear Rheometer (DSR). As a result, relevant information that may help in the improvement of asphalt mixture properties determination from bitumen properties is provided. To this end, three bitumen composing two unmodified and a modified bitumen were tested. This resulted in four experimental campaigns.

The first experimental campaign dealt with determination of the linear viscoelastic limits of two unmodified bitumen across a wide range of temperatures and three frequencies (10, 0.3, and 0.01Hz) using shear strain amplitude sweep tests. A new method to separate physical hardening effects at low temperatures from the linear viscoelastic limit was proposed. From the test results obtained, there exists a considerable increase in the LVE limits of bitumen at low temperatures due to the effect of physical hardening. The shear complex modulus corresponding to the LVE limits could be modelled by 2S2P1D model. Furthermore, the linearity strain criterion for bitumen varies from 0.2% (2000 $\mu$ m/m) to 10,000%.

The second experimental campaign dealt with the characterisation of the behaviour of two unmodified and one modified (PmB) bitumen within the linear viscoelastic domain using the shear complex modulus test. Eleven temperatures (-30, -20, -10, 0, 10, 20, 30, 40, 50, 60, 70°C) and seven frequencies (10, 3, 1, 0.3, 0.1, 0.03, 0.01 Hz) were considered for the characterisation, with the imposed strains obtained from Campaign 1. The automatic gap control function of the DSR was disabled due to its malfunction at low temperatures. It is also essential to conduct measurements at low temperatures with 4 mm parallel plates so as to enable measurements at high torque. The Time Temperature Superposition Principle (TTSP) and Partial Time Temperature Superposition Principle (PTTSP) were applicable to both unmodified and polymer-modified bitumen respectively. The shift factors of unmodified bitumen deviated from WLF law at temperature below -20°C. However, they could be fitted with the modified Kaelble equation. The linear viscoelastic properties of the bitumen could be fitted with 2S2P1D model. The glassy shear modulus  $G_0$  values of binders varied from 1.05 *GPa* to 1.3 *GPa*.



The third experimental campaign concerned the linear viscoelastic characterisation of a bitumen. Axial complex modulus test and shear complex modulus tests on bitumen on the same sample to determine axial complex modulus ( $E^*$ ) and shear complex modulus ( $G^*$ ). The test was conducted at different aspect ratios (1.14, 0.67, 0.5, 0.4) to rheologically determine the ideal specimen dimension free of stress influences. Frequencies considered were 10, 3, 1, 0.3, 0.1, 0.03, 0.01 Hz and temperatures were -5, 0, 5, 10, 20, 30°C. First, axial strain amplitude sweep test was conducted on the test bitumen at -5°C/10 Hz and 20°C/0.01 Hz to determine the LVE limit of the bitumen. The axial strain amplitude limit of bitumen varied from 0.1% (1000  $\mu\text{m}/\text{m}$ ) to 7%. Identical shift factors were fitted to WLF equation for both axial and shear complex modulus measurements. Experimental measurements were further fitted to the 2S2P1D model. The constants used to model the LVE properties of the bitumen in both test modes were identical. The glassy axial and shear moduli  $E_0$  and  $G_0$  determined were 4.5 *GPa* and 1.3 *GPa* respectively. Attempt to compute Poisson's ratio values from the measurements of  $E^*$  and  $G^*$  resulted in Poisson's ratios greater than 0.5. This result triggered a deeper analysis that led to the next Campaign.

The fourth campaign detailed the three-dimensional linear viscoelastic characterization of the three binders utilized in Campaign 2. Similar to Campaign 3, axial and shear complex modulus test on 5mm (0.4 aspect ratio) sample of bitumen were carried out using the DSR. High values of  $E^*$  were seen to be measured at low temperatures. This was however, attributed to oedometric effects which are dependent on Poisson's ratio. To eliminate this effect and enable an access to the true  $E^*$  values, an FEM was created to simulate the axial complex modulus test. It was however assumed that similar oedometric effects existed in both simulation and experimental moduli. The actual bitumen Poisson's ratios were therefore calculated with this hypothesis. Poisson's ratio values calculated ranged between 0.16 and 0.46. Finally, the axial complex modulus was computed using the Poisson's ratio determined. The corrected axial complex modulus ( $E^*$ ) and Poisson's ratio ( $\nu^*$ ) fitted with 2S2P1D resulted in glassy modulus  $E_0$  of bitumen that ranged between 2.85 *GPa* and 3.9 *GPa*.

**Keywords:** Bitumen, complex modulus, Poisson's ratio, LVE, physical hardening, strain amplitude

## RESUME

Cette thèse de doctorat a été développée au Laboratoire de Tribologie et Dynamique des Systèmes (LTDS) de l'Ecole Nationale des Travaux Publics de l'Etat (ENTPE), France. Financé par le Petroleum Technology Development Fund (PTDF) au Nigeria et le LTDS Laboratory. L'enrobé bitumineux est le matériau le plus couramment utilisé pour construire la couche de surface et la couche de base des structures de chaussée dans le monde. Les propriétés du liant bitumineux sont un facteur critique dans la détermination de la capacité portante et de la durabilité des structures de chaussée souples. La méthode rationnelle de dimensionnement des structures de chaussée se base d'un côté sur la connaissance et/ou l'estimation des conditions de chargement et des propriétés des matériaux, et d'autre part sur l'analyse structurelle basée sur des principes théoriques, la comparaison des contraintes critiques, des déformations ou des déflexions avec des valeurs admissibles, et des ajustements itératifs des matériaux ou de la géométrie jusqu'à l'obtention d'une conception satisfaisante. Il est donc indispensable de caractériser correctement les propriétés rhéologiques des matériaux de chaussée, en particulier leurs module complexe  $E^*$  et coefficient de Poisson complexe  $\nu^*$ , lesquels jouent un rôle crucial dans la détermination de la réponse mécanique de la chaussée vis-à-vis du chargement. De nombreux travaux de recherche ont étudié les relations entre les caractéristiques des bitumes et les propriétés des enrobés, telles que rigidité, résistance à l'orniérage et résistance à la fatigue. La nécessité d'une compréhension complète des caractéristiques des liants est ultérieurement renforcée par l'émergence et l'utilisation de matériaux alternatifs et de procédés comme la réutilisation d'agrégats d'enrobés.

La caractérisation rhéologique du bitume est généralement réalisée à l'aide de plusieurs appareils, y compris le rhéomètre à flexion de poutre (BBR), le rhéomètre à cisaillement annulaire (ASR) et en traction/compression (Delaporte et al. 2009; Mangiafico 2014; Babadopulos 2017; Orozco 2020). Cependant, le dispositif le plus couramment utilisé est le rhéomètre de type DSR (Büchner et al. 2019; Gražulytė et al. 2021; Laukkanen et al. 2015; Lu Uhlback & Soenen 2017). Plusieurs études ont suggéré que le durcissement physique, un processus réversible dépendant du temps se produisant à basse température dans les liants bitumineux, peut avoir un impact sur les tests de DSR en fonction du temps de conditionnement.

De plus, le module complexe  $E^*$  du bitume est généralement estimé à partir du module de cisaillement complexe  $G^*$  en utilisant un coefficient de Poisson réel constant de 0,5. Des essais visant à caractériser directement le module complexe  $E^*$  du bitume à basses températures ont

été réalisés (Di Benedetto et al. 2007). Cependant, les modules observés manquaient d'une mesure complémentaire du module de cisaillement complexe ( $E^*$  et  $G^*$  n'ont pas été mesurés sur le même échantillon). Certains essais ont été conçus pour quantifier le coefficient de Poisson complexe  $\nu^*$  afin d'étendre la description du comportement viscoélastique linéaire du bitume et des mastics au cas tridimensionnel. Cependant, ces essais sont assez difficiles à réaliser et nécessitent généralement des quantités plus importantes de bitume qu'un échantillon pour essais DSR.

Le comportement tridimensionnel du bitume dans le domaine viscoélastique linéaire a été étudié au laboratoire ENTPE. En particulier, l'objectif de la thèse est la détermination du module complexe axial  $E^*$  et du module complexe de cisaillement  $G^*$  de trois bitumes différents (B5070, B3550, PmB) sur un même échantillon, afin d'estimer le coefficient complexe de Poisson  $\nu^*$  à partir de la relation entre  $E^*$  et  $G^*$ . Les propriétés thermomécaniques des bitumes ont été étudiées à l'aide d'un nouveau rhéomètre à cisaillement dynamique (DSR) équipé d'un moteur axial. Le module complexe des liants a été obtenu sur une large gamme de températures ( $-10^\circ\text{C}$  à  $30^\circ\text{C}$ ) et de fréquences (0.01 à 10 Hz) à faibles niveaux de déformation (0.01% à 0.1%), dans le domaine viscoélastique linéaire des matériaux. Cette thèse a contribué à une meilleure compréhension des trois principales propriétés thermomécaniques ( $G^*$   $E^*$   $\nu^*$ ) des liants dans le domaine des petites déformations.

La charge de travail expérimentale pour la thèse a été divisée en deux catégories de campagnes, chacune se concentrant sur un mode de chargement spécifique et, par conséquent, sur un mode de fonctionnement particulier du DSR utilisé pour son exécution. La première catégorie de campagnes (Campagnes 1 et 2) se concentre sur la caractérisation rhéologique viscoélastique linéaire des liants en mode oscillatoire en utilisant le DSR équipé d'une plateforme inférieure fixe. Le deuxième groupe de campagnes (campagnes 3 et 4) se concentre sur la caractérisation rhéologique viscoélastique linéaire à la fois axiale (tension-compression) et en cisaillement des liants en utilisant le DSR avec un moteur axial supplémentaire connecté au plateau inférieur du rhéomètre, afin d'explorer la possibilité de déterminer le coefficient de Poisson des liants. Dans la thèse, les basses températures sont définies comme des températures  $\leq 10^\circ\text{C}$ , les températures moyennes sont des températures entre  $20^\circ\text{C}$  et  $40^\circ\text{C}$ , et les hautes températures sont des températures  $\geq 40^\circ\text{C}$ .

La première campagne de cette thèse s'est concentrée sur la détermination de la limite viscoélastique linéaire de deux bitumes non modifiés. La limite de linéarité du premier bitume

(B5070) a été étudiées des basses aux hautes températures (-25°C à 70°C). L'essai de non-linéarité pour le deuxième bitume (B3550), cependant, a été mené des basses aux moyennes températures (-25°C à 20°C). Dans le contexte de cette campagne expérimentale, le phénomène de durcissement physique a été observé à basses températures et basses fréquences lors de l'exécution des essais DSR pour étudier la limite du domaine de comportement ViscoElastique linéaire (VEL) des matériaux. Le premier objectif a été de corriger l'effet du durcissement physique sur les résultats des essais menés pour déterminer la limite VEL du bitume à basses températures. Le deuxième objectif a été de démontrer la validité du principe d'équivalence temps-température pour les limites VEL du liant déterminées par DSR, suivie de la modélisation 2S2P1D (Olard and Di Benedetto 2003) des limites VEL du liant.

La deuxième campagne de cette thèse s'est concentrée sur la caractérisation viscoélastique linéaire du comportement de deux bitumes non modifiés et d'un bitume modifié par des polymères. Le premier objectif derrière la caractérisation du comportement VEL du bitume était de réaliser correctement l'essai de module complexe sur le bitume en utilisant un Rhéomètre à Cisaillement Dynamique sur une large plage de températures et de fréquences tout en utilisant la géométrie plan-plan (plateaux parallèles) de 4 mm de diamètre pour les mesures à basses températures. Une caractérisation viscoélastique linéaire correcte des liants bitumineux, surtout à basses températures, est cruciale pour obtenir une estimation adéquate des propriétés viscoélastiques des enrobés à des températures correspondantes. Des divergences ont été observées entre les valeurs du module vitreux ( $G_0$ ) prédites à partir des données du module obtenues en utilisant le DSR et celles obtenues en utilisant d'autres équipements, tels que Métravib ou ASR (Mangiafico, 2014; Orozco, 2020). Le deuxième objectif de cette campagne était de simuler correctement les données expérimentales, y compris au-dessous de la température de transition vitreuse, à l'aide du modèle rhéologique 2S2P1D. Enfin, le troisième objectif était la détermination de la température de transition vitreuse des bitumes testés.

Pour la troisième campagne expérimentale, le premier objectif était de déterminer la meilleure géométrie d'échantillon permettant la caractérisation rhéologique du bitume en tension-compression et en cisaillement dans le domaine viscoélastique linéaire, sur un même échantillon, en utilisant le DSR équipé d'un moteur linéaire. Le deuxième objectif de cette campagne était de simuler les résultats des essais de module complexe axial et de cisaillement à l'aide du modèle rhéologique 2S2P1D et d'estimer le coefficient de Poisson du bitume. Ceci

implique la modélisation par éléments finis de l'essai de tension-compression afin de corriger l'effet œdométrique dû à la forme de l'échantillon.

Voici les conclusions tirées des campagnes expérimentales :

Campagne 1 :

- L'effet de durcissement physique sur le module complexe de cisaillement  $G^*$ , dépendant de la température et du temps, a été observé pour des durées de conditionnement jusqu'à 180 minutes.
- Le durcissement physique a un impact significatif sur les résultats des essais de balayage d'amplitude de déformation menés à des fréquences et des températures basses. Ne pas tenir compte de la rigidification du liant pendant les essais peut altérer l'estimation de la limite VEL. Une méthode de correction de l'effet du durcissement physique lors des tests de balayage d'amplitude est proposée.
- Les valeurs de la limite VEL déterminées expérimentalement pour les liants testés varient de 0,2 % à 10000 % en fonction de la température et de la fréquence de sollicitation. Elles vérifient le principe de superposition temps-température. À l'aide du modèle 2S2P1D, le module complexe de cisaillement  $G^*$  mesuré à la limite VEL a été simulé avec précision sur l'ensemble du spectre des températures et des fréquences examinées.

Campagne 2 :

- Les mesures des modules complexes de cisaillement  $G^*$  des deux liants non modifiés et du liant modifié valident le Principe de Superposition Temps-Température (TTSP) et le Principe de Superposition Temps-Température Partielle (PTTSP), respectivement. L'équation WLF ne simule pas correctement les valeurs des facteurs de translation du bitume non modifié au-dessous de  $-20^{\circ}\text{C}$ . Il est possible d'utiliser une équation modifiée pour les simuler.
- Le modèle 2S2P1D a été utilisé pour simuler les résultats des essais de module complexe  $G^*$ . Les simulations obtenues sont satisfaisantes, à l'exception des données à faibles fréquences équivalentes (hautes températures/faibles fréquences) obtenues pour le liant modifié. Les valeurs du module vitreux  $G_0$  varient de 1,05 GPa à 1,3 GPa.

### Campagne 3 :

- La limite VEL du liant testé a pu être déterminée également en traction/compression par un essai de balayage d'amplitude de déformation mené avec le DSR. La limite d'amplitude de déformation axiale des liants varie de 0,1 % (1000  $\mu\text{m}/\text{m}$ ) à 7 % en fonction de la température et de la fréquence.
- Les modules complexes axiaux  $E^*$  et de cisaillement  $G^*$  valident le principe de superposition temps-température (partiel pour le bitume modifié).
- Pour les essais de traction/compression et de cisaillement, les coefficients de translation  $a_T$  pour chaque échantillon de bitume étaient comparables.
- Les propriétés VEL,  $E^*$  et  $G^*$ , ont été simulées précisément par le modèle 2S2P1D. De plus, les mêmes constantes 2S2P1D (hormis les modules  $E_0$ ,  $E_{00}$ ,  $G_0$  et  $G_{00}$ ) et les mêmes coefficients de translation  $a_T$  ont été utilisés.
- En raison de l'effet œdométrique, le choix d'une géométrie appropriée (rapport rayon sur hauteur) pour les expériences DSR en mode axial s'est révélé essentiel pour caractériser avec précision le comportement rhéologique du liant.

### Campagne 4 :

- La qualité des signaux obtenus pour la contrainte et la déformation axiales lors des essais de module complexe en traction/compression augmente considérablement avec l'amplitude de la déformation imposée.
- Pour tenir compte de l'effet œdométrique, une correction a été appliquée sur la valeur de  $E^*$  à l'aide de calculs aux éléments finis. Le coefficient de Poisson a été calculé à l'aide des mesures corrigées de module  $E^*$  et des mesures de  $G^*$ .
- Avec un rapport rayon sur hauteur de 0,4 (entrefer de 5 mm), les distributions de contrainte et de déformation obtenues par un calcul aux éléments finis sont presque homogènes le long de l'axe horizontal de l'échantillon.
- La norme du coefficient de Poisson des bitumes varie entre 0,16 à basse température/haute fréquence et 0,46 à haute température/basse fréquence. L'angle de phase varie entre  $-4,6$  et  $0^\circ$ .

- Les données obtenues pour le coefficient de Poisson vérifient le TTSP. Des courbes maîtresses de la norme et de l'angle de phase pour le coefficient de Poisson complexe, et les modules complexes  $E^*$  et  $G^*$  ont été obtenues en utilisant des coefficients de translation  $a_T$  identiques.
- Le module vitreux  $E_0$  déterminé pour tous les bitumes non modifiés après correction variait entre 2,8 GPa et 3,9 GPa. La méthode de correction introduite n'est applicable qu'aux bitumes non modifiés.

**Mots-clés** : Bitume, module complexe, coefficient de Poisson, VEL, durcissement physique, amplitude de déformation

<b>1. Introduction</b> .....	<b>22</b>
<b>2. Literature Review</b> .....	<b>24</b>
2.1 Pavement .....	24
2.1.1 Bituminous Pavement Materials .....	25
2.1.1.1 <i>Aggregates</i> .....	26
2.1.1.2 <i>Fillers</i> .....	27
2.1.1.3 <i>Air voids</i> .....	28
2.1.1.4 <i>Bitumen</i> .....	31
2.1.1.4.1 <i>Bitumen constitution and structure</i> .....	31
2.1.1.4.2 <i>Types of bitumen</i> .....	32
2.1.1.4.3 <i>Empirical Test on Bituminous Binders</i> .....	35
2.1.1.4.4 <i>Fundamental test on bitumen</i> .....	38
2.1.1.4.5 <i>Bitumen Binder Ageing</i> .....	43
2.1.1.5 <i>Additives</i> .....	45
2.1.2 Thermomechanical Behaviour of Bituminous Materials .....	45
2.1.2.1 <i>Thermomechanical Behavioural Domains of Bituminous Pavement Materials</i> 47	
2.1.2.2 <i>Flexible Pavement Distresses</i> .....	50
2.2 Linear Viscoelasticity .....	52
2.2.1 Creep Functions.....	52
2.2.2 Relaxation Functions.....	54
2.2.3 Boltzmann Superposition Principle.....	55
2.2.4 Laplace Carson Transform .....	56
2.2.5 Response to sinusoidal loading .....	57
2.3 Time-Temperature Superposition Principle (TTSP) .....	59
2.4 Prediction of Viscoelastic Behaviour of Bituminous Materials .....	63
2.4.1 Mathematical Models .....	64
2.4.1.1 <i>Christensen and Anderson (CA) model</i> .....	64
2.4.1.2 <i>Christensen Anderson Marasteanu (CAM) Model</i> .....	65
2.4.2 Mechanical Models .....	66
2.4.2.1 <i>Discrete spectrum models</i> .....	67
2.4.2.2 <i>Continuous spectrum models</i> .....	70
2.4.3 Predictive Empirical Models .....	74
2.5 Poisson's ratio.....	75
2.5.1 Linear Elastic Poisson's Ratio.....	76



2.5.2	Linear Viscoelastic Poisson's Ratio .....	77
2.5.2.1	<i>Laplace Carsons transform relations of Poisson's ratio</i> .....	77
2.5.2.2	<i>The frequency domain Poisson's ratio</i> .....	78
2.5.3	Poisson's Ratio of Bituminous Materials .....	79
2.6	Linear viscoelastic limits of bituminous materials .....	82
<b>3.</b>	<b>Equipment, Materials and Test Procedures.....</b>	<b>84</b>
3.1.1	DSR shear oscillatory mode .....	85
3.1.2	DSR axial mode .....	87
3.2	Bitumen and bitumen preparation .....	89
3.3	Experimental procedures .....	91
3.3.1	Bitumen time sweep test .....	91
3.3.2	Bitumen linear viscoelastic limit determination in shear .....	92
3.3.3	Shear complex modulus test.....	94
3.3.4	Rheological characterization of binders using DSR axial motor configuration 100	
3.3.4.1	<i>Test sample preparation</i> .....	100
3.3.4.2	<i>Preliminary axial strain amplitude sweep test</i> .....	100
3.3.4.3	<i>Axial and shear complex modulus tests on binders</i> .....	101
3.4	Experimental Plan.....	105
3.4.1	Campaign 1 .....	105
3.4.2	Campaign 2 .....	106
3.4.3	Campaign 3 .....	107
3.4.4	Campaign 4 .....	108
<b>4.</b>	<b>Campaign 1: Shear oscillatory LVE limit of binders .....</b>	<b>109</b>
4.1	Objectives .....	109
4.2	Physical hardening study on binders .....	110
4.2.1	Effect of temperature storage on B5070 bitumen .....	110
4.2.2	Effect of temperature storage on B3550 bitumen .....	111
4.3	LVE limits of B5070 bitumen .....	113
4.3.1	Quantification and correction of physical hardening effect on the complex modulus ( $G^*$ ) of B5070 bitumen strain sweep test.....	115
4.3.2	Physical hardening effect on the phase angle ( $\phi$ ) of B5070 bitumen during a strain sweep test .....	119
4.4	LVE limits of B3550 bitumen .....	121
4.4.1	Quantification and correction of physical hardening effect on the complex modulus ( $G^*$ ) of B3550 bitumen strain sweep test.....	123

4.4.2	Physical hardening effect on the phase angle ( $\phi$ ) of B3550 bitumen during a strain sweep test .....	126
4.5	Time temperature dependence of physical hardening .....	128
4.6	Binder LVE limits time temperature dependence .....	130
4.7	2S2P1D modelling of binder LVE limits .....	133
4.8	Conclusions of Campaign 1 .....	135
<b>5.</b>	<b>Campaign 2: DSR linear viscoelastic characterisation of binders in shear .....</b>	<b>137</b>
5.1	Objectives .....	137
5.2	Rheological measurements .....	137
5.2.1	Influence of plate sizes on bitumen rheological responses .....	138
5.2.2	Repeatability .....	139
5.3	Rheological modelling .....	141
5.3.1	Horizontal shift factors .....	147
5.3.2	Discontinuity factors .....	149
5.3.3	Influence of discontinuities on the rheological properties of bitumen.....	151
5.4	Glass transition temperatures.....	154
5.5	Conclusions of Campaign 2.....	156
<b>6.</b>	<b>Campaign 3: Dynamic Shear Rheometer Determination of Axial <math>E^*</math> and Shear <math>G^*</math> Complex Moduli for Binder .....</b>	<b>158</b>
6.1	Objectives .....	158
6.2	Axial strain amplitude sweep test .....	158
6.3	Complex modulus test analysis .....	159
6.3.1	Influence of aspect ratios on the rheological response of bitumen .....	161
6.3.2	Influence of plate size on the rheological response of bitumen measured in tension-compression .....	163
6.4	DSR Peltier assembly and axial motor assembly measured shear complex moduli	165
6.5	Rheological modelling of bitumen axial and shear complex modulus.....	165
6.6	Conclusions on campaign 3 .....	169
<b>7.</b>	<b>Campaign 4: 3D Linear Viscoelastic Characterisation and Modelling of Bitumen .....</b>	<b>171</b>
7.1	Objectives .....	171
7.2	Axial and shear complex modulus test on binders of 5 mm height.....	171
7.2.1	Time temperature superposition principle.....	173
7.2.2	2S2P1D modelling of axial and shear complex modulus of binders .....	175
7.3	Poisson's ratio determination .....	179

7.3.1	Time temperature dependence of Poisson's ratio .....	181
7.3.2	2S2P1D Poisson's ratio determination.....	182
7.4	Finite element simulation of DSR axial complex modulus test .....	183
7.4.1	Finite element model description .....	183
7.4.2	Analytical solutions of materials in compression .....	185
7.4.3	Effect of Poisson's ratio on the apparent complex modulus.....	185
7.4.4	Stress and strain tensors within the bitumen finite element model .....	188
7.4.5	Bitumen stiffness influence on the simulated modulus.....	193
7.5	Correction method for measured DSR axial complex modulus .....	194
7.6	Conclusions of Campaign 4.....	205
<b>8.</b>	<b>Conclusions and Perspectives .....</b>	<b>207</b>
	<b>References .....</b>	<b>211</b>

*Table 3.1 – Technical Specifications of the rheometer in oscillatory mode*

*Table 3.2 – Technical Specifications of the rheometer in axial mode*

*Table 3.3 – Binder properties*

*Table 3.4 – Plates and temperatures used for shear strain amplitude sweep test on bitumens*

*Table 3.5 – Plates and temperatures used for shear complex modulus tests*

*Table 3.6 - Number of cycles in function of frequencies*

*Table 3.7 - Bitumen shear strain amplitude sweeps test plan*

*Table 3.8 - Shear complex modulus test plan*

*Table 3.9 - Table 3.9 - Axial and shear complex modulus test plan at different DSR gaps*

*Table 3.10 - Axial and shear complex modulus test conditions*

*Table 3.11 – Axial and shear complex modulus test plan on different bitumen*

*Table 4.1 – B5070 bitumen 2S2P1D model constants*

*Table 5.1 - a) 2S2P1D constants and b) WLF parameters of Campaign 2 bitumen*

*Table 5.2 – The Kaelble constants at  $T_{ref} = 10^{\circ}\text{C}$*

*Table 5.3 - Vertical shift factors  $b_T$  of DSR complex modulus test results for bitumen of Campaign 2 at low temperatures ( $T_{ref} = -10^{\circ}\text{C}$ )*

*Table 5.4 - a) Recalibrated 2S2P1D constants and b) shift factor model parameters of the first trials of Campaign 2 bitumen*

*Table 5.5 – Glass transition temperatures and frequencies of bitumen*

*Table 6.1 - 2S2P1D and WLF parameters for tested binder at  $T_{ref} = 10^{\circ}\text{C}$*

*Table 7.1 - 2S2P1D and WLF parameters for tested binders at  $T_{ref} = 10^{\circ}\text{C}$*

*Table 7.2 - 2S2P1D constants and WLF parameters at  $T_{ref} = 10^{\circ}\text{C}$  for B5070 and B3550 bitumen FEM corrected axial complex moduli*

### Figures

*Figure 2.1 - Basic elements of flexible pavements (left) and rigid pavements (right)*

*Figure 2.2 - 20mm Continuous and 20mm Gap-graded curve (Ramirez Cardona, Pouget, Di Benedetto, & Olard, 2015)*

*Figure 2.3 - Scheme of volumetric properties of a bituminous mixture. (Freire, 2020)*

*Figure 2.4 - Connecting, non-connecting and occluded voids (Delorme & Wendling, 2007)*

*Figure 2.5 - Asphaltenes are discontinuous agglomerates joined together by resin compounds where maltenes form a continuous phase (González, 2010) as adapted from Kennedy*

*Figure 2.6 - Fluorescent microscopy images of a polymer-modified bitumen (PMB) with (a) 3% EVA, (b) 5% EVA and (c) 7% EVA adapted from (Gordon D. Airey, 2002a).*

*Figure 2.7 - Penetration test scheme (a) device and (b) Setup Setup (O'Flaherty, 2001)*

*Figure 2.8 - Softening point test scheme (a) device (Ramirez, 2016) and (b) Setup (O'Flaherty, 2001)*

*Figure 2.9 - Fraas breaking point test scheme (Ramirez, 2016)*

*Figure 2.10 – The DSR testing configuration adapted from (Subhy, 2017)*

*Figure 2.11 – Bending Beam Rheometer, as illustrated in (G. Rowe et al., 2001)*

*Figure 2.12 – Determination of  $S(60)$  and  $m$ -value, as illustrated in (G. Rowe et al., 2001)*

*Figure 2.13 - Schematic view of the annular shear rheometer (ASR) for bitumen and mastic adapted from (Delaporte, Di Benedetto, Chaverot, & Gauthier, 2009)*

*Figure 2.14 - Metravib complex modulus test apparatus a) tension-compression from low temperature to 30°C and b) annular shearing above 30°C adapted from (Hervé Di Benedetto, Olard, Sauzéat, & Delaporte, 2004)*

*Figure 2.15 - Pavement response and traffic load scheme (Hervé Di Benedetto, 1998; Mangiafico, 2014)*

*Figure 2.16 - Pavement response and thermal load scheme (Hervé Di Benedetto, 1998; Mangiafico, 2014)*

*Figure 2.17 - Typical mechanical behaviour domains of bituminous mixtures (H Di Benedetto & Corté, 2005; Herve Di Benedetto et al., 2013)*

*Figure 2.18 – Typical mechanical behaviour domains of bitumen at intermediate temperature as a function of number of cycles and strain amplitude (Mangiafico, 2014)*

*Figure 2.19 – Typical mechanical behaviour domains of bitumen as a function of temperature and strain amplitude (Mangiafico, 2014)*

## Figures

---

*Figure 2.20 – (a) Structural rutting and (b) Non-Structural rutting (Hérve Di Benedetto et al., 2013)*

*Figure 2.21 – Differences between permanent deformation and fatigue cracking during a homogenous cyclic test (H Di Benedetto, De La Roche, Baaj, Pronk, & Lundström, 2004)*

*Figure 2.22 – Sever fatigue cracking (Miller and Bellinger 2014) as cited by (Orozco, 2020)*

*Figure 2.23 – Regions of creep behaviour at different load levels*

*Figure 2.24 – Regions of creep behaviour at different load levels (Lakes & Lakes, 2009)*

*Figure 2.25 – Relaxation and recovery*

*Figure 2.26 – Cancellation test*

*Figure 2.27 – Stress history*

*Figure 2.28 – Strain history*

*Figure 2.29 – Master curve of the norm of shear complex modulus at  $T_{ref}=25^{\circ}C$  (Forton, Di Benedetto, Mangiafico, Sauzéat, & Marc, 2019)*

*Figure 2.30 - Shift factor  $a_T$  and a WLF fitted curve of a binder (Forton et al., 2019)*

*Figure 2.31 – Modified Kaelble schema compared with WLF(Laukkanen & Winter, 2018)*

*Figure 2.32 – Linear elastic spring*

*Figure 2.33 – Linear dash-pot*

*Figure 2.34 – Maxwell model*

*Figure 2.35 – kelvin-Voigt model*

*Figure 2.36 – Generalized Maxwell model*

*Figure 2.37 – Generalized Kelvin-Voigt model*

*Figure 2.38 – Parabolic element*

*Figure 2.39 – Huet model*

*Figure 2.40 – Huet-Sayegh model*

*Figure 2.41 – 2S2P1D model*

*Figure 2.42 – Influence of 2S2P1D constants on Cole-Cole plot of bituminous materials (Mangiafico, 2014)*

*Figure 2.43 – Schematic representation of SHStS transformation in Cole-Cole plot (Mangiafico, 2014).*

*Figure 2.44 – a) Complex modulus data and b) Complex Poisson's ratio data measured directly on bituminous mixtures with the respective fitted 2S2P1D master curves (S Pouget, 2011; Simon Pouget, Sauzéat, Di Benedetto, & Olard, 2010).*

*Figure 2.45 – Comparison of the FRF and tension-compression test determined a) complex Poisson's ratio master curves b) Poisson's ratio phase angles and c) cole-cole plot of four*

## Figures

---

*different specimens (Gudmarsson, Ryden, Di Benedetto, & Sauzéat, 2015; Gudmarsson et al., 2014)*

*Figure 2.46 – Experimental result of directly determined 50/70 bitumen Poisson's ratio a) norm of  $v^*$ , b) phase angle as adapted from (Hervé Di Benedetto, Delaporte, & Sauzéat, 2007)*

*Figure 2.47 – Linear viscoelastic limit of a binder*

*Figure 3.1 – DSR equipment used for experimental campaigns*

*Figure 3.2 – a) MCR 702 with temperature hood and fixed lower plate; b) parallel plate fixtures and c) fluid circulator (Julabo FP50) at ENTPE laboratory*

*Figure 3.3 – DSR parallel plate specimen geometry (Orozco, 2020)*

*Figure 3.4 – a) MCR 702 tension-compression assembly with thermal chamber; b) fluid circulator (Julabo FP89) at ENTPE laboratory*

*Figure 3.5 – Schematic diagram of a DSR axial complex modulus test setup*

*Figure 3.6 – Bitumen proportioned in cans and aluminum cups for storage in the refrigerator*

*Figure 3.7 – Silicon moulds filled with bitumen (from left to right 25 mm, 8 mm, 4 mm diameter specimen)*

*Figure 3.8 – Scheme showing time sweep test (TST) over a 27 hours period*

*Figure 3.9 – Scheme showing the procedure for shear strain amplitude sweep test at low and medium test temperatures using a DSR with fixed lower plate and temperature hood*

*Figure 3.10a) - DSR complex shear modulus test scheme using 4 mm and 8 mm parallel plates*

*Figure 3.10b) - DSR complex shear modulus test scheme using 25 mm parallel plate*

*Figure 3.11 – B5070-1 complex modulus test results at  $-30^{\circ}\text{C}$ . a) Norm of complex modulus; and b) phase angle in function of number of cycles; c) Complex modulus average values*

*Figure 3.12 - Example of specimen preparation at 4 mm and 5 mm test heights with 4 mm parallel plate*

*Figure 3.13 – Axial stress and axial deformation of bitumen*

*Figure 3.14 - Complex modulus test scheme adopted with 4 mm parallel plate*

*Figure 3.15 - Complex modulus test scheme adopted with 8 mm parallel plate*

*Figure 4.1 – Time sweep test of bitumen B5070 over a) 27 hours period; b) initial 5-hour period at  $-20^{\circ}\text{C}/1\text{ Hz}$*

*Figure 4.2 - Time sweep test of bitumen B3550 over a) 27 hours period; b) initial 5-hour period at  $-20^{\circ}\text{C}/1\text{ Hz}$*

*Figure 4.3 – Strain amplitude sweep tests results at  $-10^{\circ}\text{C}$  and frequencies (a) 10Hz, (b) 0.01 Hz, and (c) 0.3 Hz on B5070 bitumen.*

## Figures

---

Figure 4.4 – Corrected strain amplitude sweep tests results at  $-10^{\circ}\text{C}$  and frequencies (a) 0.01 Hz, and (b) 0.3 Hz on B5070 bitumen.

Figure 4.5 - Results of strain amplitude sweep tests and estimation of physical hardening effect on  $|G^*|$  of B5070 bitumen at (a) 0.01 Hz, (b) 0.3 Hz; and (c) the rate of physical hardening at each test temperature.

Figure 4.6 – Results of strain amplitude sweep tests showing phase angles of B5070 bitumen at (a) 0.01 Hz and (b) 0.3 Hz.

Figure 4.7 – Results of strain amplitude sweep tests and estimation of physical hardening effect on  $\phi$  of B5070 bitumen at (a) 0.01 Hz and (b) 0.3 Hz.

Figure 4.8 – Strain amplitude sweep tests results at  $-10^{\circ}\text{C}$  and frequencies (a) 10Hz, (b) 0.01 Hz, and (c) 0.3 Hz on B3550 bitumen.

Figure 4.9 – Corrected strain amplitude sweep tests results at  $-10^{\circ}\text{C}$  and frequencies (a) 0.01 Hz, and (b) 0.3 Hz on B3550 bitumen.

Figure 4.10 – Results of strain amplitude sweep tests and estimation of physical hardening effect on  $|G^*|$  of B3550 bitumen at (a) 0.01 Hz, (b) 0.3 Hz; and (c) the rate of physical hardening at each test temperature.

Figure 4.11 – Plots of Physical hardening rate ( $G_b$ ) of bitumen B5070 and B3550 against temperature at frequencies 0.3 Hz and 0.01 Hz

Figure 4.12 – Results of strain amplitude sweep tests showing phase angles of B3550 bitumen at (a) 0.01 Hz and 0.3 Hz.

Figure 4.13 – Results of strain amplitude sweep tests and estimation of physical hardening effect on  $\phi$  of B3550 bitumen at (a) 0.01 Hz and 0.3 Hz.

Figure 4.14 – (a) Isotherms; (b) Master curve and (c) temperature shift factors of B5070 bitumen LVE limit physical hardening constants ( $G_b$ ) at  $T_{ref} = 10^{\circ}\text{C}$

Figure 4.15 – Plots showing B5070 bitumen (a) stress and strain limits as a function of phase angle  $\phi_{(95\%)}$  (b) stress and strain limits as a function of  $|G^*|_{95\%}$  (c) strain limit isotherms and (d) stress and strain limit master curves at  $T_{ref} = 10^{\circ}\text{C}$

Figure 4.16 – Linear viscoelastic (a) strain limits as a function of  $|G^*|_{95\%}$ ; (b) stress limits as a function of  $|G^*|_{95\%}$  from low to medium temperatures ( $-25^{\circ}\text{C}$  to  $20^{\circ}\text{C}$ )

Figure 4.17 – Plots of B5070 bitumen showing (a) Cole-Cole diagram of  $|G^*|_{95\%}$  values (b) Black diagram of  $|G^*|_{95\%}$  and  $\phi_{(95\%)}$  values, corresponding to norm and phase angle of complex shear modulus at the LVE limit, for all tested frequencies and temperatures (c) Master curves of  $|G^*|_{95\%}$  and  $\phi_{(95\%)}$  values, corresponding to norm and phase angle of complex shear



## Figures

---

*modulus at the LVE limit, and 2SP1D simulations. (d) Temperature shift factors and WLF fit used to build the master curves.*

*Figure 5.1 - Example of DSR complex modulus test results for bitumen B5070-1: a) norm of complex modulus isotherms; b) phase angle isotherms*

*Figure 5.2 - Example of DSR complex modulus test results for bitumen B5070: a) Black diagrams; b) Cole-Cole diagrams; c) normalised Cole-Cole diagrams*

*Figure 5.3 – 2S2P1D fitted complex modulus test results for bitumen B3550-1: a) Cole-Cole plot; b) Black diagram; c) master curves of norms of complex modulus and phase angle; d) WLF temperature shift factors at  $T_{ref} = 10^{\circ}\text{C}$*

*Figure 5.4 – 2S2P1D fitted complex modulus test results for bitumen PmB: a) Cole-Cole plot; b) Black diagram; c) master curves of norms of complex modulus and phase angle; d) WLF temperature shift factors at  $T_{ref} = 10^{\circ}\text{C}$*

*Figure 5.5 – Kaelble fitted shift factors  $a_T$  of all tested bitumens at  $T_{ref} = 10^{\circ}\text{C}$*

*Figure 5.6 – Comparison of shift factor equation accuracies on test bitumens*

*Figure 5.7 – Graph of vertical shift factors  $bT$  versus temperatures*

*Figure 5.8 – Refitted 2S2P1D complex modulus test results for vertically shifted bitumen B3550-1: a) Cole-Cole plot; b) Black diagram; c) master curves of norms of complex modulus and phase angle; d) temperature shift factors at  $T_{ref} = 10^{\circ}\text{C}$*

*Figure 5.9 – Master curves of imaginary shear complex modulus of a) B5070 b) B3550; c) PmB bitumen at  $T_{ref} = 10^{\circ}\text{C}$*

*Figure 6.1 - 4 mm and 8 mm parallel plate axial strain amplitude sweep test*

*Figure 6.2 – B5070 5mm height axial complex modulus  $E^*$  test results at  $-5^{\circ}\text{C}/0.01\%$ . a) Norm of complex modulus; and b) phase angle in function of number of cycles; c) Complex modulus  $E^*$  and phase angle  $\phi_E$  average values with respective standard deviations.*

*Figure 6.3 - Black diagrams of B5070 bitumen axial (left,  $E^*$ ) and shear (right,  $G^*$ ) complex modulus, obtained with 4 mm parallel plate at different aspect ratios*

*Figure 6.4 - Black diagrams of B5070 bitumen axial (left,  $E^*$ ) and shear (right,  $G^*$ ) complex modulus measured with 8 mm parallel plate at different aspect ratios.*

*Figure 6.5 – Isothermal curves of B5070 bitumen axial complex modulus (left,  $E^*$ ) and phase angle (right,  $\phi_E$ ) at 5 mm sample height ( $AR=0.5$  and  $0.8$ ).*

*Figure 6.6 - Black diagram of B5070 bitumen axial (left,  $E^*$ ) and shear (right,  $G^*$ ) complex modulus at 5 mm sample height.*

## Figures

---

Figure 6.7 – Experimental measurements of B5070 bitumen normalised complex modulus a)  $G^*_{norm}$  in Cole-Cole plane, b)  $G^*_{norm}$  in Black space obtained using the two DSR assemblies at 1.75 mm and 5 mm specimen heights

Figure 6.8 – 2S2P1D fitted B5070 bitumen axial complex modulus  $E^*$  and shear complex modulus  $G^*$  a-b) Cole-Cole curve; c-d) Black diagrams; e-f) master curves at  $T_{ref} = 10^\circ\text{C}$  and g) Experimental shift factors fitted with WLF equation at  $T_{ref} = 10^\circ\text{C}$ .

Figure 6.9 – Experimental results and fitted 2S2P1D curves of normalised complex modulus a)  $E^*_{norm}$  and  $G^*_{norm}$  in Cole-Cole plane, b)  $E^*$  and  $G^*_{norm}$  in Black space, c)  $|E^*$  and  $G^*_{norm}|$  master curves at  $T_{ref} = 10^\circ\text{C}$ , d)  $\phi E$  and  $\phi G_{norm}$  master curves at  $T_{ref} = 10^\circ\text{C}$

Figure 7.1 – B5070 axial complex modulus test results at  $-5^\circ\text{C}/0.1\%$  strain. a) Norm of complex modulus; and b) phase angle in function of number of cycles.

Figure 7.2 – Complex modulus and phase angle average values with respective deviations of B5070 bitumen at  $-5^\circ\text{C}/0.1\%$

Figure 7.3 – a) Norm of axial complex modulus isotherms; b) phase angle isotherms; c) Master curve of axial complex modulus and d) phase angle master curve e) experimental at WLF fit of B5070 bitumen at  $T_{ref} = 10^\circ\text{C}$  measured at 0.1% strain

Figure 7.4 – 2S2P1D fitted B5070 bitumen axial complex modulus  $E^*$  and shear complex modulus  $G^*$  at 5 mm test height a) Cole-Cole curve; b) Black diagrams; c) master curves at  $T_{ref} = 10^\circ\text{C}$  and d) Experimental shift factors fitted with WLF equation at  $T_{ref} = 10^\circ\text{C}$ .

Figure 7.5 – Experimental results and fitted 2S2P1D curves of normalised complex modulus of B5070 bitumen a)  $E^*_{norm}$  and  $G^*_{norm}$  in Cole-Cole plane, b)  $E^*$  and  $G^*_{norm}$  in black space, c)  $|E^*$  and  $G^*_{norm}|$  master curves d)  $\phi E$  and  $\phi G_{norm}$  master curves at  $T_{ref} = 10^\circ\text{C}$  and 0.1% axial strain

Figure 7.6 - Norm of complex Poisson's ratio  $\nu^*$  and phase angle  $\phi\nu$  of B5070 a) isotherms of experimental results; b) isochrones of experimental results

Figure 7.7 - The experimental results of the complex Poisson's ratio  $\nu^*$  of B5070 bitumen a) Master curve of norm of Poisson's ratio; b) Master curve of Phase angle of Poisson's ratio c) WLF fit of shift factors at  $T_{ref} = 10^\circ\text{C}$

Figure 7.8 - The 2S2P1D simulated results of the complex Poisson's ratio  $\nu^*$  of B5070 bitumen a) norm of Poisson's ratio; b) Phase angle of Poisson's ratio

Figure 7.9 – Finite element model of the binder

Figure 7.10 – Effect of Poisson's ratio on the simulated binder stiffnesses at varying aspect ratios

## Figures

---

Figure 7.11 – Effect of aspect ratio ( $s$ ) on stress and strain distribution along the central axis ( $r$ ) of the bitumen at a constant Poisson's ratio (0.35)

Figure 7.12 – Effect of aspect ratio ( $s$ ) on stress and strain distribution along the central axis ( $r$ ) of the bitumen at a constant Poisson's ratio near oedometric condition (0.49995)

Figure 7.13 – The distribution of stress  $\sigma_{zz}$  and strain tensor  $\varepsilon_{zz}$  in the bitumen's central region at 5 mm specimen height

Figure 7.14 – The distribution of stress  $\sigma_{rr}$  and strain tensor  $\varepsilon_{rr}$  in the bitumen's central region at 5 mm specimen height

Figure 7.15 – The distribution of stress  $\sigma_{\theta\theta}$  and strain tensor  $\varepsilon_{\theta\theta}$  in the bitumen's central region at 5 mm specimen height

Figure 7.16 – The distribution of stress  $\sigma_{rz}$  and strain tensor  $\varepsilon_{rz}$  in the bitumen's central region at 5 mm specimen height

Figure 7.17 – Effect of bitumen stiffness on stress distribution along the axis of the bitumen at a constant Poisson's ratio a)0.35; b)0.49995

Figure 7.18 – Plots of a) Simulated phase angle at  $-5^{\circ}\text{C}$ ; b) measured phase angle  $\varphi_G$  and simulated phase angle  $\varphi_E$

Figure 7.19 – Ratio of measured complex modulus and true material modulus as a function of Poisson's ratio

Figure 7.20 – Ratio of simulated apparent modulus and FEM input modulus as a function of Poisson's ratio

Figure 7.21 – B5070 bitumen Poisson's ratio determination at  $-5^{\circ}\text{C}/10\text{ Hz}$  in order to correct the complex modulus ( $E_{\text{measured}}^*$ ) and obtain ( $E_{\text{true value}}^*$ )

Figure 7.22 – Comparison between measured and simulated a) norm of axial complex modulus b) phase angles.

Figure 7.23 – 2S2P1D fitted B5070 bitumen FEM axial complex modulus  $E^*$  a) Cole-Cole curve; b) Black diagrams; c) master curves and d) shift factors fitted with WLF equation at  $T_{\text{ref}} = 10^{\circ}\text{C}$ .

Figure 7.24 – Norms and phase angles of simulated B5070 bitumen Poisson's ratio a) isotherms b) isochrones; c) 2S2P1D fitted master curves at  $T_{\text{ref}} = 10^{\circ}\text{C}$ .

Figure 7.25 – Corrected experimental results and fitted 2S2P1D curves of normalised complex modulus of B5070 bitumen measured at 0.1% axial strain a)  $E_{\text{norm}}^*$  and  $G_{\text{norm}}^*$  in Cole-Cole plane, b)  $E^*$  and  $G_{\text{norm}}^*$  in black space, c)  $|E^*$  and  $G_{\text{norm}}^*|$  master curves d)  $\varphi_E$  and  $\varphi_{G_{\text{norm}}}$  master curves at  $T_{\text{ref}} = 10^{\circ}\text{C}$

## Figures

---

*Figure 7.26 – PmB bitumen Poisson's ratio determination at -5°C/0.1 Hz.*

## 1. Introduction

Bituminous mixture is the most common material used to construct the surface course and base course of pavement structures around the world. The binding strength of the bituminous binder is a critical factor in determining the bearing capacity and durability of flexible pavement structures. The mechanistic pavement design approaches are typically executed through the specification of loading conditions, estimation of component sizes, structural analysis based on theoretical principles, comparison of critical stresses, strains, or deflections with allowable values, and iterative adjustments to materials or geometry until a satisfactory design is attained. When this strategy is implemented, the design challenge for a flexible pavement shifts towards determining the appropriate proportions of the structure to ensure that the pavement's design life does not go beyond the crucial thresholds of stress or strain. However, it is necessary to possess knowledge regarding the rheological properties of bituminous pavement materials, specifically the elastic modulus  $E$  and Poisson's ratio  $\nu$ . The modulus plays a crucial role in determining the load distribution characteristics, resistance to deformation including rutting, and fatigue resistance, which is closely linked to cracking behaviour. Scholars have persistently investigated the characteristics of bitumen in relation to its stiffness, resistance to rutting, and resistance to fatigue. Nevertheless, it is imperative to have a comprehensive understanding of the rheological characteristics of current binders due to the emergence of bitumen recycling and the advancements in sustainable binder technology. Consequently, the accurate characterization of the recently developed binders in relation to pavement performance can be achieved.

The rheological characterization of bitumen has been conducted using several apparatuses, including the Bending Beam Rheometer, Annular Shear Rheometer, and Metravib device. In recent times, the utilisation of DSR has predominantly been observed among pavement technologists and researchers. The acceptance of the test findings obtained from the 4 mm plate test in the context of low-temperature bitumen testing remains limited. The behaviour of bitumen in the linear viscoelastic strain domain was investigated at the ENTPE laboratory. Bitumen's thermomechanical properties were measured using a new dynamic shear rheometer (DSR) equipped with an axial motor.

The complex modulus of binders has been measured on a large range of temperatures and frequencies at low strain levels, where the behaviour is linear viscoelastic. This thesis was primarily a contribution to a better understanding of the three important thermomechanical

responses ( $G^*$ ,  $E^*$ ,  $\nu^*$ ) of binders to a small agitation in the frequency domain. Within the framework of the dissertation, the subsequent specific objectives are:

- To verify the existence and extent of physical hardening development on a bitumen tested with DSR shear oscillatory assembly. As well as to define in quantitative terms, the effects of physical hardening on the bitumen linear viscoelastic limit determination.
- To evaluate the LVE behaviour of binders in response to shear oscillatory loading across large temperature and frequency ranges.
- To investigate the response of bitumen to axial sinusoidal loading on the DSR by determining the appropriate sample height. As well as, to determine the LVE limit of bitumen.
- To evaluate the LVE behaviour of different binders in response to axial loading across large temperature-frequency pairs and subsequently, in shear oscillatory loading across similar temperature-frequency pairs.
- To determine the Poisson's ratio of binders across wide temperature and frequency pairs.

This thesis consists of eight chapters including introduction and conclusion. Chapter 2 consists of a literature study of the thermomechanical characterization of binders within the linear viscoelastic domain and the derivation of mixture thermomechanical properties based on known binder characteristics. Chapter 3 describes the DSR and materials investigated. In chapters 4, 5, 6, and 7, four research campaigns are presented and analysed in every chapter. Each campaign was built independently, with its own objectives, experimental plans, findings, and conclusions, despite their interdependence. The first campaign investigated the effect of physical hardening on the linearity of bitumen. During the second campaign, the thermomechanical response  $G^*$  of bitumen was studied across large temperature and frequency pairs. The third campaign proposes a new test for determining the axial ( $E^*$ ) and shear ( $G^*$ ) complex moduli of a binder using a DSR and presents the initial experimental results. The combination of both outcomes ( $G^*$ ,  $E^*$ ) provides access to Poisson's ratio values. The fourth campaign investigated the determination of Poisson's ratios for various binders. The eighth chapter provides a conclusion and perspective to all the campaigns.

## 2. Literature Review

### 2.1 Pavement

A pavement is an intricate structure composed of multiple layers, constructed on top of a subgrade, with the purpose of withstanding the stresses exerted by vehicles and the effects of climate. This should additionally offer its consumers favourable utilisation conditions, encompassing a suitable degree of comfort, cost-effectiveness, and safety. Furthermore, it is imperative that the surface of the material exhibits impermeability, or at the very least, prevents the passage of water to the underlying layers. The layers have the potential to be either bounded (consisting of a surface course and base) or unbounded (comprising a sub-base) in relation to one another. Typically, bitumen-based emulsions are employed for the purpose of glueing layers together. Both bituminous mixes and concrete (Figure 2.1) can be used to construct the surface course of a pavement. The base layer has the potential to consist of either bituminous mixes or granular materials, which may or may not have been treated with hydraulic binders. Sub-bases are often comprised of granular materials.

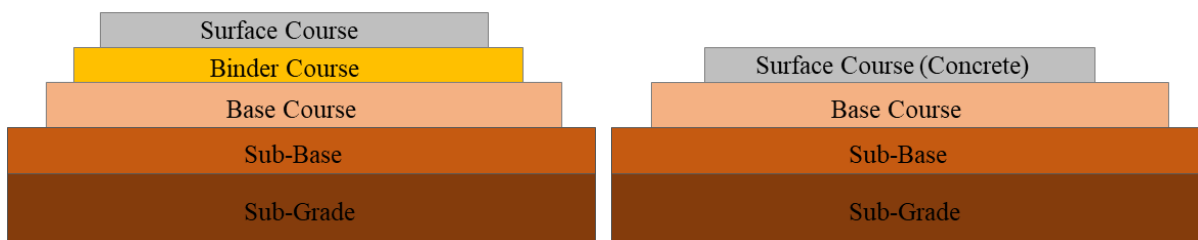


*Figure 2.1 – Basic elements of flexible pavements (left) and rigid pavements (right)*

France's transportation network encompasses many types of pavement structures. SETRA-LCPC (1994) categorises constructions into six distinct families, namely: flexible pavements, thick bituminous layer pavements, semi-rigid pavements, mixed-structure pavements, inverse-structure pavements, and rigid pavements.

Flexible pavements are distinguished by the inclusion of a slender layer of bituminous mixture in the uppermost course of the pavement. The base layer consists of a bituminous mixture with a thickness of less than 150 mm, which is placed above a sub-base layer made of non-treated granular materials. The sub-base layer accounts for a total thickness ranging between 300 and 600 mm. The utilisation of this technology is limited to routes that see modest amounts of traffic (SETRA-LCPC 1994).

Thick bituminous layer pavements consist of a surface layer made of bituminous mixture, which is spread over a base formed of one or two layers of bituminous mixture. The prescribed range for the thickness of the base layer in this particular pavement configuration is 150 to 400 mm. Furthermore, it is crucial to ensure that the interface between layers is properly bounded in order to prevent any degradation in the structural serviceability.

Semi-rigid pavements are characterised by the utilisation of materials treated with hydraulic binder as the base and sub-base layers. According to SETRA-LCPC (1994), the thickness of the treated layers typically ranges from 20 to 50cm. Simultaneously, it deposits a layer of bituminous mixture onto the surface course.

Mixed-structure pavements consist of a composite composition of a bituminous mixture layer and a treated material layer. The surface course layer of the pavement is composed of a bituminous mixture, which is situated above a bituminous base layer. Beneath the base layer lies a sub-base layer that consists of materials treated with a hydraulic binder. A pavement construction is classified as "mixed" when the ratio between the thickness of the bituminous layer and the total pavement thickness is roughly 0.5.

Inverse-structure pavements consist of layers of bituminous mixture with a combined thickness of around 150 mm, which are placed on top of a non-treated granular material layer measuring approximately 120 mm in depth. Subsequently, the aforementioned two layers are superimposed over a base consisting of material that has undergone treatment with a hydraulic binder. The overall thickness of the construction ranges from 600 to 800 mm.

In conclusion, rigid pavements exhibit the notable feature of having a surface course layer composed of concrete, regardless of whether it is reinforced or not. The typical thickness of this concrete layer is from 15 to 40cm, and it may be overlaid with a thin layer of bituminous mixture known as a wearing course. The foundation of this particular construction may consist of a material that has been treated with a hydraulic binder, such as concrete, or alternatively, an untreated drainage layer. The application of the concrete surface layer directly over the sub-grade is also a viable option.

### 2.1.1 Bituminous Pavement Materials

A bituminous mixture is a composite material composed of mineral aggregates and bitumen (H Di Benedetto & Corté, 2005). Aggregates are commonly referred to as the structural skeleton of the material, while bitumen serves as the binder. In actuality, the cohesion of a bituminous



mixture is supplied by the mastic, which is a mixture of bitumen and the finest granular fraction. Additionally, air is the third component of a bituminous mixture, occupying the spaces between aggregates that are not filled with bitumen. These voids are commonly referred to as "air voids" and have a significant impact on the behaviour of the material.

#### *2.1.1.1 Aggregates*

Typically, aggregates consist of crushed rock and sand. The rock material is primarily coarse aggregate retained on sieve No. 8 (2.36mm), sand is primarily fine aggregate passing No. 8 sieve, and filler is primarily mineral dust passing No. 200 screen.

Gradations of the total aggregate and the separate fractions are typically provided. Any mix design begins with the selection and combining of aggregates to achieve a gradation within the permitted limitations. This is sometimes called mechanical stabilisation. The optimal grading curve is the one that produces the densest feasible mixture, maximises the interparticle interaction network, and minimises the amount of air voids. However, adequate air voids must be provided to prevent bleeding or rutting caused by bitumen completely filling the crevices between aggregate particles (Lira, Jelagin, & Birgisson, 2013).

In the balanced mixture design method, the optimal binder content is determined by selecting an aggregate gradation that provides superior resistance to both fatigue and rutting. Therefore, obtaining an optimal packing of aggregates will play a significant role in balancing distresses, and will also aid in relating aggregate gradation to the rutting potential of bituminous mixtures. Illustrations of bituminous mixture design packing optimization can equally be found in (Abhijith & Kumar, 2020; François Olard, 2012).

A significant factor influencing the final properties of a bituminous mixture is the aggregate grading curve. An analysis of Particle Size Distribution (PSD) is used to determine the grading curve. A representative sample of the aggregates comprising the mixture is sieved through standard sieves, each of which corresponds to a distinct granular fraction. A curve can be obtained by plotting the percentage of aggregates (by weight) that pass (or are retained) through each sieve. Continuous grading denotes the presence of all granular classes or fractions. A discontinuous grading indicates a small amount of one or more fractions. A gap-graded grading curve occurs when a fraction is completely absent. A 0/20 gap-graded grading curve is shown in Figure 2.2

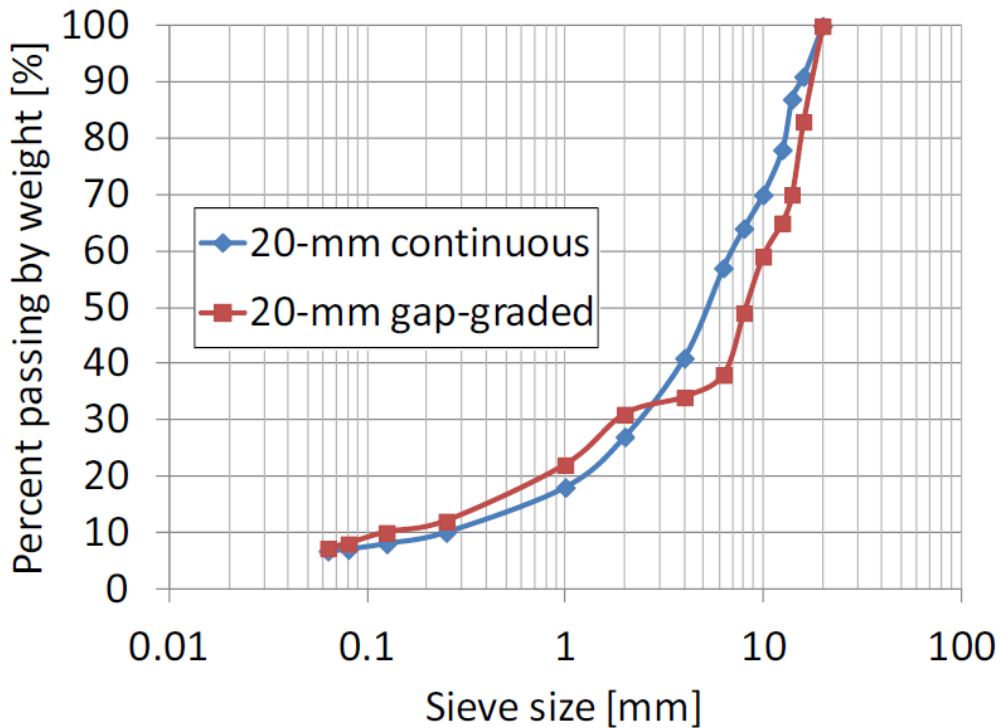


Figure 2.2 - 20mm Continuous and 20mm Gap-graded curve (Ramirez Cardona, Pouget, Di Benedetto, & Olard, 2015)

### 2.1.1.2 Fillers

According to the majority of road standards, mineral fillers are regarded as part of the aggregate and are defined as “finely divided mineral matter such as hydrated lime, rock dust, slag dust hydraulic cement, loess, fly ash, or other suitable mineral matter”. Fillers play an important role in stabilizing bituminous mixtures by filling the voids within the larger aggregate particles, and improving the consistency of the binder that cements the larger aggregate particles (Kallas, Puzinauskas, & Krieger, 1962).

In addition, fillers with a high surface area lead to an increment in absorbing bitumen, which changes the performance of bituminous mixtures (Lesueur, 2009). It was reported that filler type and content could affect the characteristics of asphalt mixtures such as resistance to permanent deformation, fatigue behaviour and moisture sensitivity (Arabani & Pedram, 2016). According to EN 13043:2003, "filler" is defined as the aggregate fraction smaller than 63  $\mu\text{m}$ . The most used ones are hydrated lime and limestone since they present very good adhesive properties with bitumen (Tapsoba, 2012).

Several studies have shown that volume filling, particle structuralizing, and physicochemical interactions are the three primary reinforcement mechanisms of filler in bituminous mastic

(Clopotel, Velasquez, & Bahia, 2012; Underwood & Kim, 2011). As volume filling and particle structuralizing involve mechanical reinforcement, filler particles create an interconnected network, accelerating stiffening with increasing volume fraction (Underwood & Kim, 2011). Physicochemical interaction involves the adsorption of bitumen polar groups (asphaltenes and resins) onto filler particles by electrostatic, dipole-dip, or Van der Waals forces (Clopotel et al., 2012). Little & Petersen, (2005) investigated the effect of filler particles and bitumen interaction on the rheological properties of mastics in terms of physical and chemical interactions. Unaged and aged bitumens with two types of fillers (limestone filler and hydrated lime filler) at one filler content of about 20% by volume were tested. The rheological results showed that the hydrated lime filler had considerable impact on the loss tangent ( $\tan \delta$ ) than the limestone filler, but the impact was bitumen dependent. Mastic with lower loss tangent value may improve the rutting resistance of asphalt pavements (Lesueur & Little, 1999).

Several researchers have found an increase in stiffness when substituting limestone filler with hydrated lime. (Bari & Witczak, 2005; Cardone, Frigio, Ferrotti, & Canestrari, 2015; Miró, Martínez, Pérez-Jiménez, Botella, & Álvarez, 2017). This increase is estimated to be 18% for bituminous mixtures at 15°C and 10 Hz when 1/3 of the limestone filler is replaced with hydrated lime. This effect increases with an increase in material temperature or a decrease in loading frequency (Phan, Di Benedetto, Sauzéat, & Lesueur, 2016).

### *2.1.1.3 Air voids*

Air voids are small air spaces or pockets of air that occur between the coated aggregate particles in the final compacted mix. A certain percentage of air voids is necessary in asphalt mixes to allow for some additional pavement compaction under traffic and to provide spaces into which small amounts of asphalt can flow during this compaction (Colorado Asphalt Pavement Association, 2023). Air-voids affect the properties of asphalt pavement, they cause fatigue damage under repeated load and exasperates the quality of asphalt mix, thereby leading to occurrence of micro cracks on pavement surface.

According to (Mauduit et al., 2010; Walubita, Jamison, & Alvarez, 2012), as cited in Cardona (2016), the air voids in a compacted asphalt mixture are in the diametric ranges of 0.5 and 1.9 mm.

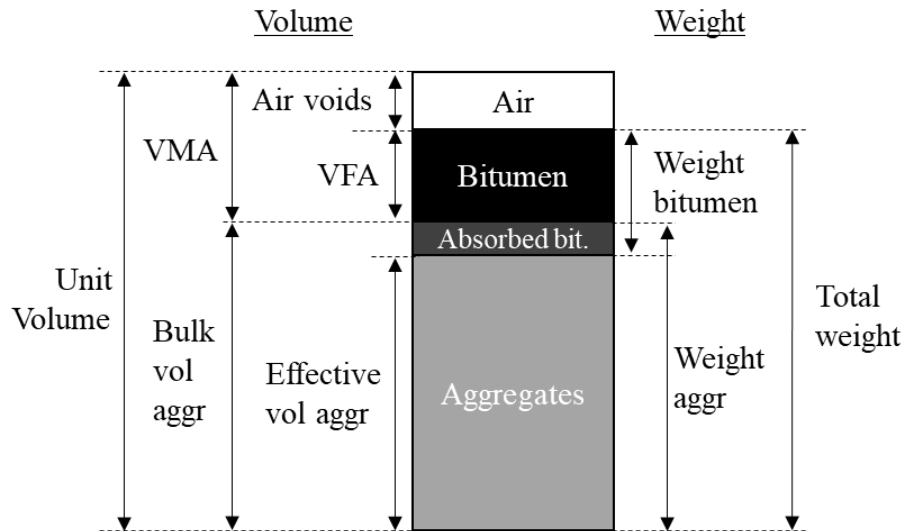


Figure 2.3 - Scheme of volumetric properties of a bituminous mixture (Freire, 2020).

Air voids greatly influences the performance of flexible pavements such as stability, stiffness or modulus; the stability increases as density increases with air voids decrease (Kassem, Masad, Lytton, & Chowdhury, 2011; Zaltuom, 2018). Five or more stability points are lost for every one percent reduction in air voids (Mallick, 1999). Laboratory investigations indicate that the fatigue life of asphalt concrete could be reduced by 35 percent (or more) for each one percent increase in air voids (Zaltuom, 2018). The impact of air void changes differs between stress controlled and strain-controlled loading.

High-design air void asphalt is utilized in high-traffic areas where the asphalt mix may be further compacted. Asphalt with lower-design air voids is used for locations with light traffic volumes where there is very little further compaction of the asphalt mix after placement. Due to the reduced air voids, this asphalt achieves high levels of durability and fatigue resistance and has a long service life. The voids within the mix exist in three distribution patterns, the first being the interconnecting voids whose geometry creates an association between two faces of a pavement layer or sample. This void pattern is sought after in porous asphalts. Non-connecting voids are opened unto the face of the pavement layer or mix while occluded voids are inaccessible.

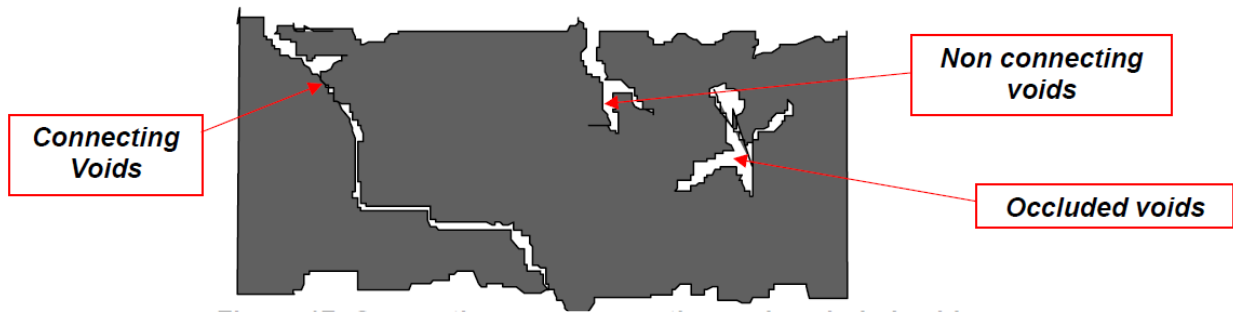


Figure 2.4 - Connecting, non-connecting and occluded voids (Delorme & Wendling, 2007)

It is reported by Kassem et al., (2011), that air void distributions in compacted mixtures are influenced by laboratory compaction methods (Masad, Muhunthan, Shashidhar, & Harman, 1999) which in turn affects the mechanical properties of the mixtures. The angle of gyration has been demonstrated by (Tashman, Masad, D'Angelo, Bukowski, & Harman, 2002), specimen diameter and height (Hall, Dandu, & Gowda, 1996) to influence the air void distribution in SGC specimens. Sample height increment represents air voids vertical heterogeneity (Chen, Huang, & Shu, 2013; Thyagarajan, Tashman, Masad, & Bayomy, 2010) although the statistical significance of these effects was not considered by (Chen et al., 2013). Leandro, Vasconcelos, & Bernucci, (2017) evaluated the compaction methods which included the Marshall, SGC with 100mm, and 150mm diameter specimen, the French gyratory shear compactor (PCG), and also the LCPC French roller compactor on the air voids, wherein the Marshall and the 100mm Superpave methods led to the same air void volume and optimum asphalt content. However, there is an effect on the size of mould. The average values of air void for 150mm diameter specimens were lower compared to the Marshall Superpave 100mm specimens which are similar. Air voids was produced by rolling compaction in the slabs, considering the Marshall optimum bitumen content (5.8%). The SGC-designed mixture would result in 8% voids in rolling compaction with a corresponding 5.2% bitumen content.

Although the PCG and SGC compactions are based on the same principle (gyratory), the PCG and the French rolling compaction produce specimens with a higher volume of air voids. The SGC represents the densification level obtained by combining constructive compaction and the one imposed by the traffic along two to three years of operation while PCG is an initial step in the French method of asphalt mixture design, which tries to represent the densification of the mixture on the road shortly after its construction (Leandro et al., 2017)

#### 2.1.1.4 Bitumen

Bitumen is a shiny black material consisting of various hydrocarbons with a high molecular weight and is utilised in asphalt mixture for the outstanding purpose of impermeability against water susceptibility and possessing good adhesive property, in all related conventional applications. Such materials as mentioned above are usually by-products of crude oil refinement process in petroleum refineries (Ziari, Farahani, Goli, & Sadeghpour Galooyak, 2014).

Bitumen used for road building consists primarily of hydrocarbons and their derivatives, which are soluble in trichloroethylene and exist as viscous liquids or semi-solids. There are two sources of bitumen: naturally occurring bitumen and bitumen derived from the refining of petroleum. Bitumen can exist in nature either in a relatively pure state or in an impregnated rock (Kett, 1998).

##### 2.1.1.4.1 Bitumen constitution and structure

Traditionally, asphaltenes and maltenes have been used to classify bitumen into two broad chemical groups (Hunter, Self, Read, & Hobson, 2015). Maltenes are the remaining portion of bitumen after precipitation of asphaltenes. The asphaltenes are further subdivided into saturates, aromatics, and resins (Hunter et al., 2015). According to González (2010), the precipitation of asphaltenes with n-heptane, followed by chromatographic separation of the remaining constituents/fractions, has been the most common method for defining bitumen constituents. Components include Saturates (S), Aromatics (A), Resins (R), and Asphaltenes (A). The presence of each fraction in bitumen is further classified by complexity, aromaticity, and molecular weight in the following order: S<A<R<A. The main characteristics of these four broad component groups and the metallic constituents are now discussed.

As stated by Lesueur (2009), 5-20% of bitumen is consisted of saturates, with a reported average molecular weight ranging between 470 -880g/mol. They are colourless, non-polar viscous oils which is composed of straight and branched-chain aliphatic hydrocarbons and cycloaliphatic compounds. Furthermore, saturates are characterized by a hydrogen-carbon ratio (H/C) of 2.

Bitumen is composed of 40 to 65% aromatics with an average molecular weight of 570 to 980g/mol. It is stated that the H/C ratio of aromatic fractions ranges between 1.4 and 1.6. Aromatics are composed of low-carbon chains attached to an unsaturated ring system, and thus constitute the majority of the dispersion medium for peptized asphaltenes (Lesueur, 2009).

As stated by (González, 2010; Lesueur, 2009), in n-heptane, resins are soluble. They are predominantly made up of hydrogen and carbon, with a small amount of oxygen, sulphur, and nitrogen atoms. Polar in nature, they are dark brown in colour, solid or semi-solid, and extremely adhesive. Resins are asphaltenes' dispersing agents or peptizes. The ratio of resins to asphaltenes partially determines whether bitumen is a solution (sol) or gelatinous (gel). The bitumen-derived resins have molecular weights ranging from 780 to 1400 g/mol and a H/C atomic ratio between 1.4 and 1.7.

Asphaltenes are insoluble in n-heptane and are black or brown amorphous solids with carbon, hydrogen, nitrogen, sulphur, and oxygen atoms. Asphaltenes are typically regarded as highly polar, complex, and molecularly heavy aromatic compounds responsible for the structure in bitumen see Figure 2.5. They are stated to have a high molecular weight of 1200 to 1200,000g/mol and H/C ratio of asphaltenes ranges from 0.98 to 1.6 (González, 2010). The asphaltene content of a bitumen has a significant effect on its rheological properties. Increasing the asphaltene content results in a harder, more viscous bitumen with a lower penetration, a higher softening point, and consequently a greater viscosity. Asphaltenes have a particle size between 2 and 5 nm and account for 5 to 25% of bitumen.

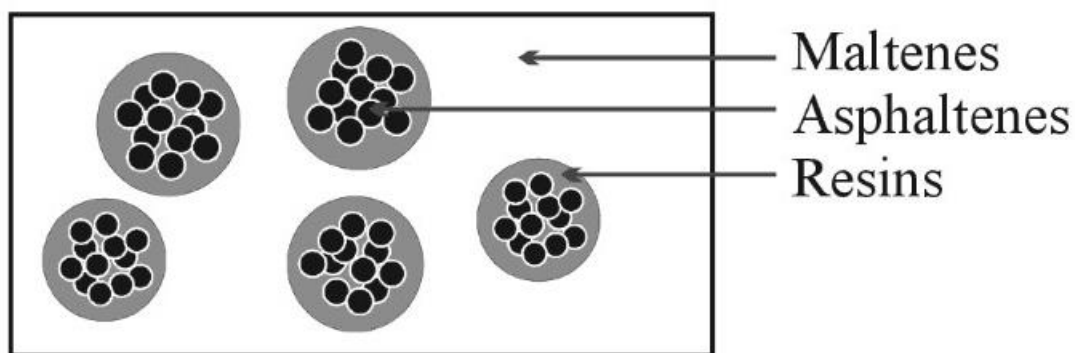


*Fig. 2.5 Asphaltenes are discontinuous agglomerates joined together by resin compounds where maltenes form a continuous phase (González, 2010) as adapted from Kennedy*

#### 2.1.1.4.2 Types of bitumen

Various types of bitumen are available on the market, depending on the refining and production processes. (European Asphalt Pavement Association & National Asphalt Pavement Association, 2011; Mangiafico, 2014):

- i. Pure bitumen: Bitumen obtained solely through atmospheric and vacuum distillation of a particular crude oil. These are the most prevalent binders used in pavement engineering.

- ii. Cutback bitumen: Pure bitumen whose viscosity has been temporarily reduced by mixing it with volatile solvents, such as kerosene, so that it can penetrate granular material layers more effectively or so that it can be sprayed at low temperatures. Common applications include tack coating and spray sealing. Once applied to the surface to be coated, the solvents evaporate and the remaining bitumen's hardness returns to values comparable to those of the original bitumen.
- iii. Fluxed bitumen: Bitumen whose viscosity has been decreased through the addition of nonvolatile oils. The flux oil differs from cutback bitumen in that it is less volatile and does not evaporate at room temperature. As with cutback bitumen, fluxed bitumen can be applied at lower temperatures and is typically used to waterproof layers beneath new pavement or as a tack coat. Additionally, they can be used to create cold-mix patching material that can be stored for extended periods.
- iv. Air-rectified bitumen: Bitumen that has undergone mild oxidation in order to increase the average molecular weight of its constituents. Air-rectification, also known as blowing, increases the concentration of asphaltenes and modifies the penetration grade.
- v. Multi-grade bitumen: Refinement processes, such as air-rectification, reduce the thermal sensitivity of bitumen. They present bitumen properties with varying grades of penetrability at high and low temperatures (i.e., soft bitumen behaviour at low temperatures and hard bitumen behaviour at high temperatures).
- vi. Bitumen emulsions: Mixture of two immiscible components, bitumen and water, with the dispersed phase depending on the relative concentrations. An emulsifying agent, typically surfactants, is utilised to maintain the stability of the emulsion. At room temperature, they are utilised in roofing and waterproofing operations, as well as in pavement engineering.
- vii. Modified bitumen: Bitumen with altered rheological properties due to the addition of non-bituminous agents. Adhesion agents, crumb rubber, polymers, polyphosphoric acid, sulphur, and waxes are the most common additives.

Currently, polymer modification is a common method for enhancing certain characteristics of pure bitumen. Typically, between 2% and 7% by weight of polymers, elastomers, or plastomers are added to effect the modification. SBS (Styrene-Butadiene-Styrene) and EVA (Ethylene-Vinyl Acetate), respectively an elastomer and a plastomer, are the two most common polymers used in pavement engineering. An elastomer exhibits a significant elastic recovery after being subjected to a strain below its rupture



point (such as rubber), whereas a plastomer does not (e.g., polyethylene). Consequently, SBS-polymer modification can have a greater impact on the rheological properties of pure bitumen than EVA modification. (Jasso et al., 2015; Zhu, Birgisson, & Kringos, 2014). SBS polymers can have a linear or radial structure, with polystyrene blocks located at both ends of a polybutadiene block. Cross-linking is used to create a uniform network of SBS molecules (Stastna, Zanzotto, & Vacin, 2003).

When combined with bitumen, polymers tend to absorb a portion of the maltenes fractions and experience swelling, whilst the asphaltenes exhibit no absorption. When subjected to examination using fluorescence microscopy, the aromatic oils that have been absorbed exhibit a visually discernible light hue inside the phase that is abundant in polymers. Conversely, the remaining maltenes and asphaltenes manifest as a black shade, thereby constituting a cohesive phase that is predominantly composed of bitumen.

Figure 2.5 illustrates the influence of polymer content on the morphology of polymer-modified bitumen (PMB). In Figure 2.6 (a), it can be observed that for low polymer content, the polymer phase is distributed inside the continuous bitumen phase. In contrast, when the polymer concentration is large, as depicted in Figure 2.6 (c), the polymer phase assumes the role of the continuous phase, while the bitumen phase is distributed within it. At an intermediate level of polymer content, the polymer-modified bitumen (PMB) exhibits a relatively unstable structure where neither the polymer phase nor the bitumen phase dominates the overall system, as depicted in Figure 2.6 (b). In a study conducted by (Gordon D. Airey, 2002a), it was noted that comparable findings were observed in the case of SBS and EVA PMBs. However, it should be noted that the structural morphology is influenced by factors other than polymer content, such as the swelling potential of the polymer and the composition of the maltenes portion in the base bitumen.

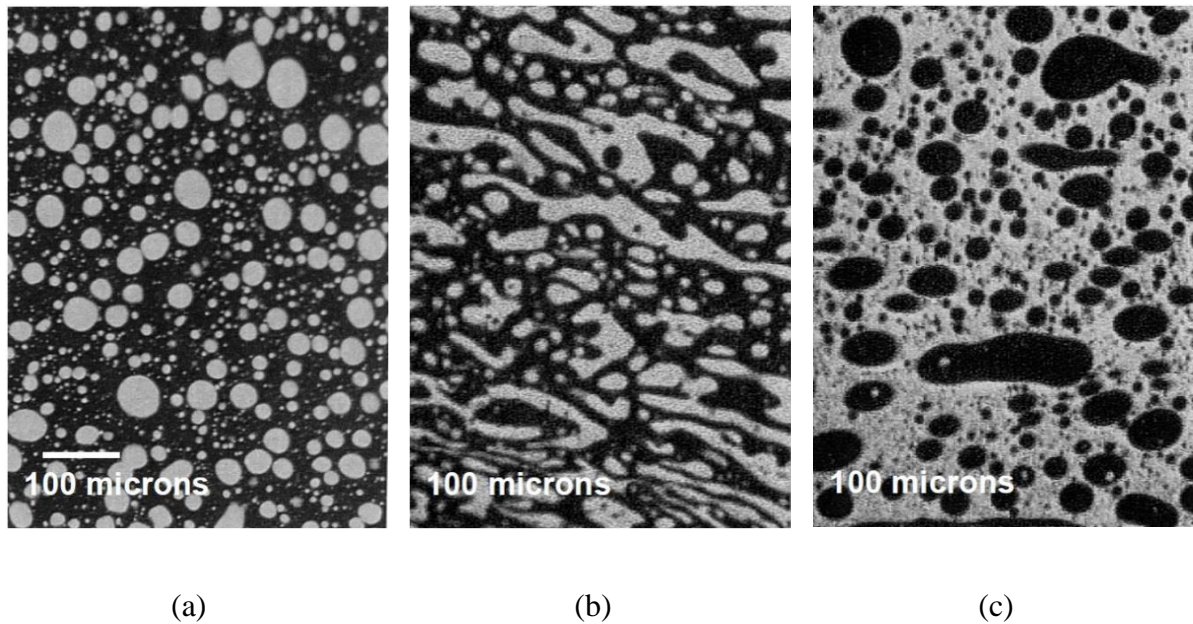


Figure 2.6 - Fluorescent microscopy images of a polymer-modified bitumen (PMB) with (a) 3% EVA, (b) 5% EVA and (c) 7% EVA adapted from (Gordon D. Airey, 2002a).

#### 2.1.1.4.3 Empirical Test on Bituminous Binders

The test generally performed on bitumen in Europe is aimed at characterizing their responses to loading effects, without considering the mechanical characteristics. These tests are therefore referred to as semi-empirical tests; which are highlighted as follows:

- i. Penetration Test - The EN 1426 penetration test determines the consistency of a penetration grade or oxidised bitumen. In this test, a needle of specified dimensions is permitted to pierce a bitumen sample under a known load at a known temperature for a known period of time. The penetration is expressed as the distance in decimillimeters (1 dmm = 0.1 mm) that a standard needle will penetrate vertically into a sample of bitumen under specified temperature, load, and load duration conditions. Typically, the applied load is 100 g, the loading duration is 5 s, and the test temperature is 25 °C. After specified conditioning at the test temperature, three separate penetration measurements are taken for each test. To the nearest integer, the average of three values is recorded. The lower the penetration value, the harder the bitumen. Inversely, the greater the penetration value, the softer the bitumen. This test serves as the basis for classifying penetration grade bitumens into standard penetration ranges. EN 12591-2009 and EN 13924-2006 outline the specifications for paving grade and hard paving grade bitumens, respectively.

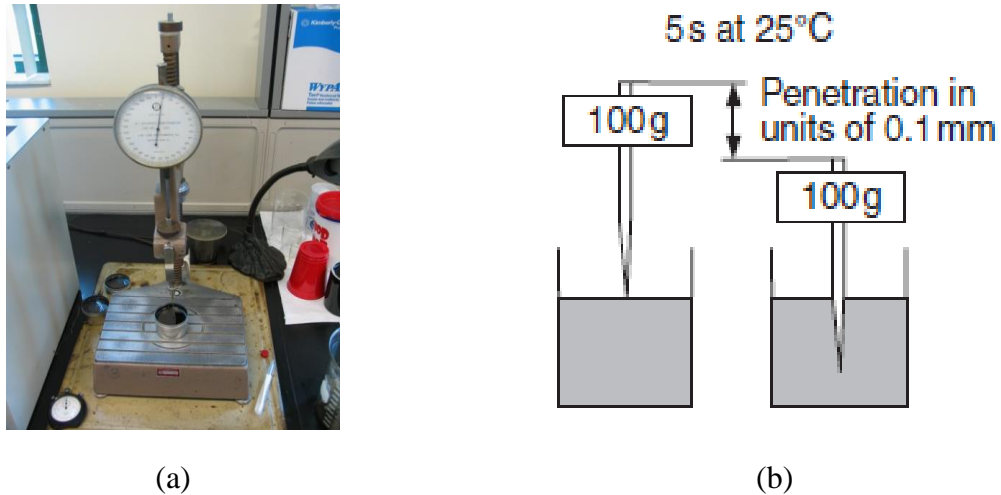


Figure 2.7 - Penetration test scheme (a) device and (b) Setup (O'Flaherty, 2001)

Softening point test - In accordance with EN 1427, a small steel ball is placed atop a bitumen sample contained in a brass ring, and the assembly is then suspended in a glass beaker containing either water or glycerine. For bitumen with a softening point above 80°C, glycerine is utilised, whereas water is used for bitumen with a softening point below 80°C. When water is utilised, the initial bath temperature is 58°C. The initial temperature of the glycerine bath is 30°C. As the temperature of the bath is increased by 5°C per minute, the bitumen softens and eventually deforms as the ball moves around the ring. The temperature displayed by the thermometer when the bitumen surrounding the ball hits the bottom plate 25 mm below the ring is the softening point temperature. The test is conducted twice, and the average of the two recorded temperatures is reported to the nearest 0.2°C for softening points below or equal to 80°C and to the nearest 0.5°C for softening points above 80 °C. The test must be repeated if the difference between the two results exceeds 1°C for softening points below 80°C or 2°C for softening points over 80 °C. The reported temperature is specified as the bitumen's softening point . The softening point is an equi-viscous temperature because it is the temperature at which all refinery bitumens have the same viscosity, which is around 1200 Pa.s. According to a rule of thumb, the mixing temperature of a penetration-grade bitumen is 110°C above its softening point; consequently, nominal 50 pen and 100 pen bitumens are frequently mixed at approximately 162°C and 156°C, respectively (O'Flaherty, 2001).

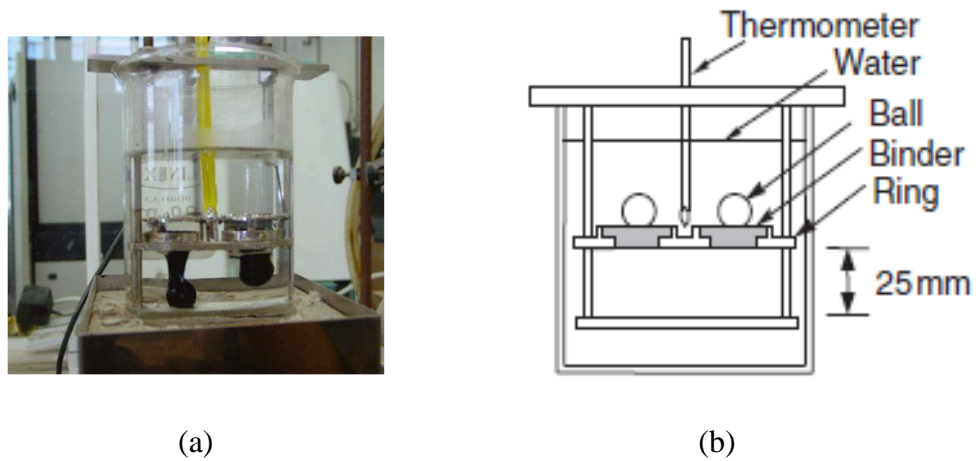


Figure 2.8 - Softening point test scheme (a) device (Cardona, 2016) and (b) Setup (O'Flaherty, 2001)

- ii. Frass breaking point - This test, which measures the (low) temperature at which bitumen achieves a critical stiffness and begins to crack, is used as a control for binders used in extremely cold areas. The Fraass breaking point is the temperature at which a thin film of bitumen adhered to a metal plate 41 mm long, 20 mm wide, and 0.15 mm thick breaks as it is slowly bent, released, and cooled at a rate of  $1^{\circ}\text{C}$  per minute (EN 12593-2015). If the penetration and softening points of a bitumen are known, the breaking point can be predicted as the temperature at which the bitumen has a penetration of 1.25 can be equated to the breaking point.

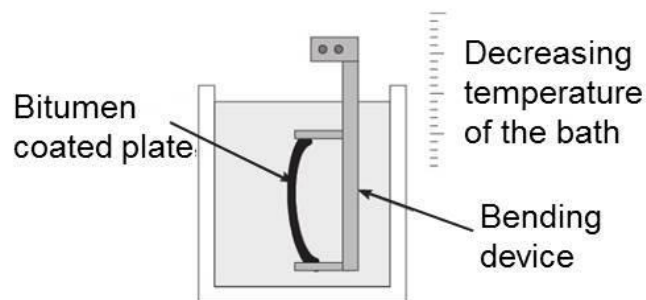


Figure 2.9 - Fraas breaking point test scheme (Cardona, 2016)

The European classification approach for bitumen is based on the previously described penetration grade classes. Classification of bitumen is possible according to the following criteria: paving bitumen is governed by (EN 12591, 2009), special hard paving bitumen is governed by (EN 13924-1, 2016), and special multi-grade paving bitumen is governed by (EN 13924-2, 2014). The primary limitations of this categorization are that it is based on semi-empirical experiments that do not account for fundamental bitumen qualities and that are

conducted at a single temperature, despite the fact that bitumen behaviour is temperature dependent.

Bitumen used in France are classified into the following penetration grade classes;

- Hard bitumen – 10/20, 15/25, 20/30, 35/50
- Semi-hard bitumen – 50/70, 70/100
- Soft bitumen – 160/200

#### 2.1.1.4.4 *Fundamental test on bitumen*

Although the semi-empirical test methods have worked reasonably well in most situations, the introduction of modified bitumens, the diversification of bitumen refinery feedstocks, and the demand for materials with greater durability have presented greater challenges for these methods.

Furthermore, the performance evaluation of asphalt pavements is not easily achieved by the physical properties as determined from the semi-empirical tests as they are subjected to complex thermal and mechanical loading conditions. Therefore, it is necessary to understand the viscoelastic behavior of bituminous binders across a wide range of temperatures and frequencies. As stated in (Anderson et al., 1994; J. Petersen et al., 1994), the performance grading system of binder classification was developed based on the fundamental testing results obtained during the Strategic Highways Research Program (SHRP) in the United States of America.

- i. Dynamic shear rheometer test – The dynamic shear rheometer (DSR) is used to measure the viscoelastic properties of binders over a wide range of frequencies and temperatures. The sinusoidal oscillatory load can either be applied in the strain or stress-controlled mode with a resulting stress or strain measured respectively. In the test, a bitumen sample sandwiched between two parallel plates is subjected to a sinusoidal torque or a sinusoidal angular displacement of constant angular frequency. The measured torque in response to the applied stress and strain to a specimen is converted into various rheological parameters. The stress response amplitude is measured by the determination of the transmitted torque through the sample as a result of the applied strain. The stress and strain are calculated based on the measured torque and angular rotation as follows:

$$\sigma = \frac{2T}{\pi r^3} \quad (2.1)$$

$$\gamma = \frac{\theta r}{h} \quad (2.2)$$

where  $\sigma$  is the shear stress ( $N/mm^2$ ),  $T$  is the torque ( $Nm$ ),  $r$  is the radius of parallel plates ( $mm$ ),  $\gamma$  is shear strain,  $\theta$  is deflection angle and  $h$  is the gap between the parallel plates ( $mm$ ).

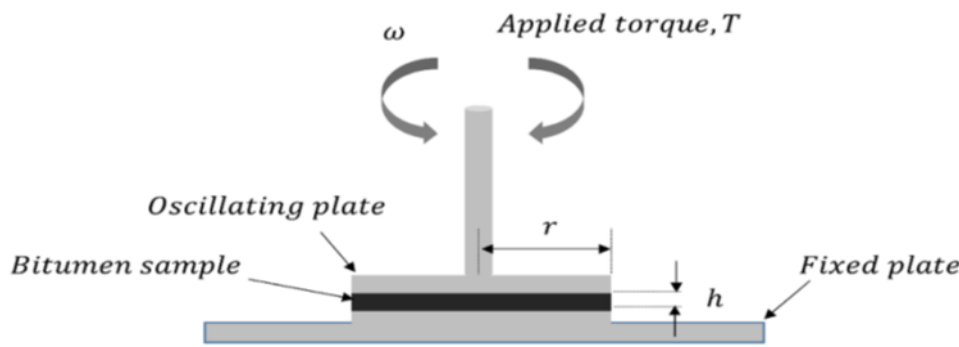


Figure 2.10 – The DSR testing configuration adapted from (Subhy, 2017)

The shear stress and strain as expressed in the Equations 2.1 and 2.2 above are dependent on the radius and gap between the parallel plates. The calculated complex modulus ( $G^*$ ) is proportional to the fourth power of the asphalt binder specimen radius. The DSR testing plates vary in sizes, which is dependent on the stiffness of the bitumen to be tested, to comply with compliance of the device. the lower the testing temperature, the smaller the diameter of the disc that needs to be used to accurately determine the dynamic properties of bituminous binders Goodrich, 1988 as cited by (Yusoff Md., 2012).

- ii. Bending beam rheometer – The bending beam rheometer (BBR) is used to measure the low temperature stiffness of binders. This test method was introduced during the strategic highway research program (SHRP) to determine binder stiffness at 60 seconds and the slope of the stiffness curve – log time versus log stiffness – the m-value (slope) (G. Rowe, Sharrock, Bouldin, & Dongre, 2001). The binder test specimen is measured (125x12.5x6.25mm) and simply supported and loaded with a constant force of 1N at mid span. The deflection produced as a function of time is used in the binder stiffness computation using equation 2.3

$$S(t) = \frac{PL^3}{4bh^3\Delta(t)} \quad (2.3)$$

Where  $S(t)$  = Creep stiffness at time,  $t$

$P$  = Applied constant load, 100g

$L$  = Distance between supports, 102 mm

$b$  = Beam width, 12.5mm

$h$  = Beam depth, 6.25 mm

$\Delta(t)$  = Deflection at time,  $t$

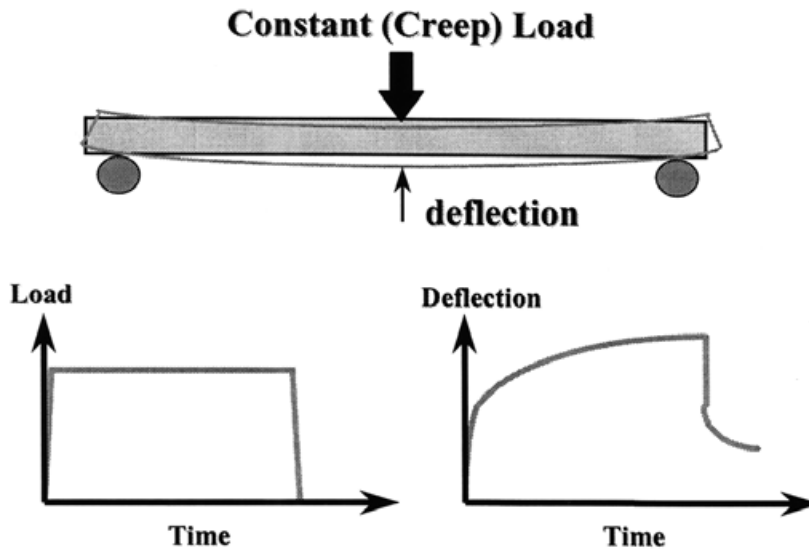


Figure 2.11 – Bending Beam Rheometer, as illustrated in (G. Rowe et al., 2001)

The creep stiffness values are determined at six loading times (8, 15, 30, 60 and 240) with  $m$  as the slope of the log creep stiffness-log time curve. The stiffness and the slope of the stiffness curve ( $m$ -value have been used in the Superpave specification as shown in Figure 2.12 (G. Rowe et al., 2001) as cited in (Yusoff Md., 2012).

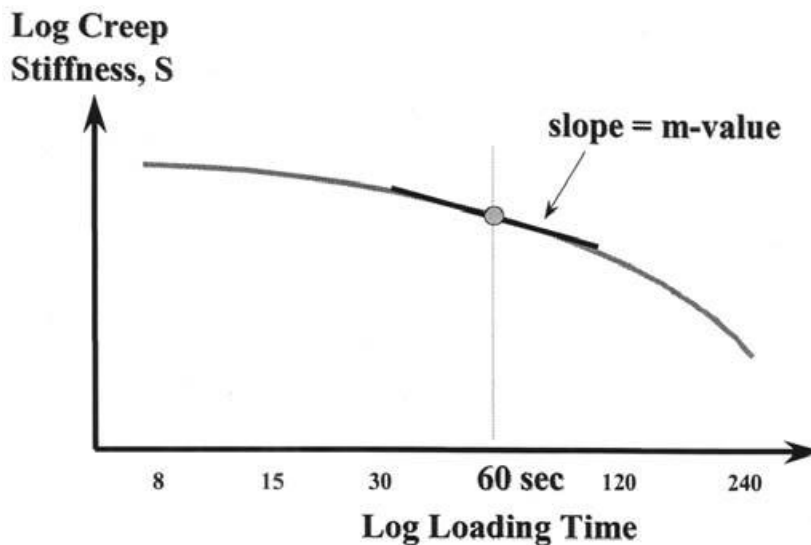


Figure 2.12 – Determination of  $S(60)$  and  $m$ -value, as illustrated in (G. Rowe et al., 2001)

As stated in J. Petersen et al., (1994), the binder meets the SHRP specification, if the creep stiffness is less than or equal to 300MPa and  $m$  value, greater than 0.3.

- iii. Annular shear rheometer test - In 2002, the ENTPE laboratory developed the Annular Shear Rheometer (ASR) Figure 2.13. According to Delaporte, (2006), the rheometer makes it feasible to test specimens of larger size than those utilized on existing equipment, allowing for the testing of materials ranging from binders to mastic to bituminous sand. The annular shear test is characterized by the use of ring-shaped specimens with a reduced cross-section, which permits the application of a quasi-homogeneous field of stress or shear distortion in the central portion of the specimen, i.e. one in which the same state of stress and strain is obtained at each point. Homogeneous tests provide access to the body's behavioural laws without requiring additional assumptions.

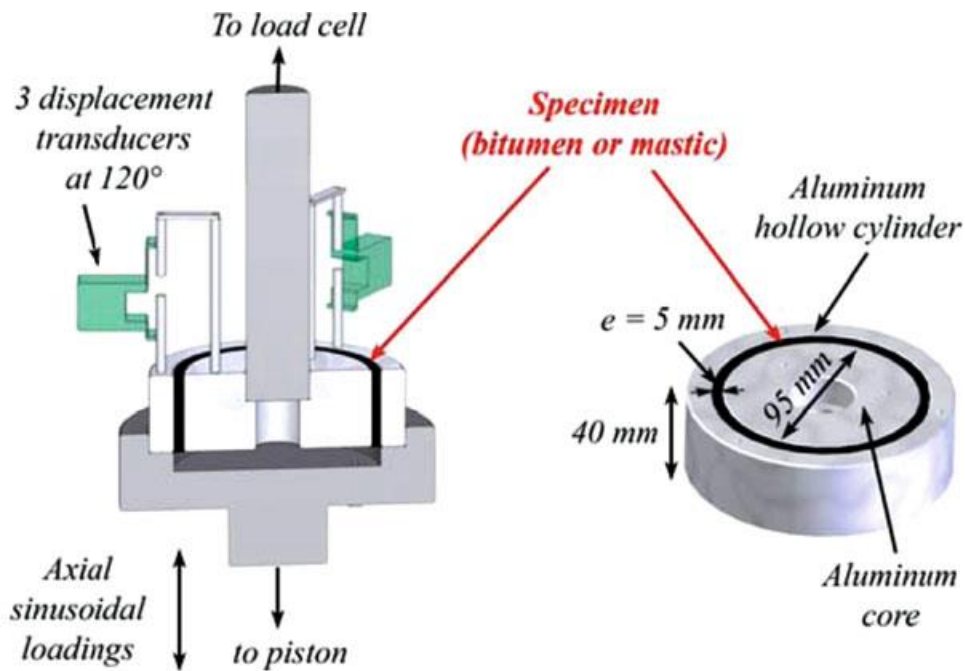


Figure 2.13 - Schematic view of the annular shear rheometer (ASR) for bitumen and mastic adapted from (Delaporte, Di Benedetto, Chaverot, & Gauthier, 2009)

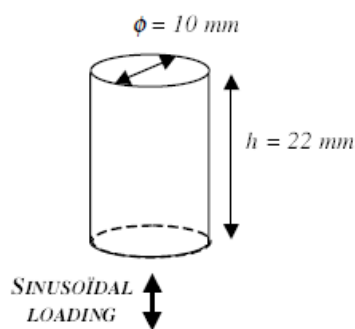
To cover a wide range of load (shear stress), low complex values are determined using a load cell with a high sensitivity (200 N) at high temperatures. It can measure load cycles with amplitudes as low as 1 N, which corresponds to a complex modulus of around 1 kPa and a distortion of 1%. With this unique load measurement technique, the annular shear rheometer can measure the shear complex modulus continuously for 7 decades ranging from approximately 1 kPa to 10 GPa (Delaporte et al., 2009).



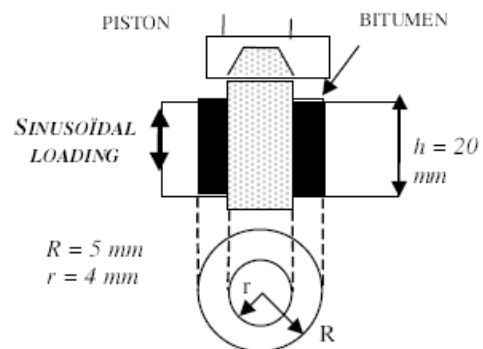
- iv. **Metravib Apparatus** – This apparatus has been used to carry out complex modulus test on bitumen in tension-compression loading. Solid cylindrical samples (diameter = 10mm, height = 22mm) as shown in Figure 2.14b are tested at low to high temperatures (30°C). From 30 to 60°C, the tests consisted of annular shearing of hollow cylindrical samples (inner diameter = 8mm, outer diameter = 10mm, height = 20mm) (Figure 2.14b). Isotropy and incompressibility are assumed, this allows the interconversion between Young's modulus ( $E^*$ ) and shear complex modulus ( $G^*$ ).



a)



b)



c)

Figure 2.14 – Metravib complex modulus test apparatus a) tension-compression from low temperature to 30°C and b) annular shearing above 30°C adapted from (Hervé Di Benedetto et al., 2004)

#### 2.1.1.4.5 *Bitumen Binder Ageing*

Bitumen ageing is a very complex process that leads to the hardening and brittleness of bitumen during both application and service, which significantly contributes to the degradation of paving applications (Mastrofini & Scarsella, 2000).

In the utilization of bitumen as a binder in the production of bituminous mixtures, there are two primary ageing stages to consider. First, "short-term ageing" occurs at elevated temperatures throughout the mixing, storage, spreading, and compaction processes. Second, "long-term ageing" refers to the process that occurs during the mixture's service life as a result of the interaction between oxygen and ultraviolet radiation. Amongst the prominent and universally accepted factors influencing the ageing phenomenon on bitumen irrespective of stage of ageing includes evaporation of the lowest molecular weighted component, oxidation and physical hardening (Bell, 1989; Zaidullin, Petrova, Yakubov, & Borisov, 2013).

As stated by (Hunter et al., 2015) evaporation of volatile components (saturates and aromatics) is also considered a process of ageing. This effect is primarily dependent on temperature (most evaporation occurs during mixing and laying, and an increase of 10 to 12°C over the mixing temperature might double the emission of volatiles). The limited effect of volatile compound evaporation compared to oxidation ageing mechanism as stated by (J. C. Petersen, 1989; Zupanick & Baselice, 1997) has been attributed to the current control in bitumen refining conditions which ensures a low concentration of these chemicals in the bitumen (Tauste, Moreno-Navarro, Sol-Sánchez, & Rubio-Gámez, 2018).

(Thurston & Knowles, 1941) as cited in (Tauste et al., 2018) confirmed that the components of bitumen, specifically asphaltenes and resins, absorb oxygen, and in later research they determined that ageing is not just the result of physical hardness, but also oxidative processes. Therefore, oxidative ageing is an irreversible diffusion-driven mechanism governed mostly by heat interactions between air oxygen and bitumen components, which modify its chemical characteristics. This ageing process is further influenced by photo-oxidation reactions that occur in the upper portion of the binder, which are exposed in surface layers of the road and can catalyse oxidative reactions (Durrieu, Farcas, & Mouillet, 2007; J. Claine Petersen, 2009). The third bitumen ageing mechanism is physical hardening. It is described by (Santagata, Baglieri, Dalmazzo, & Tsantilis, 2016) a reversible process that changes the rheological properties of the bitumen without altering its chemical composition. This process is linked to the formation of organised wax structures in the maltenes phase (Frolov, Bashkirceva, Ziganshin, Okhotnikova, & Firsin, 2016), which is impacted by the linear alkanes present in

the asphaltenes fraction (J. Claine Petersen, 2009). The behaviour is related to the inner restructuring of the binder molecules, which is typically slow to develop at ambient temperature but accelerates as the temperature drops. Its effects are mild and include a hardening effect that can be reversed with heat (Hunter et al., 2015; Mastrofini & Scarsella, 2000). An investigation was also conducted into the reaction of the recombinant material comprising bitumen to the physical hardening effect during low-temperature isothermal storage. The test results indicate that aromatics do not exhibit a physical hardening effect within the temperature range examined. However, saturates and resins demonstrate a discernible degree of physical hardening effect. The response durations of the free volume, phase angle, and complex shear modulus to the physical hardening effect vary, rendering the free volume theory insufficient in isolation to elucidate this phenomenon (Tan, He, Zhang, & Zhang, 2023).

The Strategic Highway Research Program (Anderson et al., 1994; Anderson & Marasteanu, 1999) and subsequent studies (Tabatabaee, Velasquez, & Bahia, 2012; H. Wang et al., 2011) have demonstrated that physical hardening can influence the rheological properties of bitumen when it is maintained near its glass transition temperature. (François Olard, Di Benedetto, Eckmann, & Triquigneaux, 2003) referred to glass transition temperatures as temperatures of bitumen that maximize the loss modulus at any frequency. Differential scanning calorimetry (DSC) was employed by a group of researchers (Masson & Polomark, 2001; Masson, Polomark, & Collins, 2002) to examine the low-temperature characteristics of distinct bitumen components. The DSC tests revealed that a number of these components exhibit multiple glass transition temperatures. The  $T_g$  (glass transition temperature) of bitumen is primarily influenced by the saturates and aromatics fractions. Nevertheless, the glass transition temperatures ( $T_g$ ) of the bitumen would rise proportionally with the augmentation of asphaltene concentration (T. Wang, Wang, Hou, & Xiao, 2021). The effect of physical hardening on the linear viscoelastic properties of binders will be investigated and discussed later in the fourth section of this thesis.

Several laboratory techniques have been utilized to simulate the ageing phenomena of binders during the various periods of their manufacture as well as their service life. Currently, the thin film oven test (TFOT), rolling thin film oven test (RTFOT), pressure ageing vessel (PAV) (14769, 2012), and ultraviolet (UV) testing are the most prevalent. The first two, TFOT and RTFOT, are used to mimic ageing during storage, mixing, transit, and placement (short-term ageing), and their results are comparable (Lu & Isacson, 2002), but the latter two are used to assess ageing during the service life of the material (long-term ageing). Due to the lack of a consistent approach, UV ageing has been simulated in a variety of ways, making comparisons

between outcomes more challenging. Although (Feng, Wang, Bian, Guo, & Li, 2016; W. Zeng, Wu, Wen, & Chen, 2015) and other researchers agree that a 500W lamp should be used.

#### *2.1.1.5 Additives*

Additives are introduced into the bituminous mix with the sole intent of improving its properties. They are either added at the formulation phase or during the mixing phase directly into the bitumen tank. Additives such as adhesion enhancers are tensioactive nitrogen compounds introduced in the mix to improve the bond between aggregates and binders and also maintain durability.

Low and high density polyethelene are also added to bitumen at 130°C adopting a polyethylene/bitumen proportion which can vary from 20-66% (Arabani & Pedram, 2016). However, these proportions also lie between 0.4% and 1% of the aggregate quantity (Delorme & Wendling, 2007). Further attempt has been made to add crumb rubber to bituminous mixes in the form of pellets or partially blended with bitumen (Chavez, Marcobal, & Gallego, 2019; Picado-Santos, Capitão, & Neves, 2020). As stated by (Mahmoudi et al., 2021) the addition of crumb rubber does not influence the characteristic of bituminous materials in the linear viscoelastic domain although, the mixture with crumb rubber shows lower values of norm of complex modulus at high frequencies/low temperatures.

#### *2.1.2 Thermomechanical Behaviour of Bituminous Materials*

Temperature and traffic variations are the two main sources of load applied on a pavement structure. These loads induce the bending of pavement layers, tensile stresses horizontally and strains at the bottom of each bound layer and compressive stresses and strains in the bulk section. Bituminous pavements, having a distinct behaviour, experience fatigue cracking and rutting at the bottom and vertical sections of the layers respectively as a result of repeated wheel load Figure 2.15. Due to the complexity of the characterization of strain and stresses within the pavement structure (H Di Benedetto & Corté, 2005), the simplified Burmister's model method of infinite linear elastic layers has been adopted by the French paving industry, while assuming the pavement interfaces are perfectly bound or sliding.

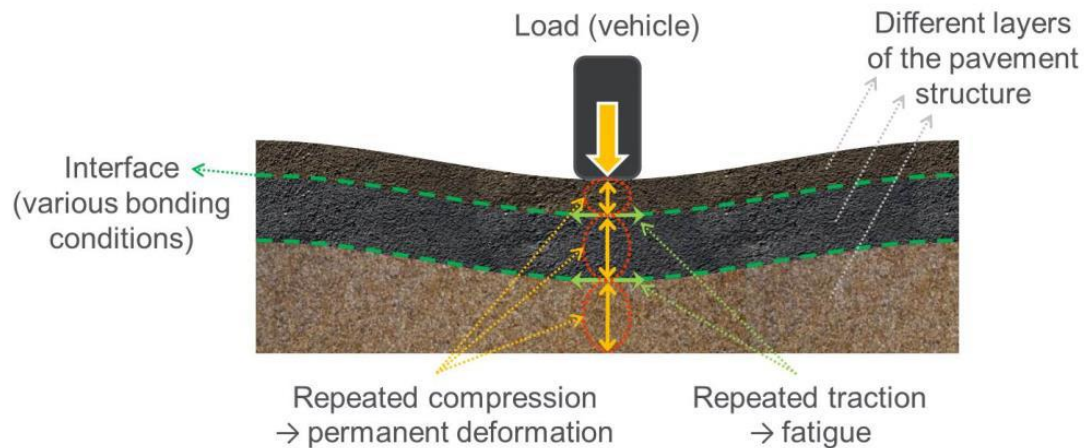


*Figure 2.15 - Pavement response and traffic load scheme (Hervé Di Benedetto, 1998; Mangiafico, 2014)*

It has been recognized that the effect of temperature is important in asphalt pavement, such as high-temperature rutting and low-temperature cracking, etc. This damage can not only impact the exterior appearance of the pavement, but also accelerate the deterioration of the pavement structure. Thermal cracking of asphalt pavement mainly occurs under variable weather conditions, when the asphalt mixture has an apparent brittleness similar to that of elastic material, so it is rational to analyse it on the basis of elastic theory, but the temperature variation always has an influence on the characteristics of the asphalt materials.

Thermal stress based on the force of contraction in the asphalt, which is a function of the properties of the asphalt binder, temperature and cooling rate may also lead to thermal fatigue. Crack propagation in the bituminous layer of a semi-rigid pavement with a cement-treated base can be associated with the thermal contraction of the cracked rigid layer due to shrinkage during hardening. Note that the thermal coefficient of contraction and expansion of the asphalt is not a constant value and it varies with the temperature of the mixture.

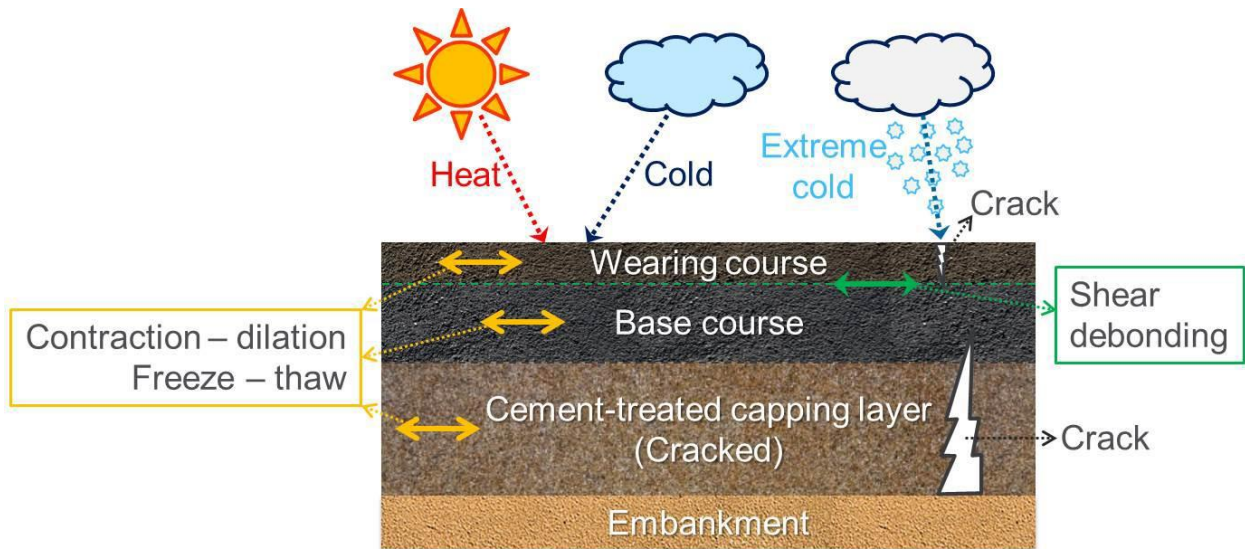


*Figure 2.16 - Pavement response and thermal load scheme (Hervé Di Benedetto, 1998; Mangiafico, 2014)*

Bituminous mixtures to perform satisfactorily in pavement systems must have the ability to distribute stresses, resist permanent deformation, resist cracking (fatigue and thermal cracking) and freeze-thaw and moisture damage. The mechanical properties of mixtures are directly linked to these requirements. There are three mechanical properties which are particularly important are;

- ✓ Mixture stiffness (within linear viscoelastic domain)
- ✓ Resistance to fatigue cracking (within and outside the linear viscoelastic domain)
- ✓ Mixture resistance to permanent deformation

### *2.1.2.1 Thermomechanical Behavioural Domains of Bituminous Pavement Materials*

The domain responses corresponding to the respective pavement distresses identified in Figures 2.15 and 2.16 are shown in Figure 2.17, as proposed by (Neifar & Di Benedetto, 2001). The domains represented as logarithm of strain amplitude ( $\epsilon$ ) versus logarithm of cycle numbers (N) indicates the continuous and smooth evolution between domains.

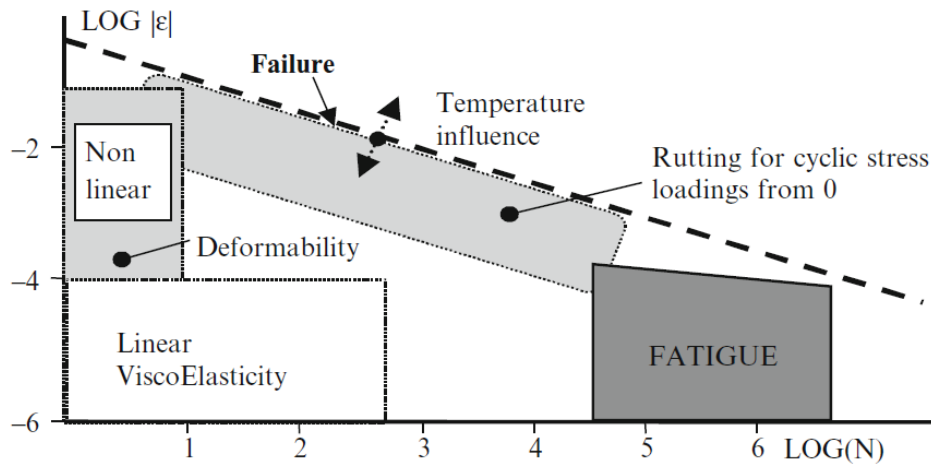


Figure 2.17 - Typical mechanical behaviour domains of bituminous mixtures (H Di Benedetto & Corté, 2005; Hérve Di Benedetto et al., 2013)

The measured behaviour is extremely nonlinear for a small number of loads and deformations of a few percent. For loads of a few hundred cycles and "small" deformations ( $10^{-4}$  m/m), viscoelastic behaviour is assumed as a first approximation. For loads of several tens of thousands of cycles and low deformations, the "fatigue" of the material shows. When stress cycles that depart from zero stress are applied, irreversible deformations occur. Non-negligible irreversible deformations exist when zero stress is applied for deformation amplitudes "near" to failure. Their accumulation results in damage.

Similarly, the typical domains of mechanical behaviour of bitumen are displayed in Figure 2.18 and Figure 2.19. The domain limits are only indications of the order of magnitude, and the shift from one domain to another is rather continuous than abrupt (e.g. for the linear and nonlinear domain (Q. T. Nguyen, Di Benedetto, & Sauzéat, 2015).

Nonlinearity is defined as the dependence of rheological parameters on strain amplitude (Doubbaneh, 1995; Q. T. Nguyen et al., 2019), among others. With increasing strain amplitude, a progressive shift between linear and nonlinear viscoelastic behaviours is observed. The linear viscoelastic (LVE) limit is therefore defined as the strain amplitude that corresponds to a 5% decrease in reference to complex modulus at low strain amplitude. Several investigations, including those conducted by (Gordon D Airey & Rahimzadeh, 2004; Gordon D Airey, Rahimzadeh, & Collop, 2002), for bitumen and mixes, addressed the definition of the LVE limit of a bituminous substance. It was noted that the LVE limit for mixes was in the order of  $100 \mu\text{m/m}$  (0.01%) and  $10,000 \mu\text{m/m}$  (1%) for bitumen.



Other studies by (Gordon D Airey et al., 2021; Coutinho, Babadopulos, Freire, Castelo Branco, & Soares, 2014; Q. T. Nguyen et al., 2019) have also emphasised the frequency and temperature dependency of non-linearity and LVE limits.

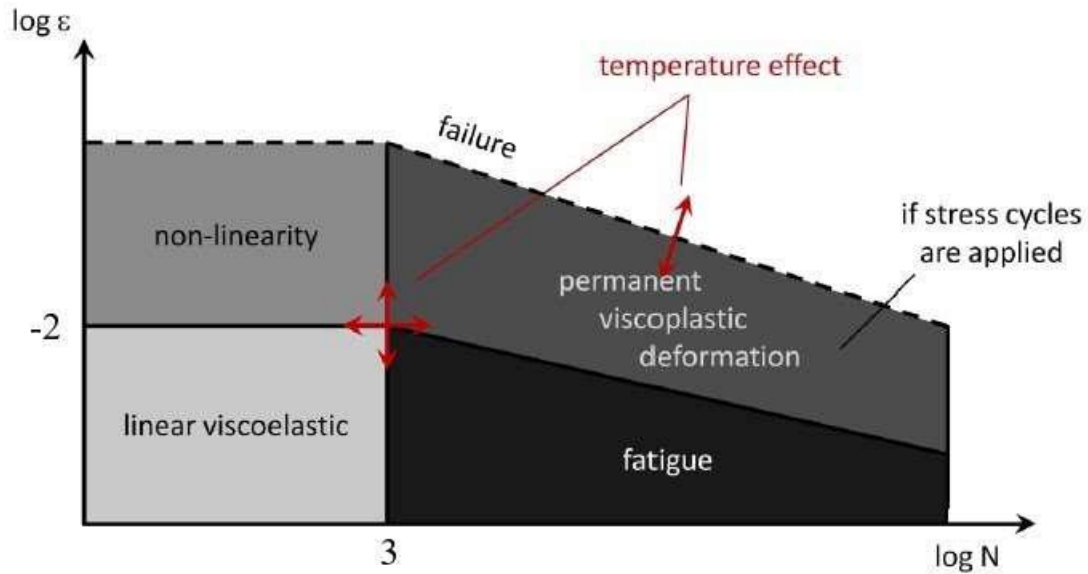


Figure 2.18 – Typical mechanical behaviour domains of bitumen at intermediate temperature as a function of number of cycles and strain amplitude (Mangiafico, 2014)

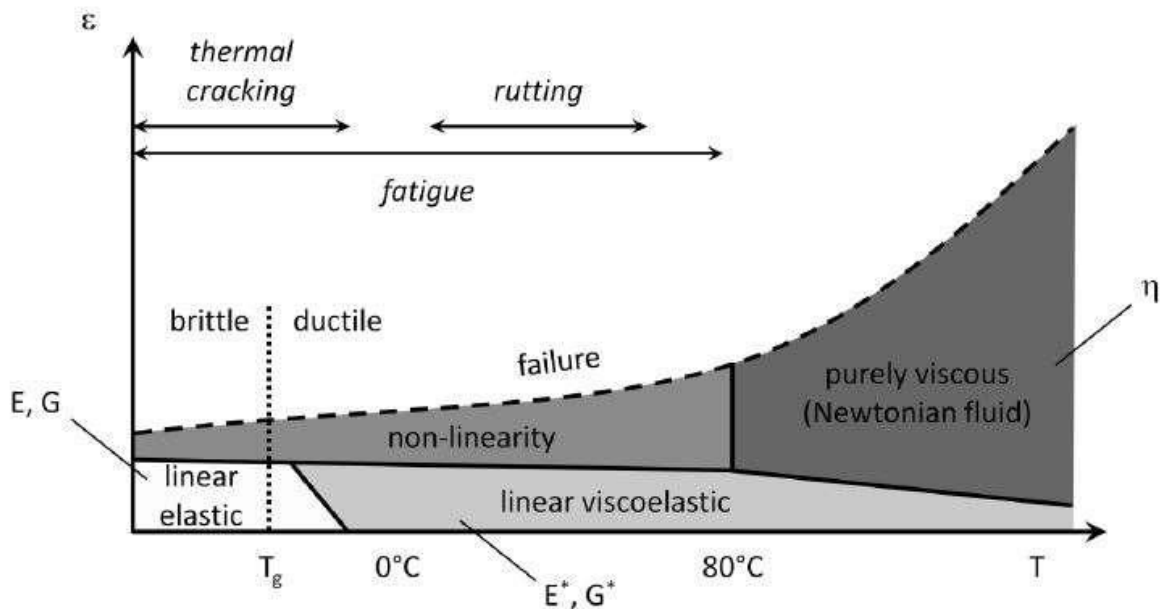


Figure 2.19 – Typical mechanical behaviour domains of bitumen as a function of temperature and strain amplitude (Mangiafico, 2014)



### 2.1.2.2 Flexible Pavement Distresses

Distresses in flexible pavements occur in different domains as illustrated in Figures 2.18 through 2.19 and the most common are briefly mentioned as follows

- I. Rutting or Permanent deformation – Rutting can occur either as structural or non-structural. Structural rutting constitutes the deformation of the lower pavement layers (see Figure 2.19a), while non-structural rutting is the permanent deformation of the asphaltic layers and is usually accompanied by the appearance of shoulders on the pavement surface at the edge of the ruts (Figure 2.19b).

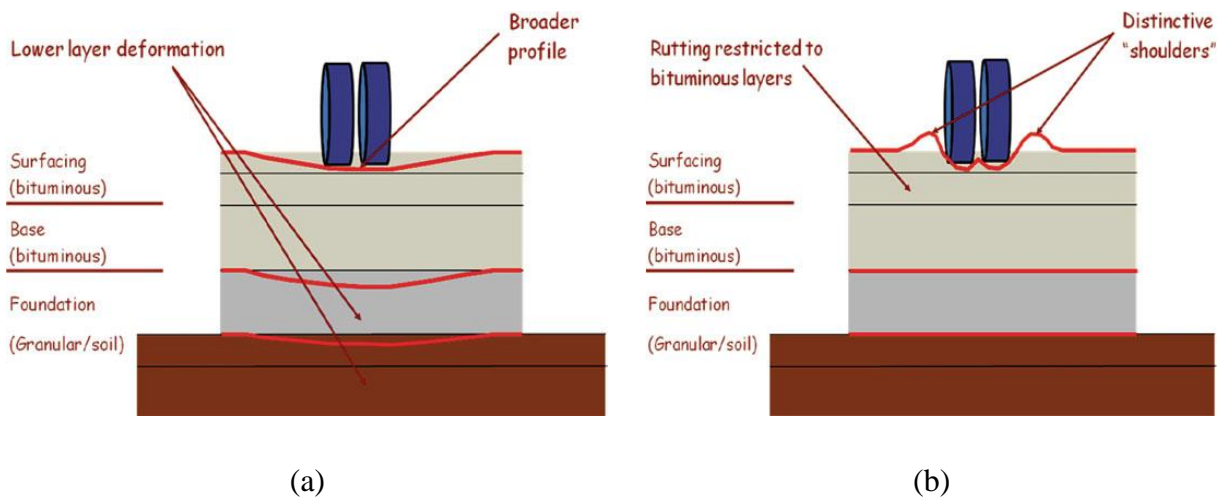


Figure 2.20 – (a) Structural rutting and (b) Non-Structural rutting (Hérve Di Benedetto et al., 2013)

Rutting is the result of permanent deformation due to a large number of vehicle passes and the small irreversible strains accumulated at each loading cycle. The rutting potential of a mixture is sometimes related to the empirical tests on bitumen, which are carried out under specific loading times and temperatures or non-homogenous tests to simulate repeated traffic load, (CEN EN, 2003; Standardization, 2003)(BS EN 12697–22:2003; AASHTO T 324 2019). The evaluation of permanent deformation of bituminous mix has been attempted by (H. Nguyen, 2010) using the homogenous complex modulus test, and different irreversible parts for cyclic loadings having same reversible strain amplitude was obtained. These could be assumed that the viscoelastic properties characterised by the shape of the elliptical loop as shown in Figure 2.21 may not be associated with the irreversible strains responsible for permanent deformation (Hérve Di Benedetto et al., 2013).

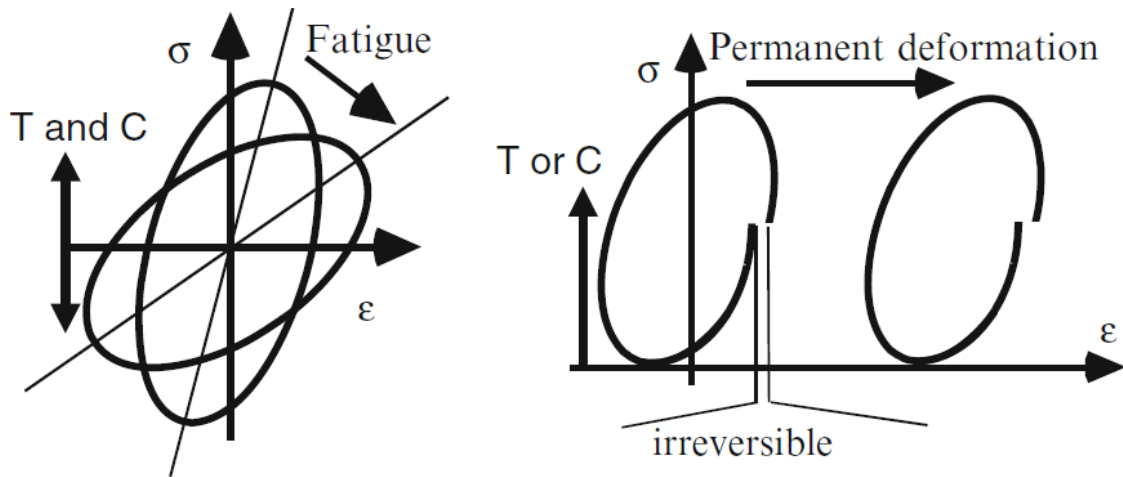


Figure 2.21 – Differences between permanent deformation and fatigue cracking during a homogenous cyclic test (H Di Benedetto, De La Roche, Baaj, Pronk, & Lundström, 2004).

- II. Fatigue cracking – Fatigue is defined as failure due to the loss of rigidity of pavement material as a result of accumulated short time loading (H Di Benedetto et al., 2004; Orozco, 2020). After certain level of damage accumulation, bottom-up fatigue cracking initiates, propagates through the asphalt layer, and shows at the surface as an alligator crack (Islam, 2015). A network of fatigue cracks on the actual pavement surface looks like an alligator skin and therefore, fatigue cracking is also known as alligator cracking, as shown in Figure 2.22



Figure 2.22 – Severe fatigue cracking (Miller and Bellinger 2014) as cited by (Orozco, 2020)

As stated by (H Di Benedetto et al., 2004), fatigue cracking constitutes two phases of degradation process. The initial phase corresponds to degradation resulting from damage that is uniformly spread in the material. Hence, this phase is manifested by the initiation and propagation of a "micro-crack" network, which leads to a reduction in

modulus. The second phase, constitutes the coalescence of micro-cracks, forming a "macro-crack" which appears within the material. The coalescence corresponds to a certain level of damage, or fatigue.

- III. Low-temperature cracking – The accumulation of damage occurs when temperature induced stresses in the pavement approaches the material stiffness, and cracks are formed (Dave & Hoplin, 2015). These cracks reduce the integrity of the pavement and consequently acts as moisture ingress pathways into the pavement layers causing substantial damages. As earlier mentioned, the thermal and mechanical conditions imposed on the pavement basically controls the formation and propagation of low-temperature cracking. As stated by (Aschenbrener, 1995), the principal cause of pavement distresses in temperate regions could be as a result of the thermomechanical phenomenon within the pavement. (Orozco, 2020), stated that attempts have been made in the laboratory to simulate the low-temperature cracking phenomenon with a test: The Thermal Stress Restrained Specimen Test (TSRST) (AFNOR 2013d) wherein a cylindrical specimen is subjected to a negative temperature ramp under a longitudinal restrained deformation.

## 2.2 Linear Viscoelasticity

Viscoelasticity is a characteristic observed in materials that exhibit simultaneous elastic and viscous behaviour, which is contingent upon the specific loading conditions, such as frequency and temperature. When exposed to high frequencies and low temperatures, the elastic behaviour prevails over the viscous behaviour. The converse phenomenon occurs when viscoelastic materials are exposed to low frequencies (characterised by gradual loading) and elevated temperatures.

Viscoelastic materials respond to constant stress with an increase in strain in time (creep), constant strain leads to a decrease in stress with time (relaxation), alternatively, a phase lag (hysteresis) occurs, as a result of cyclic loading, which leads to energy dissipation.

### 2.2.1 Creep Functions

The progressive deformation of a material under constant stress is known as creep. Viscoelastic material is tested under creep by the imposition of a constant stress  $\sigma_0$ , at an instance  $t_0$  under constant temperature as illustrated in Figure 2.23a, where at a later time  $t$ , the stress  $\sigma_{(t)}$  can be calculated with equation 2.4 and a corresponding response Figure 2.23b calculated with equation 2.5.

$$\sigma(t) = \sigma_0 H(t - t_0) \quad (2.4)$$

Where  $H$  is the unit Heavside step function:

$$H(t - t_0) = 0 \text{ if } t < t_0$$

$$H(t - t_0) = 1 \text{ if } t \geq t_0$$

$$\varepsilon(t) = \sigma_0 F(t_0, t) \quad (2.5)$$

Where:

$F(t_0, t)$  creep function of material at any time  $t$  for the stress  $\sigma_0$  applied at  $t_0$

The strain function in viscoelastic material increases with time. Creep compliance  $J(t)$  expressed by a linear viscoelastic material is the ratio;

$$J(t) = \frac{\varepsilon(t)}{\sigma_0} \quad (2.6)$$

This compliance is independent of stress level in linear viscoelastic materials.

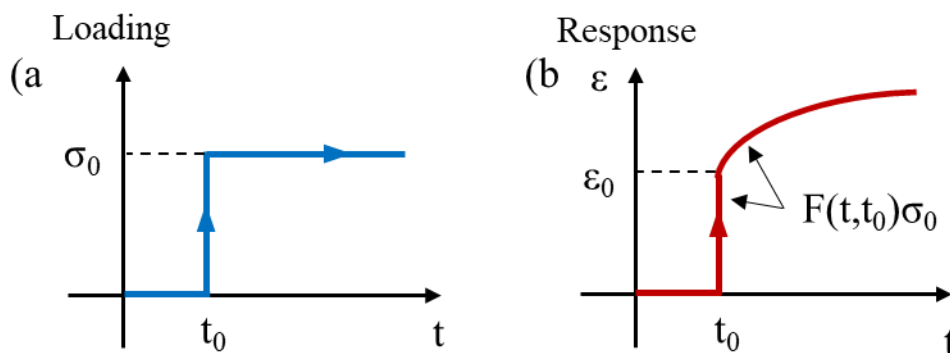


Figure 2.23 – Regions of creep behaviour at different load levels

Creep curves are divided into three regions namely primary creep wherein the curve is a concave shape with face down, secondary creep where the deformation is proportional with

time and finally tertiary creep which is characterised by the acceleration of deformation to the point of creep rupture (see Figure 2.24).

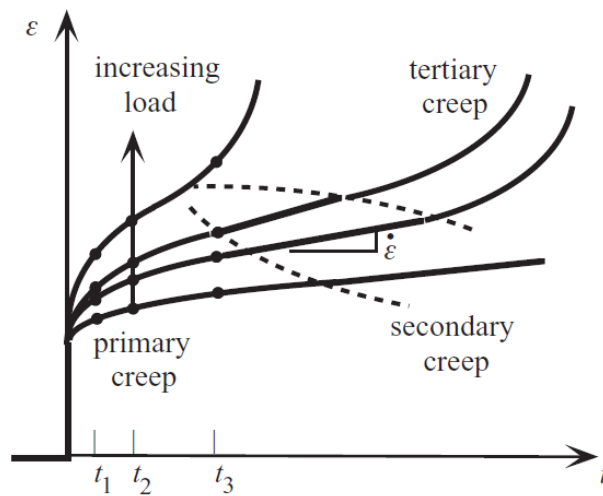


Figure 2.24 – Regions of creep behaviour at different load levels (Lakes & Lakes, 2009)

### 2.2.2 Relaxation Functions

The gradual decrease of stress at a constant strain application is termed as stress relaxation. Assuming a stepped function strain history where  $t = 0$ , therefore  $\varepsilon(t) = \varepsilon_0 H(t - t_0)$ , whereby a stress decrease  $\sigma(t) = \varepsilon_0 R(t - t_0)$ , in viscoelastic material is shown in Figure 2.25.

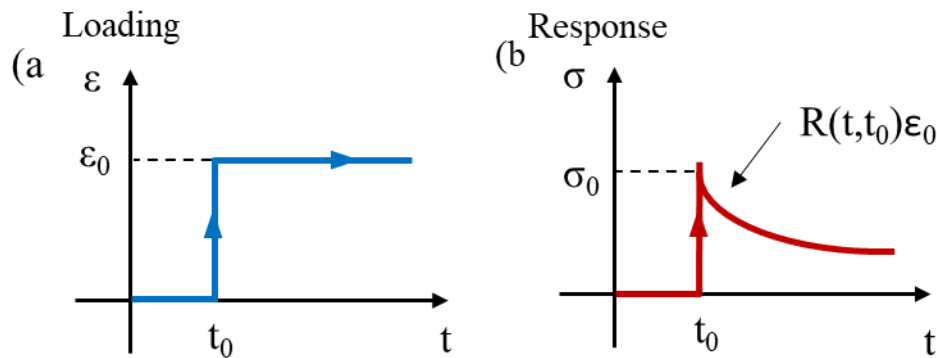


Figure 2.25 – Relaxation and recovery

The relaxation modulus  $E(t)$  experienced by a viscoelastic material can be expressed as the ratio,

$$E(t) = \frac{\sigma(t)}{\varepsilon_0} \quad (2.7)$$

### 2.2.3 Boltzmann Superposition Principle

As already described, a material is termed viscoelastic if it presents both elastic and viscous responses on application of deformation. Furthermore, viscoelasticity of non-aged material is verified by the application of a load in strain-controlled mode and its response corresponding to a complete stress recovery noted ( $\sigma_\infty = 0, t \rightarrow 0$ ), as illustrated in Figure 2.26

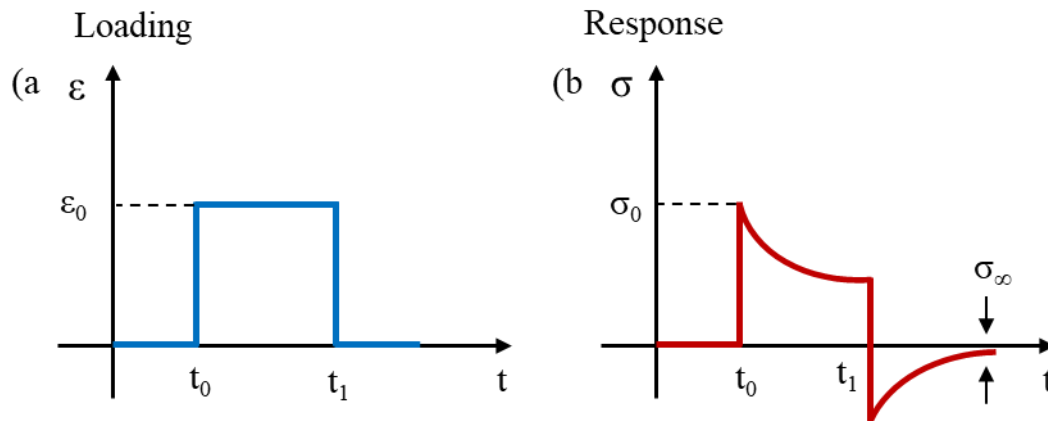
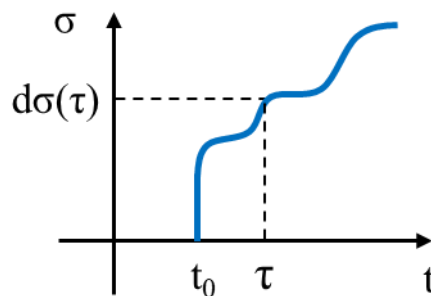


Figure 2.26 – Cancellation test

As stated by (Ferry, 1980) linear viscoelastic materials have a total response to a superposition of different loads that is equal to the sum of the individual responses to each load (Boltzmann law of superposition).

When an applied stress Figure 2.23 is not constant and consists of a stress history as illustrated in Figure 2.27, the superposition notation is used, with a corresponding variation in strain expressed as;

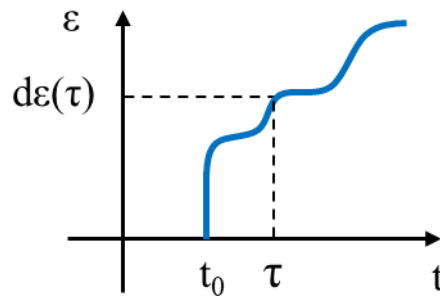
$$\varepsilon(t) = \int_{t_0}^t J(t - \tau) \frac{d\sigma(\tau)}{d\tau} d\tau \quad (2.9)$$



*Figure 2.27 – Stress history*

Using the same approach as for the creep test, for a generic strain history (Figure 2.28) where the incremental notation is used, the corresponding stress variation is expressed as;

$$\sigma(t) = \int_{t_0}^t E(\tau) \frac{d\varepsilon}{d\tau} (t - \tau) d\tau \quad (2.10)$$

*Figure 2.28 – Strain history*

#### 2.2.4 Laplace Carson Transform

It is desired to have a relationship between the creep function  $J(t)$  and the relaxation function  $E(t)$ . These functions can be found in the Boltzmann superposition integrals discussed above (equations 2.9 and 2.10). Integral transforms, such as the Laplace transform, can be used to manipulate such integral equations. Laplace transformation, in particular, converts a linear integral equation or a linear differential equation into an algebraic equation.

The convolution theorem and derivative theorem for the Laplace transform is used to convert the constitutive equations 2.9 and 2.10 to;

$$\bar{\sigma}(s) = s\bar{E}(s)\bar{\varepsilon}(s) \quad (2.11)$$

$$\bar{\varepsilon}(s) = s\bar{J}(s)\bar{\sigma}(s) \quad (2.12)$$

Where,  $s$  represents the transformation variable.

$$\frac{\bar{\sigma}(s)}{\bar{\varepsilon}(s)} = s\bar{E}(s) \quad (2.13)$$

$$\frac{\bar{\sigma}(s)}{\bar{\varepsilon}(s)} = \frac{1}{s\bar{J}(s)} \quad (2.14)$$

Assuming equations 2.13 and 2.14 are equal,

$$\bar{E}(s)\bar{J}(s) = \frac{1}{s^2} \quad (2.15)$$

Resolving the inverse transform by utilising the convolution theorem, the following relationships are obtained.

$$\int_0^t J(t-\tau)E(\tau)d\tau = \int_0^t E(t-\tau)J(\tau)d\tau = t \quad (2.16)$$

Rearranging equation 2.16 in the Laplace plane a different form is obtained (equation 2.17)

$$1 = J(0)E(t) + \int_0^t E(t-\tau) \frac{dJ(\tau)d\tau}{d\tau} \quad (2.17)$$

### 2.2.5 Response to sinusoidal loading

Sinusoidal loading is applied to a viscoelastic material either as stress amplitude  $\sigma_0$  or strain amplitude  $\varepsilon_0$  as a function of frequency or time. The resultant response is equally sinusoidal with a corresponding phase difference  $\phi$  after achieving a steady state (few cycles). In complex notations, complex modulus can be expressed as the ratio of sinusoidally applied stress to a sinusoidally applied strain. There is no phase lag seen between the stress and strain signals when dealing with elastic materials, and the complex modulus shows just a real portion, which is identical to the material's elastic qualities. The same line of reasoning can be used to define complex compliance, which is represented in complex notation as the ratio between sinusoidal strain and sinusoidal stress. The reciprocal relationship between complex modulus and complex compliance can thus be seen to be obvious in the context of sinusoidal loading. Going by these definitions, sinusoidal stresses and strains as a function of frequency can be expressed in equations 2.18 and 2.19 as;

$$\sigma(t) = \sigma_0 \sin \omega t \quad (2.18)$$



$$\varepsilon(t) = \varepsilon_0 \sin(\omega t - \varphi) \quad (2.19)$$

Where  $\omega = 2\pi f$ ,

$$\varphi = \omega t \quad (2.21)$$

The stiffness  $E^*$  can be represented as a complex number due to the phase lag between stress and strain.

$$E^* = \frac{\sigma}{\varepsilon} = \frac{\sigma_0 e^{j\omega t}}{\varepsilon_0 e^{j(\omega t - \varphi)}} = |E^*| e^{j\varphi} \quad (2.22)$$

$$E^* = E'(\omega) + E''(\omega); \quad E' = |E^*| \cos \varphi \quad \text{and} \quad E'' = |E^*| \sin \varphi \quad (2.23)$$

$$|E^*| = \sqrt{(E')^2 + (E'')^2} \quad (2.24)$$

$E'$  shows the elastic part of the material behaviour, also known as the “storage modulus”;  $E''$  represents the viscous part of the material behaviour known as the loss modulus. The phase angle  $\varphi$  varies between  $0^\circ$  and  $90^\circ$ . The material is regarded as linear elastic if  $\varphi = 0^\circ$  and purely viscous if  $\varphi = 90^\circ$ .

Shear complex modulus  $G^*$  equation 2.25 is obtained if shear sinusoidal loading is applied to a viscoelastic material. Shear stress is represented by  $\tau$  and shear strain amplitude represented by  $\gamma$ . The phase lag between the stress and strain signals is also represented by  $\varphi$ .

$$G^* = \frac{\tau^*}{\gamma^*} = \frac{\tau_0 e^{j\omega t}}{\gamma_0 e^{j(\omega t - \varphi)}} = \frac{\tau_0}{\gamma_0} e^{j\varphi} \quad (2.25)$$

Moreover, if the tested material is isotropic, the following relationship between  $E^*$  and  $G^*$  are valid:

$$G^* = \frac{E^*}{2(1 + \nu^*)} \quad (2.26)$$

Where  $v^*$  is the complex Poisson's ratio defined for the radial strain  $\varepsilon_2^*$  on the axial deformation  $\varepsilon_1^*$  in case of uniaxial loading  $\sigma_1^*$

$$v^* = -\frac{\varepsilon_2^*}{\varepsilon_1^*} = \frac{\varepsilon_{02} e^{j(\omega t - \varphi + \pi + \varphi_v)}}{\varepsilon_{01} e^{j(\omega t - \varphi)}} = |v^*| e^{j\varphi_v} = |v^*| \cos \varphi_v + j|v^*| \sin \varphi_v \quad (2.27)$$

Where;  $|v^*|$  represents the norm of complex Poisson's ratio and  $\varphi_v$  the phase angle of the Poisson's ratio. Linear viscoelastic Poisson's ratio is discussed in section 2.5 of this thesis in detail.

The response of a viscoelastic material as a function of temperature and frequencies are generally highlighted on the following graphical plots:

- Isothermal curves – The norms of  $|E^*|$ ,  $|G^*|$  and are plotted as a function of frequencies in a logarithmic or semi-logarithmic scale;
- Isochronal curves – The norms of complex modulus  $|E^*|$ ,  $|G^*|$  values are plotted as a function of the test temperature in a semi-logarithmic scale.
- Cole-Cole plots - This is the plot of the imaginary part of norm of complex modulus  $E''$  as a function of the real part of the norm of complex modulus  $E'$ . TTSP validity for LVE behaviour can be verified. The vector representation can be used to analyse the behaviours of bituminous materials at low temperatures.
- Black diagrams – The plot of norm of complex modulus  $|E^*|$ ,  $|G^*|$  as a function of phase angle  $\varphi$  in a semi-logarithmic scale. TTSP validity for LVE behaviour can also be verified if this plot describes a unique curve. The material is considered thermorheologically simple. However, PmB cannot be described by a smooth curve but can be described by a unique master curve.

### 2.3 Time-Temperature Superposition Principle (TTSP)

There exists an equivalence between frequency variation and temperature change on the LVE behaviour of thermorheologically simple materials (defined in section 2.2.5). Complex modulus measurements at different temperatures is fitted to one continuous curve at a reduced frequency (time scale). This curve represents the material behaviour at a temperature within a large frequency range. The principle that creates an equivalency between frequency and temperature resulting in a master curve is termed TTSP.

$$E^*(f, T) = E^*(a_T \cdot f, T_{ref}) \quad (2.28)$$

$$a_T = a_T(T, T_{ref}) \quad (2.29)$$

$$a_T = a_T(T_{ref}, T_{ref}) = 1 \quad (2.30)$$

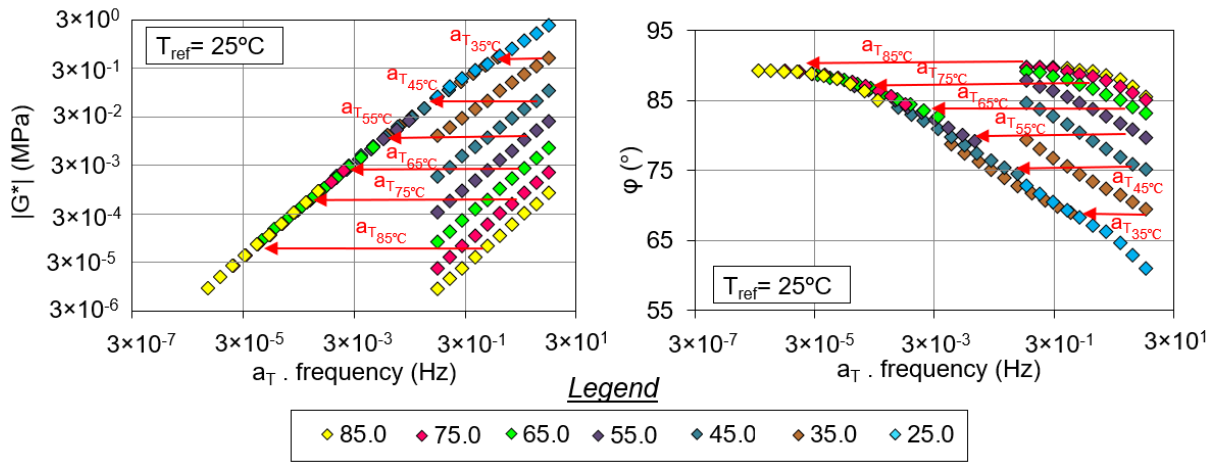


Figure 2.29 – Master curve of the norm of shear complex modulus at  $T_{ref} = 25^\circ\text{C}$  (Forton, Di Benedetto, Mangiafico, Sauzéat, & Marc, 2019)

The isothermal curves shown in Figure 2.29 are shifted based on a factor  $a_T$  along the frequency axis. An equivalent frequency domain based unique master curve is thereby formed at an arbitrary reference temperature with a null shift.

Studies by (H. M. Nguyen, Pouget, Di Benedetto, & Sauzéat, 2009) have verified TTSP in the non-linear viscoelastic domain of bituminous mixtures.

The William-Landel-Ferry (WLF) equation (Equation 2.31)(M. L. Williams, Landel, & Ferry, 1955) is commonly used to fit the shift factors as a function of temperature. This equation consists of two fitting constants  $C_1$  and  $C_2$  which are material dependent. Bitumen and bituminous mixtures are often fitted with this equation as demonstrated by (Babadopulos, 2017; H. M. Nguyen et al., 2009).

$$\log a_T = \frac{-C_1(T - T_{ref})}{(T - T_{ref}) + C_2} \quad (2.31)$$

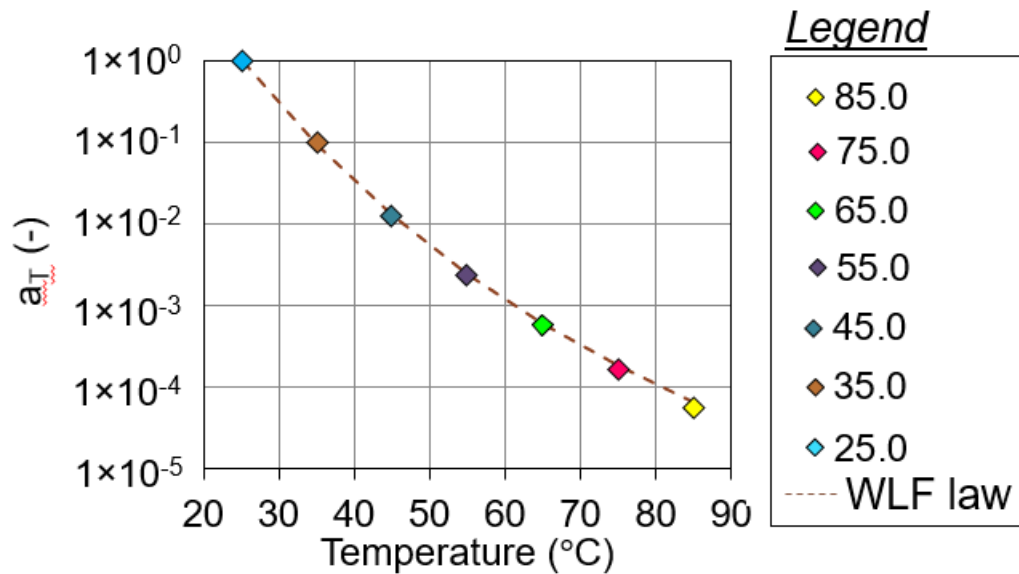


Figure 2.30 - Shift factor  $a_T$  and a WLF fitted curve of a binder (Forton et al., 2019)

As already highlighted, PmB are not thermorheologically simple as a result of their inability to be described by a unique black diagram. However, isothermal translations can be performed to form a unique master curve, in this case, it is called the partial time-temperature superposition principle (PTTSP) as described by (Hervé Di Benedetto et al., 2004; François Olard & Di Benedetto, 2003; F Olard, Di Benedetto, Dony, & Vaniscote, 2005).

Temperature dependency is a basic concept that describes how the relaxation process within bitumen changes with temperature. In general, various alternative  $a_T$  functions other than the WLF can be employed to describe the time-temperature equivalency of bitumen and asphalt mixtures. Here are a few examples:

- Arrhenius Equation: This equation can be described as follows:

$$\log a_T = \frac{0.4347E_a}{R} \left( \frac{1}{T} - \frac{1}{T_{ref}} \right) \quad (2.31)$$

Where  $E_a$  is the activation energy (J/mol) and  $R$  is the universal gas constant (8.314 J/mol.K). Other parameters remain same from before. This equation only requires one constant,  $E_a$ , which defines the minimal amount of energy required before any intermolecular movement may occur.

- Modified Kaelble equation: Bitumen is known to be a complex glass-forming liquid (Laukkanen & Winter, 2018; Laukkanen, Winter, Soenen, & Seppälä, 2018) with a glass transition temperature ( $T_g$ ) of roughly  $-20\text{ }^\circ\text{C}$ , with the actual glass transition temperature depending primarily on the crude oil from which it is derived (Laukkanen et al., 2018; Turner & Branthaver, 1997). Bitumen has exceptional rheological properties when compared to most other glass-forming liquids due to its great chemical and structural complexity. Most critically, there is a considerable broadening of the viscoelastic glass transition (Laukkanen et al., 2018).

The Williams-Landel-Ferry (WLF) equation has traditionally been used to predict the temperature dependence of relaxation patterns near  $T_g$ . The temperature dependence of viscoelastic characteristics, on the other hand, deviates from the WLF behaviour below and above  $T_g$ . (G. M. Rowe & Sharrock, 2011) presented a variation to the standard WLF equation that uses a single relation to represent the temperature dependence of relaxation processes both above and below  $T_g$ . This is known as the modified Kaelble equation.

$$\log a_T = -C_1 \left( \frac{T - T_d}{C_2 + |T - T_d|} - \frac{T_{ref} - T_d}{C_2 + |T_{ref} - T_d|} \right) \quad (2.31)$$

where  $T_d$  is the temperature at which the positive to negative curvature of the S-shaped  $\log a_T$  vs  $T$  curve shifts. The modified Kaelble equation accurately captures the temperature dependence of various bitumen and mixes above and below  $T_g$  (Laukkanen & Winter, 2018; Laukkanen, Winter, & Soenen, 2015; Laukkanen, Winter, Soenen, & Seppälä, 2016; G. M. Rowe & Sharrock, 2011). A sigmoidal-type curve is presented in Figure 2.31, which does not result in overly high values of  $a_T$  as the temperature decreases.

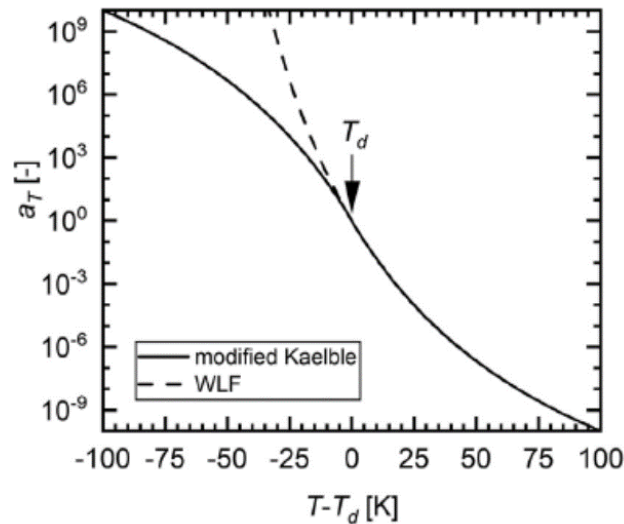


Figure 2.31 – Modified Kaelble schema compared with WLF(Laukkanen & Winter, 2018)

However, when compared to the original WLF estimation, the Modified Kaelble technique underestimates unmodified bitumen at low temperatures (Yusoff, Chailleux, & Airey, 2011).

- Other shift factor laws includes: Numerical, Non-linear least squares shift, log-linear equation, viscosity temperature susceptibility (VTS) equation, Laboratoire central des ponts et chaussées (LCPC) approach (Yusoff, Chailleux, et al., 2011)

#### 2.4 Prediction of Viscoelastic Behaviour of Bituminous Materials

Rheological models are alternative tools used to describe the viscoelastic properties of binders, mastics and mixtures at any temperature and frequency pair with an acceptable accuracy. Linear viscoelastic models consist of mathematical models with formulations fitted to curves generated with experimental results. Secondly, analogical models which consists of spring (elastic response) and linear dashpot (viscous response) combinations to simulate the mechanical response of LVE materials. As stated in (Yusoff Md., 2012), majority of the rheological models available are governed by the construction of master curves and the determination of shift factors  $aT$ . These implies that both time-temperature superposition principle (TTSP) and partial time temperature superposition principle (PTTSP) holds for the materials.(Anderson et al., 1994; François Olard & Di Benedetto, 2003)

### 2.4.1 Mathematical Models

#### 2.4.1.1 Christensen and Anderson (CA) model

(Anderson et al., 1994; Christensen & Anderson, 1992) developed a mathematical model during the SHRP using 8 core bitumen, noting the four primary parameters required to characterise the bitumen properties. This model expresses the complex shear modulus of bitumen  $|G^*|$  and phase angle  $\delta$  as a function of frequency  $\omega$ :

$$|G^*| = G_g \left[ 1 + \left( \frac{\omega_c}{\omega} \right)^{\frac{(\log 2)}{R}} \right]^{-\frac{R}{\log 2}} \quad (2.32)$$

Where  $G_g$  is the glassy modulus which is the complex modulus of bitumen at high frequencies and low temperatures. The value can equally be taken as 1GPa in shear and 3GPa in flexure.  $\omega_c$  is the crossover frequency, that is the frequency where  $\tan \delta$  is 1 at a given temperature A shape parameter R, called rheological index, which is the difference between the glassy modulus  $G_g$ , and the shear complex modulus at the cross over frequency  $|G^*(\omega_c)|$ .

$$\delta = \frac{90}{\left[ 1 + \left( \frac{\omega_c}{\omega} \right)^{\frac{(\log 2)}{R}} \right]} \quad (2.33)$$

$$R = \frac{(\log 2) \times \log \left( \frac{|G^*|}{G_g} \right)}{\log \left( 1 - \frac{\delta}{90} \right)} \quad (2.34)$$

(Anderson et al., 1994) reported that the values of R obtained with equation 2.34 are near accurate where  $\delta$  is between  $10^\circ$  and  $70^\circ$  with the best results obtained at  $\delta = 45^\circ$ . The drawback of this model as stated by (Anderson, Christensen, Roque, & Robyak, 1992; Da Silva, de Camargo Forte, de Alencastro Vignol, & Cardozo, 2004) is that the model cannot accurately fit bitumen behaviours at high temperature and low frequency regions. Secondly, the model cannot fit modified bitumen behaviours (Gordon Dan Airey, 1997). Furthermore, according to the Kramers-Kronig relations equations (2.35 and 2.36), the dynamic properties of a linear material

$E'$  and  $E''$  (or  $J'$  and  $J''$  are derived from the same transient function, they cannot be independent. therefore, it is not possible to define  $|G^*|$  and  $\delta$  separately.

$$J'(\omega) - J'(\infty) = \frac{2}{\pi} \left[ \wp \int_0^{\infty} \frac{\bar{\omega} J''(\bar{\omega})}{\bar{\omega}^2 - \omega^2} d\bar{\omega} \right] \quad (2.35)$$

$$J''(\omega) = \frac{2\omega}{\pi} \left[ \wp \int_0^{\infty} \frac{J'(\bar{\omega}) - J'(\infty)}{\omega^2 - \bar{\omega}^2} d\bar{\omega} \right] \quad (2.36)$$

#### 2.4.1.2 Christensen Anderson Marasteanu (CAM) Model

Considering the draw backs CA model presented as stated in section 2.5.1.1, (Marasteanu & Anderson, 1999), developed a model to improve on the fitting capabilities of the CA model for both unmodified and modified bitumen. The following equations were proposed:

$$|G^*| = G_g \left[ 1 + \left( \frac{\omega_c}{\omega} \right)^v \right]^{-\frac{w}{v}} \quad (2.37)$$

$$\delta = \frac{90w}{\left[ 1 + \left( \frac{\omega_c}{\omega} \right)^v \right]} \quad (2.38)$$

Where  $v = \log \frac{2}{R}$  and  $w$  is a parameter affecting the rate of data convergence at the two asymptotes as the frequency tends to zero or infinity (Marasteanu & Anderson, 1999). Similar to the CA model, at high temperatures and low frequencies, the CAM model presented a lack of fit (Da Silva et al., 2004).

#### 2.4.1.3 Bahia and Co-workers' Model

(Hussain U Bahia et al., 2001; M. Zeng, Bahia, Zhai, Anderson, & Turner, 2001) proposed an extension to the CAM model, which is capable of modelling both bitumen and mixtures. However, the same drawbacks shown for bitumen by CAM model is also expressed by Bahia's model. This model is expressed based on CAM model as earlier stated and generalised law model (Hussain U Bahia et al., 2001; Yusoff Md., 2012; M. Zeng et al., 2001):



$$|G^*| = G_g + \frac{G_g - G_0}{\left[1 + \left(\frac{\omega_c}{\omega}\right)^k\right]^{\frac{m}{k}}} \quad (2.37)$$

Where  $G_0$  is the static modulus, which is taken as zero for bitumen,  $k$  and  $m$  are dimensionless shape parameters.

Other mathematical models which the reader can consult includes Jongepier and Kuilman's model, Dickinson and Witt's model, Dobson's model, Fractional model, Polynomial model, Al-Qadi and co-workers' model, Sigmoidal model, Generalized sigmoidal model, LCPC master curve construction method, and the new complex modulus and phase angle predictive model as cited in the works of (Anderson et al., 1994; Yusoff Md., 2012; Yusoff, Shaw, & Airey, 2011).

#### 2.4.2 Mechanical Models

LVE analogical models are composed of two basic elements: The linear elastic spring of stiffness  $E$  where both stress and strain are directly proportional expressed as

$$\varepsilon(t) = \frac{1}{E} \sigma(t) \quad (2.38)$$

With the creep function, relaxation functions and complex modulus  $E^*$  given respectively as

$$\left. \begin{aligned} J(t) &= \frac{1}{E} \\ R(t) &= E \\ E^*(\omega) &= E \end{aligned} \right\} \quad (2.39)$$



Figure 2.32 – Linear elastic spring

And, linear viscous dash-pot which responds with a strain rate proportional to stress:

$$\sigma(t) = \eta \frac{d\varepsilon}{dt}(t) \quad (2.40)$$

With the creep function, relaxation functions and complex modulus ( $E^*$ ) given respectively as

$$J(t) = \frac{t}{\eta} \quad (2.41)$$

$$R(t) = \eta \delta(t) \quad (2.42)$$

$$E^*(\omega) = i\omega\eta \quad (2.43)$$

Where  $i$  is a complex number,  $i^2 = -1$  and  $\delta$  is a dirac function.

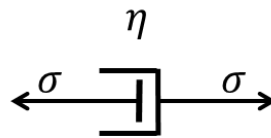


Figure 2.33 – Linear dash-pot

#### 2.4.2.1 Discrete spectrum models

These models consist of a combination of a spring and a linear dashpot in series or parallel arrangements. The simplest examples of such models being Maxwell (viscoelastic liquid) and Kelvin-Voigt (viscoelastic solid) models (François Olard & Di Benedetto, 2003). These models in complex associations, form the basic elements and cannot properly the complex behaviours of bituminous materials (François Olard & Di Benedetto, 2003). The creep and relax



Figure 2.34 – Maxwell model

The creep, relaxation function and complex modulus of the Maxwell model is given as;

$$J(t) = \frac{1}{E} + \frac{t}{\eta} \quad (2.44)$$

$$R(t) = E e^{-\frac{t}{\tau}} \quad (2.45)$$

Where  $\tau$  is taken as the relaxation time, and expressed as;

$$\tau = \frac{\eta}{E} \quad (2.46)$$

$$E^*(\omega) = E \frac{i\omega\tau}{1 + i\omega\tau} \quad (2.47)$$

The Kelvin-voigt model which consists of similar elements in parallel is shown in Figure 2.35 And the accompanying creep function, relaxation function and complex modulus equations expressed as,

$$J(t) = \frac{1}{E} \left( 1 - e^{-\frac{t}{\tau}} \right) \quad (2.48)$$

$$R(t) = E + \eta\delta \quad (2.49)$$

$$E^*(i\omega) = E + i\omega\eta \quad (2.50)$$

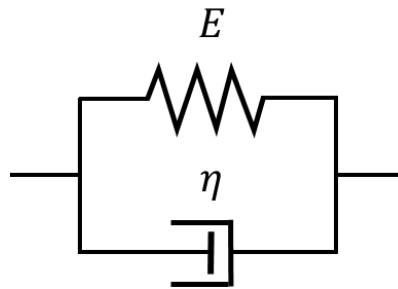


Figure 2.35 – kelvin-Voigt model

The generalized Maxwell (Prony series) model constitutes in parallel a group,  $n$  Maxwell elements with a linear spring  $E_0$  and dashpot  $\eta_\infty$  in parallel. This model is characterised by a discrete relaxation spectrum, with a finite number of relaxation times  $\tau_i = \frac{\eta_i}{E_i}$ .

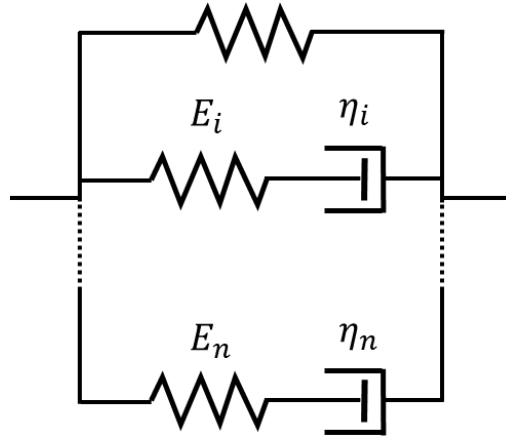


Figure 2.36 – Generalized Maxwell model

The relaxation function and complex modulus is expressed as:

$$R(t) = E_o + \eta_\infty \delta(t) + \sum_{i=1}^n E_i e^{-\frac{t}{\tau}} \quad (2.51)$$

$$E^*(\omega) = E_o + i\omega\eta_\infty + \sum_{i=1}^n E_i \frac{i\omega\tau_i}{1 + i\omega\tau_i} \quad (2.52)$$

Similarly, the generalized Kelvin-Voigt model is composed of  $n$  Kelvin-Voigt elements assembled in series with an additional spring and dashpot.

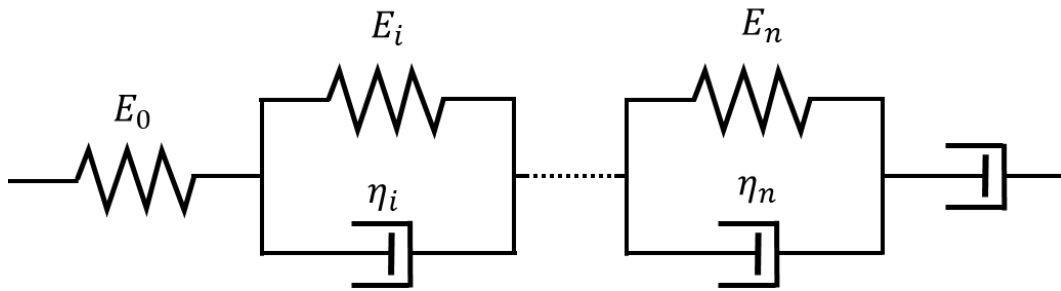


Figure 2.37 – Generalized Kelvin-Voigt model

The creep function and complex modulus associated with the GKV model are:

$$J(t) = \frac{1}{E_0} + \sum_{i=1}^n \frac{1}{E_i} \left(1 - e^{-\frac{t}{\tau}}\right) \quad (2.53)$$

$$E^*(\omega) = \left( \frac{1}{E_0} + \frac{1}{i\omega\eta_0} + \sum_{i=1}^n \frac{1}{E_i + i\omega\eta_i} \right)^{-1} \quad (2.54)$$

The generalised Maxwell and Kelvin-voigt models describes satisfactorily, the viscoelastic behaviour of bituminous materials with a consideration of  $n$  sufficient numbers of elements with 8 as the minimum (François Olard & Di Benedetto, 2003). The accuracy of these models increases as  $n$  tends to infinity therefore translating to a continuous spectrum model.

#### 2.4.2.2 Continuous spectrum models

These analogical models are characterised by an infinite number of KV elements assembled in series or Maxwell elements assembled in parallel possessing a physical meaning and representation.

(François Olard & Di Benedetto, 2003) stated that parabolic elements are analogical models with a parabolic creep function expressed as

$$J(t) = a \left( \frac{t}{\tau} \right)^h \quad (2.55)$$

And its complex modulus is expressed as,

$$E^*(i\omega\tau) = \frac{(i\omega\tau)^h}{a\Gamma(h+1)} \quad (2.56)$$

Where  $a$  is a dimensionless constant,  $h$  is an exponent such that  $0 < h < 1$ ,  $\Gamma$  is gamma function defined by the equation 2.57 and  $\tau$  is the characteristic time whose value is dependent only on temperature variation and validates the TTSP.

$$\Gamma(n) = \int_0^{\infty} t^{n-1} e^{-t} dt, \quad n > 0 \quad (2.57)$$

$$\tau(T) = \tau_0 a_T(T) \quad (2.58)$$

Where  $\tau_0$  is  $\tau$  at reference temperature and  $a_T(T)$ , the shift factor at temperature  $T$ . The evolution of shift factor  $\tau$  across all test temperatures can be fitted with the WLF equation.

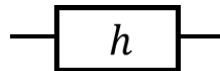


Figure 2.38 – Parabolic element

(Huet, 1963) proposed the use parabolic elements to model the LVE behaviour of bituminous materials. Huet model consists of a spring with stiffness  $E_0$  and two parabolic elements in series.

The parabolic elements, creep compliance function and complex modulus are expressed as follows:

$$J_1(t) = at^h \text{ and } J_2(t) = bt^k \quad (2.59)$$

$$J(t) = \frac{1}{E_0} \left( 1 + \delta \frac{\left(\frac{t}{\tau}\right)^k}{\Gamma(k+1)} + \delta \frac{\left(\frac{t}{\tau}\right)^h}{\Gamma(h+1)} \right) \quad (2.60)$$

$$E^*(i\omega\tau) = \frac{E_0}{1 + \delta(i\omega\tau)^{-k} + (i\omega\tau)^{-h}} \quad (2.61)$$

Where  $E_0$  is the complex modulus when frequency tends to infinity;  $h, k$  are exponents such that  $1 > h > k > 0$  and  $\delta$  a dimensionless constant.

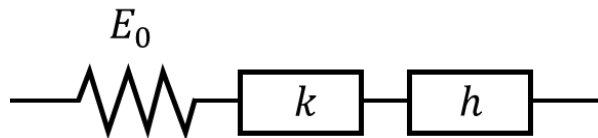


Figure 2.39 – Huet model

The Huet model has no analytical expression of the relaxation function with an inability to model LVE behaviours of mixtures at high temperature/low frequency domains since they exhibit a minimum stiffness value  $E_{00}$  due to the aggregate skeletons.

Due to the drawbacks of the Huet model, (Sayegh, 1965) proposed a model for bituminous mixtures wherein he improved the Huet model by adding a spring of small rigidity  $E_{00}$  compared to  $E_0$  in parallel. It is to be noted that this model has no analytical expression of the creep function. The complex modulus is expressed as follows:

$$E^*(i\omega\tau) = \frac{E_0 - E_{00}}{1 + \delta(i\omega\tau)^{-k} + (i\omega\tau)^{-h}} \quad (2.62)$$

Where  $E_{00}$  is the static modulus when  $\omega\tau \rightarrow 0$  and the other notations are same as stated previously in the Huet model.

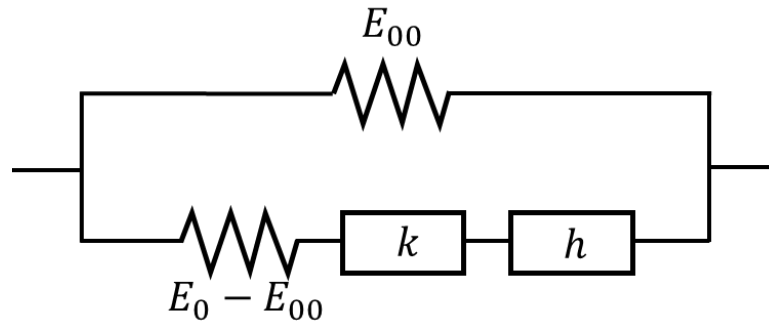


Figure 2.40 – Huet-Sayegh model

The Huet-Sayegh model requires only six constants ( $\delta, k, h, E_0^{say}, E_{00}^{say}$  and  $\tau_0$ ) to fit the LVE behaviour of a bituminous material at a given temperature, consequently, it fits correctly the LVE behaviour of bituminous mixes across all temperatures and frequencies. Huet and Huet-Sayegh models become identical if  $E_{00}$  is equal to zero therefore cannot model the LVE behaviour of bitumen at high temperatures/low frequency domain. In this domain, the model represents the purely viscous behaviour of bitumen as a parabolic element whereas it is a linear dashpot behaviour.

The drawbacks of the Huet-Sayegh model has been corrected by (François Olard & Di Benedetto, 2003) wherein, a linear dashpot was added in series to the parabolic elements in the Huet-Sayegh model to achieve the 2S2P1D (2 Springs, 2 Parabolic elements and 1 Linear dashpot) model. Its analogical scheme is shown in Figure 2.40.

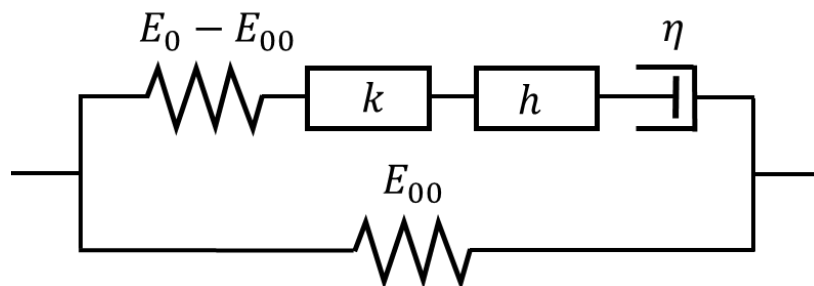


Figure 2.41 – 2S2P1D model

The model requires 7 constants ( $\delta, k, h, E_0, E_{00}, \tau_0, \beta$ ) in order to accurately fit the LVE behaviour of bituminous materials at a given temperature. The complex modulus of these materials is expressed by equation 2.63a for mixtures, whereas equation 2.63b provides the complex modulus specifically for bitumen.

$$E^*(i\omega\tau) = E_{00} + \frac{E_0 - E_{00}}{1 + \delta(i\omega\tau)^{-k} + (i\omega\tau)^{-h} + (i\omega\beta\tau)^{-1}} \quad (2.63a)$$

$$E^*(i\omega\tau) = \frac{E_0}{1 + \delta(i\omega\tau)^{-k} + (i\omega\tau)^{-h} + (i\omega\beta\tau)^{-1}} \quad (2.63b)$$

Where  $\beta$  is dimensionless and relates with the Newtonian viscosity as follows:

$$\eta = (E_0 - E_{00})\beta\tau \quad (2.64)$$

$E_{00}$  in equation 2.63b can be taken as zero in modelling binders, and the number of constants reduced to six.  $\tau$  is a temperature dependent parameter present in both Huet and Huet-Sayegh models, which is responsible for the TTSP phenomenon. Its evolution can be approximated by the WLF equation within the observation temperature ranges. This implies that the WLF constants  $C_1$  and  $C_2$  can be used to model the temperature susceptibility of the test material and the numbers of constants required for the model amounts to 9.

(Hervé Di Benedetto et al., 2007; Hervé Di Benedetto, Mondher, Sauzéat, & Olard, 2007) proposed a three-dimensional extension to the model, introducing two additional parameters  $\nu_0$  and  $\nu_{00}$  representing the poisson's ratio. The expression for the complex poisson's ratio is as expressed in equation 2.65.

$$\nu^*(\omega) = \nu_{00} + (\nu_0 - \nu_{00}) \frac{E^*(\omega) - E_{00}}{E_0 - E_{00}} \quad (2.65)$$

Where  $\nu_0$  and  $\nu_{00}$  are glassy and static Poisson's ratio respectively.

The shape of the cole-cole curve of a bituminous material is influenced by six of the 2S2PID parameters ( $\delta, k, h, E_0, E_{00}, \tau$ ) as shown in Figure 2.42



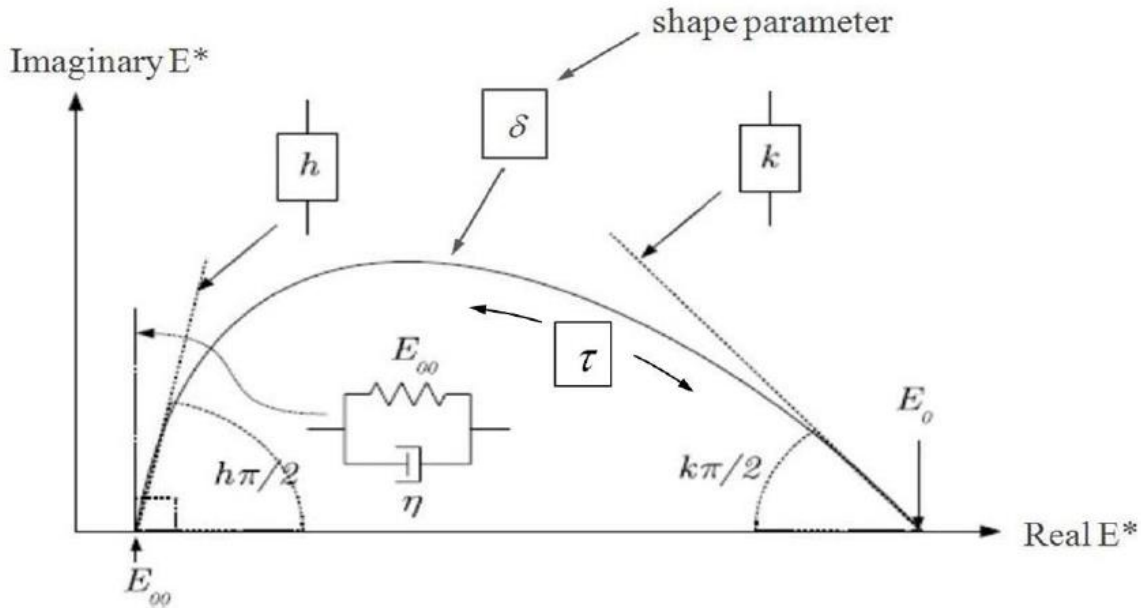


Figure 2.42 – Influence of 2S2PID constants on Cole-Cole plot of bituminous materials (Mangiafico, 2014).

### 2.4.3 Predictive Empirical Models

The laboratory characterization of the linear viscoelastic behaviour of bituminous mix is time consuming, in this light, researchers (Heukelom & Klomp, 1964) Hekeulom and Klomp model, (Ugé, Gest, Gravois, & Bonnaure, 1977) Ugé et al., (Christensen & Bonaquist, 2015; Christensen Jr, Pellinen, & Bonaquist, 2003) Hirsch model developed models to relate bitumen stiffness with the corresponding mixture stiffness. These models which are statistical test result of mixtures establish the relationships between a pair of temperature and frequency condition, whereby subsequent recalibration of other frequency-temperature pair is needed. This forms a major drawback of the existing models. The Witzcak model (Bari & Witzcak, 2007; Witzcak & Fonseca, 1996) introduced frequency dependency using TTSP.

(Hervé Di Benedetto et al., 2004) observed that the LVE behaviours of mastic and mixtures are dependent on the behaviour of the constituent bitumen LVE behaviour. This observation led to the proposition of a geometric transformation (Shift, Homothety, Shift, Time Shift) to predict complex modulus and complex Poisson's ratio of mixtures from binder complex modulus values. It is to be emphasized that this transformation is independent of any LVE model. The requirements for transformation include the asymptotic moduli  $E_{00,mix}$ ,  $E_{0,mix}$  of mixtures considered, time shift parameter  $\alpha$  dependent on the mix aggregate matrix and binder ageing occurring during mixing. The complex modulus and Poisson's ratio expressions are shown in equation 2.66 and 2.67 respectively.

$$E_{mix}^*(\omega, T) = E_{00\_mix} + [E_{binder}^*(10^\alpha \omega, T) - E_{00\_binder}] \frac{E_{0\_mix} - E_{00\_mix}}{E_{0\_binder} - E_{00\_binder}} \quad (2.66)$$

$$v_{mix}^*(\omega, T) = v_{00\_mix} + [E_{binder}^*(10^\alpha \omega, T) - E_{00\_binder}] \frac{v_{0\_mix} - v_{00\_mix}}{E_{0\_binder} - E_{00\_binder}} \quad (2.67)$$

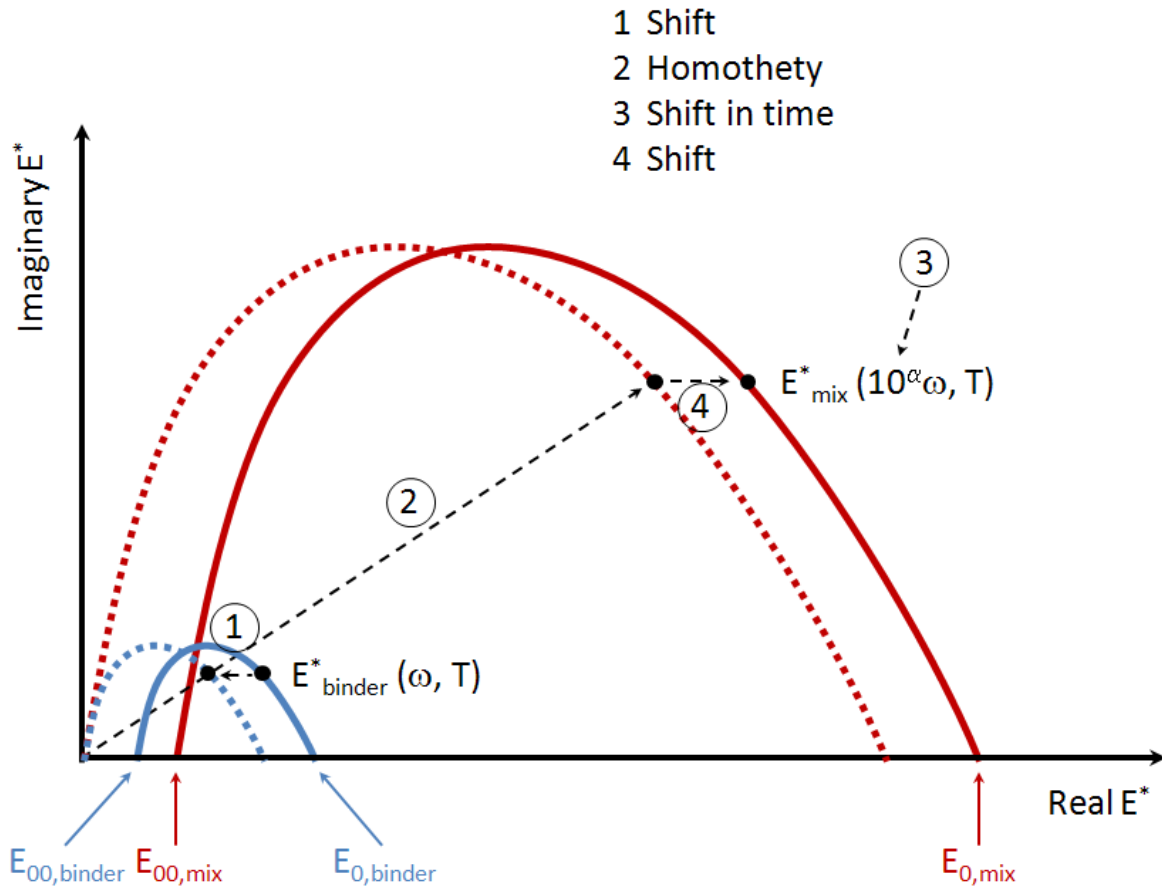


Figure 2.43 – Schematic representation of SHStS transformation in Cole-Cole plot (Mangiafico, 2014).

Several studies (S Pouget, 2011; Simon Pouget et al., 2010; Ramirez Cardona et al., 2015; Riccardi, Falchetto, Losa, & Leandri, 2017) have been used to validate the SHStS transformation.

## 2.5 Poisson's ratio

(Eringen, 1962) has defined a time dependent material constant called Poisson's ratio, as the ratio of the lateral contraction to the elongation in an infinitesimally small uniaxial extension assuming an idealized purely elastic compressible material. The lateral contraction in the

infinitesimal deformation of any real, i.e. viscoelastic, material is a time or frequency dependent material function (Tschoegl, 1989).

### 2.5.1 Linear Elastic Poisson's Ratio

The response of an isotropic elastic material as a result of the infinitesimal deformation to changes in size and shape are expressed by bulk modulus  $K$  and shear modulus  $G$  respectively. These constants may be referred to as derived elastic constants. In principle, every elastic constant may be derived from any two others, and each derived constant can be connected to the fundamental constants. The longitudinal modulus is defined by the expression

$$M = \frac{\sigma_1}{\varepsilon_1}, \varepsilon_2, \varepsilon_3 = 0 \quad (2.68)$$

Where the applied stress and strain in direction 1 are  $\sigma_1$  and  $\varepsilon_1$  respectively. Deformations are being prevented in the other two lateral dimensions.

Conversely, the Young's or stretch modulus  $E$  which is the deformation in uniaxial tension is expressed as

$$E = \frac{\sigma_1}{\varepsilon_1}, \sigma_2, \sigma_3 = 0 \quad (2.69)$$

During the measurement of the stretch modulus, the uniaxial extension is accompanied by contractions in the two transverse directions, as the lateral expansion is unrestricted. The ratio between the respective lateral contractions,  $-\varepsilon_2, -\varepsilon_3$  which are equal and uniaxial stretch  $\varepsilon_1$  is referred to as Poisson's ratio  $\nu$ . In terms of the two fundamental experimentally accessible moduli  $E$  and  $G$ ;

$$\nu = \frac{E}{2G} - 1 \quad (2.70)$$

For an incompressible material, Poisson's ratio approaches 0.5 from equation 2.70. This value is the maximum that the ratio can ever attain either the ratio is elastic or viscoelastic (frequency or time dependent) in an infinitesimal uniaxial stretch. The range of Poisson's ratio in an isotropic material as shown in elastic theory is given by  $-1 \leq \nu \leq 0.5$  (Malvern, 1969). It can therefore take on negative values, suggesting an expansion in the transverse directions rather than a contraction.

### 2.5.2 Linear Viscoelastic Poisson's Ratio

As with the other quantities mentioned in Section 2.6.1, Poisson's ratio is an elastic constant. Therefore, they are all defined for a (hypothetical) substance whose mechanical properties exhibit no time dependence. Such a substance is hypothetical because, strictly speaking, it does not exist. In accordance with the second law of thermodynamics, a portion of the deformational energy is invariably dissipated by viscous forces during any mechanical deformation. This dissipation is responsible for the time dependence of any material's mechanical properties. Therefore, real materials are viscoelastic. The theory of elasticity can only be applied to a real material if the time dependence of its mechanical properties can be disregarded (Tschoegl, Knauss, & Emri, 2002). Frequency-dependent Poisson's ratio is described as the lateral contraction ratio measured in an infinitesimally small uniaxial deformation of a viscoelastic material in response to a steady-state sinusoidally oscillating strain (Tschoegl et al., 2002).

#### 2.5.2.1 Laplace Carsons transform relations of Poisson's ratio

The formulation of problems in the complex Laplace transform plane greatly simplifies manipulations involving the material functions of the linear theory of viscoelasticity. The function  $f(t)$  is transformed to the  $\bar{f}(s)$  by

$$\bar{f}(s) = s \int_0^{\infty} f(t) \exp(-st) dt \quad (2.71)$$

Where the integral equation represents the Laplace transform and  $s$  is complex. The frequency dependent viscoelastic response function lies along the real axis of the transform plane where  $b$  tends to zero in  $s = b + iw$ . The complex plane relation is retransformed to the imaginary frequency axis.

If an elastic solution to a stress analysis problem is known, the viscoelastic solution to the same problem in the transform plane can be obtained by substituting the appropriate complex-plane transforms for the elastic quantities. And hence, the stress-strain relations of the theory of elasticity are transformed into relations between the Laplace transforms of the stress and strain, where the moduli are replaced by the corresponding relaxances, the Laplace transforms of the impulse response functions (Tschoegl et al., 2002).

Frequently, the Carson transform relations can be simplified by discarding the transform variable,  $s$ , from both sides of an equation or from the numerator and denominator of a fraction. Therefore  $v(s)$  is expressed in terms of two fundamentally accessible moduli from equation 2.70 as:

$$\bar{v}(s) = \frac{\bar{E}(s)}{2s\bar{G}(s)} - \frac{1}{s} \quad (2.72)$$

The correspondence principle simply requires that the elastic constants be replaced by the corresponding complex quantities when dealing with a sinusoidally steady-state excitation rather than the imposition of a step function of time. Equation 2.70 becomes

$$v^*(\omega) = \frac{E^*(\omega)}{2G^*(\omega)} - 1 \quad (2.73)$$

### 2.5.2.2 The frequency domain Poisson's ratio

In accordance with correspondence principle, the response of a material to a sinusoidal steady state excitation of a unit amplitude in the frequency domain by applying a steady-state sinusoidal strain with amplitude  $\varepsilon_0$ , the frequency dependent Poisson's ratio is expressed as;

$$v^*(\omega) = \frac{-\varepsilon_2^*(\omega)}{\varepsilon_0} \quad (2.74)$$

Where  $-\varepsilon_2^*(\omega)$  is the complex sinusoidal steady-state lateral contraction.

Expressions of Poisson's ratio is as shown in equation 2.75

$$v^*(\omega) = v'(\omega) + iv''(\omega) \quad (2.75)$$

Furthermore, it is expressed in polar coordinates as;

$$v^*(\omega) = |v^*|e^{i\omega\varphi_v} = |v^*|[\cos \varphi_v(\omega) + i \sin \varphi_v(\omega)] \quad (2.76)$$

$$|v^*| = \sqrt{[v'(\omega)]^2 + [v''(\omega)]^2} \quad (2.77)$$

$$\varphi_v = \tan^{-1} \frac{v''(\omega)}{v'(\omega)} \quad (2.78)$$

The real and imaginary part of Poisson's ratio expressed as functions of two other response function in both Cartesian forms is expressed as follows;

$$v'(\omega) = \frac{E'(\omega)G'(\omega)+E''(\omega)G''(\omega)}{2\{(G'(\omega))^2+(G''(\omega))^2\}} - 1 \quad (2.79)$$

$$v''(\omega) = \frac{E'(\omega)G''(\omega)+E''(\omega)G'(\omega)}{2\{(G'(\omega))^2+(G''(\omega))^2\}} \quad (2.80)$$

In polar coordinates in terms of shear and stretch responses;

$$v'(\omega) = \frac{E^*(\omega)}{2G^*(\omega)} \cos(\varphi_E - \varphi_G) - 1 \quad (2.81)$$

$$v''(\omega) = \frac{E^*(\omega)}{2G^*(\omega)} \sin(\varphi_G - \varphi_E) \quad (2.82)$$

### 2.5.3 Poisson's Ratio of Bituminous Materials

Two approaches namely the direct and indirect approaches can be used to obtain Poisson's ratio of a linear viscoelastic material. The first approach utilises the direct comparison of the measured longitudinal and transverse deformations, however in the second approach, the isotropy hypothesis is applied to two other viscoelastic functions to obtain Poisson's ratio. Errors can be greatly avoided in Poisson's ratio determination by measuring the required viscoelastic functions simultaneously on the same sample while adapting similar experimental conditions (Tschoegl et al., 2002). Over the last decade, attempts have been made by researchers ((Hervé Di Benedetto et al., 2007; Andrea Graziani, Bocci, & Canestrari, 2014; Kassem, Grasley, & Masad, 2013; Mahmoudi et al., 2021; Perraton et al., 2016; Pham et al., 2015)) to obtain and model the Poisson's ratios  $v^*$  of bituminous materials by adapting uniaxial test methods used to obtain the Young's modulus ( $E^*$ ) of bituminous mixtures (T342, 2011) (C EN, 2012) see Figure 2.44. This method as stated by (A Graziani et al., 2017) recommends the simultaneous measurements of  $E^*$  and  $v^*$  of cored cylindrical asphalt mixtures by means of sinusoidal axial tests carried out within the LVE domain. Furthermore, the material response function calculation within the frequency domain is made during steady state regime putting into consideration transient effects (Q. T. Nguyen, Di Benedetto, Sauzéat, & Tapsoba, 2013) (Hervé Di Benedetto, Nguyen, & Sauzéat, 2011).

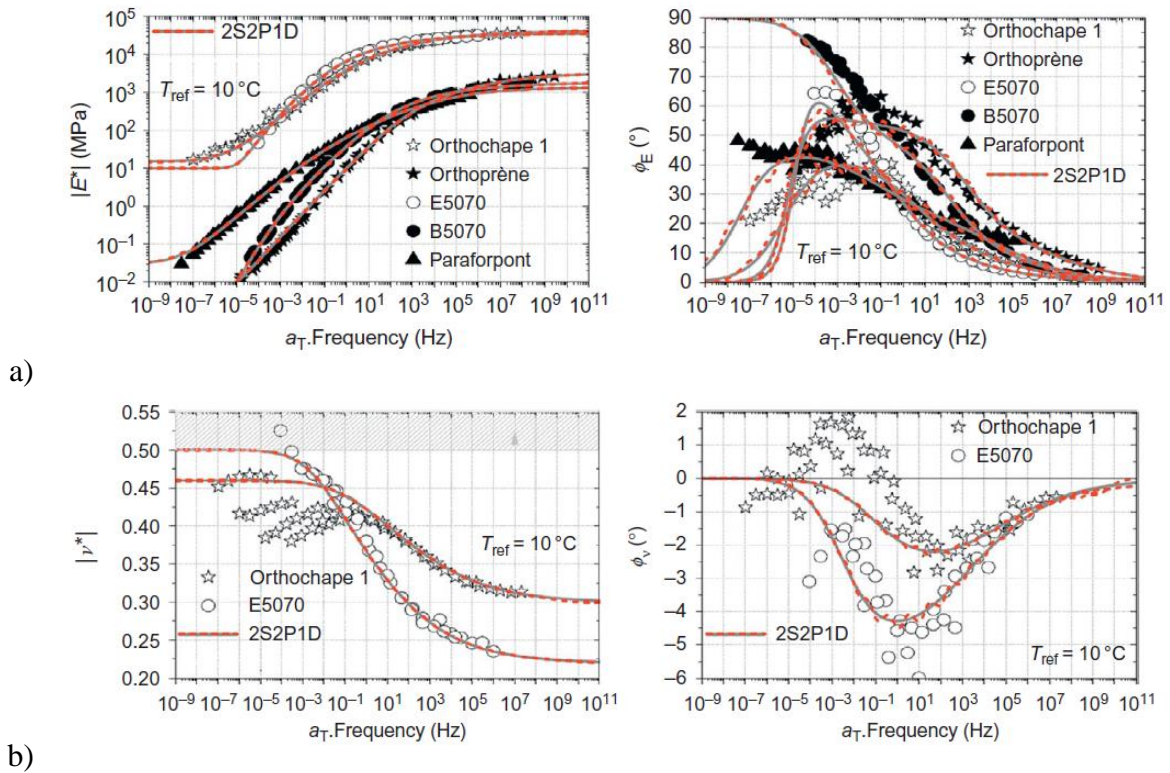


Figure 2.44 – a) Complex modulus data and b) Complex Poisson's ratio data measured directly on bituminous mixtures with the respective fitted 2S2P1D master curves (S Pouget, 2011; Simon Pouget et al., 2010).

Poisson's ratio of bituminous mixtures has also been determined by other test methods (indirect) such as seismic methods (Gudmarsson et al., 2014) with a higher Poisson's ratio difference of 0.1 as shown in Figure 2.45 comparing it to Poisson's ratio determined by tension-compression test; ultrasonic wave propagation (Hervé Di Benedetto, Sauzéat, & Sohm, 2009) (Mounier, Di Benedetto, & Sauzéat, 2012), cyclic and dynamic modal testing (Gudmarsson et al., 2015).

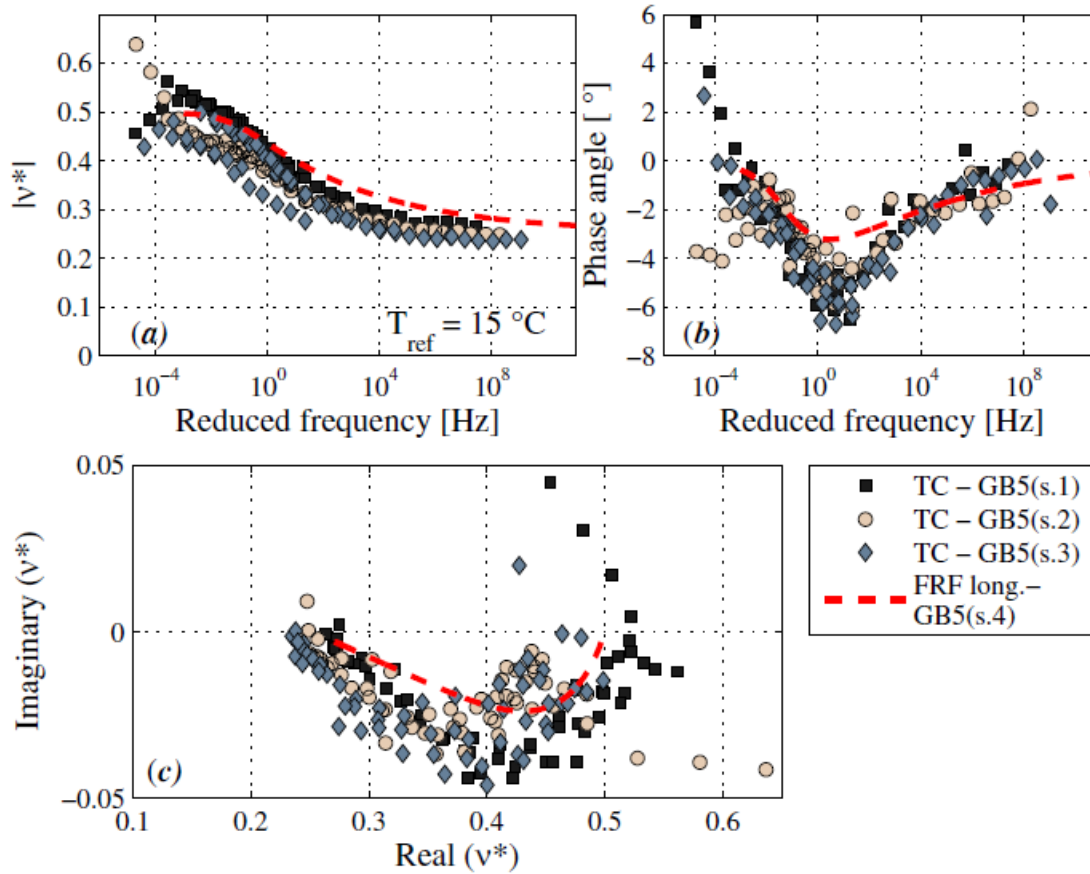


Figure 2.45 – Comparison of the FRF and tension-compression test determined a) complex Poisson's ratio master curves b) Poisson's ratio phase angles and c) cole-cole plot of four different specimens (Gudmarsson et al., 2015; Gudmarsson et al., 2014).

The prediction of bituminous mixtures characteristics from constituent binder characteristics through the application of transformation equations (Hervé Di Benedetto et al., 2004) (François Olard & Di Benedetto, 2003) has necessitated the measurement of binder Poisson's ratio to improve the model prediction accuracies. (Hervé Di Benedetto et al., 2007) demonstrated the Poisson's ratio of bitumen not to be static but varies between 0.35 at low temperature/high frequency to 0.5 at high temperature/low frequency. Furthermore, the phase angle is very small and negative, which varied between 0 and  $-1.8^\circ$  as illustrated in Figure 2.46.



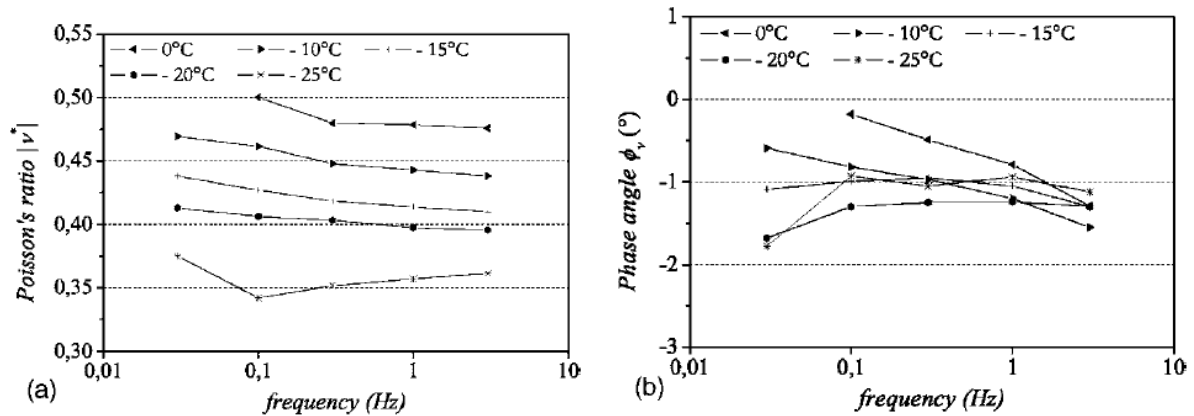


Figure 2.46 – Experimental result of directly determined 50/70 bitumen Poisson's ratio a) norm of  $\nu^*$ , b) phase angle as adapted from (Hervé Di Benedetto et al., 2007)

This thesis therefore aims to establish a new method to determine the Poisson's ratio of different binders by adopting the indirect method of measurement through the determination of the shear  $G^*$  and axial  $E^*$  complex moduli of binders using a DSR capable of both oscillatory and tension-compression measurements.

## 2.6 Linear viscoelastic limits of bituminous materials

The presence of nonlinearity in bituminous materials leads to a systematic reduction in the norm and an increase in the phase angle of the equivalent modulus when subjected to higher levels of loading amplitude. The boundaries of the linear viscoelastic (LVE) region in bituminous materials, with regards to stress or strain, are often determined by the point at which a certain proportion of the magnitude of the complex modulus is attained. The utilisation of a threshold value of 95% for the complex modulus has been prevalent following its proposition by the American Strategic Highway Research Programme (SHRP) as documented by (Anderson et al., 1994) as illustrated in Figure 2.47. According to (G. D. Airey, B. Rahimzadeh, & A. C. Collop, 2003), the strain amplitude limit ( $\epsilon_{95\%}$ ) for bituminous mixtures subjected to axial tension-compression is approximately  $100\mu\text{m}/\text{m}$ . On the other hand, (G. D. Airey et al., 2003) Airey, Collop, and Dongre (2002) found that the shear strain amplitude limit ( $\gamma_{95\%}$ ) for binders tested on a Dynamic Shear Rheometer is approximately  $10000\mu\text{m}/\text{m}$ , which corresponds to a 1% deformation. The study conducted by (Q. T. Nguyen et al., 2015) suggests that the nonlinearity effects on the moduli of bituminous mixtures do not vary based on the loading directions. This is because the complex Poisson's ratio of these mixtures, as observed in three-dimensional experimental results, appears to be independent of strain amplitude.

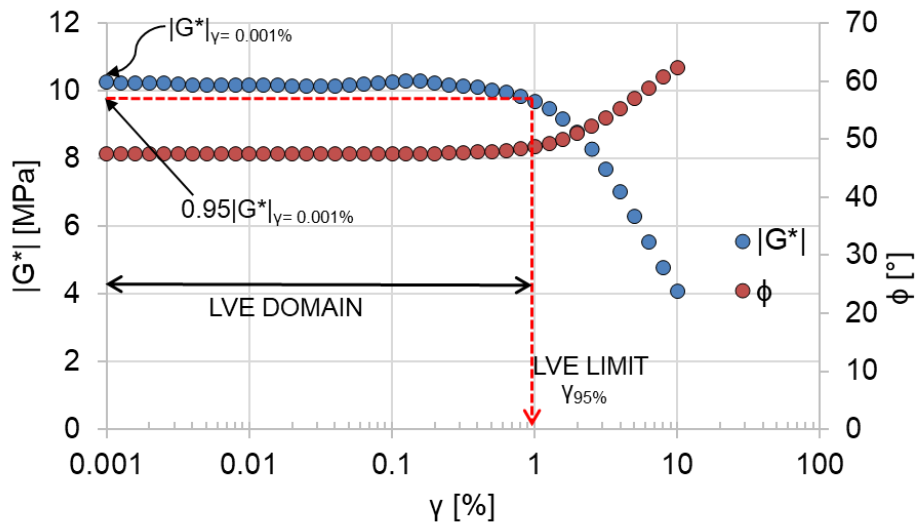


Figure 2.47 – Linear viscoelastic limit of a binder

Recent studies have demonstrated that the TTSP is also acknowledged and adhered to, employing the identical shift factor utilised for the complex modulus (Babadopulos, 2017; Q. T. Nguyen et al., 2015).

### 3. Equipment, Materials and Test Procedures

This chapter provides a comprehensive overview of the technical specifications of the equipment utilised in the experimental campaigns, as well as the examined bitumen commercial standards and the corresponding test protocols for each campaign.

#### 3.1 Dynamic Shear Rheometer and accessories

For the experimental campaigns in this thesis, DSR was utilised. The DSR is a Modular Compact Rheometer (MCR) 702 by Anton Paar, located at the ENTPE laboratory (see Figure 3.1). This rheometer is equipped with a lower motor capable of axial movements in tension-compression and the conventional upper motor utilised for the shear oscillatory tests.

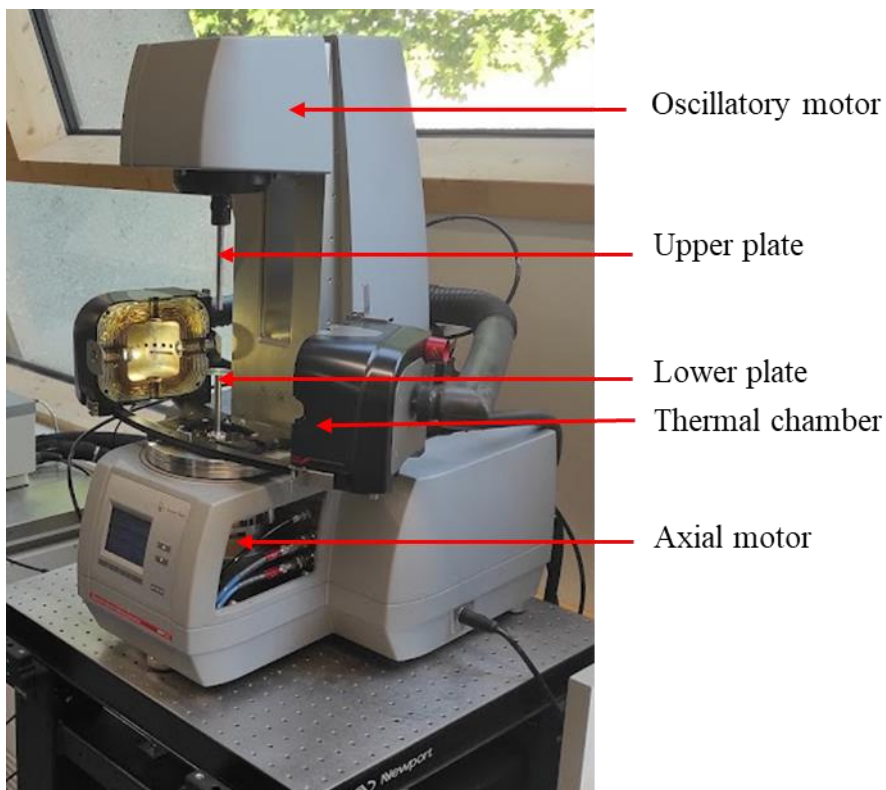


*Figure 3.1 – DSR equipment used for experimental campaigns*

The detailed specifications given by the manufacturers of the rheometer in terms of its limit are stated in the Tables 3.1 and 3.2

*Table 3.1 – Technical specifications of the rheometer in oscillatory mode.*

<b>Property</b>	<b>Upper Motor</b>
Torque Oscillation range	0.5 nNm – 230 mNm
Deflection angle resolution	0.05 $\mu$ rad
Frequency range	$10^{-7}$ – 100 Hz
Normal force range	0.005 – 50 N
Normal force resolution	0.5 mN

*Table 3.2 – Technical Specification of the rheometer in axial mode.*

<b>Property</b>	<b>Lower Motor</b>
Force range	0.0005 – 40 N
Displacement range	0.01 – 9400 $\mu$ m
Frequency range	0.001 – 100 Hz

The DSR presents two possible usable configuration modes namely, the shear oscillatory mode (classical) and axial mode.

### 3.1.1 DSR shear oscillatory mode

The assembly of this function mode is represented in Figure 3.2. The DSR is fitted with a water-cooled double Peltier system in addition to the temperature hood (H-PTD200) which functions as the temperature control device. Furthermore, a counter cooling system known as the Julabo FP50 is installed to aid temperature regulation. The fluid contained in the counter-cooling system (Julabo FP50) shown in Figure 3.2c is glycol with anti-freeze up to  $-24^{\circ}\text{C}$ . Parallel plates of various sizes as shown in Figure 3.2b are adaptable to the DSR in this configuration.

### 3. Equipment, Materials and Test Procedures

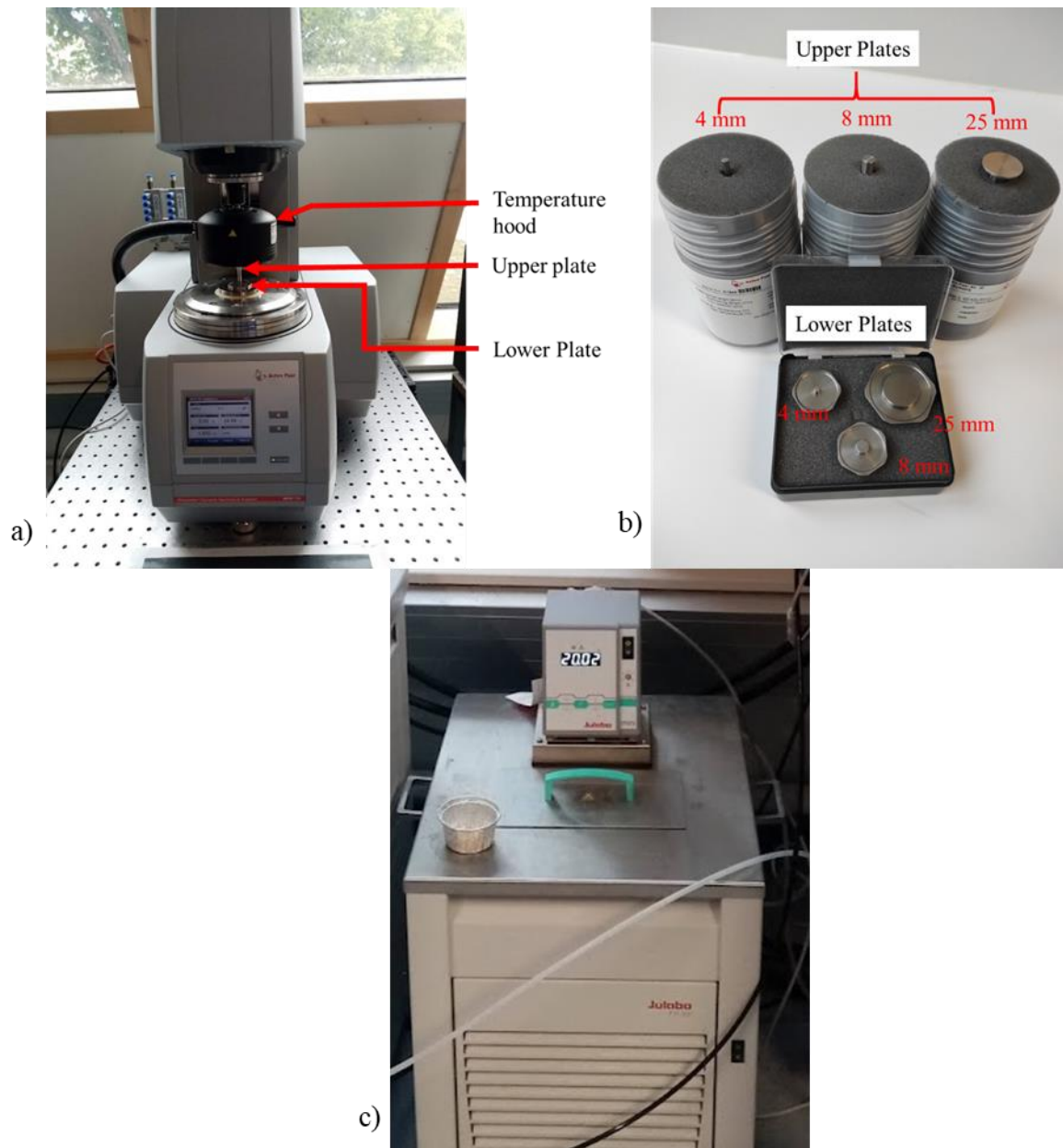


*Figure 3.2 – a) MCR 702 with temperature hood and fixed lower plate; b) parallel plate fixtures and c) fluid circulator (Julabo FP50) at ENTPE laboratory*

To conduct a rheological test with this configuration, a cylindrical bitumen sample is sandwiched between two plates (upper and lower plates). The bottom plate remains stationary while the other moves, thereby applying a shear load to the sample. The mode of loading can be either stress control or strain control. The angle of rotation of the moving plate and the applied torque are measured continuously.

Based on the type of test being conducted, sample diameter (equal to plate diameter) and thickness can vary.

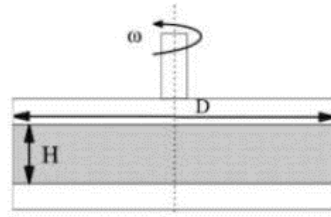


*Figure 3.3 – DSR parallel plate specimen geometry (Orozco, 2020)*

The maximum shear stress and strain values calculated from spindle diameter  $D$  and specimen height  $H$  (Figure 3.3) are retained for analysis when parallel plate configuration is utilized. These measurements taken within the linear viscoelastic domain, are calculated as shown in Equation 2.1 and 2.2. The torque measured is adjusted based on the DSR spindle's compliance.

#### 3.1.2 DSR axial mode

The second configuration (axial mode configuration) shown in Figure 3.4 utilises a convection temperature device (CTD 600), identified as thermal chamber, for bitumen sample temperature conditioning. The 25 mm diameter lower plate is equipped with a temperature sensor that aids in the regulation of the specimen temperature. This configuration makes use of two counter cooling systems namely Julabo FP89 (see Figure 3.4b) and the aforementioned Julabo FP50 respectively. Julabo FP50 is dedicated solely to maintain the axial motor at ambient temperature. However, FP89 fluid circulator is dedicated to regulate the temperature of the CTD 600. This fluid circulator contains a silicon based anti-freeze cooling fluid with a threshold of  $-50^{\circ}\text{C}$ .

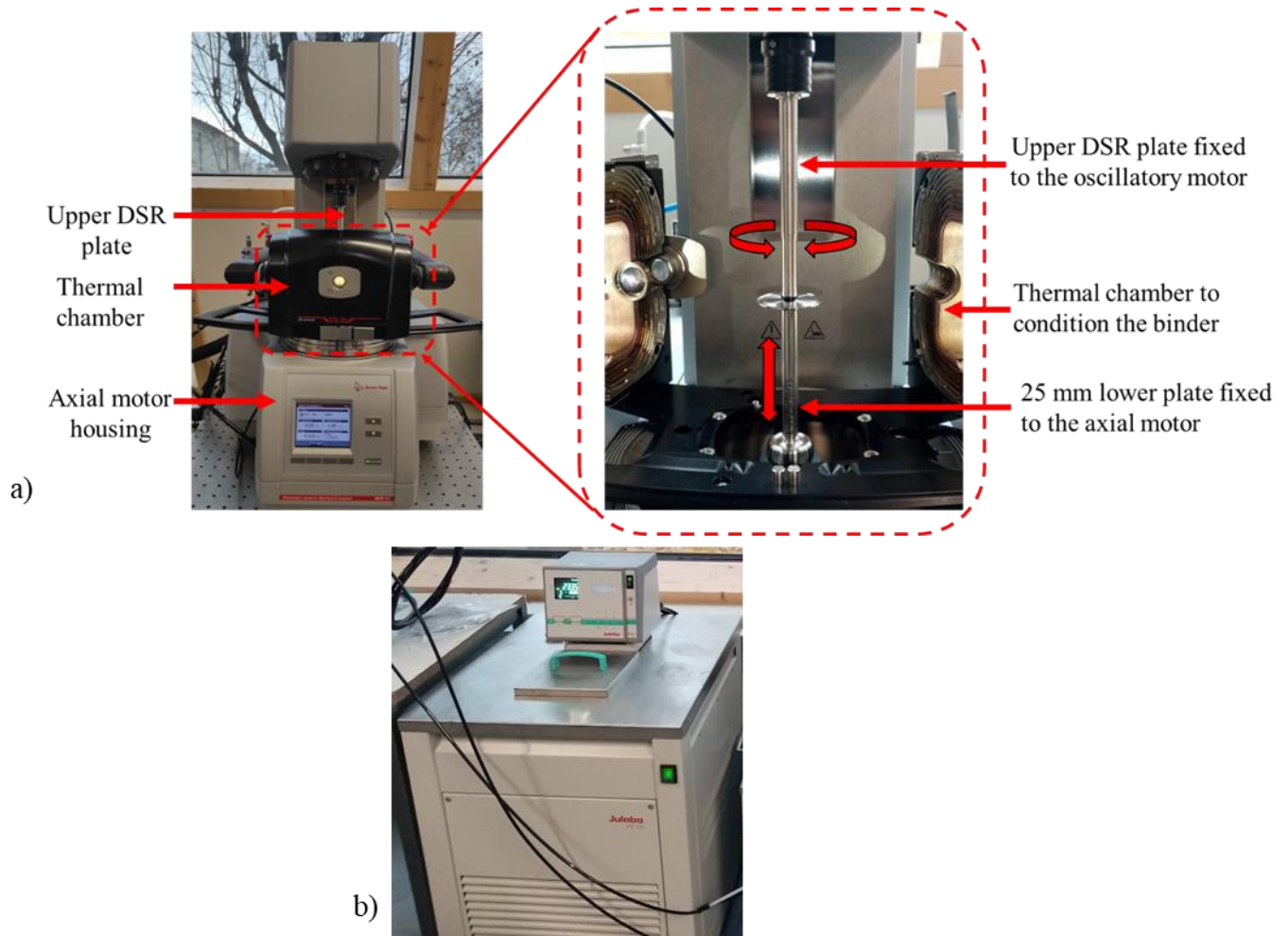


Figure 3.4 – a) MCR 702 tension-compression assembly with thermal chamber; b) fluid circulator (Julabo FP89) at ENTPE laboratory

Cylindrical bitumen is sandwiched between two plates (Figure 3.5), fixed upper plate (equal in diameter to the test sample) and a lower plate (25 mm diameter) capable of applying force  $F$  in the axial direction through the axial motor of the DSR. The bitumen is loaded in the axial direction sinusoidally (tension/compression). Tests are either carried out in strain or stress control mode, by applying a sinusoidal loading centered at zero. The exerted force ( $F$ ) on the specimen is continuously measured. The stress  $\sigma$  (in the direction of force) in the material is calculated by dividing the measured force by the specimen's cross-sectional area, according to the Equation 3.1.

$$\sigma = \frac{4F}{\pi D^2} \quad (3.1)$$

Where  $D$  is the diameter of the sample

The corresponding axial strain is expressed in equation 3.2 where  $l$  is the height of the specimen and displacement  $\Delta l$ .

$$\varepsilon_{zz} = \frac{\Delta l}{l} \quad (3.2)$$

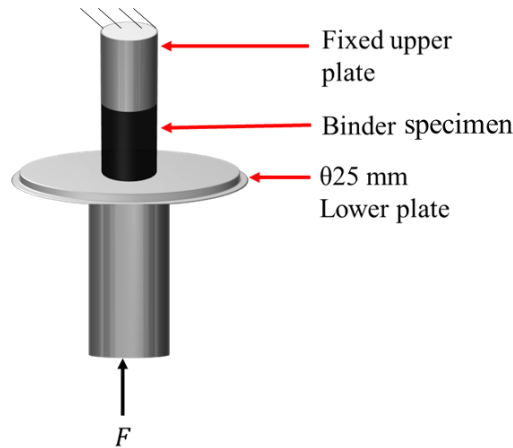


*Figure 3.5 – Schematic diagram of a DSR axial complex modulus test setup*

In addition to the axial functionality of this configuration (Figure 3.4a), an oscillatory test can also be performed. The oscillatory (classical) test is performed by applying a shear load to the sample by the upper plate and the lower plate remains fixed. These tests are performed alternately on a bitumen sample due to the limitations of the DSR.

#### **3.2 Bitumen and bitumen preparation**

The bitumen, contained in 10-liter cans, were subjected to heating in an oven until it reached its ring and ball temperatures. Subsequently, the bitumen was homogenized by stirring with a stirring rod and then transferred into 1-liter cans for the purpose of storage. The purpose of this action is to mitigate the accelerated ageing of the bitumen. The bitumen present in the 1-liter cans was afterwards divided into aluminium cups and securely covered with aluminium papers (see Figure 3.6) prior to being stored in the refrigerator.





Figure 3.6 – Bitumen proportioned in cans and aluminum cups for storage in the refrigerator

The three binders utilized throughout this thesis include two pure bitumen 35/50 labelled B3550 and 50/70 (B5070), a 50/70 polymer modified bitumen labelled PmB. They were all supplied by Eiffage company. Results of some classical semi-empirical tests on these binders are highlighted in Table 3.3

Table 3.3 – Binder properties

Binder	Ring and Ball Temperature (°C)	Penetration ( $10^{-1}$ mm)
B3550	53.2	41
B5070	49.4	59
PmB	76.4	40

Throughout this thesis, bitumen to be tested were preheated at temperatures equal to the ring and ball temperature plus  $100^{\circ}\text{C}$  (B3550- $155^{\circ}\text{C}$ , B5070- $150^{\circ}\text{C}$ , PmB- $178^{\circ}\text{C}$ ) followed by manual stirring with a glass rod to ensure homogenization and poured in the respective silicon moulds of the desired sample size (4 mm, 8 mm and 25 mm diameter) as shown in Figure 3.7. To allow for proper filling of the moulds with bitumen, and avoiding bubble formation at the bottom of the sample, the moulds were preheated at a temperature of  $120^{\circ}\text{C}$ . The filled silicon moulds were allowed to cool for 10 minutes at room temperature. The samples were afterwards

### 3. Equipment, Materials and Test Procedures

---

placed in a refrigerator to facilitate their cooling and facilitate the removal of the test samples from their moulds.

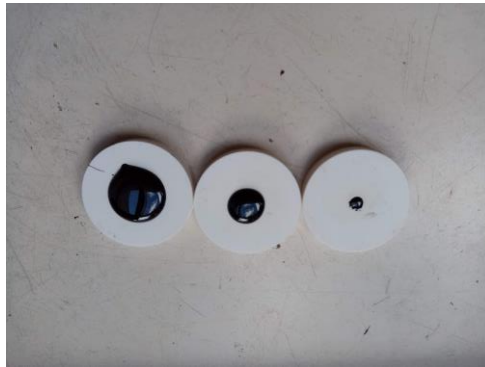


*Figure 3.7 – Silicon moulds filled with bitumen (from left to right 25 mm, 8 mm, 4 mm diameter specimen)*

The method used to prepare bitumen for testing, utilising both DSR variants (oscillatory and linear motor), follows a standardised technique defined in (EN14770, 2012). The DSR plates were preheated to the specific ring and ball temperature of the test material prior to conducting the experiment. The bitumen chip was positioned onto the lower plate and subjected to preheating. The upper plate was cautiously lowered in order to achieve the intended trimming gap. The trimming gap is comprised of the testing gap  $H$  (as shown in Figure 3.3) plus an additional 0.150 mm or 0.050 mm. The extent of the trimming gap, however, is contingent upon the diameters of the test plates. The trimming of the sample is conducted at this specific interval to mitigate the potential damage caused by stripping resulting from the thermal contraction of both the axis and the bitumen throughout the cooling process (Orozco, 2020). As per the guidelines outlined in the (EN14770, 2012), it is advised to maintain a cooling rate of 2°C per minute. Additionally, a period of 30 minutes is deemed necessary to achieve thermal equilibrium before initiating any testing procedures.

#### **3.3 Experimental procedures**

This section of the thesis consists of the experimental procedures executed in each campaign

##### **3.3.1 Bitumen time sweep test**

According to (EN14770, 2012), bitumen samples were sandwiched between two DSR parallel plates (4 mm). The temperature was conditioned to the required test temperature (-20°C) as shown in the scheme illustrated in Figure 3.8. Although the test is recommended to start only

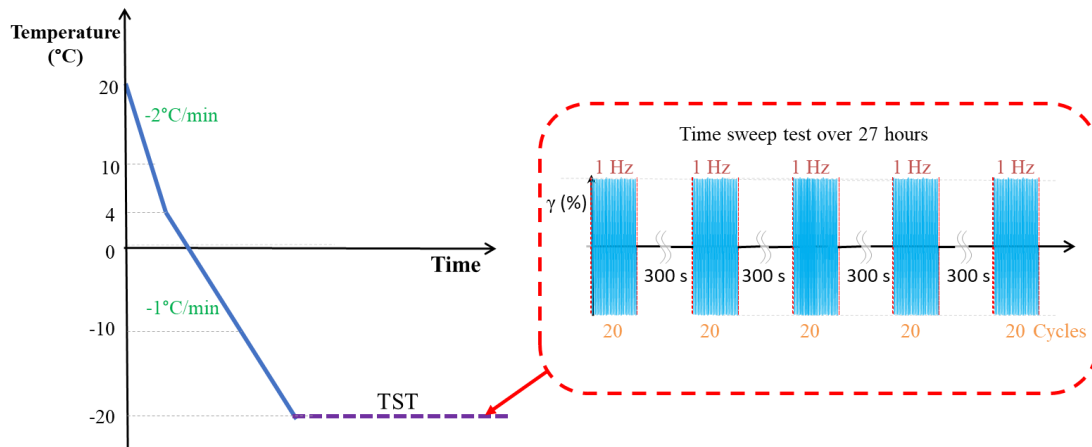


Figure 3.8 – Scheme showing time sweep test (TST) over a 27 hours period

after the temperature has remained at the desired temperature for at least 10 minutes, the test commenced immediately after the Peltier temperature reached  $-20^{\circ}\text{C}$  as displayed on the DSR. This was intended to study the evolution of the bitumen modulus within the required thermal conditioning periods. A small strain amplitude of 0.005% was imposed on the binder at every 20 cycles and a constant frequency 1 Hz. Rest periods of 5 minutes were observed in between each frequency sweeps over a 27 hours period.

### 3.3.2 Bitumen linear viscoelastic limit determination in shear

After specimen preparation, (EN14770, 2012) compliant shear strain amplitude sweep tests (SSAST) were conducted at a constant temperature and frequency, with strain amplitude increasing from 0.001% to 10%. 51 distinct tests were conducted with 51 distinct temperature/frequency combinations. Six temperatures and three frequencies were selected:  $-25^{\circ}\text{C}$ ,  $-20^{\circ}\text{C}$ ,  $-10^{\circ}\text{C}$ ,  $0^{\circ}\text{C}$ ,  $10^{\circ}\text{C}$ , and  $20^{\circ}\text{C}$ , and 10 Hz, 0.3 Hz, and 0.01 Hz, respectively. The test was conducted on a distinct sample for each temperature and frequency combination. For test temperatures of  $-25^{\circ}\text{C}$ ,  $-20^{\circ}\text{C}$ ,  $-10^{\circ}\text{C}$ , and  $0^{\circ}\text{C}$ , the specimen temperature was decreased from  $20^{\circ}\text{C}$  to  $4^{\circ}\text{C}$  at a rate of  $2^{\circ}\text{C}/\text{min}$  before being brought to the target test temperature at a rate of  $1^{\circ}\text{C}/\text{min}$  as shown in Figure 3.9. This procedure was followed in order to prevent the formation of microcracks within the sample due to a stiffening effect as a result of a rapid temperature decrease.

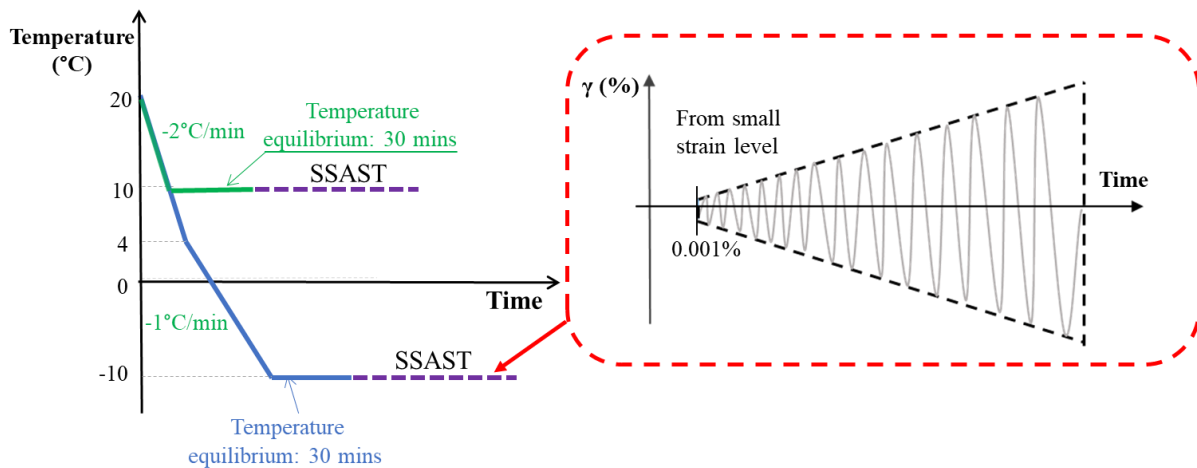


Figure 3.9 – Scheme showing the procedure for shear strain amplitude sweep test at low and medium test temperatures using a DSR with fixed lower plate and temperature hood.

For 10°C tests, the sample temperature was decreased from 20°C to the test temperature at a rate of 2 °C per minute. A normal force of 0 N was maintained on the sample throughout all temperature changes, which were carried out in normal force control mode. Prior to testing, specimens were conditioned to thermal equilibrium for 30 minutes (EN14770, 2012; Gražulytė et al., 2021) at the test temperature. All shear strain amplitude sweep intervals were executed in gap control mode while the normal force was monitored. The shear complex modulus  $G^*$  was determined from DSR measurements (torque and rotation angle). The temperatures and corresponding plates used for the tests are presented in Table 3.4.

Table 3.4 – Plates and temperatures used for shear strain amplitude sweep test on bitumens

Parallel Plate (mm)	Temperature (°C)
4	-25, -20, -10, 0, 10
8	20, 30
25	40, 50, 60, 70

For low temperature asphalt binder testing, the instrument shear compliance must be taken into account due to the high material rigidity. Torsional compliance, expressed in rad/Nm, signifies the angular displacement caused by the rheometer drive system and the test fixture. RheoCompass software, which is typically implemented in the DSR, corrects rheological test

### 3. Equipment, Materials and Test Procedures

---

results pertaining to the corresponding torsional compliance automatically. Additionally referred to as shear compliance, torsional compliance is specific to each measuring geometry. This was modified and reviewed within the RheoCompass application. Although the values are usually supplied by the manufacturer of the instrument, they were manually determined using the superglue method in accordance with (Farrar, Sui, Salmans, & Qin, 2015) and modified in this instance. The radial compliance determined for both PP4 and PP8 were 0.0232 and 0.0185 respectively.

#### 3.3.3 Shear complex modulus test

The procedure of complex shear modulus tests described in this section consisted of frequency sweep tests from 10 to 0.01Hz at eleven different temperatures from -30°C to 70°C. Furthermore, the test consisted of three series of frequency sweep tests for each bitumen, as shown in Figures 3.10. The test plates utilised at each temperature are highlighted in Table 3.5.

*Table 3.5 – Plates and temperatures used for shear complex modulus tests*

Test plate	Test temperatures
PP4 (4 mm)	$\leq 10^{\circ}\text{C}$
PP8 (8 mm)	$10^{\circ}\text{C} - 30^{\circ}\text{C}$
PP25 (25 mm)	$30^{\circ}\text{C} - 70^{\circ}\text{C}$

Frequency sweep tests from 10 to 0.01Hz were applied at a constant shear strain amplitude of 0.1% for each isotherm after a 20-minutes rest to obtain thermal equilibrium. Subsequently a 300-seconds rest were observed in between each frequency sweeps. For the tests at low temperatures, the 1.75 mm height test samples are mounted on the lower plate of the DSR and conditioned to 20°C. The DSR is equipped with a function known as the Automatic Gap Control (AGC). Samples of bitumen tend to exhibit changes in response to variations in temperature, specifically in terms of contraction and expansion. Nevertheless, the Automatic Gap Control (AGC) is designed to effectively regulate these fluctuations in bitumen sample responses to temperature. However, the utilisation of this tool often leads to the occurrence of cracks in the specimen. Hence, it is evident that there exists an issue pertaining to the tool that lacks clarity in its understanding. Consequently, the tool was deactivated before the commencement of each low temperature test (specifically, the test involving PP4). Temperature ramps of 1°C/minute

was imposed on all test samples from 4°C to -30°C to allow a gradual contraction of the test binders thereby preventing a crack of the test samples due to temperature shocks.

The temperature at which physical hardening is at its peak in bitumen is -20°C (Tabatabaee et al., 2012). The longer physical hardening persists further below the T<sub>g</sub>, the material is aged (McKenna, 2012). Physical hardening has been studied in section 4.2, and it was observed that the increase in bitumen stiffness and reduction in phase angle continued over the test period of 27 hours for both bitumen (B5070 and B3550). The B5070 bitumen had a stabilisation phase, characterised by a modulus incremental rate of 0.035MPa/min and a reduction in phase angle of 0.1°, occurring 8 hours following the equilibrium period. This increment is however insignificant. Physical hardening has just minor effect on linear viscoelastic characteristics below the T<sub>g</sub> and takes less than 10-hours to complete (Laukkanen et al., 2018). Furthermore, the hardening does not reach a limiting value within the limits of the experiment. As a result, a compromise duration of a 12-hour equilibrium period was implemented during the frequency sweep tests conducted in shear to minimize the effects of physical hardening.

For each temperature-frequency pair, a series of cycle acquisitions is utilised to determine the phase angle and the norm of the complex modulus. To keep the test time short, we record only a few cycles at low frequencies. At high frequencies, though, we can select more points. The number of acquisition cycles chosen for each frequency is shown in Table 3.6. It should be noted that because the total number of cycles investigated is relatively small, fatigue-related phenomena are minimal. In addition, between frequency loadings, the material is given a 5-minute rest time.

### 3. Equipment, Materials and Test Procedures

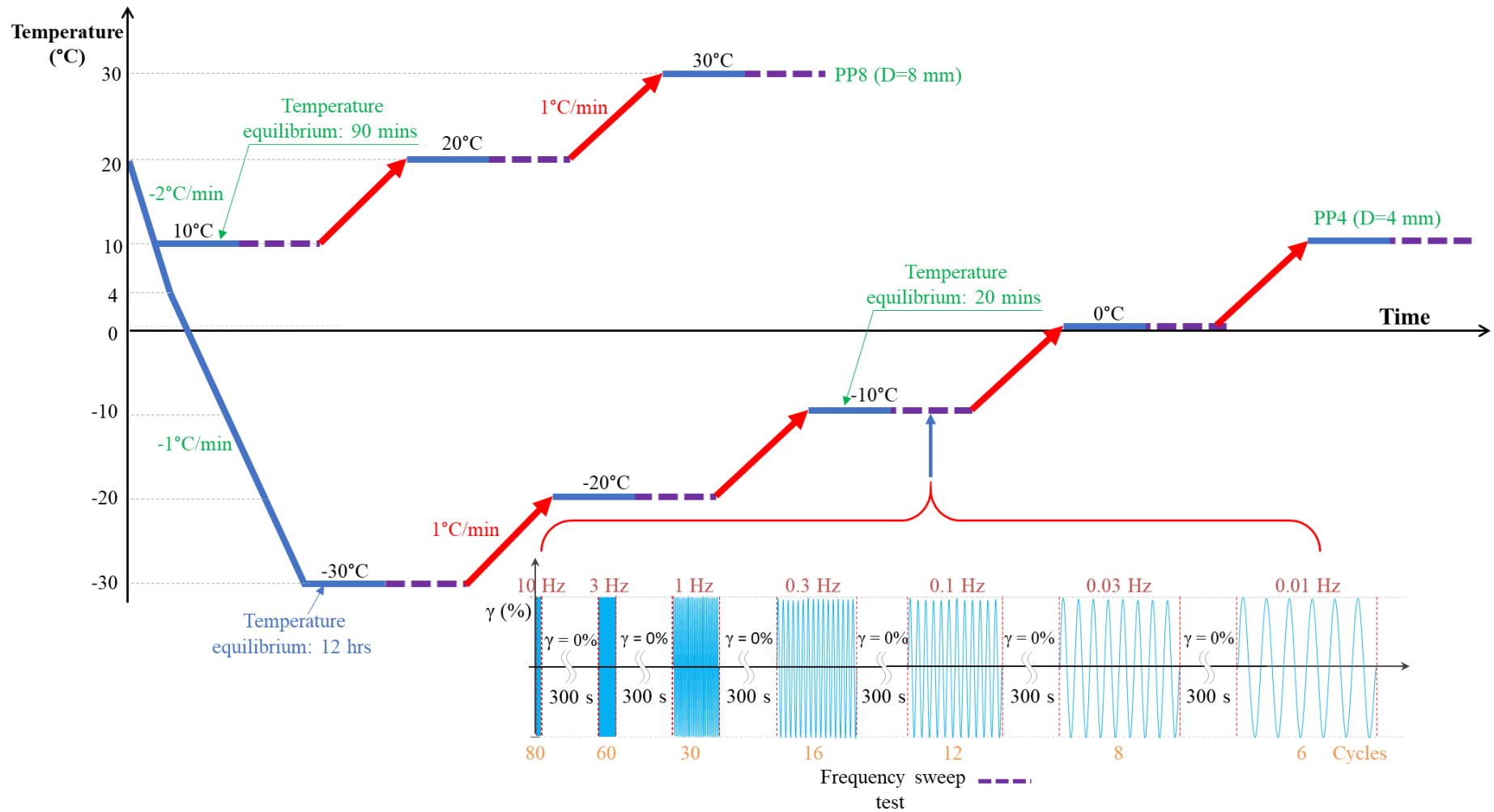


Figure 3.10a) - DSR complex shear modulus test scheme using 4 mm and 8 mm parallel plates

### 3. Equipment, Materials and Test Procedures

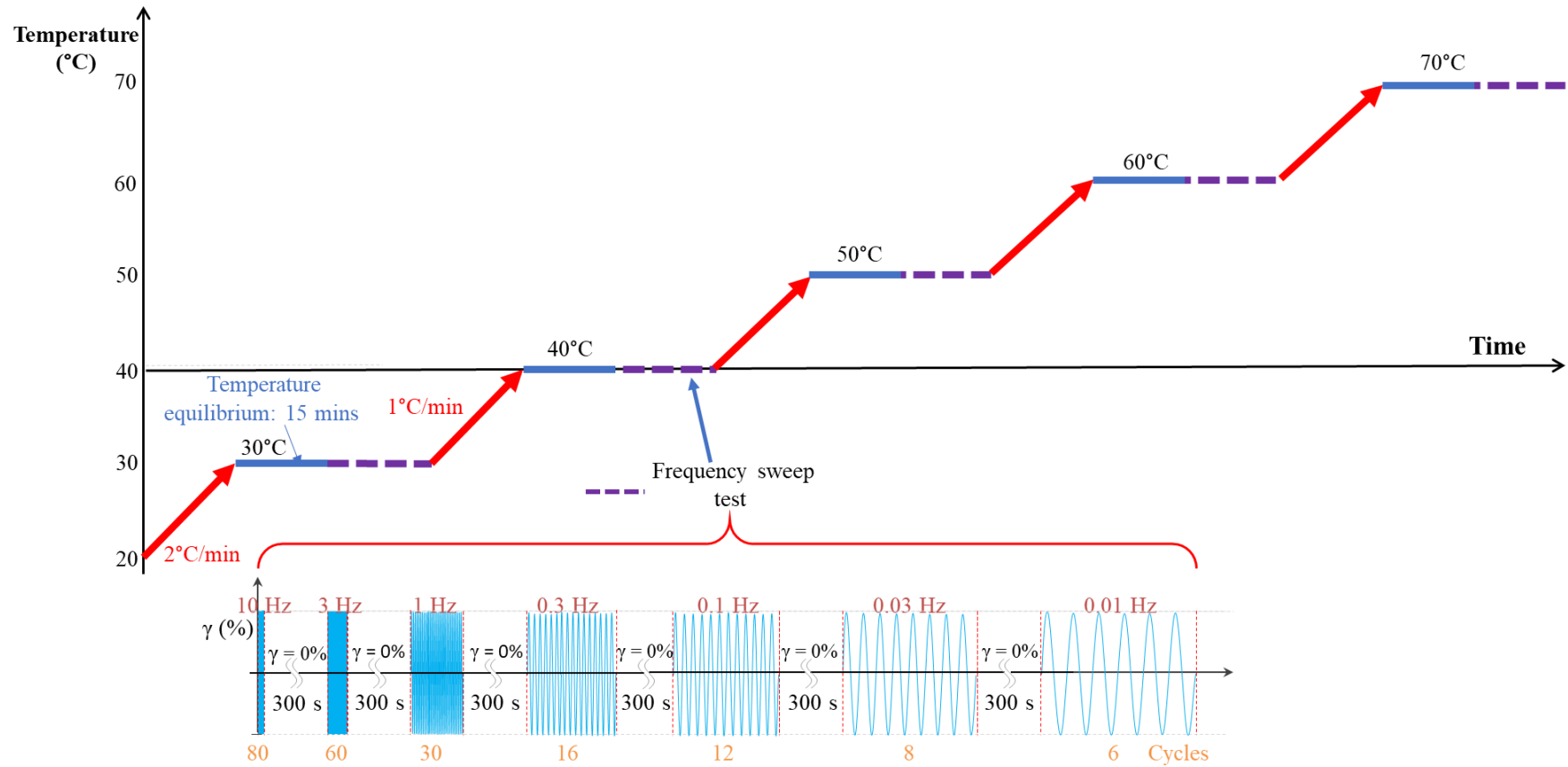


Figure 3.10b) - DSR complex shear modulus test scheme using 25 mm parallel plate

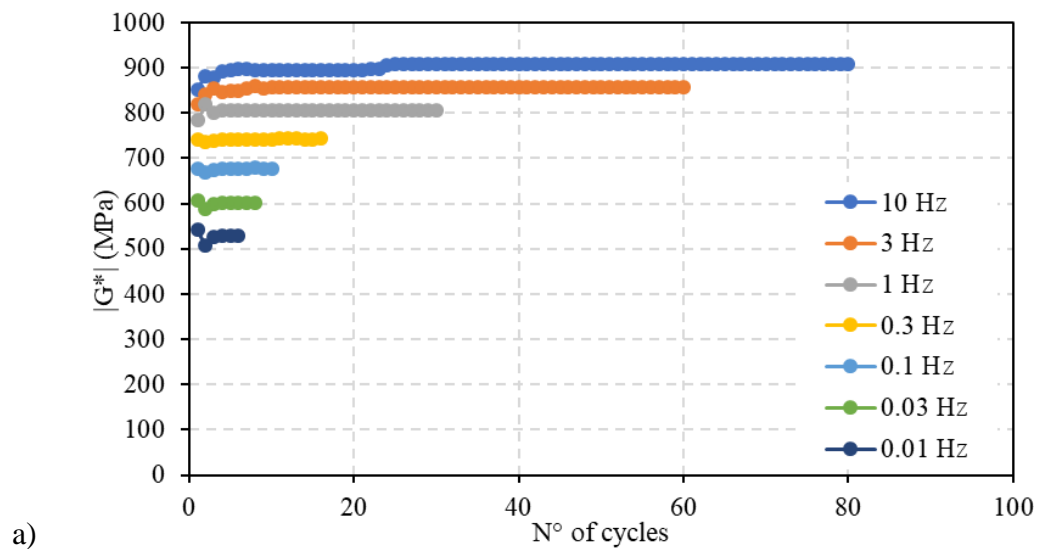


### 3. Equipment, Materials and Test Procedures

Table 3.6 – Number of cycles in function of frequencies

frequency (Hz)	No of cycles	No of last cycles averaged
0.01	6	3
0.03	8	5
0.1	10	5
0.3	16	7
1	30	10
3	60	10
10	80	10

The graph in Figures 3.11a-b depicts the evolution of the complex modulus (in norm and phase angle) as a function of the number of cycles for the B5070-1 test at  $T = -30^{\circ}\text{C}$ .



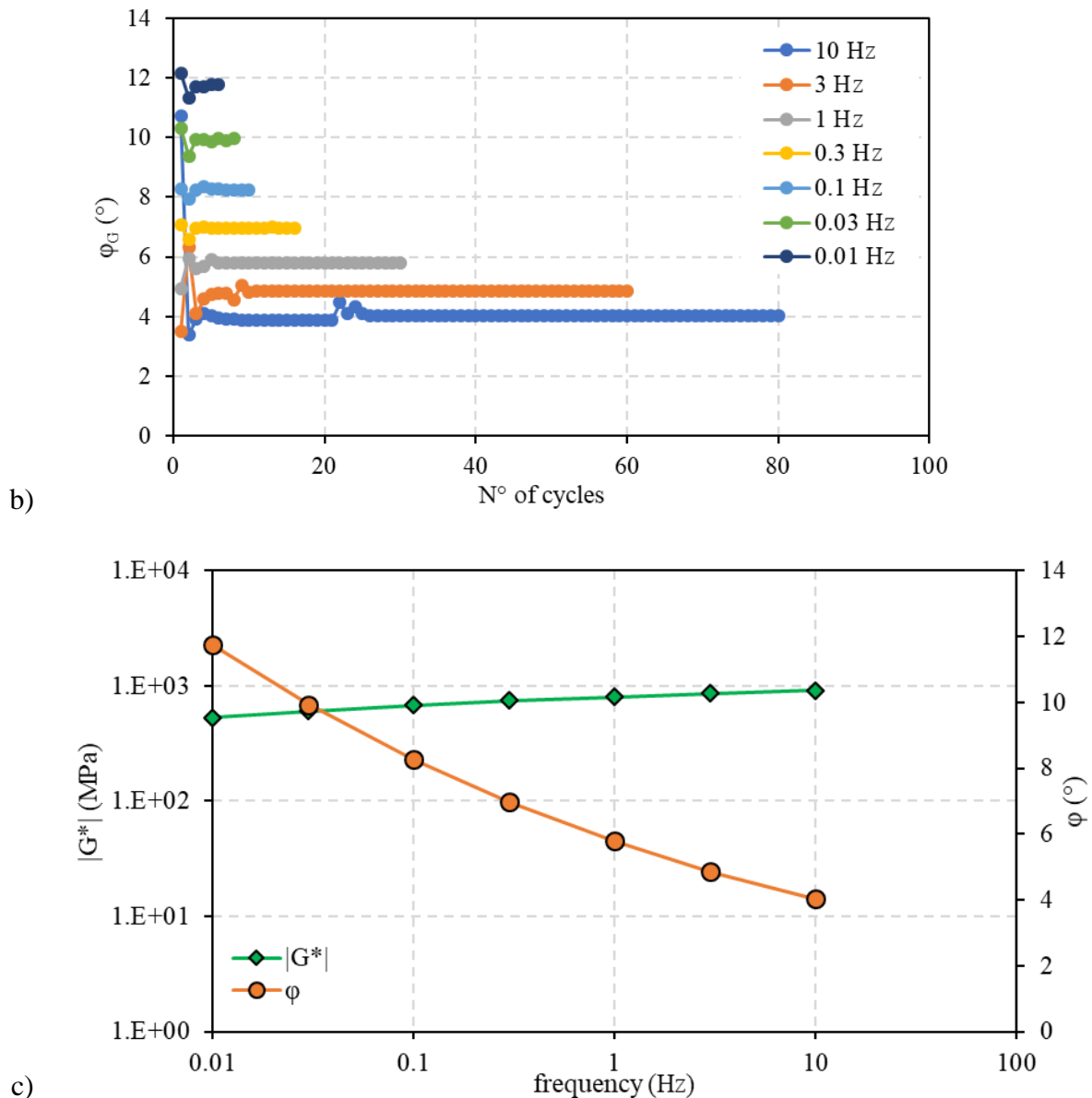


Figure 3.11 – B5070-1 complex modulus test results at  $-30^{\circ}\text{C}$ . a) Norm of complex modulus; and b) phase angle in function of number of cycles; c) Complex modulus average values.

Due to transient effects during a complex modulus test, the first 3-4 cycles are not considered in the modulus evaluations (Gayte, Di Benedetto, Sauzéat, & Nguyen, 2016). The attainment of stabilisation in the complex modulus and phase angle measurements may be shown in Figures 3.11a and b, where it is evident that this occurs after the initial two cycles. The norm and phase angle of the complex modulus for each frequency are derived by calculating the average of the last values obtained throughout the specified number of acquisition cycles, as presented in Table 3.6. Despite the achievement of stabilisation, there are still some inconsistencies observed in the measurements as seen after 2 seconds at 3 and 10 Hz. However,

### 3. Equipment, Materials and Test Procedures

---

it is important to note that these anomalies can be attributed to a manufacturing defect in the DSR as this appeared in all measurements. Figure 3.11c illustrates the averaged values of shear complex modulus at every frequency shown in Figure 3.11a.

#### 3.3.4 Rheological characterization of binders using DSR axial motor configuration

##### 3.3.4.1 Test sample preparation

Two DSR testing geometries were used for this section of experimental campaigns (Campaigns 3 and 4); 4 mm parallel plate (PP4) and 8 mm parallel plate (PP8). The DSR plates are preheated to the ring and ball temperature of the test bitumen for 5 minutes to improve the adherence of the binder to the plates. The upper plate is moved to loading position (15 mm) and the specimen is mounted to the upper plate for binder test heights 1.75 mm, 2 mm and 3 mm. The upper plate is moved to a 5 mm waiting position.

It is important to note that in the absence of a sizeable mould, tests at 4 mm and 5 mm specimen heights were carried out by scooping a considerable amount of bitumen and placed directly on the lower plates (Figure. 3.12a). A higher waiting position (8 mm) is maintained in this case. In all cases, the specimen is allowed to condition for 5 minutes at 30°C and finally brought to a trimming gap 5% higher than the final test gap. Trimming of the specimen (Figures. 3.12b-d) was executed with a heated stainless-steel spatula and the plate moved to the final test gap followed by specimen temperature reduction to 20°C.

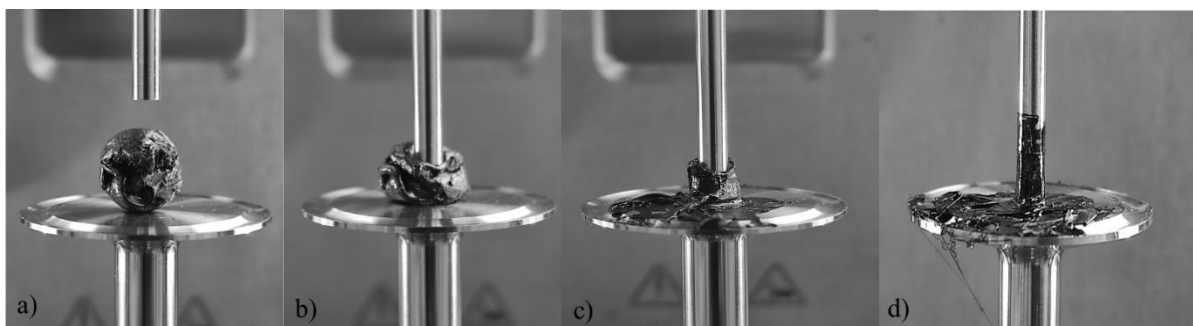


*Figure 3.12 - Example of specimen preparation at 4 mm and 5 mm test heights with 4 mm parallel plate.*

##### 3.3.4.2 Preliminary axial strain amplitude sweep test

As a first attempt in the axial rheological characterization of bitumen, it is pertinent to determine its linear viscoelastic domain. The bitumen was subjected to axial strain sweep tests at -5°C/10 Hz and 20°C/0.01 Hz, with strain amplitude ranging from 0.001 % to high strain

amplitude or failure strain. It is worth mentioning that strain amplitude sweeps were performed only in the axial test mode.

As an example of the axial strain sweep procedure at  $-5^{\circ}\text{C}/10\text{Hz}$ , following the specimen preparation as described above, the sample temperature was decreased from  $20^{\circ}\text{C}$  to  $-5^{\circ}\text{C}$  at the rate of  $1^{\circ}\text{C}/\text{min}$  and maintained at  $-5^{\circ}\text{C}$  for 30 minutes to attain thermal equilibrium (Büchner, Wistuba, Remmler, & Wang, 2019). Axial complex modulus  $|E^*|$  and the corresponding phase angle  $\varphi_E$  were determined over the whole range of strain amplitudes applied. Based on the results reported in Campaign 1, the shear strain amplitude  $\gamma$  of 0.1% was chosen for all shear complex modulus tests (frequency sweep tests).

#### 3.3.4.3 Axial and shear complex modulus tests on binders

Frequency sweep tests were performed on cylindrical bitumen test samples of varying heights at temperatures of  $-5^{\circ}\text{C}$ ,  $0^{\circ}\text{C}$ ,  $5^{\circ}\text{C}$ ,  $10^{\circ}\text{C}$ ,  $20^{\circ}\text{C}$  and  $30^{\circ}\text{C}$ , at frequencies of 10 Hz, 3 Hz, 1 Hz, 0.3 Hz, 0.1 Hz, 0.03 Hz and 0.01 Hz. The respective test heights were chosen based on the trimming convenience offered by the DSR. Tests with PP4 at heights 1.75 mm, 3 mm were carried out at only two temperatures 0 and  $10^{\circ}\text{C}$ . It is important to highlight the fact that both shear  $G^*$  and axial  $E^*$  complex moduli were determined on the same sample, by applying axial and oscillatory sinusoidal loading, successively. This is necessary to address the repeatability issue seen in the preceding chapter wherein change in the test specimen led to a decrease in modulus. It is important to acknowledge that the geometry of the specimen has an influence in this regard.

The test was initiated following the specimen preparation steps stated above with a gradual decrease in the sample temperature from  $20^{\circ}\text{C}$  to  $-5^{\circ}\text{C}$  as the first test temperature at the rate of  $1^{\circ}\text{C}/\text{min}$ . Thermal equilibrium time adopted in this test procedure was 90 minutes to approach thermodynamic equilibrium and therefore allow for physical hardening to manifest before loading. Axial norm  $|E^*|$  and phase angle  $\varphi_E$  of complex modulus  $E^*$  were then determined with an imposed axial strain amplitude ( $\epsilon$ ) of 0.01 % across all test frequencies. Example of the stress and strain signals plotted as a function of time is shown in Figure 3.13.

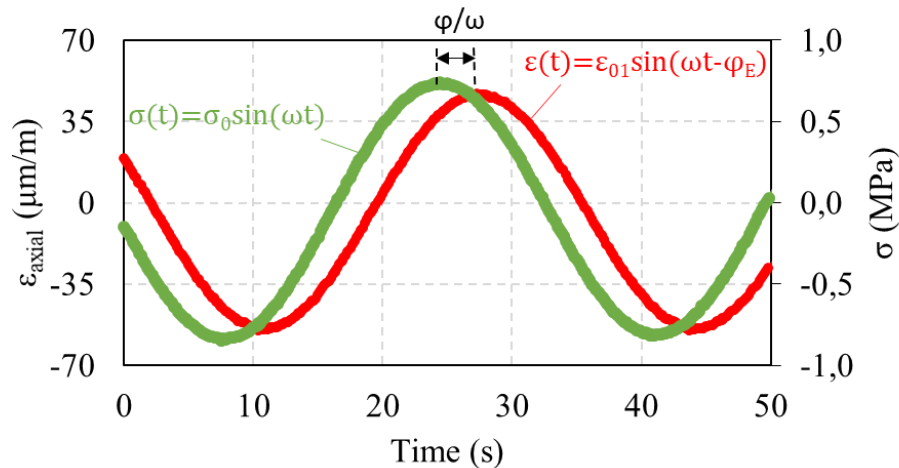


Figure 3.13 – Axial stress and axial deformation of bitumen

Subsequently, higher test temperatures were attained by a temperature increase of  $1^\circ\text{C}/\text{min}$  and temperature equilibrium times of 15 minutes adopted. Figure 3.14 shows the thermal conditioning protocol used for axial and shear complex modulus tests with 4 mm parallel plate geometry. It is worthy of note that a similar test procedure was followed with 8 mm parallel plate geometry adopting  $0^\circ\text{C}$  as its initial test temperature (Figure 3.15). As an illustration of the general complex modulus test sequence, axial complex modulus test was initially performed on a 5mm binder sample from temperature/frequency pair ( $-5^\circ\text{C}/10$  Hz) to  $10^\circ\text{C}/0.01$  Hz) followed by a shear complex modulus test on the same sample from ( $-5^\circ\text{C}/10$  Hz) to  $10^\circ\text{C}/0.01$  Hz). For every axial complex modulus test carried out using a geometry across all temperatures and frequencies, a corresponding shear complex modulus test across similar temperature and frequency selections are performed. It is necessary to note that, the shear complex modulus test sequence was manually initiated due to a peculiar drawback of the rheocompass software. This is its inability to combine both axial and shear complex modulus functions in one template. Shrinkage of bitumen samples under temperature ramps are not observed under the axial setup. This prompted the launch of the axial complex modulus test prior to shear complex modulus test. However, if the test is performed in the reverse sequence, the bitumen sample height is altered during temperature ramps due to shrinkage. This leads to a false height recorded during the subsequent axial test. Therefore, it could further greatly affect the axial complex modulus measured.

### 3. Equipment, Materials and Test Procedures

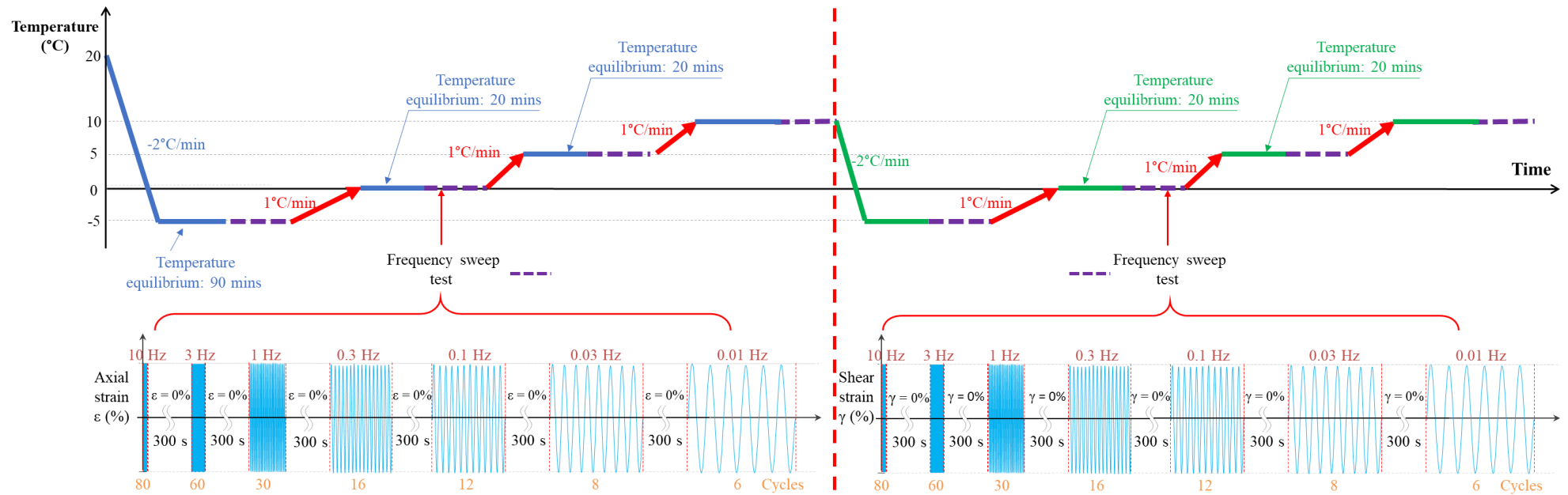


Figure 3.14 - Complex modulus test scheme adopted with 4 mm parallel plate

### 3. Equipment, Materials and Test Procedures

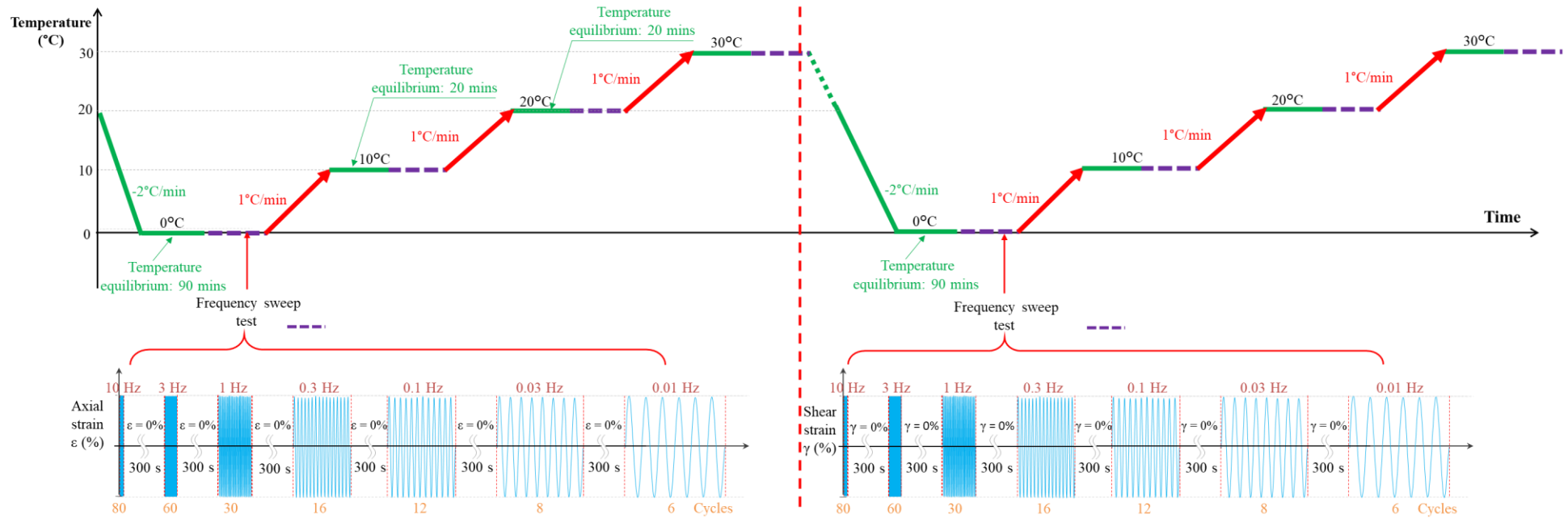


Figure 3.15 - Complex modulus test scheme adopted with 8 mm parallel plate

### 3.4 Experimental Plan

The experimental workload for the thesis has been divided broadly into two categories of campaigns, each focusing on a particular assembly of DSR utilized for its execution. The first category of campaigns, (Campaign 1 and 2), focuses on the linear viscoelastic rheological characterization of binders using DSR equipped with temperature hood and fixed lower plate (Figure 3.2). The second group of campaigns (campaign 3 and 4) focuses on the axial and shear linear viscoelastic rheological characterization of binders and at the same time exploring the possibility of Poisson's ratio determination utilizing DSR with tension-compression assembly (Figure 3.4).

#### 3.4.1 Campaign 1

Two bitumen B5070 and B3550 were subjected to shear strain amplitude sweep test in Campaign I (Chapter 4). Three different testing plate geometries and spacings were utilised: 4-mm parallel plates with a 1.75-mm gap; 8-mm parallel plates with a 2-mm gap and 25-mm parallel plates with a 1-mm gap.

Firstly, the evolution of B5070 and B3550 bitumen shear complex modulus over time at  $-20^{\circ}\text{C}$  were studied. Furthermore, the effect of the evolution of shear complex modulus on the LVE limit determination of the two binders were also studied over three frequencies (10 Hz, 0.3 Hz and 0.01 Hz) and temperatures ranging from  $-25^{\circ}\text{C}$  to  $70^{\circ}\text{C}$ . These tests are presented in Table 3.7.

*Table 3.7 – Bitumen shear strain amplitude sweep test plan*

Temperatures (°C)	B5070			B3550		
	Frequency					
	0.01 Hz	0.3 Hz	10 Hz	0.01 Hz	0.3 Hz	10 Hz
-25	X	X	X	X	X	X
-20	X	X	X	X	X	X
-10	X	X	X	X	X	X



0	X	X	X	X	X	X
10	X	X	X	X	X	X
20	X	X	X	X	X	X
30	X	X	X			
40	X	X	X			
50	X	X	X			
60	X	X	X			
70	X	X	X			

## 3.4.2 Campaign 2

Three bitumen B5070, B3550 and PmB were subjected to shear complex modulus test in campaign II (Chapter 5). This resulted in 7 complex modulus tests in total which are all presented in Table 3.8.

*Table 3.8 – Shear complex modulus test plan*

<b>Binder</b>	<b>Repetitions</b>		
	<b>1</b>	<b>2</b>	<b>3</b>
B5070	B5070-1	B5070-2	B5070-3
B3550	B3550-1	B3550-2	B3550-3
PmB	PmB		

### 3. Equipment, Materials and Test Procedures

Temperatures were varied from -30°C to 70°C and frequencies 0.01, 0.03, 0.1, 0.3, 1, 3, and 10 Hz. The shear strain amplitude of 0.1% was imposed on the bitumen specimen deduced from the results in Campaign 1 (Chapter 4). Three different DSR plate geometries and testing gaps were utilised: 4 mm parallel plates with a 1.75 mm gap, 8 mm parallel plates with a 2 mm gap and 25 mm parallel plates with a 1 mm gap as specified in (Farrar et al., 2015; Test, 2010). The moving profile “viscoelastic” was selected on the software interface for this test.

#### 3.4.3 Campaign 3

This campaign consists of axial complex modulus test and shear oscillatory complex modulus tests performed on the same sample. This is made possible by the DSR fixed with lower axial motor described in section 3.1.2. Bitumen B5070 is tested in this campaign utilising 4 mm and 8 mm parallel plate testing geometries. Binder specimen tested varied at different heights such as 1.75 mm, 2 mm, 3 mm, 4 mm and 5 mm. The selection of test height is based on the trimming convenience offered by the DSR with the current configuration. The experimental plan is highlighted in Tables 3.9 and 3.10 respectively

*Table 3.9 - Axial and shear complex modulus test plan at different DSR gaps*

DSR geometry type	DSR sample size					
	Diameter (mm)	Sample height (mm)				
		1.75	2	3	4	5
<b>Parallel plate</b>	4	x		x	x	x
<b>Parallel plate</b>	8		x	x	x	x

*Table 3.10 - Axial and shear complex modulus test conditions.*

Geometry	PP4	PP8
<b>Axial strain amplitude <math>\varepsilon</math> (%)</b>	0.01	0.05
<b>Shear strain amplitude <math>\gamma</math> (%)</b>	0.1	0.1

### 3. Equipment, Materials and Test Procedures

---

<b>Temperature (°C)</b>	-5, 0, 5, 10	0, 10, 20, 30
<b>Frequency (Hz)</b>	0.01, 0.03, 0.1, 0.3, 1, 3, 10	

It is however important to state beforehand that the DSR moving profile used to perform these tests is the dynamic mechanical analysis (DMA).

#### 3.4.4 Campaign 4

The test in Campaign 3 was repeated in this campaign (Chapter 7) whereby the imposed axial strain amplitude was increased to 0.1% for B5070 bitumen. This is to study the effect of the axial strain amplitude on the axial complex modulus and phase angles measured. Furthermore, the test was extended to two other binders (B3550 and PmB) at strain levels listed in Table 3.11. The specimen height adopted was 5 mm, deduced from Campaign 3 (Chapter 6). The test temperatures ranged between -10°C to 30°C and frequencies 0.01, 0.03, 0.1, 0.3, 1, 3, 10 Hz. The complex modulus test is all presented in Table 3.11.

*Table 3.11 – Axial and shear complex modulus test plan on different bitumen*

<b>Bitumen</b>	<b>B5070</b>	<b>B3550</b>	<b>PmB</b>
<b>Test</b>	B5070-1	B3550-1	PmB
<b>Axial strain amplitude <math>\epsilon</math> (%)</b>	0.1	0.05	0.05

## **4. Campaign 1: Shear oscillatory LVE limit of binders**

### **4.1 Objectives**

This thesis's first campaign focused on the determination of linear viscoelastic limit of two unmodified bitumen. The first bitumen (B5070) linearity limit is considered from low to high temperatures. The nonlinearity for the second bitumen (B3550) however ranged from low to medium temperatures. Low temperatures in this thesis is considered temperatures  $\leq 10^{\circ}\text{C}$ ,  $20 - 30^{\circ}\text{C}$  (medium) and  $\geq 40^{\circ}\text{C}$  (high).

The possibility of using a DSR for low-temperature testing has been investigated, especially with a 4-mm parallel plate geometry. Researchers such as (Büchner et al., 2019; Gražulytė et al., 2021; Laukkanen et al., 2015; Lu, Uhlback, & Soenen, 2017) recorded a success in the testing of bitumen samples following the 4-mm DSR test protocols. However, studies by (D. Wang, Cannone Falchetto, Riccardi, Westerhoff, & Wistuba, 2021) suggested that physical hardening can affect low-temperature DSR tests with a conditioning time of 180 minutes.

Physical hardening is a time-dependent reversible process observed in bituminous binders above and below glass transition temperatures, (Anderson & Marasteanu, 1999) which can produce changes in rheological and electrical properties, without altering the chemical composition of the material (Anderson et al., 1994; Lu & Isacsson, 2000). The phenomenon is linked to the internal structuring of polar fractions and crystallization of waxes in conjunction with free-volume collapse. (Baglieri, Dalmazzo, Barazia, Tabatabaee, & Bahia, 2012; Ferry, 1980; Struik, 1977) The physical hardening rate was observed to be material- and temperature-dependent. Moreover, if the material is conditioned at a constant temperature, the rate is higher at an early stage and decreases rapidly with time.(Anderson et al., 1994; Hussain U. Bahia & Anderson, 1993; Lu, Isacsson, & Ekblad, 2003; Tabatabaee et al., 2012) The studies carried out during the Strategic Highway Research Program(Anderson et al., 1994; Anderson & Marasteanu, 1999) and subsequent studies by researchers (Tabatabaee et al., 2012; D. Wang et al., 2021) have shown that physical hardening can affect the rheological properties of bitumen when maintained around its glass transition temperature.

(François Olard et al., 2003) referred to glass transition temperatures as bitumen temperatures that maximize the loss modulus at any frequency.

In the context of this experimental campaign, the phenomenon of physical hardening was observed at low temperatures and low frequencies when performing DSR tests to investigate the LVE limit. The progression of physical hardening on the two tested bitumen were first studied as the first objective to confirm the existence and extent (in time) of this phenomenon.

## 4. Campaign 1: Shear oscillatory LVE limit of binders

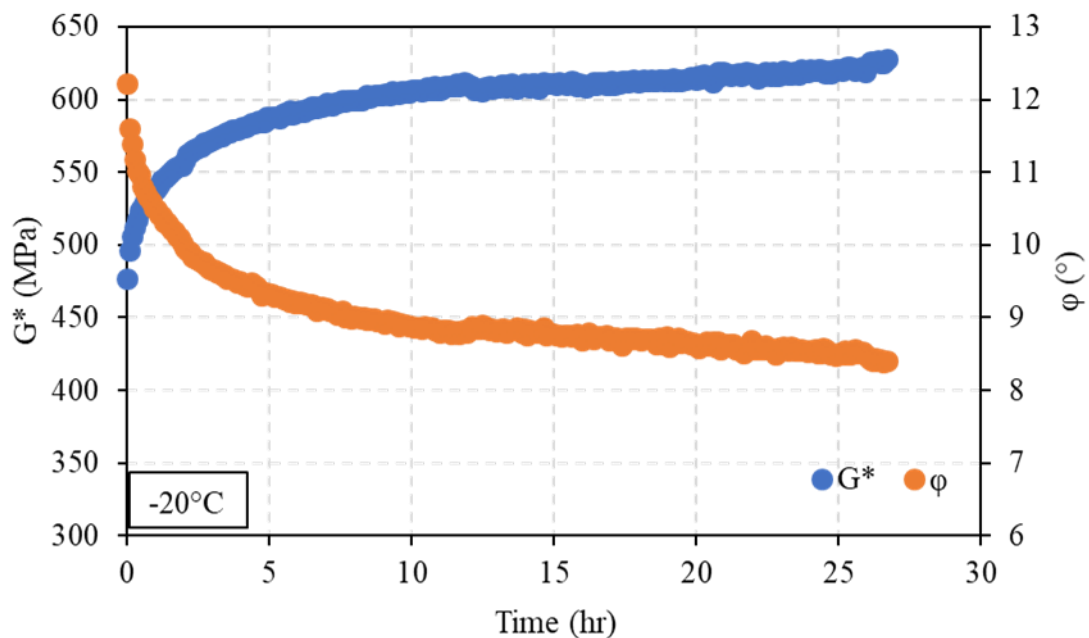
A method to correct the effect of physical hardening on the test results used to determine the LVE limit of bitumen at low temperatures is then introduced as the second objective. The time-temperature equivalence of binder LVE limits is demonstrated as the third objective followed by the 2S2P1D modelling of binder LVE limits.

### 4.2 Physical hardening study on binders

The time sweep test on bitumen was performed to determine the effect of temperature storage on the increment of the bitumen shear complex modulus and phase angle values determined at  $-20^{\circ}\text{C}$ .

#### 4.2.1 Effect of temperature storage on B5070 bitumen

The plot of modulus  $G^*$  and phase angle  $\phi$  against time is illustrated in Figure 4.1 for bitumen B5070. Figure 4.1a shows the plots over 27 hours, followed by 4.1b over the first 5-hour period.



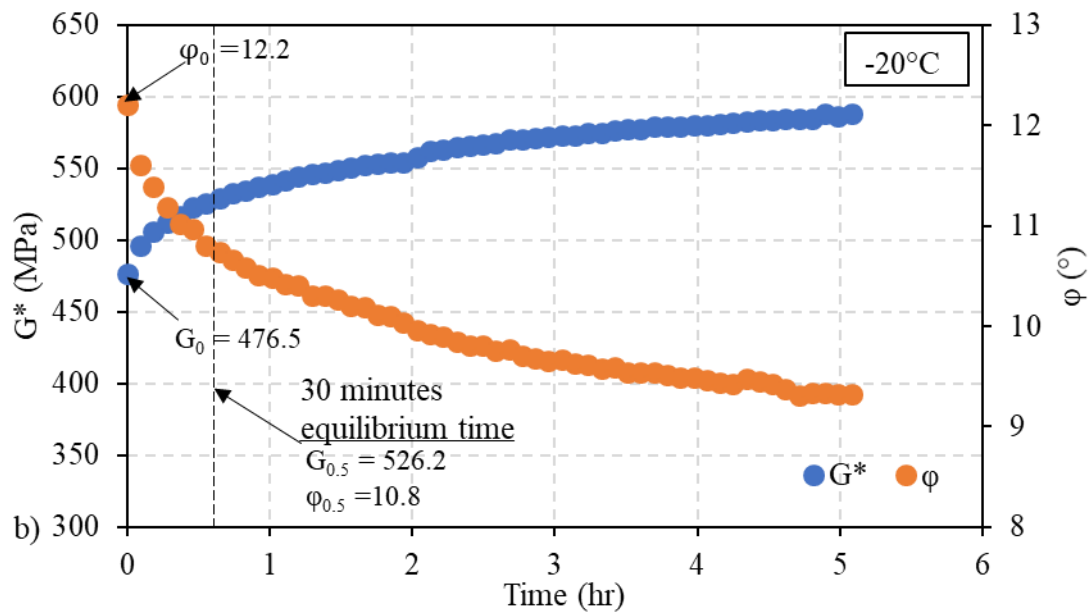


Figure 4.1 – Time sweep test of bitumen B5070 over a) 27 hours period; b) initial 5-hour period at -20°C/1 Hz

The values  $G_0$  and  $G_{0.5}$  correspond to the moduli of the bitumen at the initiation of the test, specifically after the Peltier temperature has reached -20°C, and the suggested duration for achieving thermal equilibrium, respectively. Both  $\phi_0$  and  $\phi_{0.5}$  accurately represent the respective phase angles. During the thermal equilibrium period, it was noted that the modulus exhibited a linear increase with a rate of 1.48MPa/min. However, it is anticipated that the modulus of the bitumen will exhibit minimal variation beyond this timeframe. Nonetheless, there was still an observed increase in the measured modulus as time progressed. The observed rise in bitumen modulus during the duration of storage can be ascribed to the phenomenon known as physical hardening, as elucidated in section 2.1.1.4.5. Following the attainment of equilibrium, a gradual increase in modulus at a rate of 0.41MPa/min was seen during the initial hour. However, this rate exhibited a decline in each successive hour. The phase angles exhibited corresponding reductions.

#### 4.2.2 Effect of temperature storage on B3550 bitumen

The time sweep test conducted on bitumen B3550 is depicted in Figures 4.2a and 4.2b, respectively. The initial shear complex modulus, denoted as  $G_0$ , was determined to be 634.7 MPa, while the corresponding phase angle,  $\phi_0$ , was measured to be 8.9°. However, it was observed that the modulus increased at a rate of 1.46MPa/min during the thermal equilibrium time. The measured rate is comparable to that which has been recorded with the B5070 bitumen. Moreover, it can be observed that the rate of increase in modulus over the course of the next

4. Campaign 1: Shear oscillatory LVE limit of binders

hour (0.35MPa/min) exhibited a decrease in comparison to the same rate achieved using B5070 bitumen.

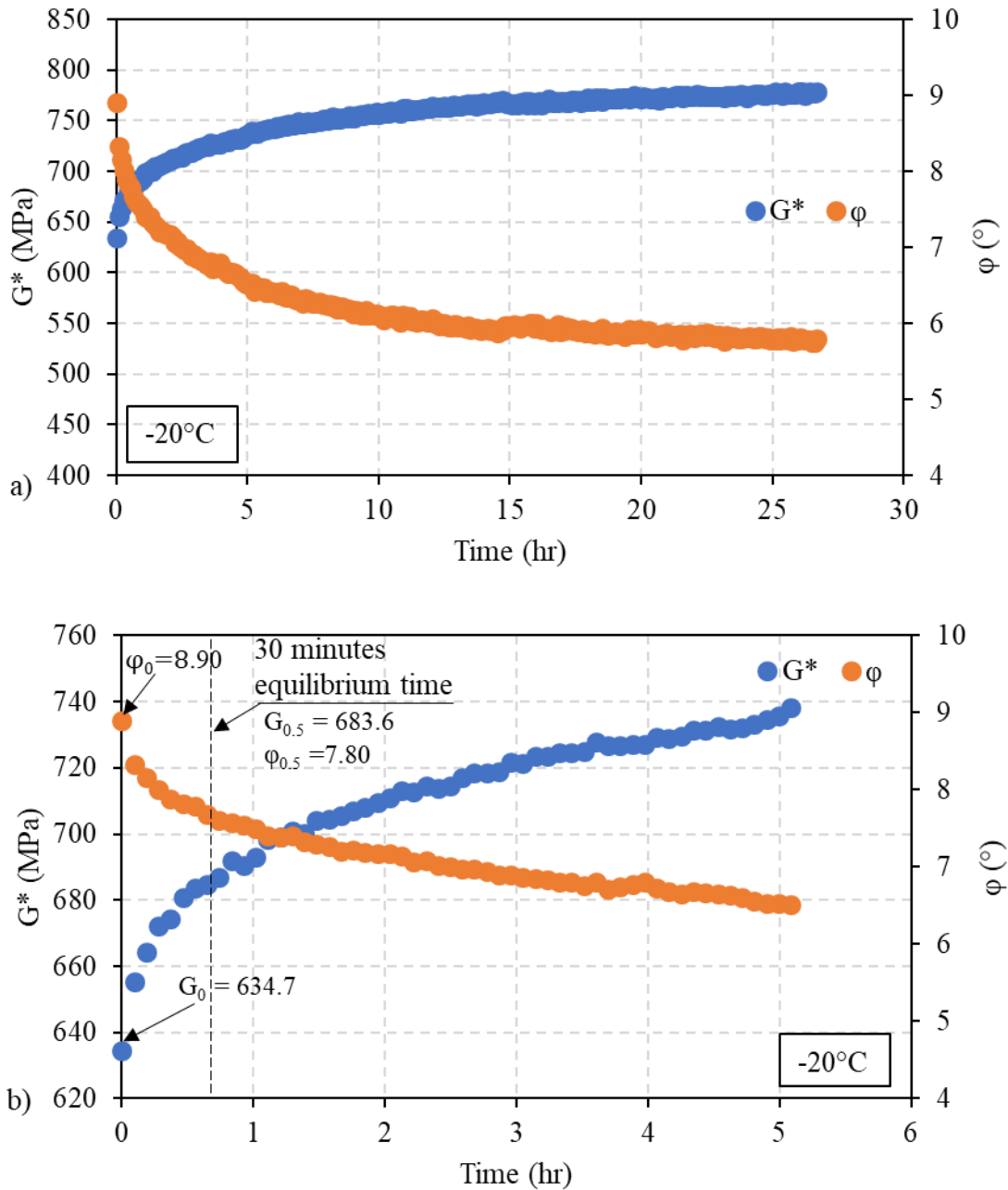


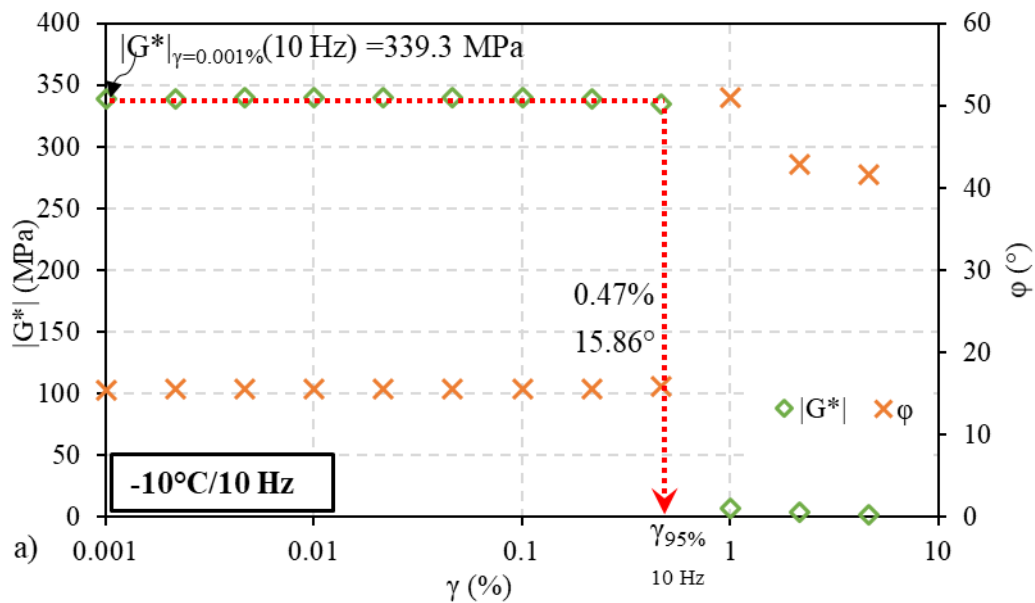
Figure 4.2 – Time sweep test of bitumen B3550 over a) 27 hours period; b) initial 5-hour period at -20°C/1 Hz

When examining both bitumen examples (B5070 and B3550), it has been noted that the shear complex modulus values experience a significant increase after the thermal equilibrium period of 30 minutes, which is the required duration to allow before conducting any rheological test on the binder using the Dynamic Shear Rheometer (DSR). This suggests that the modulus obtained from rheological experiments exhibits higher values compared to the actual material

properties. In this context, the subsequent section presents a methodology for quantifying and distinguishing the physical hardening impact on the rheological characteristics of bitumen, specifically in the context of a shear strain amplitude sweep test. This test, which occurs over a short duration following temperature equilibrium, serves as the basis for the proposed method. In order to mitigate the physical hardening effects during shear complex modulus tests, a longer equilibrium period is necessary. This will be demonstrated in the forthcoming Campaign (Chapter 5).

### 4.3 LVE limits of B5070 bitumen

The LVE limit  $\gamma_{95\%}$  of the binder was determined for each combination of temperature and frequency, from strain amplitude sweep test results, as the strain amplitude value corresponding to a 5 % reduction of the initial shear complex modulus  $|G^*|$  value at lowest shear strain amplitude. In this thesis, the lowest shear strain amplitude considered for tested bitumen (B5070) is 0.001%.





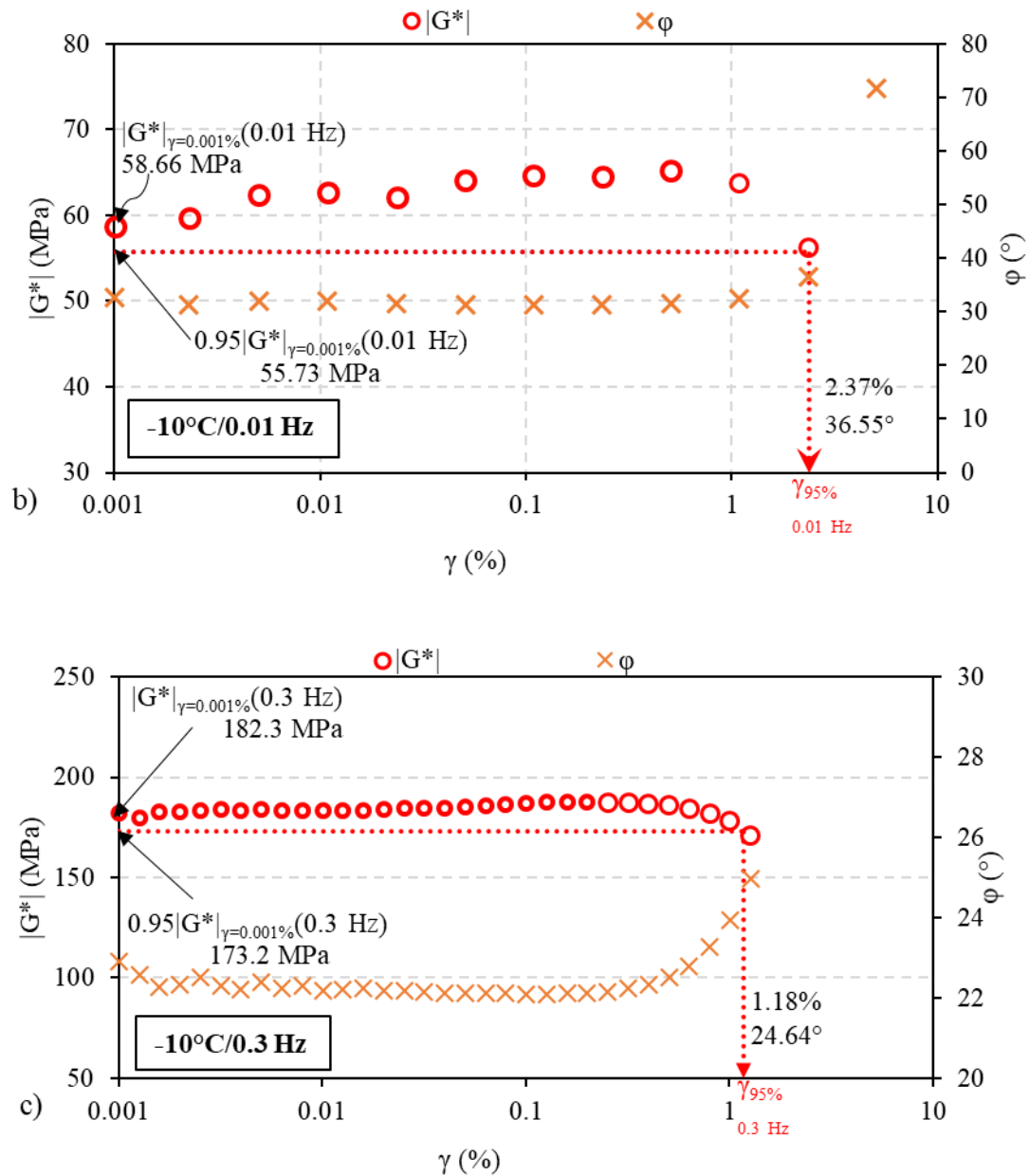


Figure 4.3 - Strain amplitude sweep tests results at  $-10^\circ\text{C}$  and frequencies (a) 10Hz, (b) 0.01 Hz, and (c) 0.3 Hz on B5070 bitumen.

As an illustration, Figure 4.3 depicts the outcomes of three strain amplitude sweep tests conducted at  $-10^\circ\text{C}$  and at 10 Hz, 0.3 Hz, and 0.01 Hz.  $|G^*|$  and  $\phi$  are plotted as a function the strain amplitude. The 10 Hz test (Figure 4.3a) revealed a significant decline in  $|G^*|$  between 0.47% and 1% strain amplitudes (due to the failure of the sample). The initial value of  $|G^*|$  for an amplitude of 0.001% strain is 339.3 MPa. The LVE limit  $\gamma_{95\%}$  (10 Hz) was calculated as the strain amplitude of the final valid data point before sample failure (0.47%), which corresponded to a  $|G^*|$  value of 339.3 MPa. The recorded shear complex modulus and phase angles values beyond this point are regarded as invalid.

Furthermore, at 0.01 Hz frequency (Figure 4.3b), the strain value  $\gamma_{95\%}$  corresponding to a 5% decrease in  $|G^*|_{\gamma=0.001\%(0.01\text{ Hz})}$  is equal to 2.37% and a corresponding phase angle ( $\phi_{95\%}$ )  $36.55^\circ$ . Similar procedure adopted at 0.3 Hz translated to an LVE limit of 1.18% and  $\phi_{95\%}$  of  $24.64^\circ$ .

The values of  $|G^*|$  at 0.01 Hz (Figure 4.3b) appear to increase from 0.001% to 0.51% strain amplitude before decreasing. Similar behaviour is seen between 0.001% and 0.2% strain amplitude at a frequency of 0.3 Hz (Figure 4.3c).

However, this increase in  $|G^*|$  with strain amplitude is not observable at 10Hz. The 0.01 Hz and 0.3 Hz tests are 50 and 20 times slower (longer) than the 10 Hz test (3,000 s and 1,200 s, respectively, as opposed to 58 s). Given the low temperature of the experiments depicted in Figure 4.3 ( $-10^\circ\text{C}$ ), the increase in  $|G^*|$  seen during the tests can be attributed to physical hardening. The duration of the 10 Hz testing is insufficient for the physical hardening effect to occur, resulting in no apparent fluctuations in  $|G^*|$  during the course of the tests.

#### 4.3.1 Quantification and correction of physical hardening effect on the complex modulus ( $G^*$ ) of B5070 bitumen strain sweep test

To examine and separate the effects of physical hardening and strain amplitude dependency, a logarithmic regression was performed on the data obtained from 0.001% to 0.51% strain amplitudes (Figure 4.4a), as shown in equation (4.1) and (4.2), where  $|G^*|_{\gamma=0.001\%}$  is the estimated value of complex modulus at 0.001% strain amplitude,  $G_b$  is the slope of the regression line in logarithmic axis, and  $\gamma$  is the shear strain amplitude in percentage:

$$|G^*| = G_b \log \frac{\gamma}{0.001\%} + |G^*|_{\gamma=0.001\%} \quad (4.1)$$

$$|G^*|_{\text{Corrected}} = |G^*|_{\text{Measured}} - G_b \log \left( \frac{\gamma}{0.001\%} \right) \quad (4.2)$$

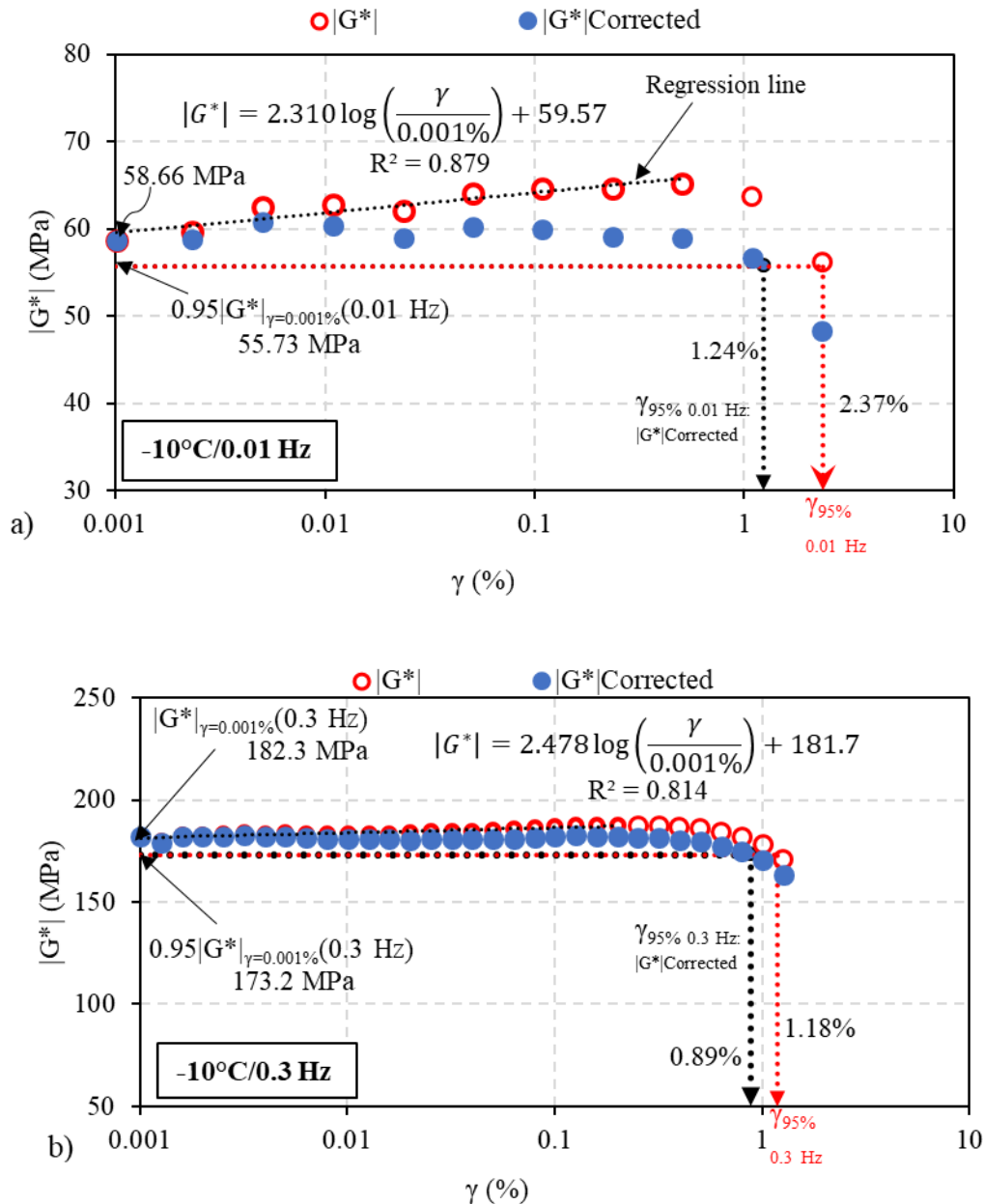
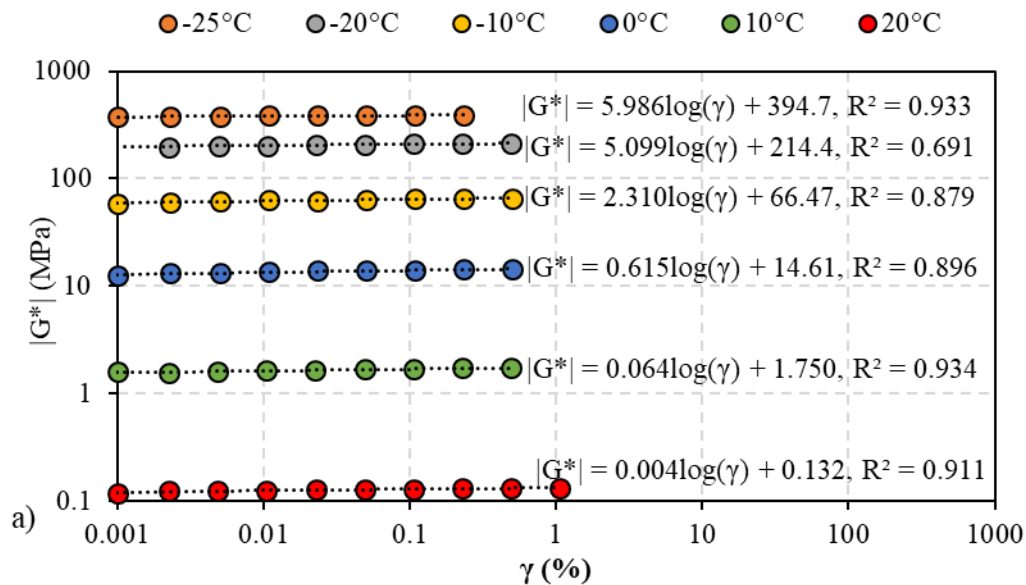


Figure 4.4 – Corrected strain amplitude sweep tests results at  $-10^\circ\text{C}$  and frequencies (a) 0.01 Hz, and (b) 0.3 Hz on B5070 bitumen.

As a first estimate, the  $G_b$  value can be regarded as the rate of increase of  $|G^*|$  within the LVE domain due to physical hardening, which is below the LVE limit. Then, corrected values of  $|G^*|$  were determined by subtracting the physical hardening effect indicated by  $G_b \log \gamma$  in equation (4.1) from the experimental values of  $|G^*|$  evaluated for the regression as illustrated in equation (4.2). Corrected values of  $|G^*|$  were finally considered to calculate the 5% reduction designated as the threshold for the LVE domain as indicated in section 4.3. The corrected LVE limit  $\gamma_{95\%:|G^*|_{\text{Corrected}}}$  at 0.01 Hz (Figure 4.4a) was calculated by linear

interpolation of the data acquired at strain amplitudes of 1.1% and 2.4%, resulting in 1.24%. If the  $|G^*|$  values are used to calculate the LVE limit without considering the effect of physical hardening as illustrated in Figures 4.3b, a value of 2.37% ( $\gamma_{95\%}$ ) is obtained, which corresponds to a  $|G^*|$  value of 55.73 MPa and an increase in LVE limit of 1.13% strain (and a decrease in phase angle of  $3.6^\circ$ ). Similar technique was used to calculate the corrected LVE limit  $\gamma_{95\%:|G^*|Corrected}$  at 0.3 Hz as depicted in Figure 4.4(b). A strain amplitude value of 0.89% was determined, as opposed to the value of 1.18% ( $\gamma_{95\%}$ ) that would be achieved without the consideration of physical hardening. The uncorrected LVE limit value at  $\gamma_{95\%(0.3\text{ Hz})}$  corresponds to a  $|G^*|$  value of 173.2 MPa and a strain increase of 0.29%. As noted from the plots, however, the effect of physical hardening on the calculation of the LVE limit of the bitumen under consideration at low frequencies is not negligible.

Figures 4.5(a) and 4.5(b) summarises the regressions of  $|G^*|$  as a function of  $\gamma$  computed from the results of strain amplitude sweep tests at all test temperatures at 0.01 Hz and 0.3 Hz. The regression intervals were chosen, considering the intervals reflecting the effect of physical hardening as before described. LVE limits were calculated for all low-temperature and frequency combinations.



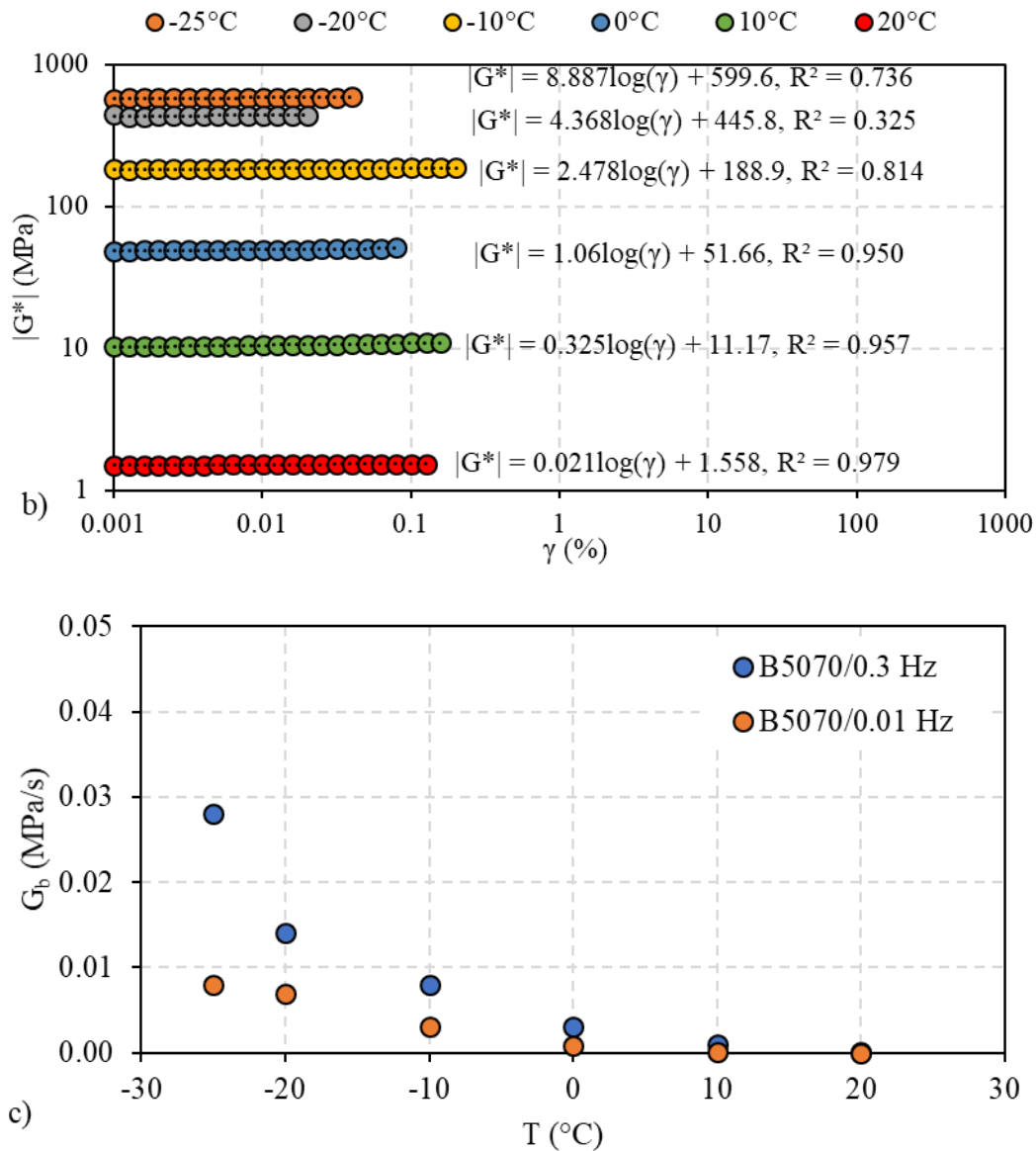


Figure 4.5 – Results of strain amplitude sweep tests and estimation of physical hardening effect on  $|G^*|$  of B5070 bitumen at (a) 0.01 Hz, (b) 0.3 Hz; and (c) the rate of physical hardening at each test temperature.

As previously explained, the effect of physical hardening is seen to be obvious at 0.01 Hz due to the low speed of the test. However as seen in the Figure 4.5c which illustrates the plot of the physical hardening rate ( $G_b$ ) against temperature, the rate of physical hardening increased with a reduction in temperature. Furthermore, the physical hardening rate is higher at 0.3 Hz than at 0.01 Hz as it seemed in Figures 4.4. Again, physical hardening effect is seen to be non-existent at 20°C.

#### 4.3.2 Physical hardening effect on the phase angle ( $\varphi$ ) of B5070 bitumen during a strain sweep test

The LVE limits of bitumen were computed using simply, the evolution of  $|G^*|$  with strain amplitude as previously described. Interpolation of the phase angle values obtained for the two strain amplitudes near to the corrected LVE limit (below and above) yielded corresponding phase angle values ( $\varphi_{95\%}$ ) at each temperature and frequency combination. There is no discernible decrease in phase angle values due to physical hardening as shown in Figure 4.6.

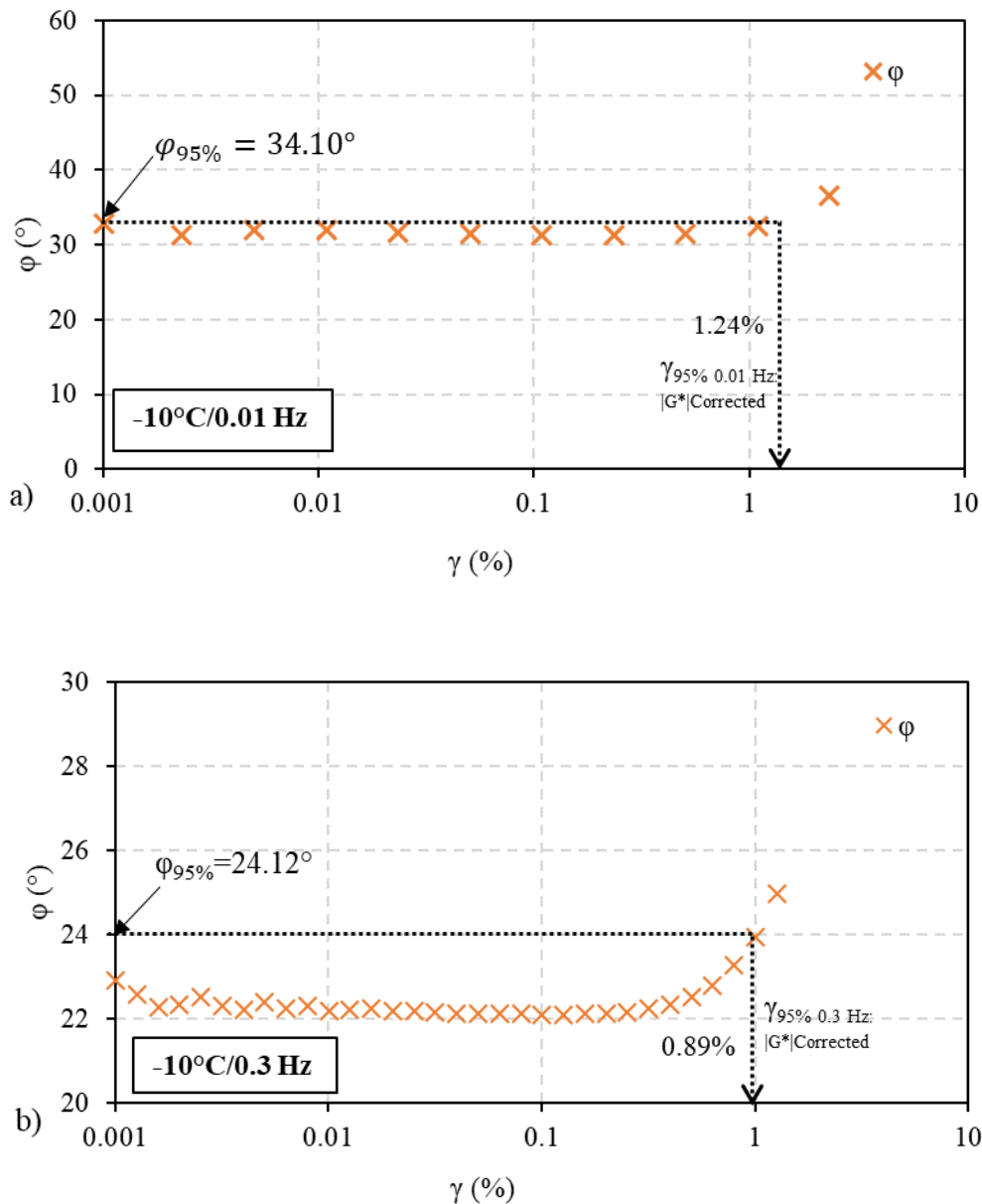
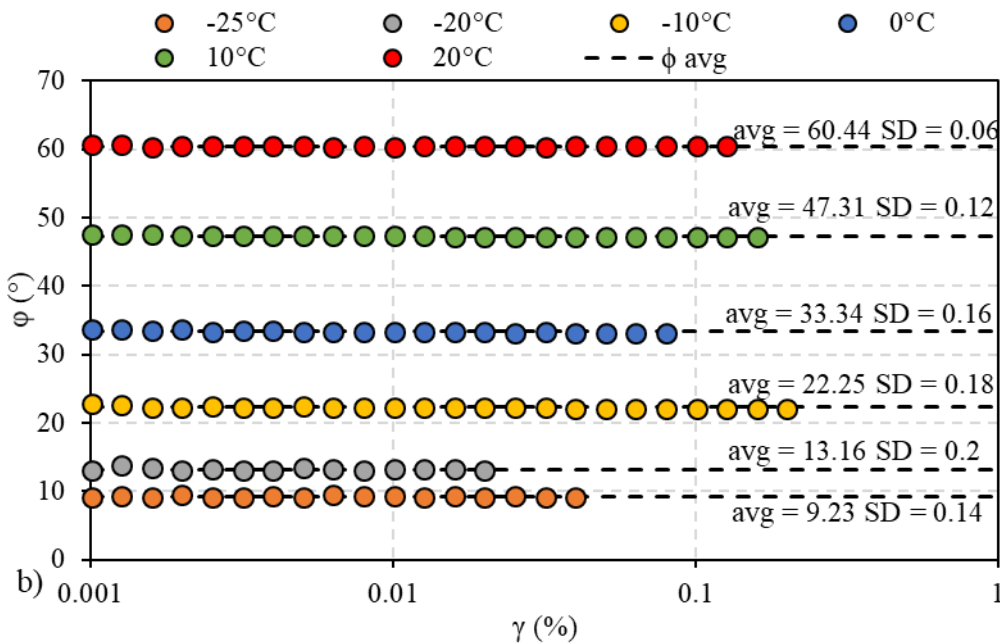
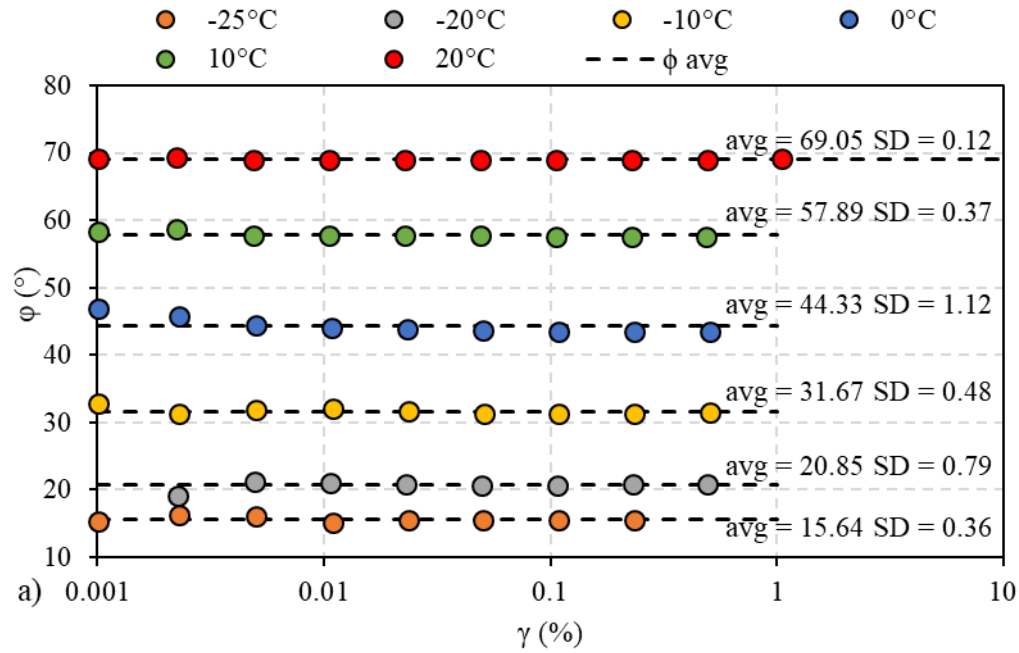


Figure 4.6 – Results of strain amplitude sweep tests showing phase angles of B5070 bitumen at (a) 0.01 Hz and (b) 0.3 Hz.

The modest increase in phase angle between 0.001% and 0.01% shown in figure 4.6(b) (test at 0.3 Hz) can be attributable to transient viscoelastic effects and experimental noise. In reality, if this slight variation in phase angle were due to physical hardening, it would be more obvious during a longer test, such as the one conducted at 0.01 Hz. The phase angle values obtained for each temperature at each strain amplitude were however averaged (avg) and standard deviation (SD) calculated as illustrated in Figures 4.7(a) and 4.7(b). These figures depict the mean and standard deviation for each temperature/frequency pair.



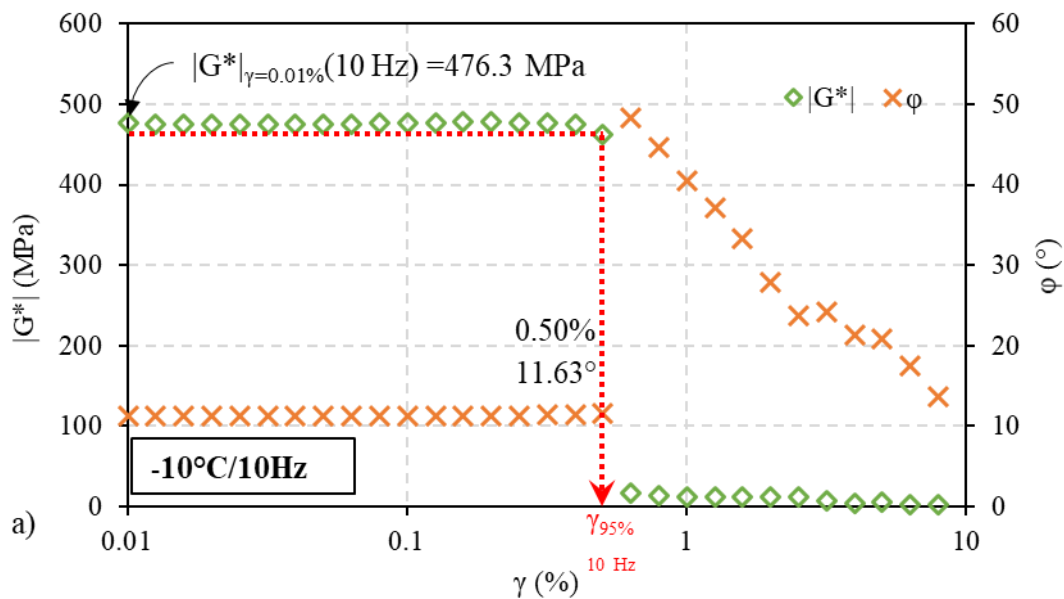
#### 4. Campaign 1: Shear oscillatory LVE limit of binders

Figure 4.7 – Results of strain amplitude sweep tests and estimation of physical hardening effect on  $\phi$  of B5070 bitumen at (a) 0.01 Hz and (b) 0.3 Hz.

Figures 4.7(a) and 4.7(b) depict the phase angles corresponding to each  $|G^*|$  considered for the regression (Figures 4.5(a) and 4.5(b)) and the average values at each test temperature, with maximum deviations of  $1^\circ$  at 0.01 Hz and  $0.2^\circ$  at 0.3 Hz. However, it is observed that phase angles increased with temperature and reduced with frequency.

#### 4.4 LVE limits of B3550 bitumen

Similar strain amplitude tests performed on bitumen B5070 were carried out on bitumen B3550 wherein, at 10 Hz an abrupt decline in  $|G^*|$  and  $\phi$  as a function of shear strain  $\gamma$  was recorded between 0.50% and 0.63% strain amplitudes as a result of the sample failure due to the binder stiffness. Therefore, the LVE limit at this frequency was recorded as 0.50% and this strain corresponds to a  $|G^*|$  of 462.7 MPa. This is illustrated in Figure 4.8a.





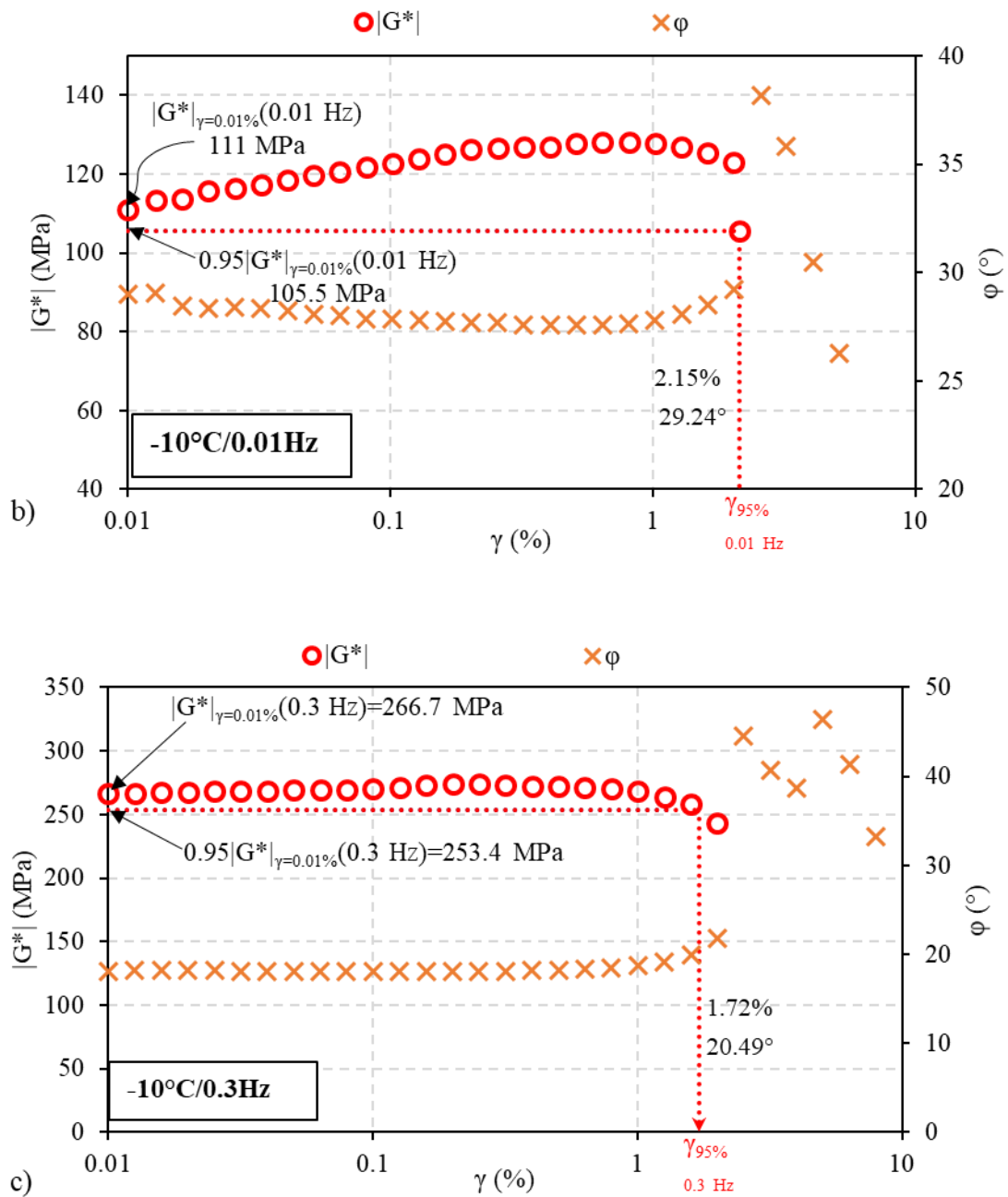


Figure 4.8 - Strain amplitude sweep tests results at  $-10^{\circ}\text{C}$  and frequencies (a)  $10\text{ Hz}$ , (b)  $0.01\text{ Hz}$ , and (c)  $0.3\text{ Hz}$  on B3550 bitumen.

LVE limit of B3550 bitumen was therefore determined at other test frequencies ( $0.3\text{ Hz}$ ,  $10\text{ Hz}$ ) based on the aforementioned principle of 5% reduction in initial measured shear complex modulus  $|G^*|_{\gamma=0.01\%}$ . The lowest shear strain amplitude considered for this bitumen is  $0.01\%$ . The strain limits at  $0.01\text{ Hz}$   $\gamma_{95\%(0.01\text{ Hz})}$  corresponded to  $2.15\%$  with a phase angle  $\phi_{95\%}$  of  $29.24^{\circ}$  and a modulus  $(0.95|G^*|_{\gamma=0.01\%(0.01\text{ Hz})})$   $105.5\text{ MPa}$  as indicated in Figure 4.8b. Again, at frequency  $0.3\text{ Hz}$ , a strain limit of  $1.72\%$  and phase angle  $20.49^{\circ}$  were recorded. This

corresponds to a modulus of 253.4 MPa (Figure 4.8c). increments in the values of  $|G^*|$  were also observed with the test on B3550 from 0.01% to 0.81% at 0.01 Hz and from 0.01% to 0.50% at 0.3 Hz frequencies respectively. This increment in modulus obviously confirms the existence of physical hardening during strain amplitude sweep tests at low temperatures on unmodified bitumen, although this effect diminished over frequency increments. That is, the phenomenon increased over time as illustrated in Figures 4.8b and c.

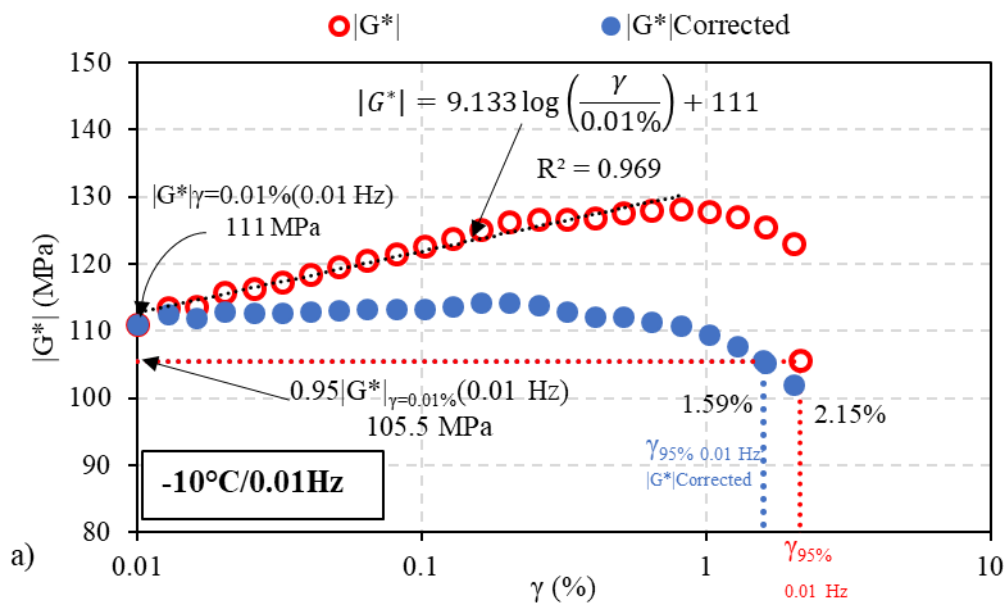
#### 4.4.1 Quantification and correction of physical hardening effect on the complex modulus ( $G^*$ ) of B3550 bitumen strain sweep test

Again, considering results obtained from the shear amplitude sweep test performed on B3550 bitumen, similar logarithmic regression was performed on the data obtained from 0.01% to 0.81% strain amplitude which corresponds to the peak increment in modulus, as shown in equation (4.3) and (4.4), where  $|G^*|_{\gamma=0.01\%}$  is the estimated value of complex modulus at 0.01% strain amplitude. The equation terms are as defined previously in equations 4.1 and 4.2.

$$|G^*| = G_b \log \frac{\gamma}{0.01\%} + |G^*|_{\gamma=0.01\%} \quad (4.3)$$

$$|G^*|_{Corrected} = |G^*|_{Measured} - G_b \log \left( \frac{\gamma}{0.01\%} \right) \quad (4.4)$$

Figure 4.9a and 4.9b illustrates the outcomes of shear complex modulus  $|G^*|$  and phase angle  $\phi$  for frequencies 0.3 Hz, and 0.01 Hz at  $-10^\circ\text{C}$  in function of strain amplitudes ( $\gamma$ ) measured on bitumen B3550 during shear strain amplitude sweep tests. The regression line present in both figures are represented by the logarithmic equations respectively.



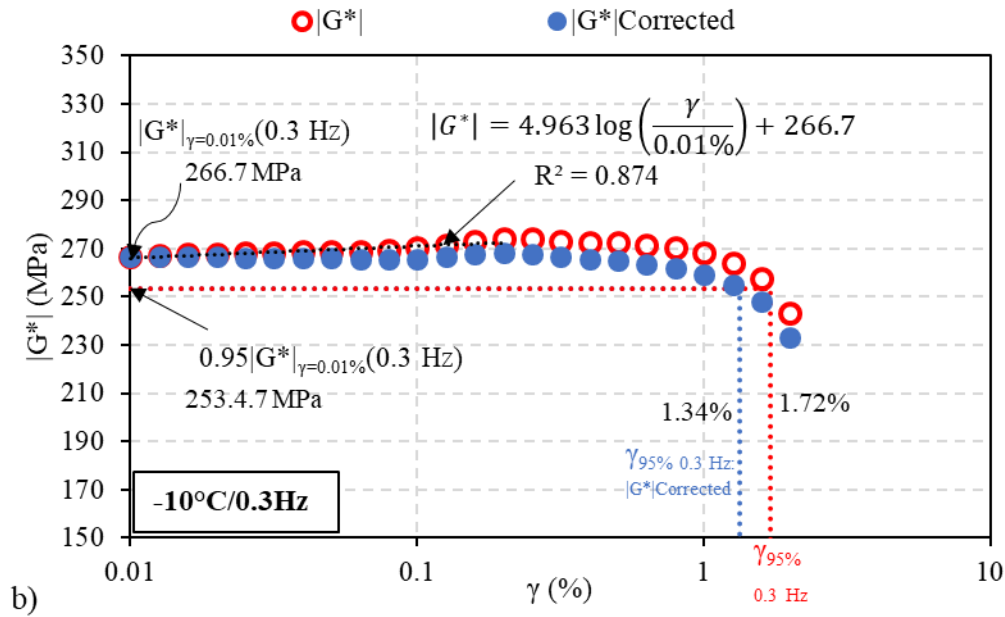
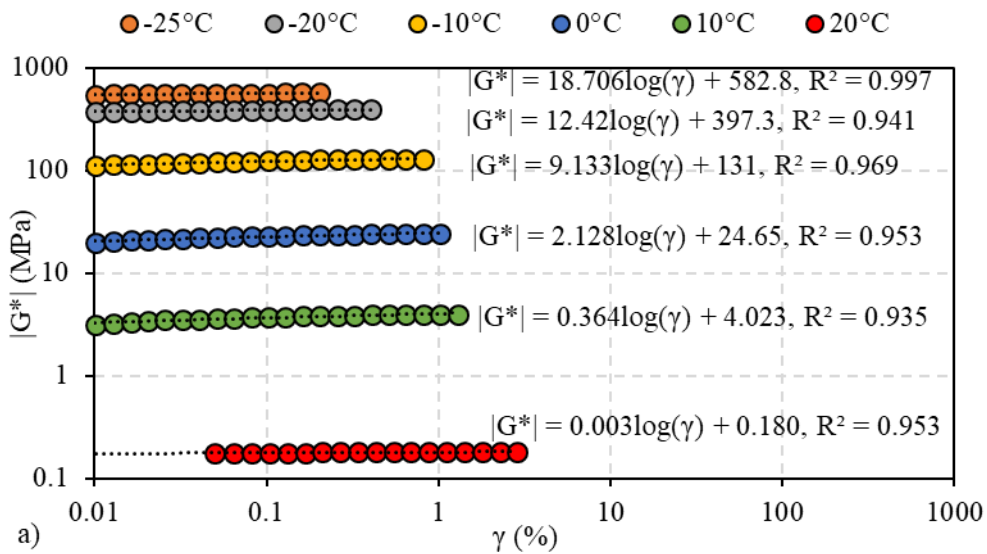


Figure 4.9 – Corrected strain amplitude sweep tests results at  $-10^{\circ}\text{C}$  and frequencies (a) 0.01 Hz, and (b) 0.3 Hz on B3550 bitumen.

The quantification of and separation of physical hardening effect was performed as described in section 4.3.2. As expected, similar trends in terms of increase in the physical hardening rate ( $G_b$ ) with a decrease in temperature, non-negligible physical hardening effect on determined linearity thresholds at low frequencies were observed. Physical hardening however has been seen to account for a minimum increase in strain amplitude by 0.5 on both bitumen B5070 and B3550.



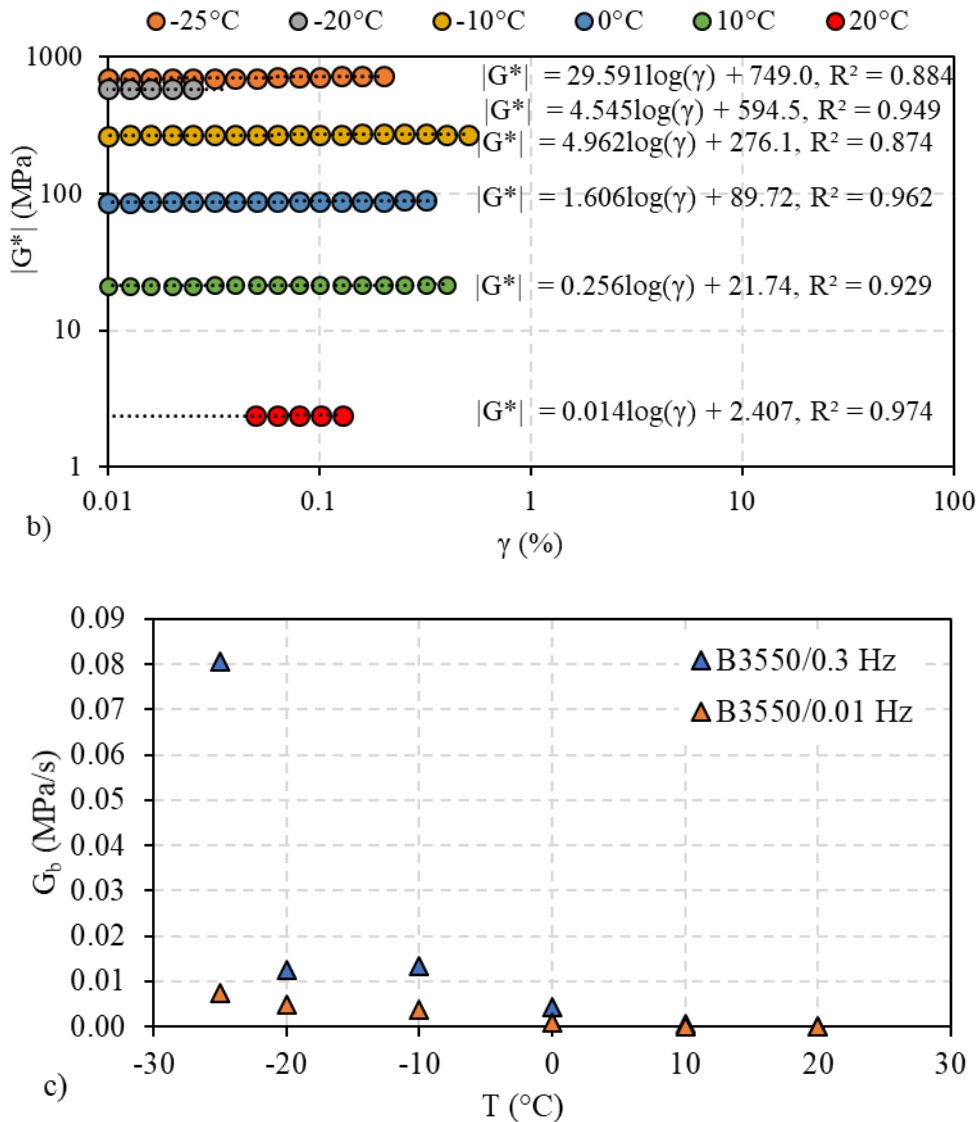


Figure 4.10 – Results of strain amplitude sweep tests and estimation of physical hardening effect on  $|G^*|$  of B3550 bitumen at (a) 0.01 Hz, (b) 0.3 Hz; and (c) the rate of physical hardening at each test temperature.

Figures 4.10a and 4.10b illustrate the regressions of  $|G^*|$  as a function of strain amplitude sweep test outcomes at 0.01 Hz and 0.3 Hz for all test temperatures. As previously explained, the regression intervals were selected with the effect of physical hardening in mind. As predicted, the rate of rise in shear complex modulus ( $G_b$ ), which reflects an estimate of physical hardening, is highest at -25°C and declines with increasing temperature as shown in the Figure 4.10c. Again, the physical hardening rate of B3550 bitumen is seen to be higher at 0.3 Hz. However, the effect of physical hardening is seen to be non-existent at temperatures 10°C and 20°C. The plot of physical hardening rates of both test bitumen B5070 and B3550 against temperature is shown in Figure 4.11. It is seen that the physical hardening rate is higher with

#### 4. Campaign 1: Shear oscillatory LVE limit of binders

B3550 bitumen. This is however, indicative of the heavier molecular weight of B3550 bitumen (Anderson & Marasteanu, 1999)

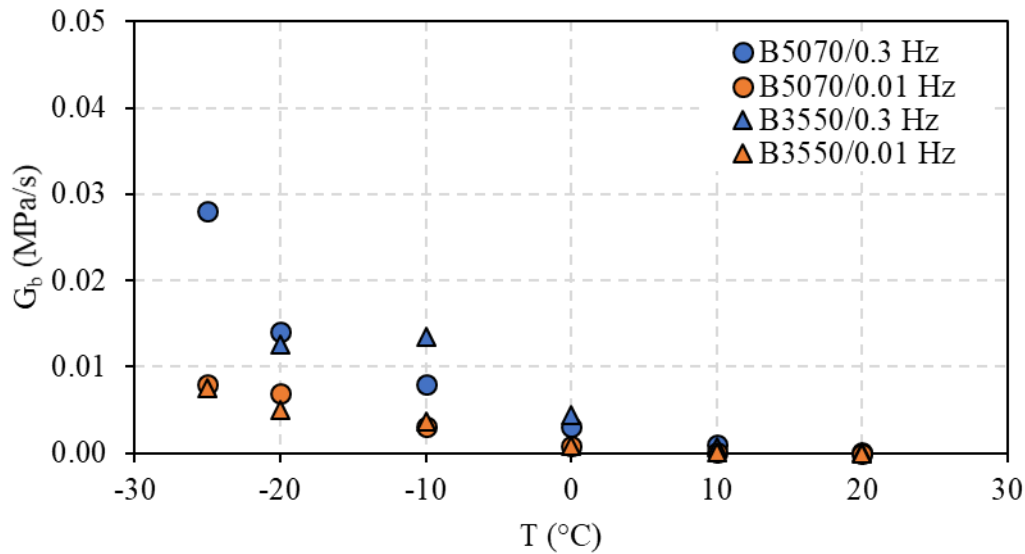
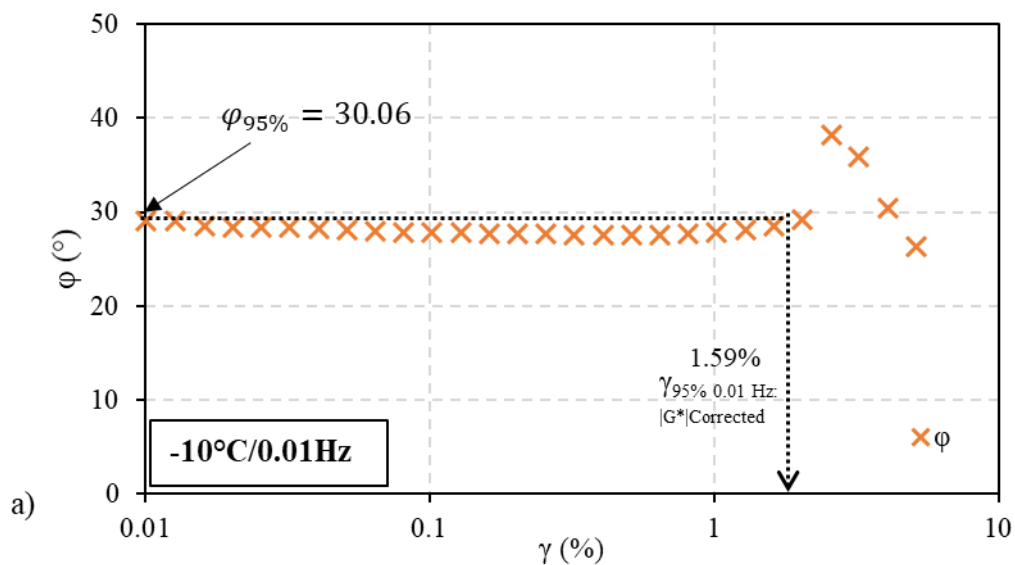


Figure 4.11 – Plots of Physical hardening rate ( $G_b$ ) of bitumen B5070 and B3550 against temperature at frequencies 0.3 Hz and 0.01 Hz

#### 4.4.2 Physical hardening effect on the phase angle ( $\varphi$ ) of B3550 bitumen during a strain sweep test

Physical hardening effect is not also seen within the phase angle results of bitumen B3550 as shown in Figures 4.12. As indicated in section 4.3.2, phase angle corresponding to the corrected LVE limit is selected as the LVE limit phase angle ( $\varphi_{95\%}$ ).



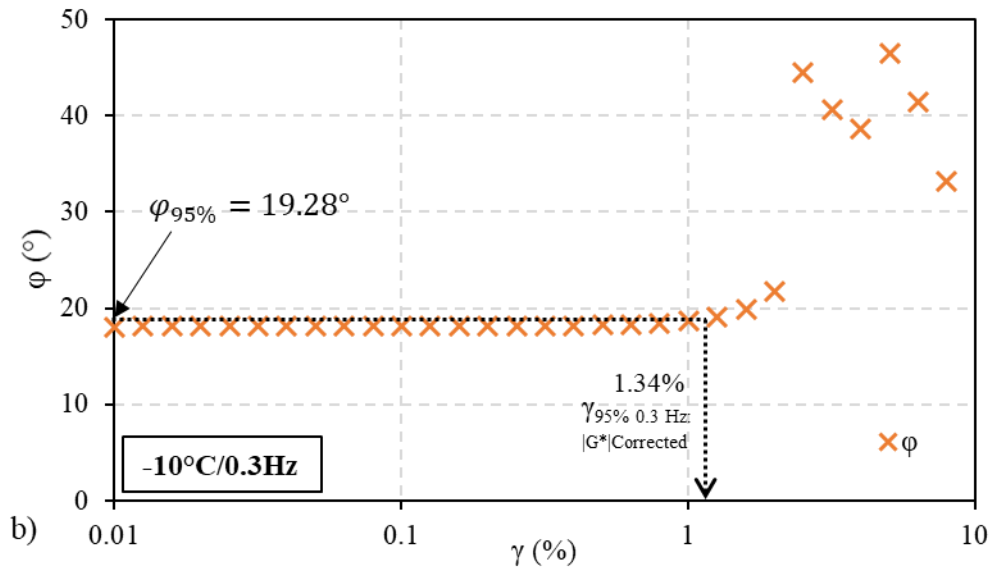
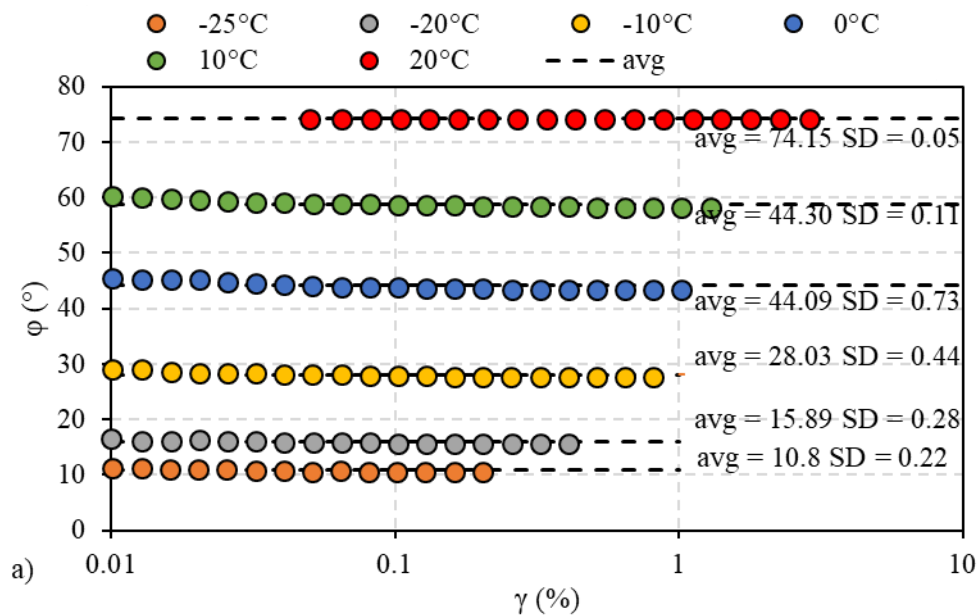


Figure 4.12 – Results of strain amplitude sweep tests showing phase angles of B3550 bitumen at (b) 0.01 Hz and 0.3 Hz.

The scattered points beyond the LVE limits represents the phase angles at the bitumen failed states. The phase angles corresponding to each regression points were averaged and standard deviations evaluated at each temperature and frequency pair.

Figures 4.13a and 4.13b depict the phase angles associated with each  $|G^*|$  evaluated for the regression (Figures 4.10a and 4.10b) and the average values at each test temperature, with maximum deviations of  $0.73^\circ$  at 0.01 Hz and  $0.2^\circ$  at 0.3 Hz.



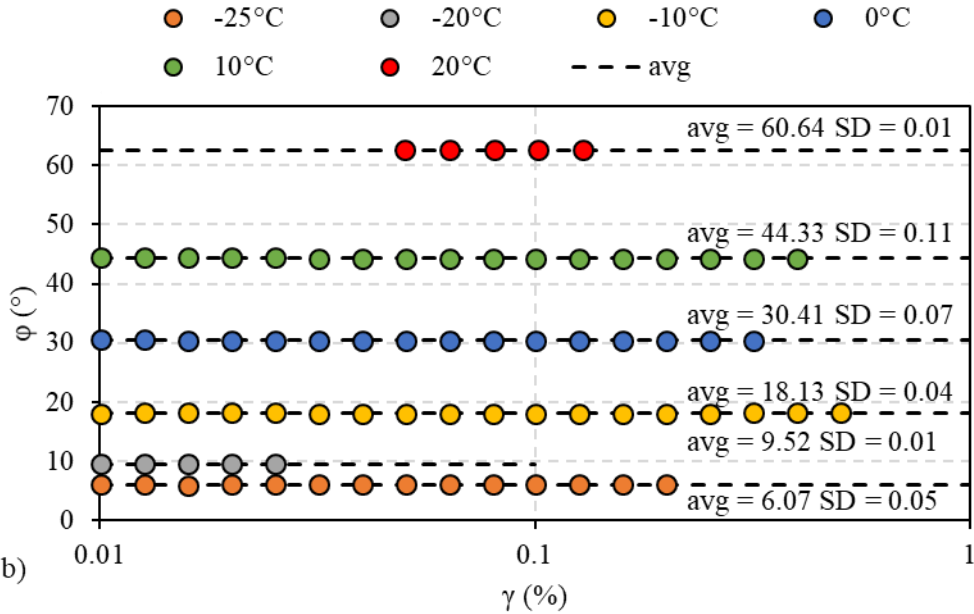


Figure 4.13 – Results of strain amplitude sweep tests and estimation of physical hardening effect on  $\phi$  of B3550 bitumen at (b) 0.01 Hz and 0.3 Hz.

Physical hardening has been shown in this study to diminish with temperature. This phenomenon can be considered to be non-existent at 20°C as illustrated in the Figures 4.5 and 4.10. Therefore, this phenomenon is not considered beyond this temperature. It is pertinent to note that the Figures 4.3 – 4.12 expressed as a function of strain ( $\gamma$ ) can also be expressed in function of time (Figures 4.5c, 4.10c and 4.11) as the points were taken at the same time interval.

**4.5 Time temperature dependence of physical hardening**

Plots of  $G_b$  as a function of test frequencies and reduced frequency are shown in Figure 4.14(a) and 4.14(b) respectively.

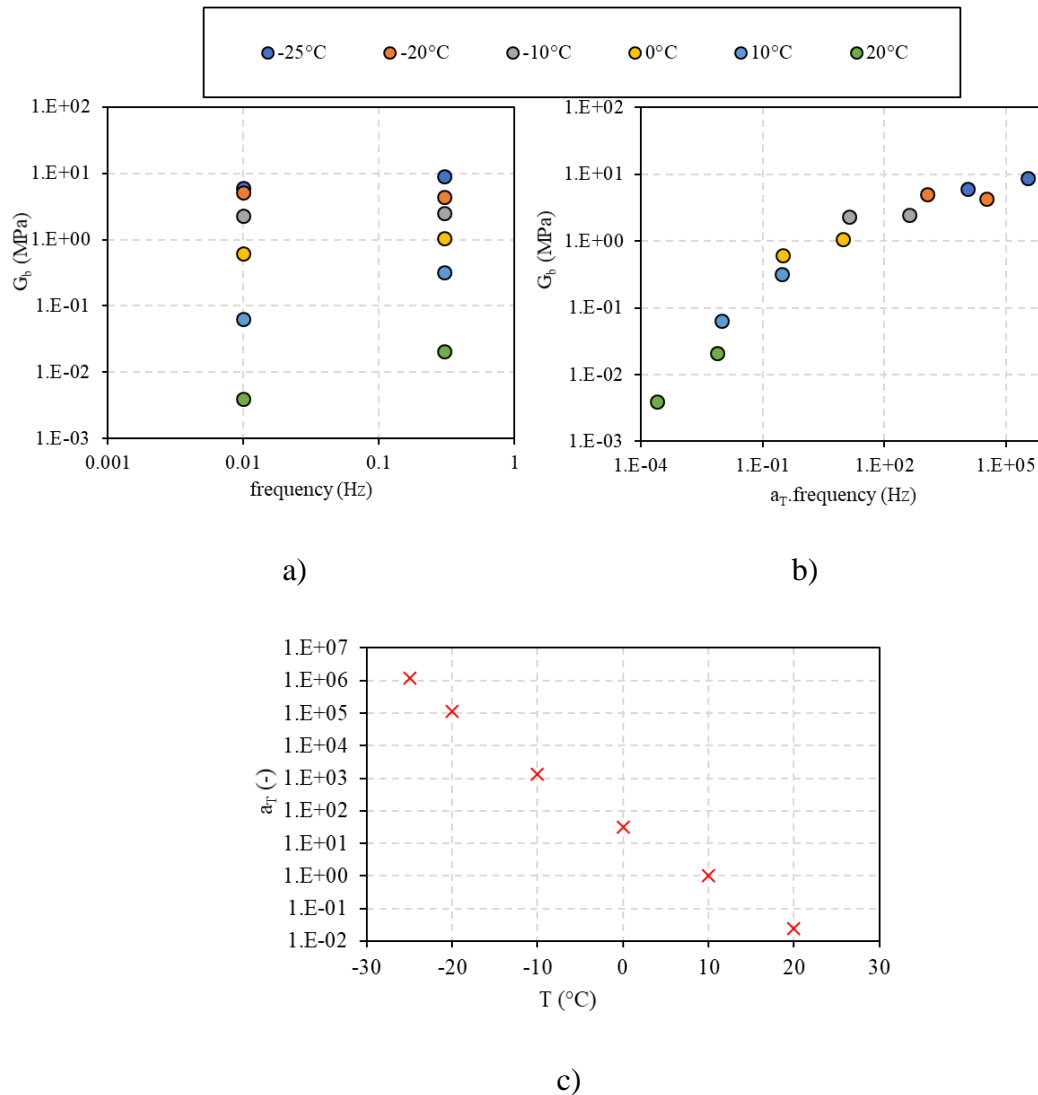


Figure 4.14 – (a) Isotherms; (b) Master curve and (c) temperature shift factors of B5070 bitumen LVE limit physical hardening constants ( $G_b$ ) at  $T_{ref} = 10^\circ\text{C}$

The effect of physical hardening is in a manner similar to that of decreasing temperature. From Figure 4.14, the representation of  $G_b$  as a function of reduced frequency Figure 4.14(b) results in a unique smooth curve. This indicates that the time-temperature superposition principle applies for the LVE limit, and that the same time-shift behaviour is obtained for the physical hardening parameter  $G_b$ . Unlike the shift factor, the rate of rise in shear complex modulus ( $G_b$ ) did not always increase with decreasing test temperature (Lu & Isacsson, 2000). This variation is demonstrated within the results of B3550 bitumen as shown in the Figure 4.10b and Table A-2(b). Results of time temperature dependence of B3550 are shown in Figure A1.



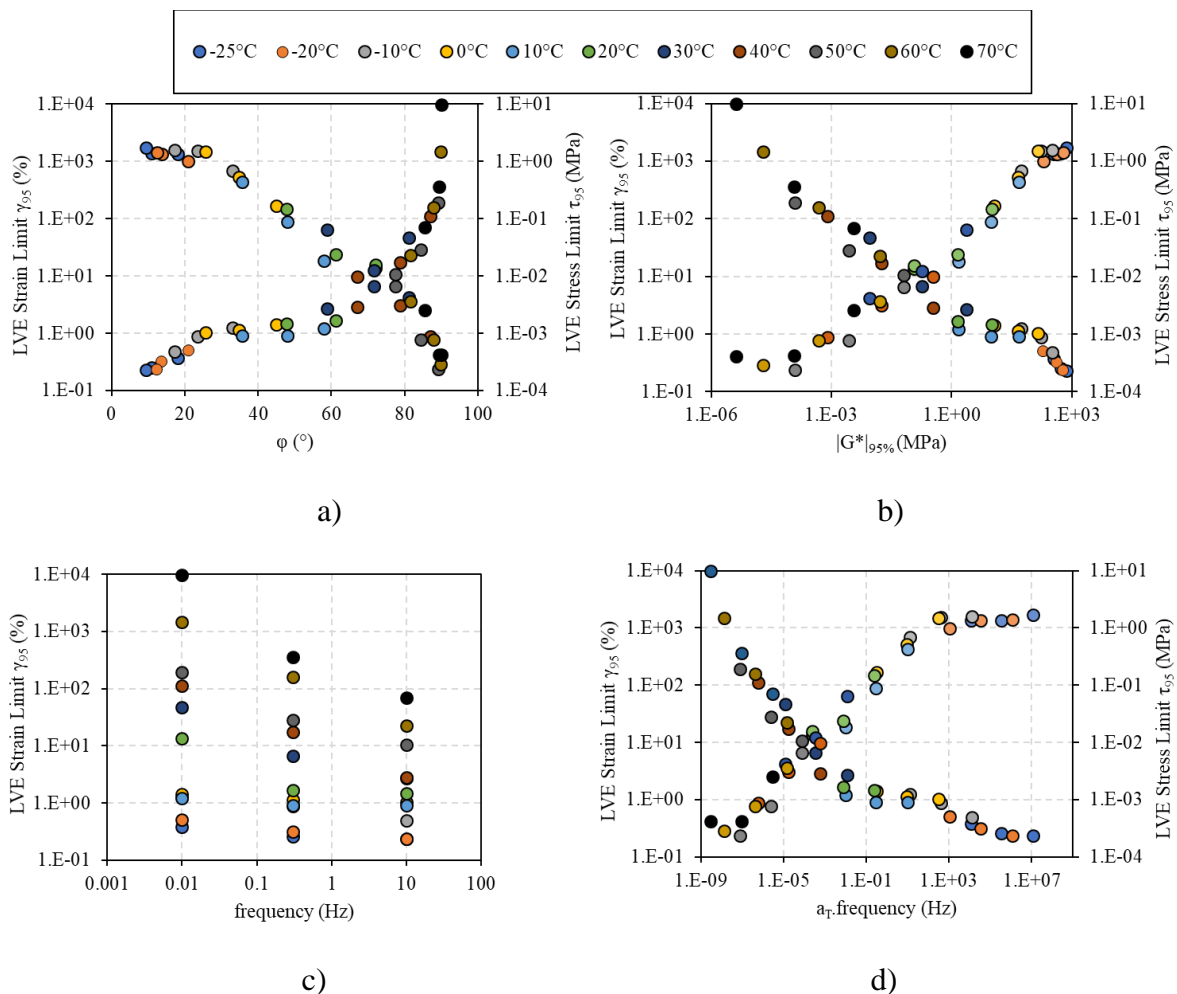
#### 4.6 Binder LVE limits time temperature dependence

Bitumen LVE limits were determined from strain amplitude sweep test results, with the criterion of 5% reduction in the norm of complex modulus  $|G^*|$  corresponding to the lowest measured strain. Strain amplitude threshold ( $\gamma_{95\%}$ ) were interpreted as the strain amplitude. A stress amplitude threshold ( $\tau_{95\%}$ ) can also be calculated by multiplying strain amplitude by the norm of complex modulus measured at the strain LVE limit threshold, as shown in equation (4.5). The norm of complex modulus corresponding to the threshold strain denoted as  $|G^*|_{95\%}$ .

$$\tau_{95\%} = |G^*|_{95\%} \gamma_{95\%} \quad (4.5)$$

It is however important to note that physical hardening effect corrections on strain limits are not considered above 20°C. This is due to the fact that at 20°C, the values of  $G_b$  which represents the effect of physical hardening are rather insignificant as seen in Figures 4.5 and 4.10.

Figure 4.15 shows the obtained LVE limits in terms of strain amplitude and stress amplitude for the various tested temperatures and frequencies. The results are plotted against the phase angles, measured modulus and the reduced frequency at 10°C in the figure.



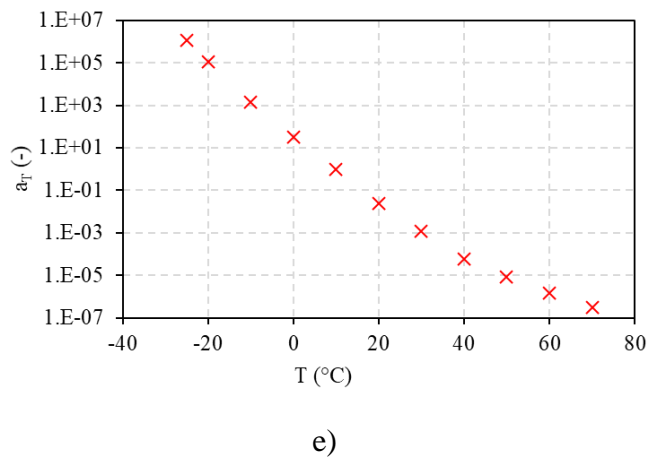


Figure 4.15 – Plots showing B5070 bitumen (a) stress and strain limits as a function of phase angle  $\varphi_{95\%}$  (b) stress and strain limits as a function of  $|G^*|_{95\%}$  (c) strain limit isotherms and (d) stress and strain limit master curves at  $T_{ref} = 10^\circ\text{C}$

As a function of phase angle, Figure 4.15(a-b) provides a distinct indication of the viscous nature of the bitumen at high temperature, which leads to a stress-dependent LVE criterion of 0.4 kPa, as established by (G. D. Airey et al., 2003). Figure 4.15(b) shows the evolution of stress and strain limits in function of the complex modulus  $|G^*|$ . Knowing the evolution of complex modulus in function of frequency and temperature, it can be deduced that as the complex modulus  $|G^*|$  increases, the LVE limit in terms of shear strain amplitude decreases, whereas the shear stress amplitude increases. Furthermore, shear strain amplitude increases with a reduction in frequency and an increase in temperature as seen in Figure 4.15(c). The bitumen has low shear strain limits (low temperatures/high frequencies) of approximately 0.2% (2000 $\mu\text{m}/\text{m}$ ) and high strain limits (high temperatures/low frequencies) of approximately 10,000%. In addition, as depicted in Figure 4.15(a), a maximal stress of 1500kPa is reached, which corresponds to the nonlinear stress limit of bitumen at low temperature/high frequency. This thesis broadens the LVE limit ranges for bitumen in terms of strain and stress amplitudes. Results by (G. Airey, B. Rahimzadeh, & A. Collop, 2003; G. D. Airey et al., 2003; Babadopoulos, 2017) demonstrated that unique curves were obtained when plotting LVE limits versus the norm of complex modulus. This strongly suggests that the same time-shift law as for the linear small strain amplitude modulus can be applied.

Regardless of how the LVE limits are represented in terms of stress or strain amplitudes as functions of equivalent frequency, the bitumen yields a unique, smooth curve as shown in Figure 4.15(d). This indicates that the LVE limit is subject to the time-temperature

#### 4. Campaign 1: Shear oscillatory LVE limit of binders

superposition principle. This is further evidenced by the unique plot of shift factors  $a_T$  as a function of test temperatures as shown in Figure 4.15(e). Results associated with B3550 are equally provided as Figure A2 in the appendix.

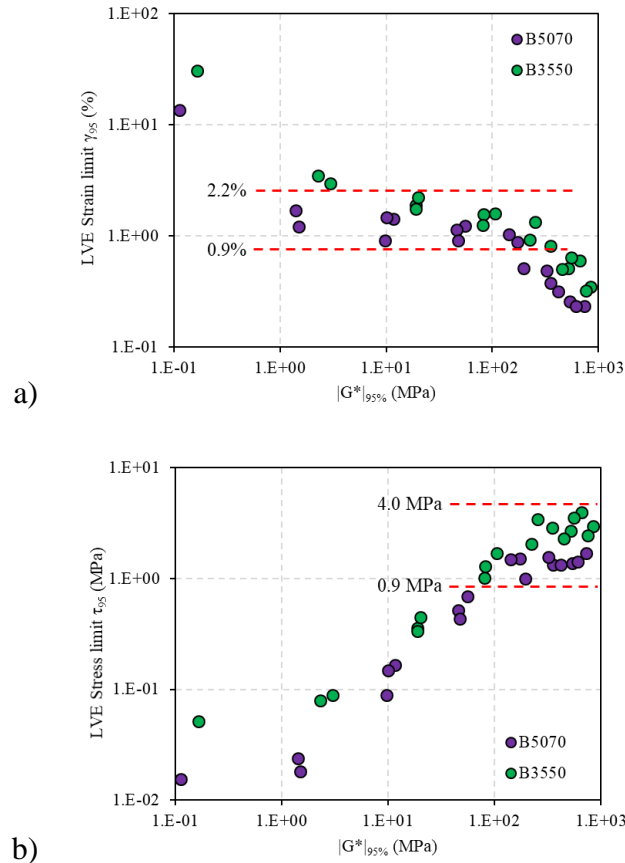


Figure 4.16 – Linear viscoelastic (a) strain limits as a function of  $|G^*|_{95\%}$ ; (b) stress limits as a function of  $|G^*|_{95\%}$  from low to medium temperatures ( $-25^\circ\text{C}$  to  $20^\circ\text{C}$ )

The Linear viscoelastic strain and stress limits are shown as functions of complex modulus in Figure 4.16.

The trends of strain and stress limits for the two bitumen as a function of complex modulus are very similar. The LVE strain limit of B3550 bitumen, is greater than that of B5070. As anticipated, there is a general increase in the strain limit as the complex modulus of the bitumen decreases. The linearity performance of the binders is comparable in terms of the LVE stress limits in Figure 4.16, with the B3550 bitumen having a higher stress limit.

Bitumen B3550 obviously has greater stress and strain limits. This is not the anticipated behaviour of a lower penetration grade bitumen. Furthermore, this trend does not correspond to

the findings obtained by (G. Airey et al., 2003) with similar bitumen grades. The linearity findings show that low penetration grade bitumen has narrower linear ranges and thus lower linearity limits. The plots of the LVE strain and stress limits as a function of complex modulus should eliminate any stiffening effect on the narrowing of the linear range, allowing the linear limit reduction to be attributed purely to penetration grade criteria.

According to Figures 4.16(a), both bitumen shows two strain regimes separated by a horizontal line: intermediate and low temperature strain regimes. The results indicate that at intermediate to low temperatures (20°C to 0°C), the strain dependent LVE criteria ranges between 0.9% and 2.2%. Furthermore, these binders have a stress dependent LVE criteria ranging from 0.9MPa to 4MPa at high stiffness and low temperatures (0°C to -25°C) as shown in Figure 4.15(b).

There exists a significant difference in magnitude between the strain dependent linearity criterion identified by (G. Airey et al., 2003; G. D. Airey et al., 2003) for DSR tests (2% to 6%) and that identified in this thesis (0.9% to 2.2%). This difference is due to insufficient torque measured with the 8 mm parallel measuring plate used at low temperatures by (G. Airey et al., 2003) whereas in this thesis, 4 mm parallel plate was utilised. Furthermore, the stress dependence of the transition between linear and nonlinear behaviour of bitumen at low temperatures is identified.

#### 4.7 2S2P1D modelling of binder LVE limits

Norm $|G^*|_{95\%}$  of complex modulus corresponding to the LVE limits calculated as a function of strain and for the tested temperatures and frequencies, are given in Figure 4.17. In the figure, results of  $|G^*|_{95\%}$  are plotted as a cole-cole curve, black diagram and master curves at 10°C reference temperature. Furthermore, 2S2P1D rheological model has been fitted on experimental data. Table 4.1 gives the obtained material constants and  $G^*$  calculated with 2S2P1D model.

From Figure 4.17, the plot of shear complex modulus corresponding to LVE limits as a function of the respective phase angles forms a unique curve, showing that the test binder is thermorheologically simple. As a first approximation, the TTSP is validated at the threshold of the LVE domain at all tested temperatures and frequencies. The perfect curves formed by shifting the isothermal curves of the norms of complex modulus ( $|G^*|_{95\%}$ ) and corresponding phase angles ( $\phi_{95\%}$ ) along the horizontal axis by the factors  $a_T$  indicates the time temperature super position principle of the binder. The same time-shift behaviour as for the nonlinearity parameter is obtained for this complex modulus ( $|G^*|_{95\%}$ ).

The simulation of experimental values with the 2S2P1D model is possible because of the similarities between the shear complex modulus at the strain limits ( $|G^*|_{95\%}$ ) and shear

complex modulus ( $|G^*|_{LVE}$ ) measured within the LVE limit of the bitumen. The successful WLF fit of the temperature shift factors used is also shown.

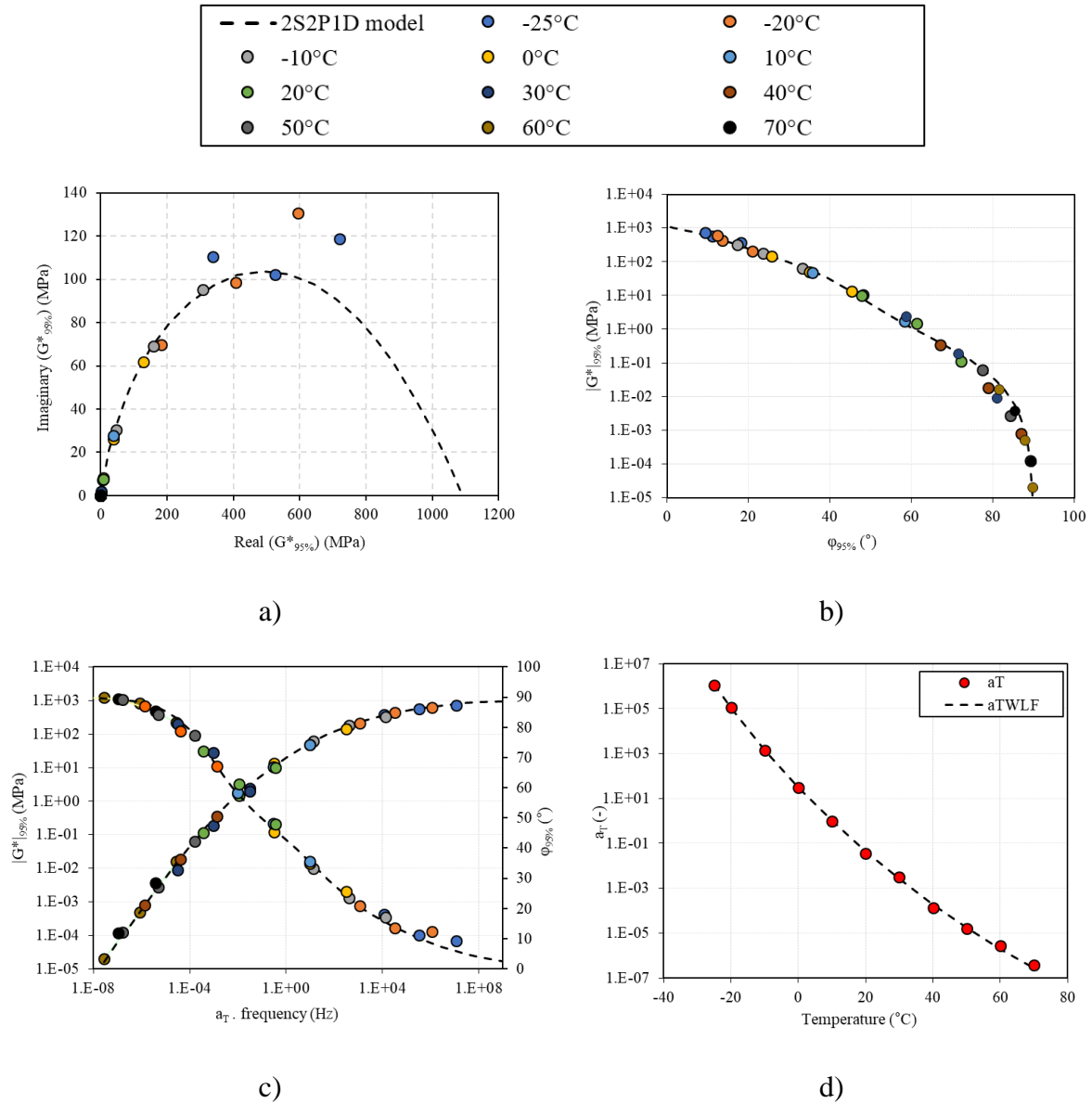


Figure 4.17 – Plots of B5070 bitumen showing (a) Cole-Cole diagram of  $|G^*|_{95\%}$  values (b) Black diagram of  $|G^*|_{95\%}$  and  $\phi_{95\%}$  values, corresponding to norm and phase angle of complex shear modulus at the LVE limit, for all tested frequencies and temperatures (c) Master curves of  $|G^*|_{95\%}$  and  $\phi_{95\%}$  values, corresponding to norm and phase angle of complex shear modulus at the LVE limit, and 2SP1D simulations. (d) Temperature shift factors and WLF fit used to build the master curves.

#### 4. Campaign 1: Shear oscillatory LVE limit of binders

Table 4.1 – B5070 bitumen 2S2P1D model constants

$G_{00}$ (MPa)	$G_0$ (MPa)	$k$	$h$	$\delta$	$\tau_{G95\%}$ (10°C)	$\beta$	$C_1$	$C_2$
0	1090	0.23	0.56	3.50	2.2E-04	400	28	198

The Bitumen B3550 LVE limits were also fitted using the 2S2P1D model. The outcomes of this analysis are displayed in Figure A3 and Table A3, which may be found in the appendix.

#### 4.8 Conclusions of Campaign 1

The results obtained highlights the effect of physical hardening on LVE properties of unmodified bitumen (B5070 and B3550) and its effect on the determination of the LVE limits of the material at different temperatures and frequencies.

- There was a significant increase in the shear complex modulus of binders tested at low temperature after the recommended 30 minutes equilibrium time was observed.
- Physical hardening effects on  $|G^*|$  appear to be temperature and time dependent. The effect of physical hardening appears to be nonnegligible when performing strain amplitude sweep tests at low temperature and low frequency. If not properly considered, the stiffening effect of the binder during tests can increase the estimation of its LVE limit by a minimum factor of 0.5.
- Physical hardening rate ( $G_b$ ) increased from medium to high temperatures. Furthermore, it is negligible at 20°C.
- There were no variations due to physical hardening effects on the phase angle values of binders
- Physical hardening rates are higher at 0.3 Hz compared to 0.01 Hz. Furthermore, it is highest with B3550 bitumen at 0.3 Hz and 0.01 Hz
- Values of LVE limits obtained over a wide range of temperatures and three frequencies appear to validate time-temperature superposition principle.
- The 2S2P1D model was used to successfully simulate the behaviour of the tested bitumen at the LVE limit, over the whole range of tested temperatures and frequencies.
- The binders showed a stress dependent LVE criteria between 0.9MPa and 4Mpa at low temperatures (-10°C to -25°C) as well as strain dependent LVE criteria between 0.9% and 2.2% at intermediate to low temperatures (20°C to 0°C).
- There is no necessarily a reduction of the linearity range for low penetration grade bitumen. The linearity strain criterion for bitumen varies from 0.2% (2000µm/m) to 10,000%.

#### 4. Campaign 1: Shear oscillatory LVE limit of binders

---

- Finally, because there appears to be no reduction in linearity limits for low penetration grade bitumen when compared to higher penetration grade bitumen, additional strain sweep tests on similar grades of bitumen are required to reaffirm the assumption of bitumen penetration grade linearity independence.

### **5. Campaign 2: DSR linear viscoelastic characterisation of binders in shear**

#### **5.1 Objectives**

The second campaign of this thesis focused on the linear viscoelastic characterisation of the behaviour of two unmodified bitumen and a polymer modified bitumen.

The first objective behind the characterisation of LVE behaviour of bitumen was to correctly perform complex modulus test on bitumen using a Dynamic Shear Rheometer across a wide temperature and frequency range while making use of the 4 mm parallel plate at low temperature measurements.

The proper linear viscoelastic characterisation of bituminous binders using the DSR most importantly at low temperatures, is crucial to the correct prediction of asphalt mixtures viscoelastic properties at corresponding temperatures. Discrepancies have been observed between the predicted glassy modulus ( $G_0$ ) values using the DSR complex shear modulus measurements and those obtained from other apparatuses such as Metravib apparatus, Annular Shear Rheometer (ASR) (see section 2.1.1.4.4) (Mangiafico, 2014; Orozco, 2020).

As earlier stated, the temperature dependence of bitumen viscoelastic properties deviates from the WLF law below the glass transition temperature ( $T_g$ ). This led to the adoption of the modified Kaelble equation (see section 2.4). The second objective of this campaign was to correctly fit the experimental results from the DSR linear viscoelastic characterisation which spans below the glass transition temperatures of the test bitumen to the 2S2P1D rheological model (Olard and Di Benedetto 2003) adopting the modified Kaelble equation as the shift factor predictive equation. This equation replaces the traditional WLF equation utilised with the 2S2P1D rheological model. Finally, the third objective was to determine the glass transition temperatures of the test binders.

#### **5.2 Rheological measurements**

The rheological response of bitumen is comprehensively characterized through Dynamic Shear Rheometry (DSR), resulting in data representations such as Cole-Cole curves, Black diagrams, and master curves. This analysis highlights variations among these measurements and illuminates the limitations and constraints inherent in the measurement process.



## 5. Campaign 2: DSR linear viscoelastic characterisation of binders in shear

### 5.2.1 Influence of plate sizes on bitumen rheological responses

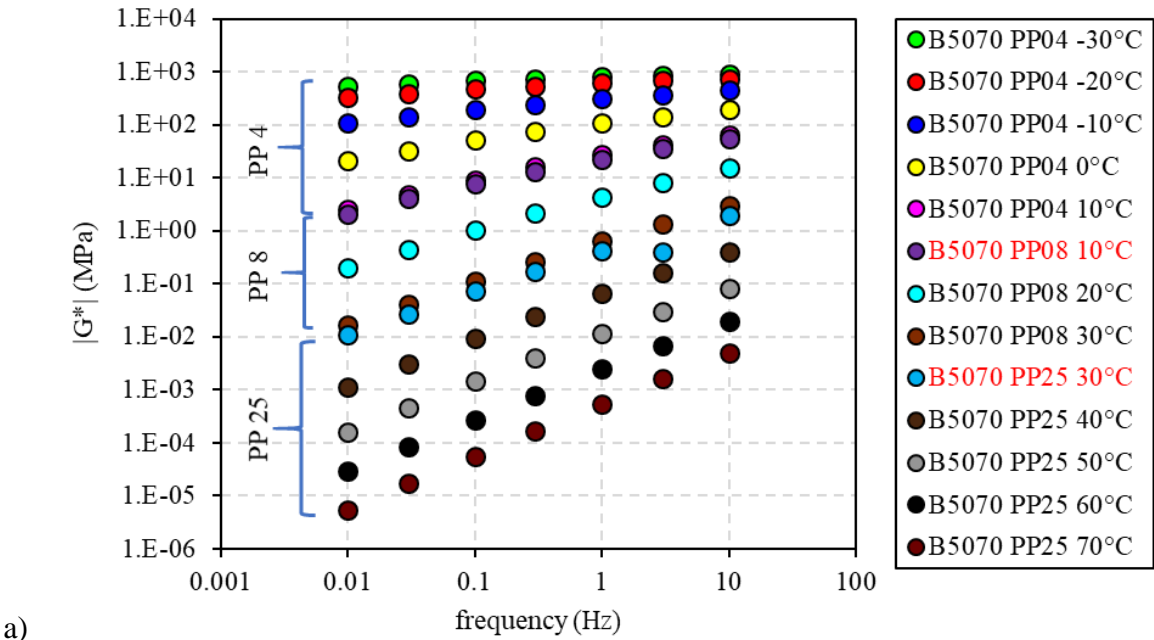
Figure 5.1 shows the plots of norms of complex shear modulus  $|G^*|$  and phase angle  $\phi$  against frequencies for bitumen B5070-1. Care is recommended to be taken when selecting the most appropriate test geometries over wide temperature and frequency ranges at the transition between test geometries (Gordon D. Airey, 2002b; Gordon D Airey et al., 2021).

There exists an obvious discrepancy in the stiffness measured by the 25 mm parallel plate at high frequency 3 Hz (Figure 5.1a). The stiffness is underestimated at 30°C as compared to the measurement with the 8 mm plate. Again, a reduction in phase angle values were observed at the same frequency (3 Hz) shown in Figure 5.1b,

Considering the measurement at 10°C with 4 mm and 8 mm plates, the phase angle isotherms tend to superimpose since there was no discernible differences, hence the invisibility of the 8 mm data points (Figure 5.1b). However, a higher stiffness is measured by the 4 mm parallel plate to a maximum difference of 21%.

The observed disparities in the measurements suggest deficiencies in the accuracy of the measuring plates at specific temperatures. Hence, the isotherms PP08 10°C and PP25 30°C were eliminated in subsequent plots for analysis.

DSR results provided accurate measurements of the norm of complex modulus over 9 decades from ( $5 \times 10^{-6} \text{ MPa}$  to  $10^3 \text{ MPa}$ ) and phase angles from  $4^\circ$  to  $90^\circ$ .



## 5. Campaign 2: DSR linear viscoelastic characterisation of binders in shear

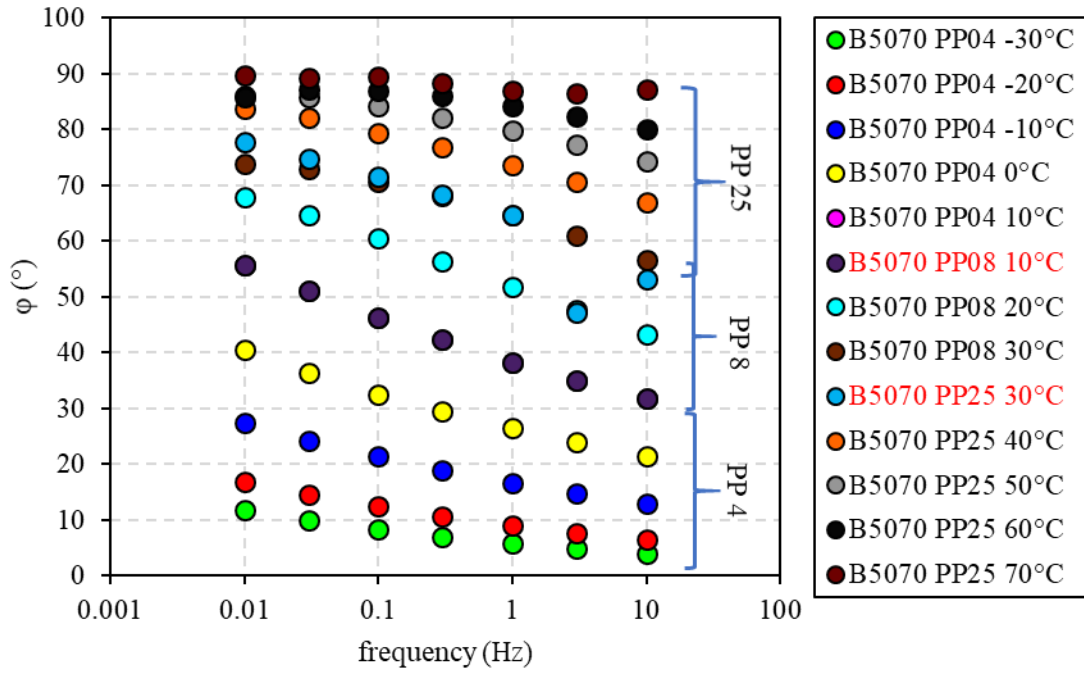


Figure 5.1 - Example of DSR complex modulus test results for bitumen B5070-1: a) norm of complex modulus isotherms: b) phase angle isotherms

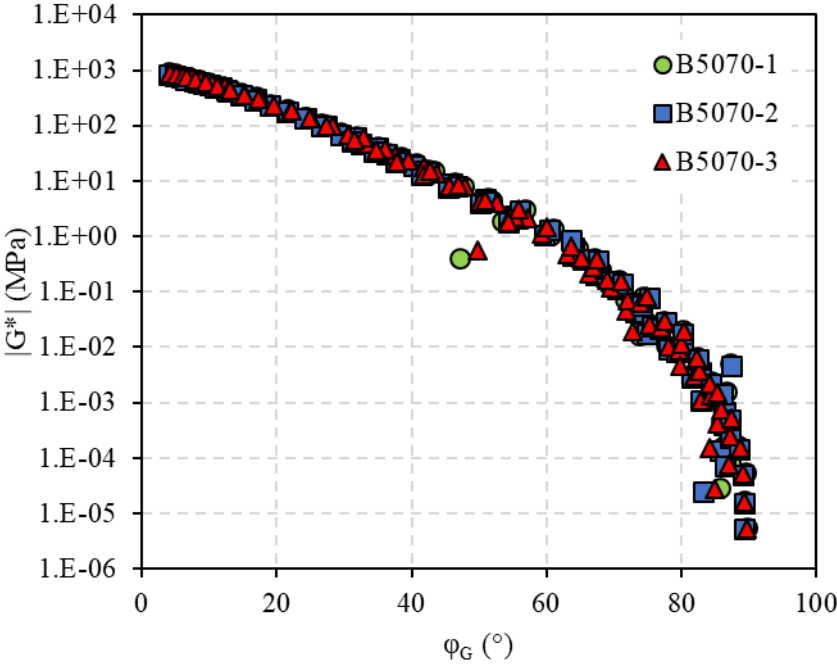
### 5.2.2 Repeatability

Figure 5.2 illustrates the plots of norms of shear complex modulus against corresponding phase angles and plots of real versus the imaginary forms of complex modulus for the three repetitions of B5070 bitumen. The comparison of bitumen responses at high temperatures can be made utilising the black diagram whereas similar feat is only achievable at low temperatures using the Cole-Cole diagram. The Black diagrams of each B5070 bitumen repetitions overlap quite well with unobservable variations (Figure 5.2a). However, there exists observable variations in the stiffnesses of the second (B5070-2) test trial at low temperatures ( $\leq 10^{\circ}\text{C}$ ). These variations account for a maximum of 5.4% (47 MPa) difference between the mean values of the stiffnesses of the three trials at low temperatures. The phase angle difference between the average measured phase angle is found to be at the maximum of  $0.8^{\circ}$ . Furthermore, the exclusion of the second trial from the accuracy analysis indicates a maximum mean deviation of 8 MPa. However, a further analysis is carried out by the normalisation of the Cole-Cole plots in accordance with Equation 5.1.

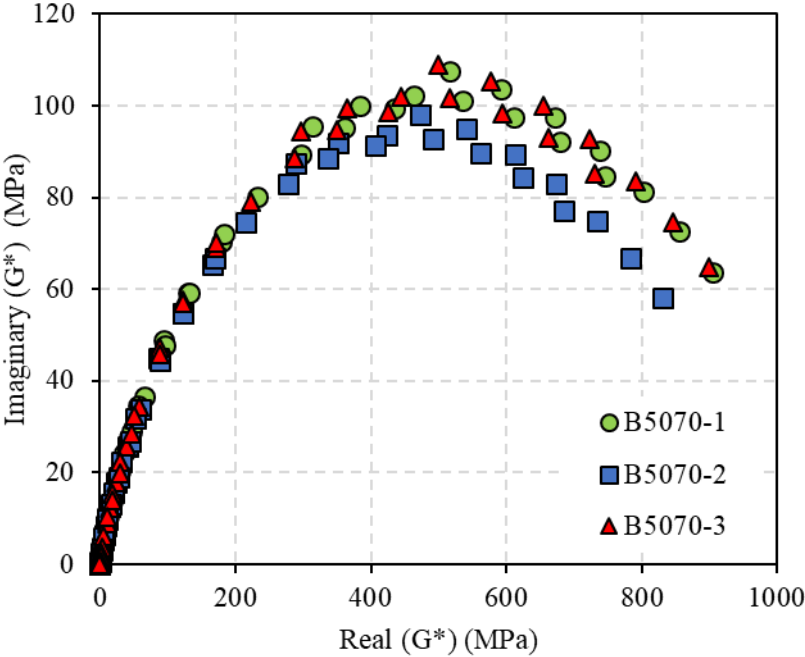
$$G_{norm}^* = \frac{G^* - G_{00}}{G_0 - G_{00}} \quad (5.1)$$

5. Campaign 2: DSR linear viscoelastic characterisation of binders in shear

The normalised Cole-Cole curves are as shown in the Figure 5.2c. The curves superimpose quite well, which implies that the variation in the moduli observed between B5070-2 and the other trials can be attributed to sample geometry factors. Hence the test was highly repeatable. The jumps seen at low temperatures on the Cole-Cole plots (Figure 5.2b) have also been observed with mixtures. Although in the case of mixtures, only one jump was observed between 0°C and -10°C. This was however attributed to the presence of moisture within the mixture matrix. Contrary to this, several jumps were observed with bitumen below 0°C.



a)



b)

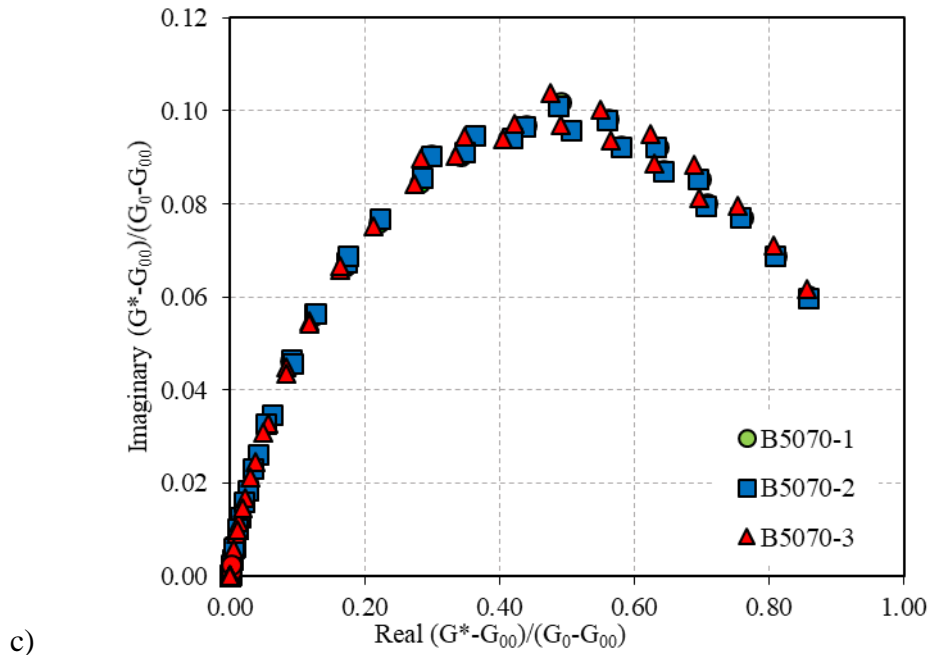
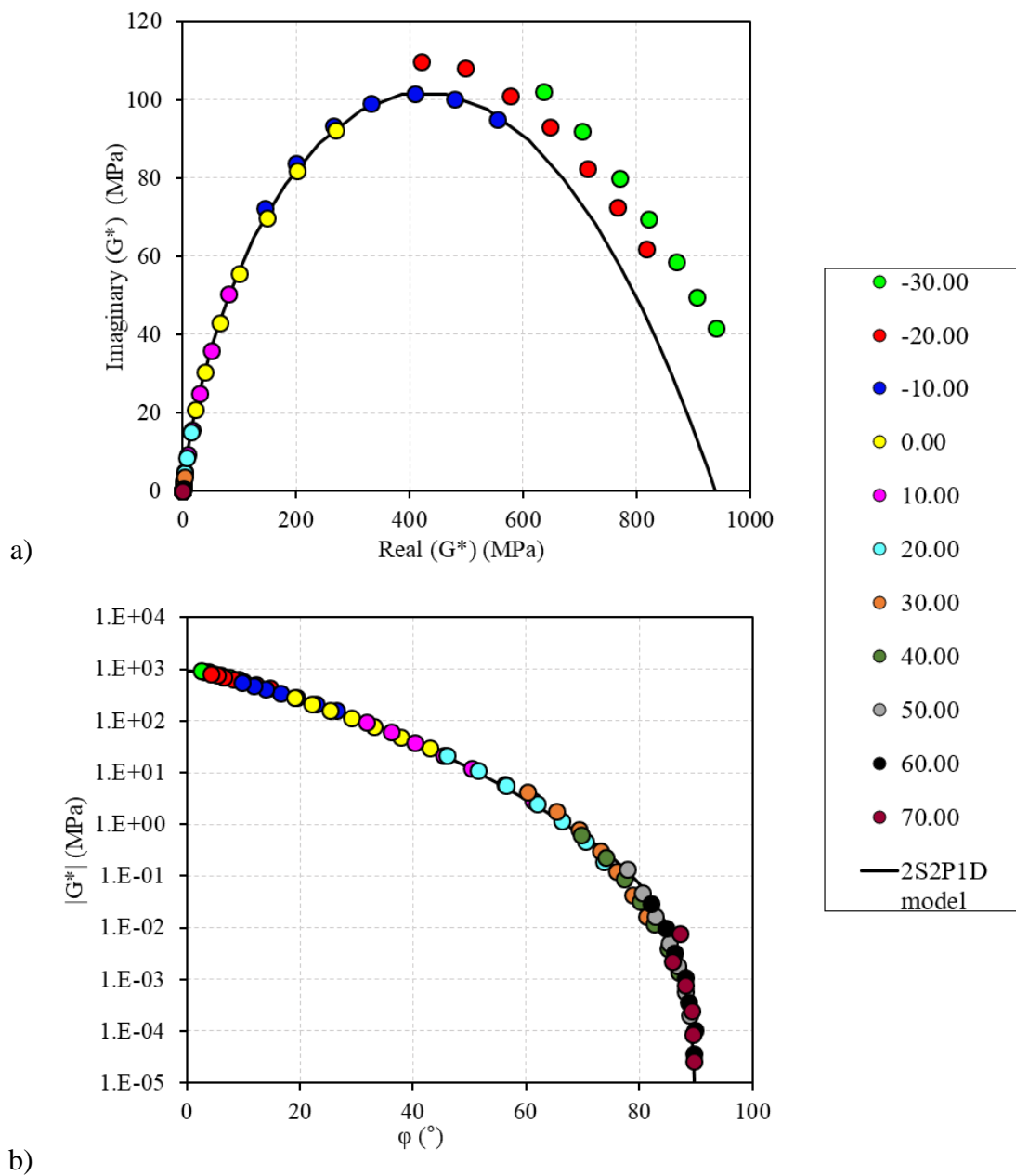


Figure 5.2 - Example of DSR complex modulus test results for bitumen B5070: a) Black diagrams; b) Cole-Cole diagrams; c) normalised Cole-Cole diagrams

### 5.3 Rheological modelling

The second step of analysis was the fitting of the experimental data to the 2S2P1D model. Master curves of norms of complex shear modulus  $|G^*|$  and phase angle  $\phi$  were plot at  $10^\circ\text{C}$  reference temperature ( $T_{\text{ref}}$ ) for all materials. Time temperature superposition principle (TTSP) and Partial time temperature superposition principle (PTTSP) were verified for the unmodified and polymer modified bitumen respectively (François Olard & Di Benedetto, 2003; F Olard et al., 2005; François Olard et al., 2003). Temperature shift factors  $a_T$  were found and master curves were derived from experimental results at the reference temperature. The shift factors are observed to deviate from the WLF equation at low temperature below  $-20^\circ\text{C}$ . This was attributed to temperature measurement problems in some PhDs. As an example, the fitting of bitumen B3550-1 and PmB are shown in Figure 5.3 and 5.4 respectively.

## 5. Campaign 2: DSR linear viscoelastic characterisation of binders in shear



5. Campaign 2: DSR linear viscoelastic characterisation of binders in shear

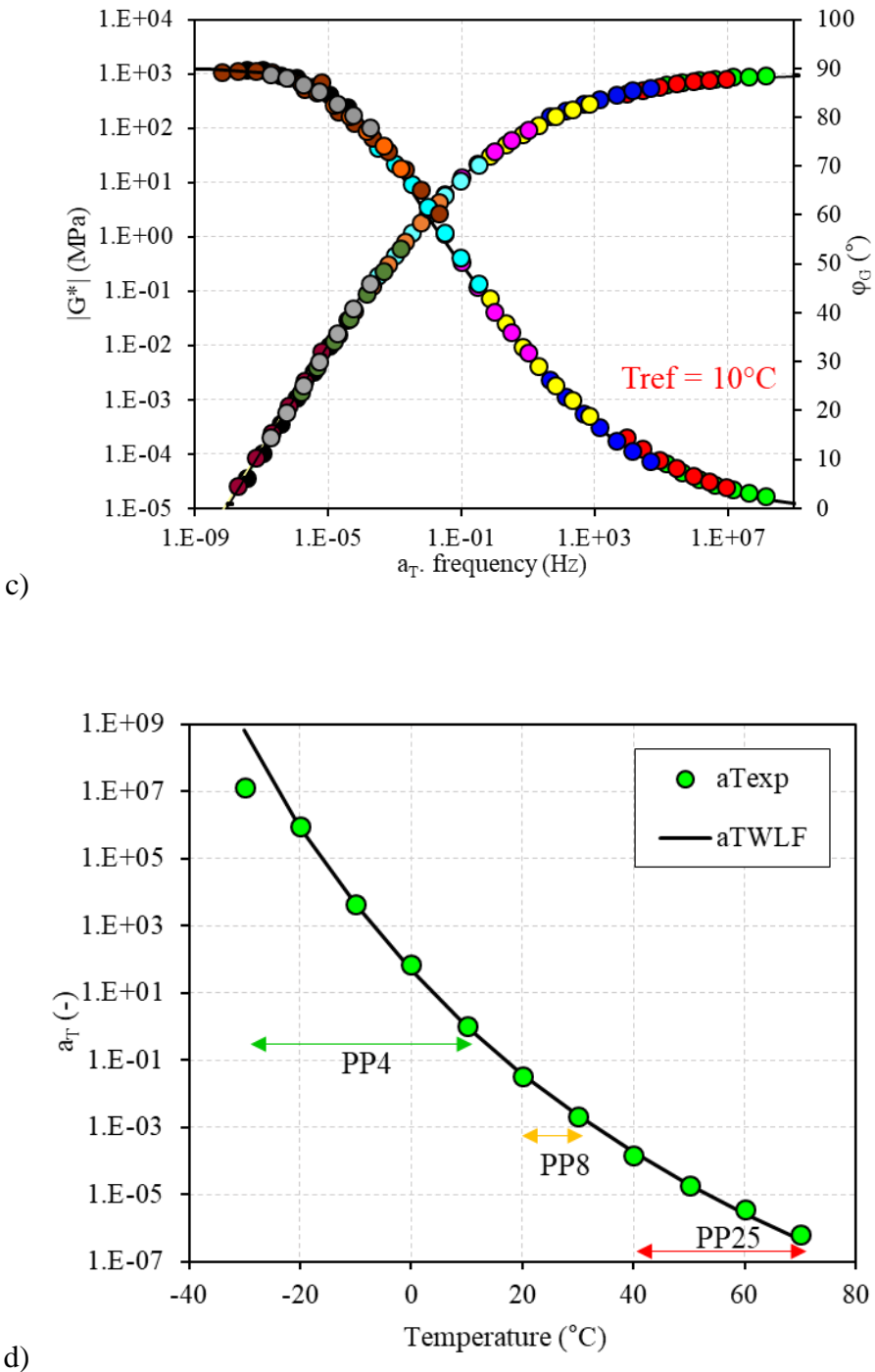
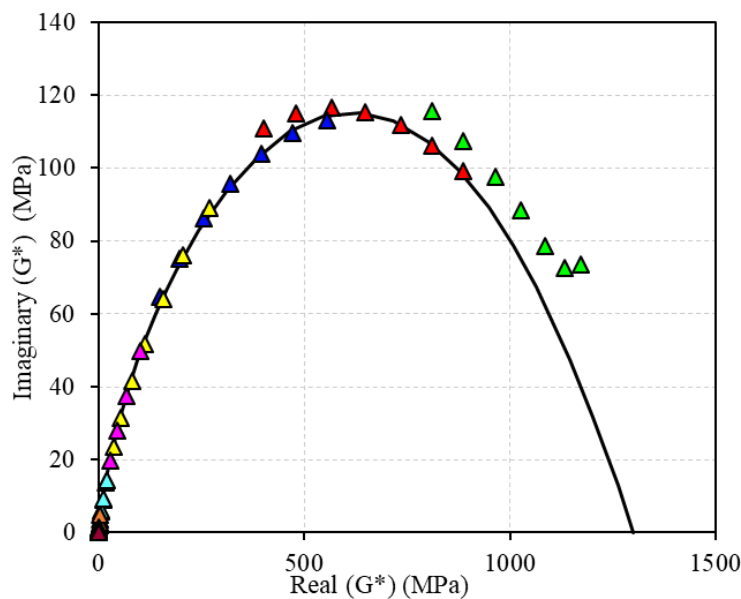


Figure 5.3 – 2S2P1D fitted complex modulus test results for bitumen B3550-1: a) Cole-Cole plot; b) Black diagram; c) master curves of norms of complex modulus and phase angle; d) WLF temperature shift factors at  $T_{ref} = 10^\circ\text{C}$

Figure 5.3 shows the plots of imaginary against the real shear complex modulus, plots of norms of complex shear modulus against phase angle and reduced frequency, finally the shift factors against test temperatures. As seen in Figure 5.3a, a perfect Cole-Cole curve is formed from high

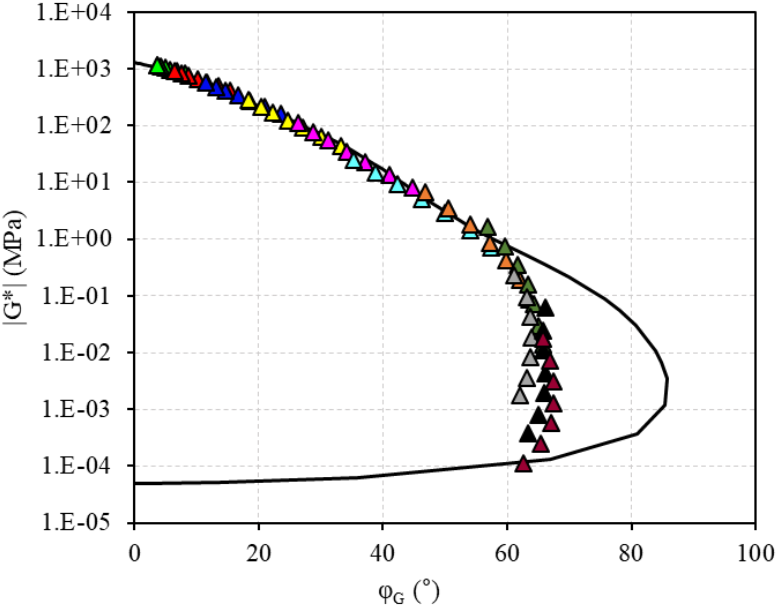
## 5. Campaign 2: DSR linear viscoelastic characterisation of binders in shear

temperature (70°C) to low temperature (-10°C). However, vertical shifts appear at temperatures below -10°C. These vertical shifts were earlier observed with bitumen B5070. Furthermore, the perfect Black diagram formed as a first approximation confirms the thermorheological simplicity of the test bitumen. The isothermal shift of the norms of complex shear modulus and phase angles along the reduced frequency axis which forms perfect curves verifies the TTSP. 2S2P1D model fit quite well the experimental data represented in the plots of Figure 5.3(a-c) at  $T_{ref} = 10^\circ\text{C}$ . 2S2P1D model parameter values and WLF parameters for all materials are given in Table 5.1.  $G_{00}$  was imposed equal to zero for all bitumen. In this work, the DSR prediction corresponded very well with the literature  $G_0$  value around 1 GPa (Büchner, Wistuba, & Klüter, 2020; Hunter et al., 2015). Similarly, calculating the values of  $E_0$  from  $G_0$  values by applying an arbitrary constant Poisson's ratio equal to 0.5 ( $E^* = 3G^*$ ) as commonly done, resulting  $E_0$  values comprised between 2.1 to 3 GPa (François Olard & Di Benedetto, 2003; F Olard et al., 2005) for all bitumen.

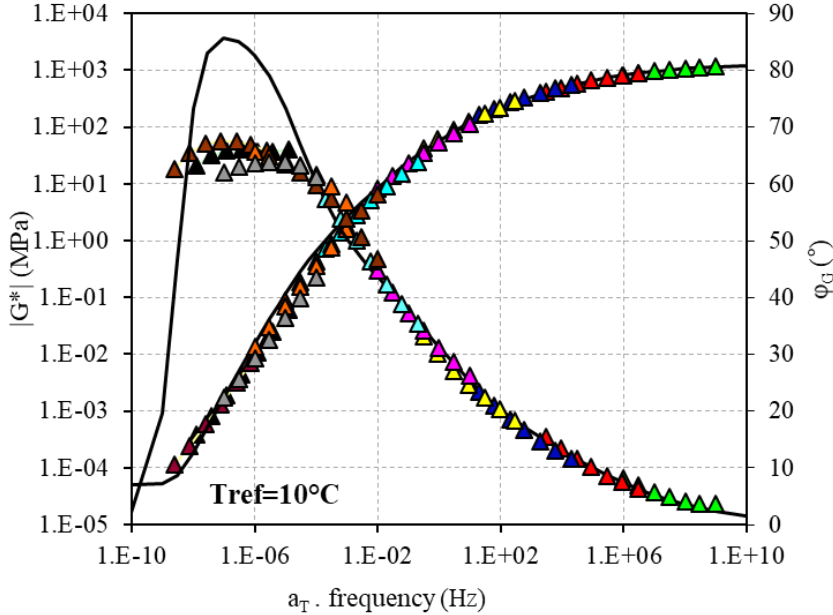


a)

5. Campaign 2: DSR linear viscoelastic characterisation of binders in shear



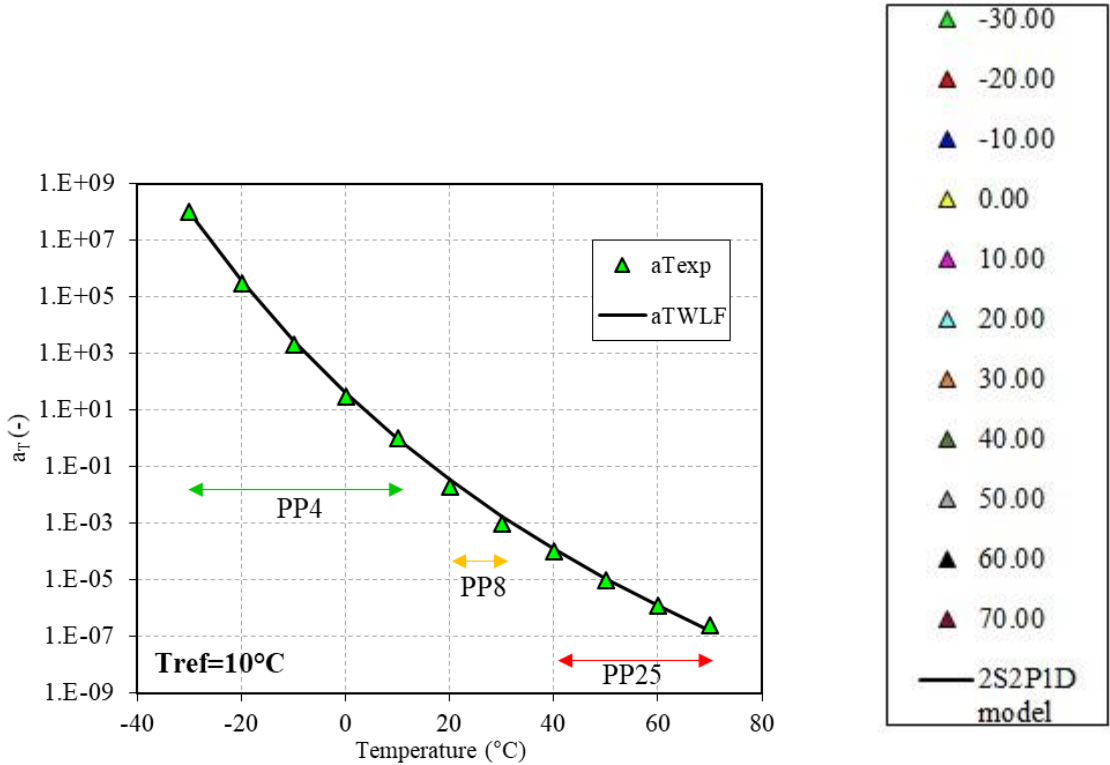
b)



c)



5. Campaign 2: DSR linear viscoelastic characterisation of binders in shear



d)

Figure 5.4 – 2S2P1D fitted complex modulus test results for bitumen PmB: a) Cole-Cole plot; b) Black diagram; c) master curves of norms of complex modulus and phase angle; d) WLF temperature shift factors at  $T_{ref} = 10^{\circ}\text{C}$

In general, the 2S2P1D model predicts well the linear viscoelastic properties of the unmodified binders. Furthermore, in the case of modified binder (PmB), the model fits the Cole-Cole diagram and the norms of complex modulus master curve. However, the 2S2P1D model only fits the black diagram and phase angle master curve from low temperatures ( $-30^{\circ}\text{C}$ ) to medium temperatures ( $30^{\circ}\text{C}$ ). Beyond these temperature ranges, the model faltered due to Partial time tempperature superposition principle (PTTSP) of the bitumen. 2S2P1D model fittings of Cole-Cole, Black diagram, and master curves, together with values of  $a_T$  and WLF curves, based on test results for all bitumens of Campaign 2 are reported in Appendix B.

## 5. Campaign 2: DSR linear viscoelastic characterisation of binders in shear

Table 5.1 - a) 2S2P1D constants and b) WLF parameters of Campaign 2 bitumen

Bitumen	2S2P1D constants						
	<b>G<sub>00</sub></b> (MPa)	<b>G<sub>0</sub></b> (MPa)	<b>k</b>	<b>h</b>	<b>δ</b>	<b>τ<sub>0</sub></b> (s)	<b>β</b>
B5070-1	0	1055	0.24	0.59	5.0	8.0E-04	330
B5070-2	0	970	0.24	0.59	5.5	8.0E-04	300
B5070-3	0	1050	0.24	0.60	5.0	8.0E-04	300
B3550-1	0	940	0.25	0.60	3.4	2.2E-03	90
B3550-2	0	950	0.26	0.60	3.4	2.2E-03	90
B3550-3	0	890	0.25	0.60	3.2	2.1E-03	90
PmB	5.0E-05	1300	0.22	0.53	4.5	1.5E-03	1100

a)

Bitumen	WLF parameters			MNE
	<b>T<sub>ref</sub></b> (°C)	<b>C<sub>1</sub></b> (-)	<b>C<sub>2</sub></b> (°C)	
B5070-1	10	23.11	149.56	3.89
B5070-2	10	22.61	140.17	4.11
B5070-3	10	24.10	151.65	3.69
B3550-1	10	20.37	132.54	3.48
B3550-2	10	20.20	131.71	3.72
B3550-3	10	18.93	124.42	3.45
PmB	10	25.94	169.68	2.41

b)

### 5.3.1 Horizontal shift factors

The deviation of the shift factors  $a_T$  at  $-30^\circ\text{C}$  from the WLF curve (Figures 5.3d) has been said to occur near the glass transition temperatures of the binder (see section 2.3). Furthermore, the Kaelble equation has been recommended to be utilised for fitting of shift factors at temperatures

## 5. Campaign 2: DSR linear viscoelastic characterisation of binders in shear

below glass transition temperatures. Therefore, without changing the 2S2P1D constants, the WLF equation were replaced with the modified Kaelble equation.

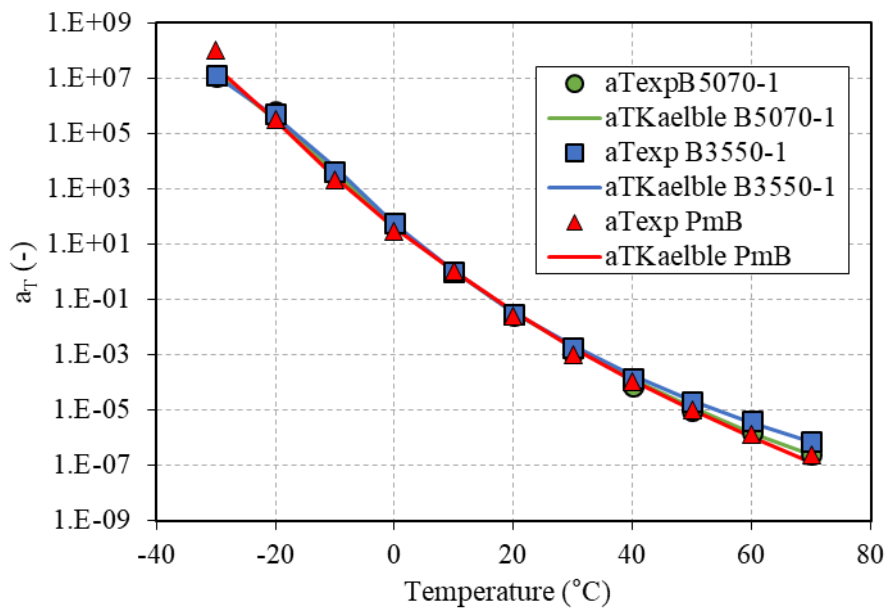


Figure 5.5 – Kaelble fitted shift factors  $a_T$  of all tested bitumens at  $T_{ref} = 10^\circ\text{C}$

The modified Kaelble equation accurately approximated the shift factors of the unmodified bitumens, as depicted in Figure 5.5. In Table 5.3, all modified Kaelble parameter values are enumerated. In comparison to the values derived from the WLF equation for unmodified binders, as presented in Table 5.1b, the modified Kaelble predictions exhibit a notably higher level of accuracy, as indicated by lower mean normalised error (MNE) values (Table 5.2). The MNE is related to the overall discrepancy between measured and predicted data. Based on the plot shown in Figure 5.4d, it can be concluded that the WLF equation effectively fits the shift factors of PmB. Conversely, the modified Kaelble model had difficulties in accurately fitting the shift factors of PmB. This is a consequence of the increased complexity of the rheological response following oxidation and increased structuration. A summary of the accuracy comparison of both shift factor fitting equations on the three tested bitumen is shown in the chart below as Figure 5.6

## 5. Campaign 2: DSR linear viscoelastic characterisation of binders in shear

Table 5.2 – The Kaelble constants at  $T_{ref} = 10^{\circ}\text{C}$

Bitumen	Modified Kaelble parameters				MNE
	$T_{ref}$ ( $^{\circ}\text{C}$ )	$T_d$ ( $^{\circ}\text{C}$ )	$C_1$ (-)	$C_2$ ( $^{\circ}\text{C}$ )	
B5070-1	10	-10	25.50	118.44	2.71
B3550-1	10	-5	19.95	90.83	1.46
PmB	10	-18	32.86	154.54	3.92

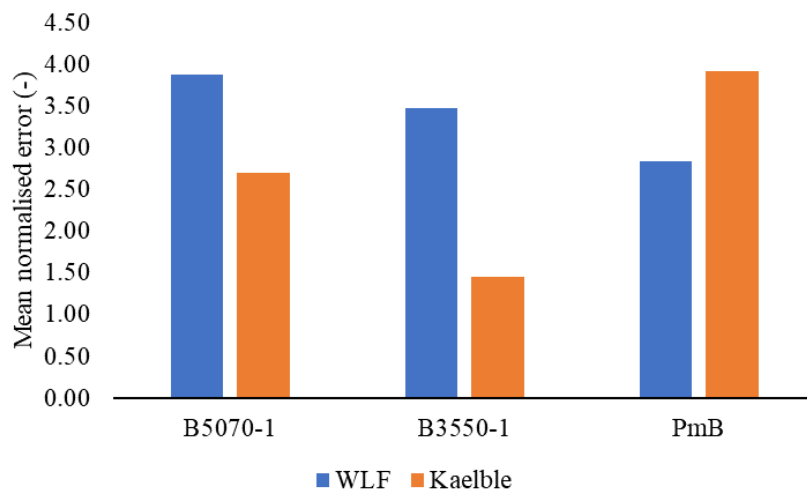


Figure 5.6 – Comparison of shift factor equation accuracies on test bitumens

### 5.3.2 Discontinuity factors

Discontinuities have been observed in the Cole-Cole diagrams of all bitumen at the low temperature regions. These changes are not due to the loss of TTSP. As shown in Figure 5.3c, the TTSP has been validated. This clearly seen due to the linearly scaled axes of the Cole-Cole plot, which magnifies the high-modulus component of the data. At a reference temperature of  $-0^{\circ}\text{C}$ , a vertical adjustment of the affected isotherms to form a perfect Cole-Cole curve was also achieved. Similar to  $a_T$  representing the horizontal shift of isotherms on the master curve,  $b_T$  is the term for the discontinuities (Laukkanen et al., 2018; Yusoff, Chailleux, et al., 2011) and this is expressed in the form of Equations 5.2-5.4.

$$G^* = g(a_T \cdot \omega) \cdot b_T \quad (5.2)$$

5. Campaign 2: DSR linear viscoelastic characterisation of binders in shear

$$G^* = Re(G^*)(\omega a_T) + i Im(G^*)(\omega a_T) \tag{5.3}$$

$$G^* = [Re(G^*) + i Im(G^*)]b_T \tag{5.4}$$

Although these discontinuities are small in magnitude and close to unity, as shown in Table 5.3, this can be seen to affect only the modulus axis (Yusoff, Chailleux, et al., 2011).

Table 5.3 - Discontinuity factors  $b_T$  of DSR complex modulus test results for bitumen of Campaign 2 at low temperatures ( $T_{ref} = -10^\circ\text{C}$ )

Bitumen	Shift factors $b_T$ (-)			
	0°C	-10°C	-20°C	-30°C
B5070-1	1.000	1.000	0.955	0.920
B3350-1	1.000	0.980	0.900	0.870
PmB	1.000	1.000	0.950	0.910

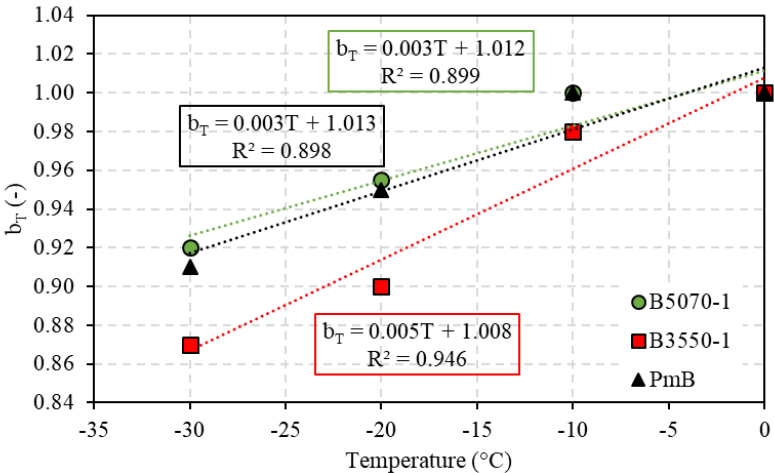


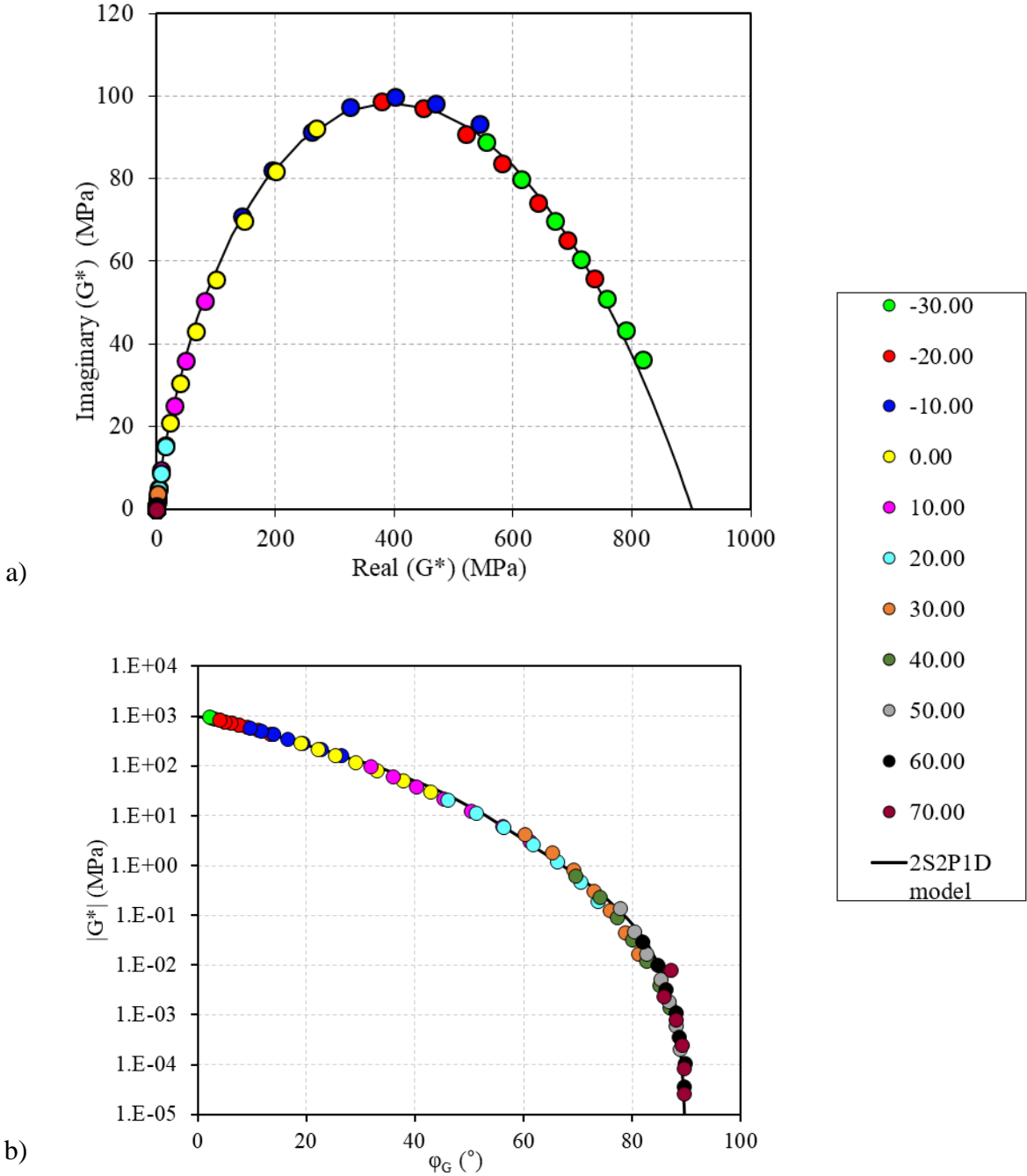
Figure 5.7 – Graph of discontinuity factors  $b_T$  versus temperatures

Figure 5.7 shows the plots of bitumen vertical shift factors against temperatures. Discontinuity factors for all tested bitumen correlates linearly with the respective test temperatures. Moreover, a similar pattern can be observed in the case of bitumen B5070-1 and PmB. This suggests that the behaviour remains unaffected by the bitumen modification. There is a general reduction of the discontinuity factors  $b_T$  with a reduction in temperature. This is contrary to the horizontal shift factors  $a_T$  which increases with a reduction in temperature.

## 5. Campaign 2: DSR linear viscoelastic characterisation of binders in shear

### 5.3.3 Influence of discontinuities on the rheological properties of bitumen

In the light of the previous discontinuities, the complex shear modulus tests results were recalculated and plotted. For the purpose of brevity, only the results of bitumen B3550-1 are fully displayed in Figure 5.8. The 2S2P1D recalibrated complex modulus test results in Cole-Cole plot, Black diagram, master curves of  $|G^*|$  and  $\varphi$  as well as the shift factors  $a_T$  are presented. For other bitumens, please refer to appendix B.



5. Campaign 2: DSR linear viscoelastic characterisation of binders in shear

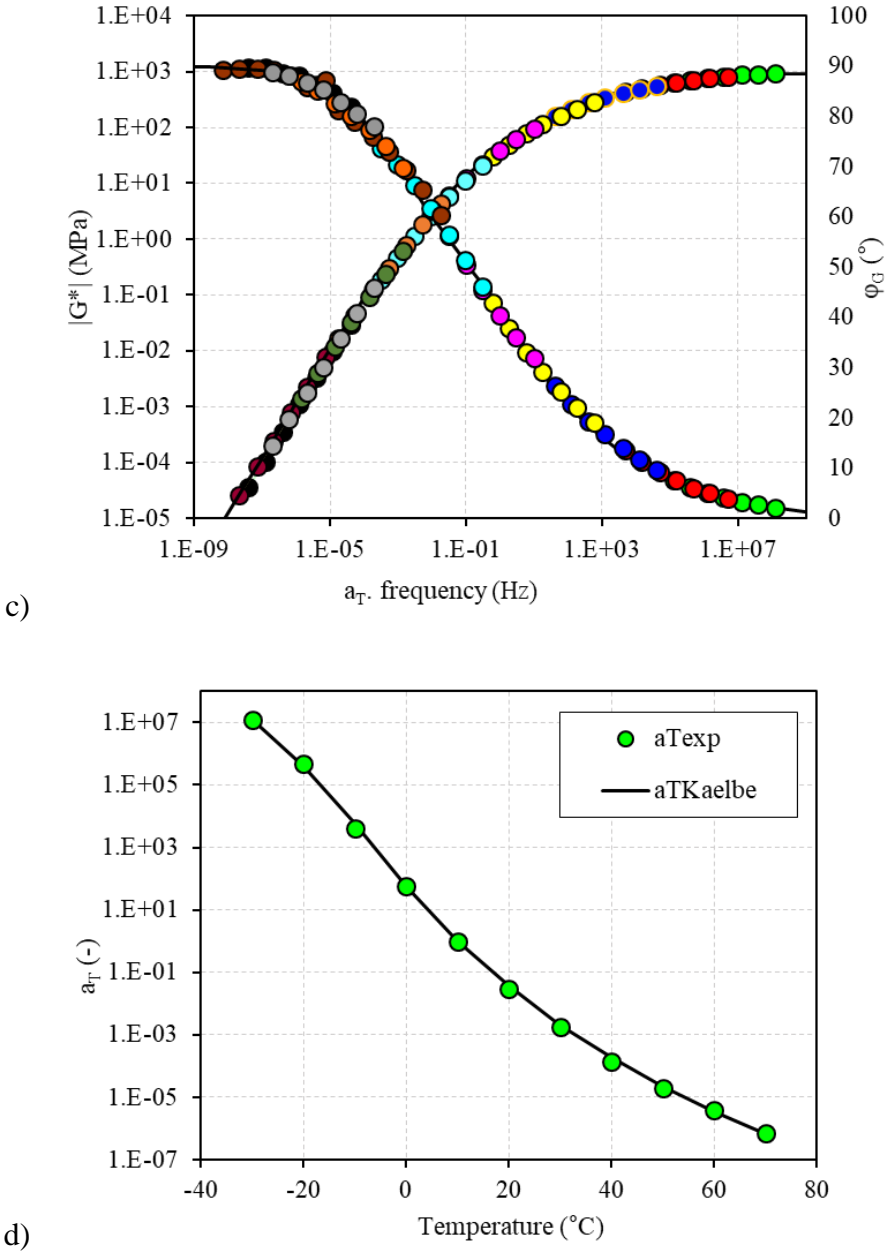


Figure 5.8 – Refined 2S2PID complex modulus test results for vertically shifted bitumen B3550-1: a) Cole-Cole plot; b) Black diagram; c) master curves of norms of complex modulus and phase angle; d) temperature shift factors at  $T_{ref} = 10^\circ C$

The Time-Temperature Superposition Principle (TTSP) was validated for unmodified bitumen and the PTTSP was validated for modified bitumen from a general point of view. Figure 5.8c illustrates an example of master curves for norms of complex shear modulus and phase angle at  $10^\circ C$  reference temperature.

## 5. Campaign 2: DSR linear viscoelastic characterisation of binders in shear

Table 5.4 - a) Recalibrated 2S2P1D constants and b) shift factor model parameters of the first trials of Campaign 2 bitumen

Bitumen	2S2P1D constants						
	$G_{00}$ (MPa)	$G_0$ (MPa)	$k$	$h$	$\delta$	$\tau_0$ (s)	$\beta$
B5070-1	0	1010	0.24	0.59	4.50	8.0E-04	330
B3550-1	0	902	0.25	0.60	3.00	2.0E-03	90
PmB	5.0E-05	1240	0.22	0.53	4.20	1.5E-03	1100

a)

Bitumen	Shift factor model parameters				MNE
	$T_{ref}$ (°C)	$T_d$ (°C)	$C_1$ (-)	$C_2$ (°C)	
B5070-1	10	-10	25.50	118.44	2.71
B3550-1	10	-5	19.99	90.38	1.59
PmB	10	-	25.94	169.68	1.81

b)

The 2S2P1D calibration constants are listed in Table 5.4a. The glassy shear moduli comprised between 902 and 1240 MPa. The unmodified bitumen also exhibited static moduli of 0 MPa which tended to be purely viscous at high temperature and low frequency. PmB also exhibited a static modulus of 5.0E-5 MPa as a result of the exhibited elastic skeleton by the network of polymers (François Olard & Di Benedetto, 2003; Orozco, 2020). Furthermore, some 2S2P1D constants were quite different after proper fitting by the consideration of discontinuities in the Cole-Cole diagrams. As an example,  $G_0$ , and  $\delta$  values showed a decrease across all the three bitumen. However, the values of  $k$ ,  $\beta$ , and  $h$  remained constant for the three-bitumen under consideration. Furthermore, a reduction of 5%-6% in the glassy moduli of the three binders were observed.

Overall, the fitting of the 2S2P1D model was excellent for pure bitumen, with less than 10% error on bitumen B5070 over 10 decades of reduced frequency (from  $10^{-5}$  to  $10^8$  Hz for  $T_{ref} = 10^\circ\text{C}$ ). However, the model failed to predict the phase angle of PmB at low equivalent



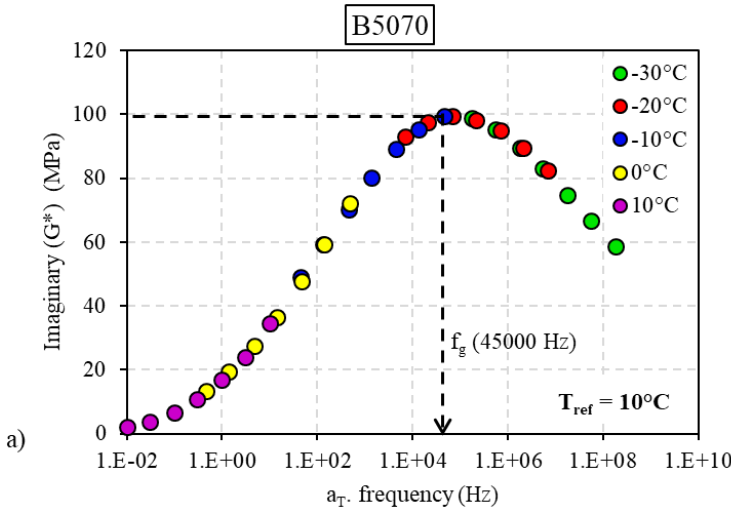
5. Campaign 2: DSR linear viscoelastic characterisation of binders in shear

frequencies, as illustrated in the master curves of the norm of complex shear modulus and phase angle in Figure B6(d) (see appendix). The loss of TTSP at low equivalent frequencies is also influenced by polymer chain network.

5.4 Glass transition temperatures

Bitumen is characterised by its low temperature property known as the glass transition temperature ( $T_g$ ). The thermal transition known as  $T_g$  is closely linked to alterations in the mechanical characteristics of the bitumen. The observed change in the mechanical properties of the material (bitumen) can potentially be explained by the use of free volume theories (Turnbull & Cohen, 1961), kinetic theories, and thermodynamic theories. From a rheological point of view, in literatures,  $T_g$  is identified as the temperature that corresponds to the highest imaginary modulus at 7.8 Hz frequency. However, (François Olard et al., 2003) proposed to extend this definition to any frequency, identified as the glass transition frequency  $f_g$ . The phenomenon of the peak loss moduli shifting towards higher temperatures as the frequency increases has been seen to be consistent with the WLF equation (Equation 2.31).

Figure 5.9 shows the plots of the imaginary complex shear modulus against reduced frequency, indicating the glass transition frequencies of the considered bitumen. These values for each bitumen are listed out in Table 5.5.



5. Campaign 2: DSR linear viscoelastic characterisation of binders in shear

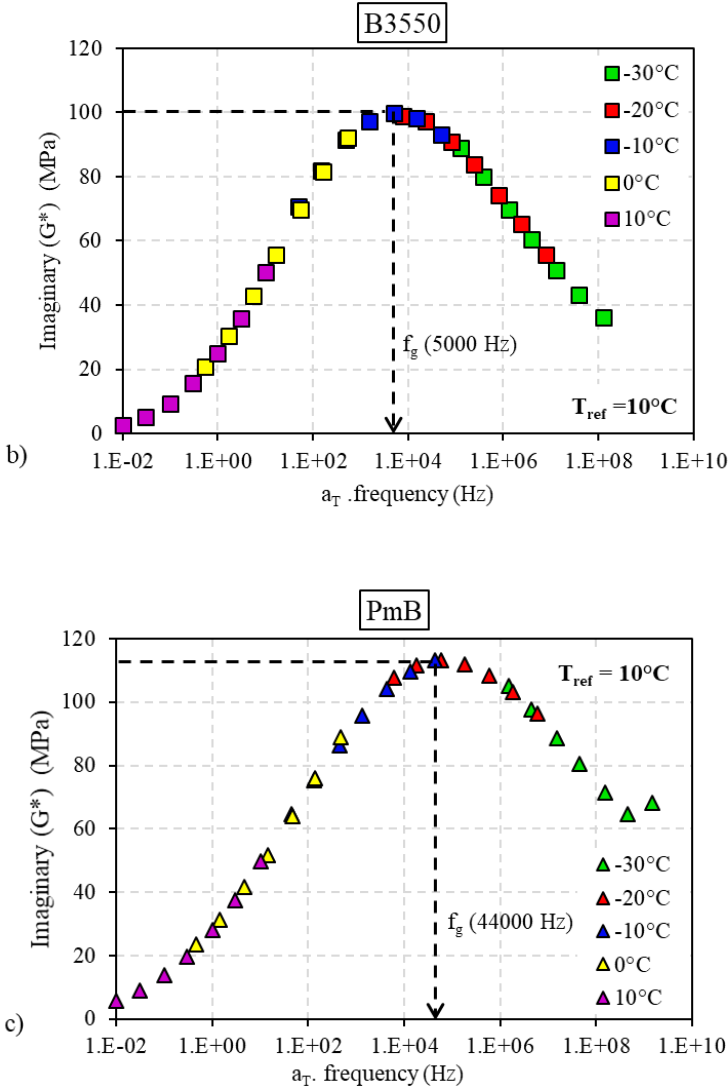


Figure 5.9 – Master curves of imaginary shear complex modulus of a) B5070 b) B3550; c) PmB bitumen at  $T_{ref} = 10^\circ\text{C}$

Table 5.5 – Glass transition temperatures and frequencies of test bitumen

Bitumen	$T_g$ (7.8Hz) ( $^\circ\text{C}$ )	$f_g$ ( $T_{ref} = 10^\circ\text{C}$ ) (Hz)
B5070	-4.5	45000
B3550	-5.3	5000
PmB	-5.0	44000

The glass transition temperatures identified for the unmodified bitumen were observed to be higher than the values stated in the literatures. This can be attributed to the variations in bitumen origins. However, the glass transition frequency values converged with literatures. The glass

## 5. Campaign 2: DSR linear viscoelastic characterisation of binders in shear

---

transition frequencies of both B5070 and PmB are identical. The increment in glass transition temperatures of bitumen, which is the effect of polymer modification is however not seen.

### 5.5 Conclusions of Campaign 2

The linear viscoelastic properties of two unmodified (B3550, B5070) and one polymer-modified (PmB) bitumens were investigated.

- Concerning the LVE characterization of bitumens, it is evident that the torque measured at low temperatures with an 8 mm parallel plate is underestimated. Nonetheless, it is essential to conduct low-temperature measurements with a 4-mm parallel plate. In addition, deactivating the AGC function of the MCR 702 enables measurements at low temperatures.
- With a maximal modulus deviation of 5.4% and a phase angle difference of  $0.8^\circ$  between the three test trials, the measurements proved to be highly repeatable after the normalisation. DSR results provided accurate measurements of the norm of complex modulus over 9 decades from ( $5 \times 10^{-6} \text{ MPa}$  to  $10^3 \text{ MPa}$ ) and phase angles from  $4^\circ$  to  $90^\circ$ .
- The TTSP and PTTSP were applicable to both unmodified and polymer-modified bitumen respectively. However, below  $-20^\circ\text{C}$ , the WLF equation does not fit the unmodified bitumen shift factors. In contrast, the modified Kaelble equation modelled the shift factors of the unmodified bitumen. Furthermore, there was no observable improvement with the PmB shift factor prediction with the modified Kaelble equation. The 2S2P1D model was utilised to simulate the LVE behaviour of each bitumen sample. Overall, the model was excellent, but the phase angle of PmB at high equivalent frequency lacked precision. At low equivalent frequency, the PmB exhibited an asymptotic static modulus, whereas pure bitumens tended to be viscous.
- The glassy modulus  $G_0$  values of binders varied from  $1.05 \text{ GPa}$  to  $1.3 \text{ GPa}$ .
- The Cole-Cole plot of binders exhibit vertical variations below the glass transition temperatures. The magnitudes of the linear correlation between the discontinuity factors  $b_T$  and the test temperatures are close to unity. In addition, the discontinuity factors decrease as the temperature decreased. The shift of the Cole-Cole curves at low temperature to form a perfect curve induces a decrease in the 2S2P1D constants  $G_0$  and  $\delta$ .

## 5. Campaign 2: DSR linear viscoelastic characterisation of binders in shear

---

- The glass transition temperatures and frequencies of binders were identified. The frequencies are however identical to those reported in the literatures. Furthermore, the effect of polymer modification of bitumen on glass transition temperature was not observed.

## 6.Campaign 3: Dynamic Shear Rheometer Determination of Axial $E^*$ and Shear $G^*$ Complex Moduli for Binder

---

### **6. Campaign 3: Dynamic Shear Rheometer Determination of Axial $E^*$ and Shear $G^*$ Complex Moduli for Binder**

#### **6.1 Objectives**

In order to evaluate and characterise binders in terms of performance-related properties, one of the most common tests performed on bitumen is the complex modulus test. Researchers such as (Büchner et al., 2020; Gražulytė et al., 2021) among others have succeeded in the rheological characterisation of bitumen, using the Dynamic Shear Rheometer (DSR) and a similar feat was achieved by (Babadopulos, 2017; Delaporte et al., 2009) using an Annular Shear Rheometer (ASR) developed at the ENTPE. However, the aforementioned tests are expressed in terms of the shear complex modulus and phase angle of the bitumen meanwhile, the mechanistic-empirical pavement model inputs are functions of complex modulus  $E^*$  of bitumen which are derived by approximation from the shear complex modulus  $G^*$  by considering a constant real Poisson's ratio equal to 0.5. It is therefore evidently important to develop an accurate experimental method to allow for the direct determination of binder complex modulus  $E^*$ . In recent years, some attempts have been made to determine the complex modulus  $E^*$  of bitumen directly at low temperatures for practical reasons (Hervé Di Benedetto et al., 2007). However, the measured moduli lacked a complementing shear complex modulus measurement ( $E^*$  and  $G^*$  are not measured on the same sample).

The first objective of this experimental campaign was to rheologically determine the best specimen dimension that allows the proper characterisation of the same bitumen sample in tension compression and shear oscillation within the linear viscoelastic domain using a DSR equipped with a linear motor. In the second objective, an attempt was made to fit the axial and shear complex modulus test results to the 2S2P1D rheological model. This would also allow the estimation of bitumen Poisson's ratio.

#### **6.2 Axial strain amplitude sweep test**

Figure 6.1 illustrates the results of axial strain amplitude sweep tests with the axial complex modulus  $|E^*|$  expressed as a function of incremental axial strain amplitude  $\varepsilon$ . Different geometries (PP4 and PP8) were used depending on the temperature of the tests.

## 6.Campaign 3: Dynamic Shear Rheometer Determination of Axial $E^*$ and Shear $G^*$ Complex Moduli for Binder

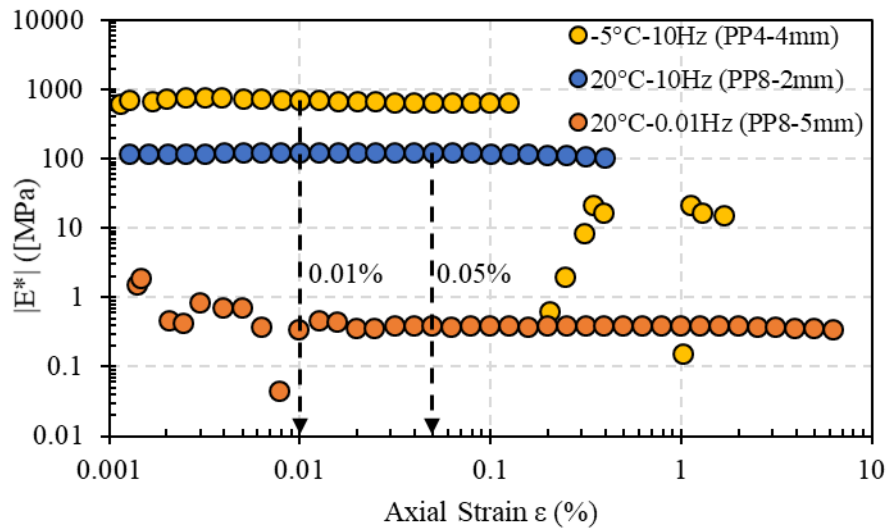


Figure 6.1 - 4 mm and 8 mm parallel plate axial strain amplitude sweep test

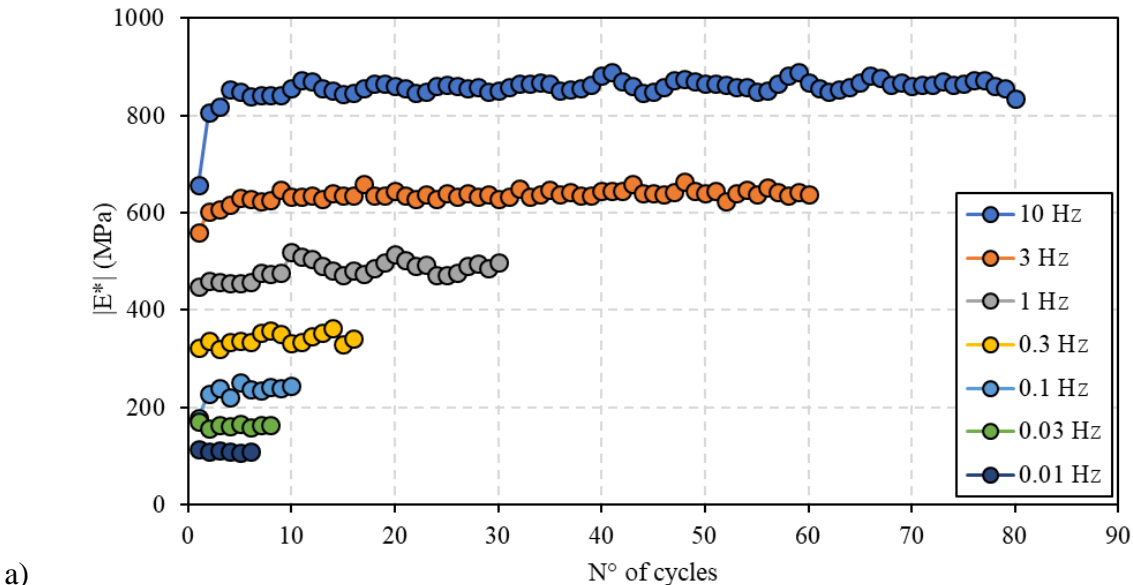
Failure of the test sample at  $-5^{\circ}\text{C}$  was observed at a strain 0.12%, for a norm of complex modulus of 643 MPa (Figure 6.1). The abrupt failure of the sample at  $-5^{\circ}\text{C}$  can be attributed to the development of cracks within the specimen due to its glassy behaviour. Tests at higher temperatures were stopped when higher values of strain amplitude were reached. Based on the results obtained, two values of axial strain amplitude were selected for frequency sweep tests, both well within the linear viscoelastic domain of the material. For tests at temperature equal or higher than  $20^{\circ}\text{C}$  (with PP8 geometry), 0.05% strain amplitude was chosen. For tests at temperature lower than  $20^{\circ}\text{C}$  (with PP4 geometry), 0.01% strain amplitude was chosen. Noises were identified in the moduli measured between strain levels 0.001% and 0.01% at  $20^{\circ}\text{C}/0.01\text{Hz}$ . These noises generated are attributed to instrument limits. Strain levels were however selected taking note of these irregularities. The axial strain amplitude limit of bitumen varies from 0.1% (1000  $\mu\text{m}/\text{m}$ ) to 7%.

### 6.3 Complex modulus test analysis

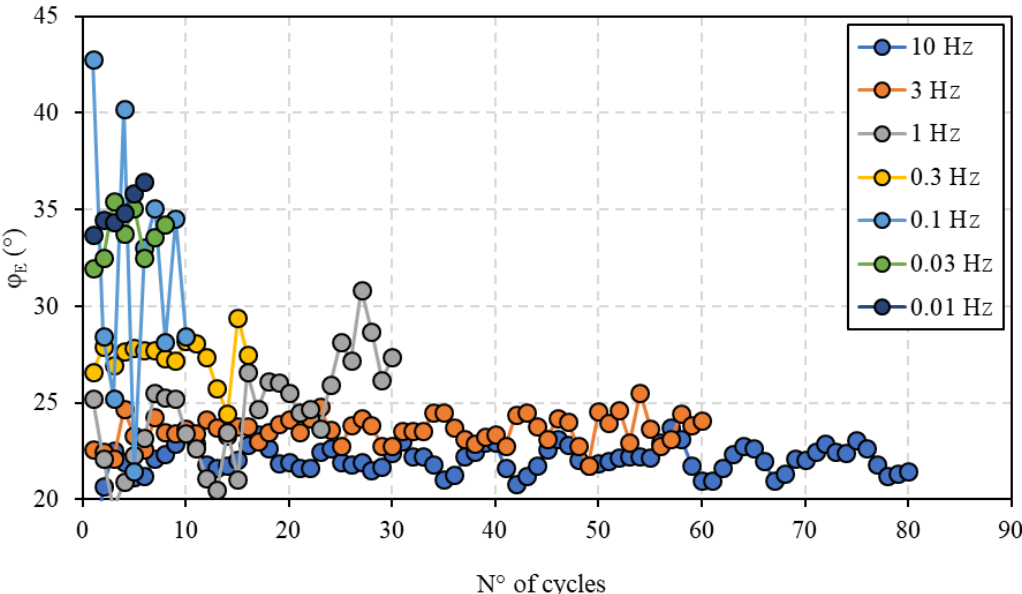
Figure 6.2 illustrates the cycle acquisitions utilised to determine the norm of the axial complex modulus and corresponding phase angles. As described earlier in the previous campaign (see section 5.2) the test time was kept short by recording few cycles at low frequencies. Similar number of acquisition cycles were also chosen while taking note of cyclic effects. Stable axial complex modulus signals are observed. The maximum variation of 13 MPa is recorded at frequency 1 Hz. This however is inferior of the 5% confidence interval.

### 6.Campaign 3: Dynamic Shear Rheometer Determination of Axial $E^*$ and Shear $G^*$ Complex Moduli for Binder

Figure 6.2b illustrates the phase angle signals as function of the numbers of cycles tested. It was equally observed that the variations of the phase angles at frequencies 0.1, 0.3 and 1 Hz are superior of the 5% confidence level. This is to a maximum excess of  $10^\circ$  at 0.1 Hz as indicated in Figure 6.2.



a)



b)

## 6.Campaign 3: Dynamic Shear Rheometer Determination of Axial $E^*$ and Shear $G^*$ Complex Moduli for Binder

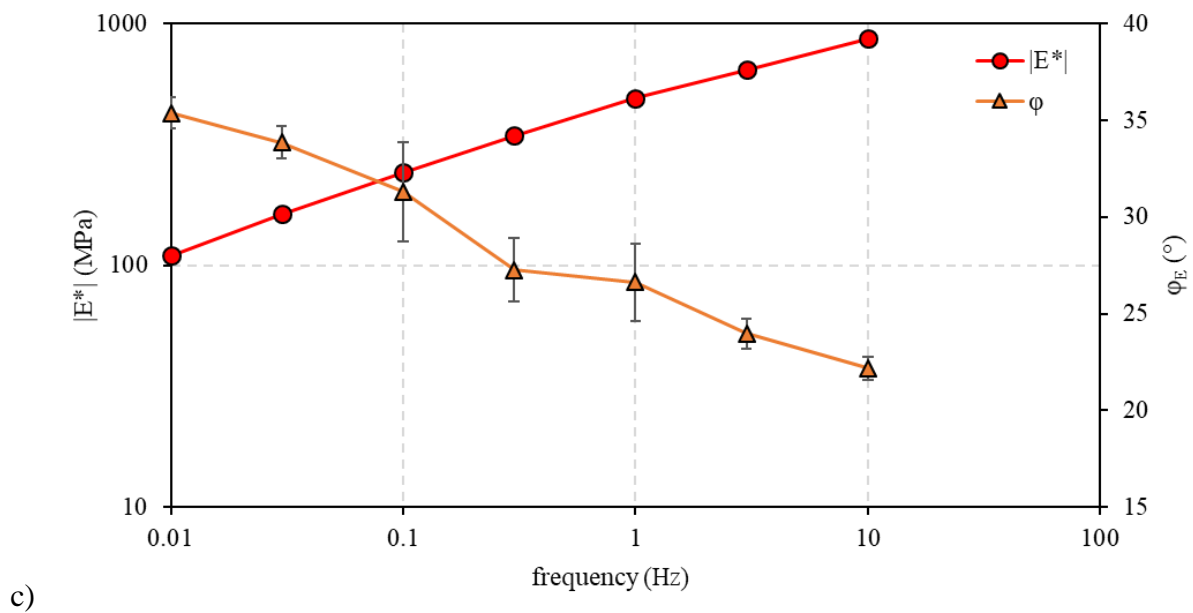


Figure 6.2 – B5070 5mm height axial complex modulus  $E^*$  test results at  $-5^\circ\text{C}/0.01\%$ . a) Norm of complex modulus; and b) phase angle in function of number of cycles; c) Complex modulus  $E^*$  and phase angle  $\phi_E$  average values with respective standard deviations.

### 6.3.1 Influence of aspect ratios on the rheological response of bitumen

Figure 6.2c illustrates the average values of norms of axial complex modulus and corresponding phase angles as a function of test frequencies. It is to be noted that these results were achieved under strain-controlled test mode.

As a first approximation, an attempt is made to identify inconsistencies in the rheological measurement using the Black diagram. The Black diagrams of axial  $E^*$  and shear  $G^*$  complex modulus obtained with a 4 mm parallel plates (temperatures from  $-5^\circ\text{C}$  to  $10^\circ\text{C}$ ) and different sample thicknesses (1.75 to 5 mm) are shown in Figure 6.3 respectively. Bitumen aspect ratios are denoted as AR. This is given as the ratio of the test specimen radius to the height. Tests at 3 mm ( $\text{AR} = 0.67$ ) and 1.75 mm ( $\text{AR} = 1.14$ ) heights were carried out only at  $0^\circ$  and  $10^\circ\text{C}$ . At these tests heights it was observed that the DSR experienced difficulty in taking axial complex modulus  $E^*$  measurements due to an increase in test time. This was associated with the high aspect ratios of the test specimen.

As seen in the Figure 6.3, the axial complex modulus  $E^*$  values obtained at a thickness of 1.75 mm exhibit divergence from all other curves. However, the shear complex modulus  $G^*$  curves exhibited unique characteristics at all tested heights.



### 6.Campaign 3: Dynamic Shear Rheometer Determination of Axial $E^*$ and Shear $G^*$ Complex Moduli for Binder

Considering the axial complex modulus  $E^*$  curves, the maximum stiffness at 3 mm is limited to 599 MPa at 0°C. This modulus is however, identical to that measured at 4 mm and 5 mm sample heights although with a higher phase angle difference of 4°. Therefore, the divergence of the curves is mainly associated with the increased measured phase angle values  $\phi_E$ . However, axial complex modulus  $E^*$  obtained at both 4 mm and 5 mm thickness approaches a maximum, with modulus of 954MPa observed for 4 mm sample thickness.

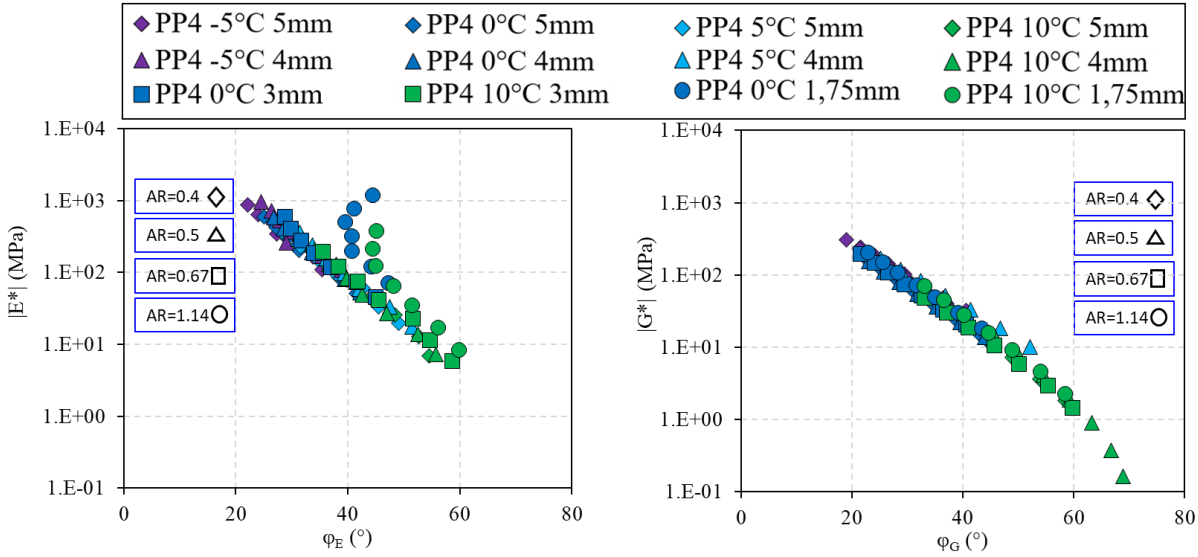


Figure 6.3 - Black diagrams of B5070 bitumen axial (left,  $E^*$ ) and shear (right,  $G^*$ ) complex modulus, obtained with 4 mm parallel plate at different aspect ratios

Figure 6.4 shows Black diagrams of axial and shear complex modulus obtained with 8 mm parallel plates (temperatures from 0°C to 30°C) and different sample aspect ratios (thicknesses 2 to 5 mm). At low temperatures (0°C and 10°C), axial complex modulus  $E^*$  isotherms diverge similarly to what is observed in Figure 6.3. Typically, these divergence as seen and stated earlier was attributed to a higher phase angle measured. It was observed that at 0°C, the  $E^*$  measurements peaked at 1GPa at all aspect ratios. However, the phase angles increased with an increase in aspect ratio. Shear complex modulus Black curves at all aspect ratios again superimpose with very minute variations as seen with 4 mm plate measurements. Overall, a higher scatter is observed for  $E^*$  data obtained with PP8 geometry than both for  $G^*$  data obtained with PP8 geometry and  $E^*$  data obtained with PP4 geometry. This can be attributed to insufficient slenderness ratio of the sample, leading to non-negligible “oedometric effect”.

### 6.Campaign 3: Dynamic Shear Rheometer Determination of Axial $E^*$ and Shear $G^*$ Complex Moduli for Binder

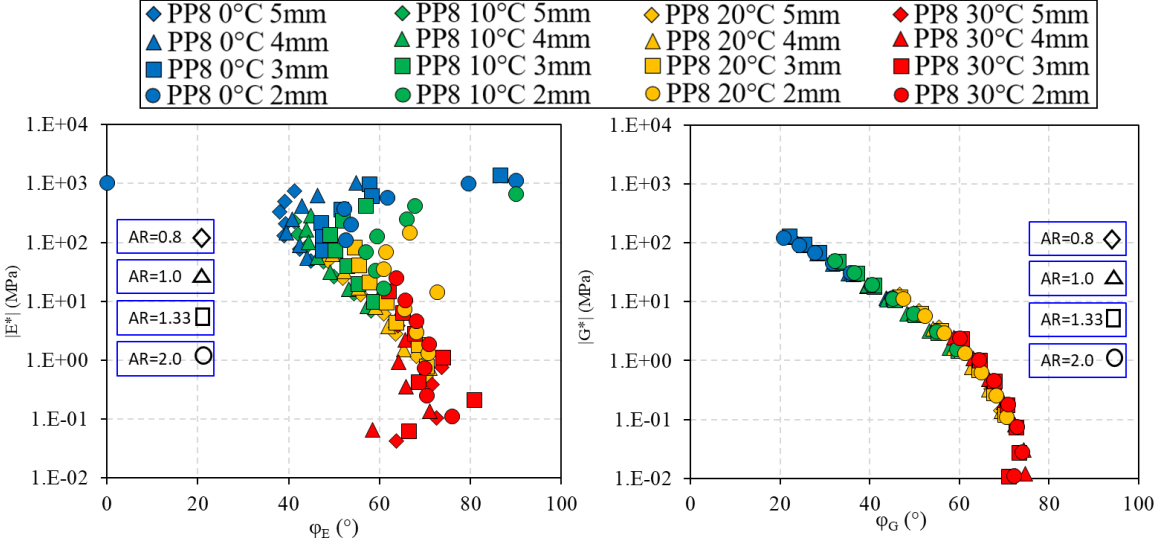


Figure 6.4 - Black diagrams of B5070 bitumen axial (left,  $E^*$ ) and shear (right,  $G^*$ ) complex modulus measured with 8 mm parallel plate at different aspect ratios.

It is evident from the plots of axial complex modulus diagrams (Figures 6.3 and 6.4) that the accuracy of modulus measurements increases with the height of the test specimen.

#### 6.3.2 Influence of plate size on the rheological response of bitumen measured in tension-compression

Axial  $E^*$  complex modulus and phase angle  $\phi_E$  measurements at the lowest aspect ratios (0.4 and 0.8) were isolated and plotted in function of frequencies as shown in the Figure 6.5. As described earlier in the previous Campaign (Chapter 5), the isothermal curves assist in the selection of the ideal plates size required to take measurements for a good viscoelastic characterisation. It is seen in Figure 6.5 that the  $|E^*|$  isotherms measured with PP4 and PP8 plates overlap at 0 and 10°C. Variations between both isotherms are seen to occur at high frequency ranges (1-10 Hz). Similar occurrence was seen at the same temperature (10°C) with the share complex modulus measurement in Campaign 2.

Considering the phase angles of the respective isotherms, measurements at aspect ratio 0.8 is observed to increase (diverge) from frequency 0.1 to 10 Hz. These divergences are also seen in the Black diagram shown in the Figure 6.6. Isotherm at 30°C was also seen to falter at low frequencies (0.1-0.01 Hz). This can be attributed to a reduced bitumen stiffness. Measurements with a larger plate (25 mm) was however impossible due to the flow of bitumen at this temperature. Phase angle measurements were also seen to increase from 0.3 Hz to 0.01 Hz at -5°C. Therefore, to allow for a proper viscoelastic characterisation of B5070 bitumen, the

### 6.Campaign 3: Dynamic Shear Rheometer Determination of Axial $E^*$ and Shear $G^*$ Complex Moduli for Binder

defective measurements were eliminated in the subsequent analysis. It is therefore appropriate to recommend a specimen height of 5 mm for this campaign.

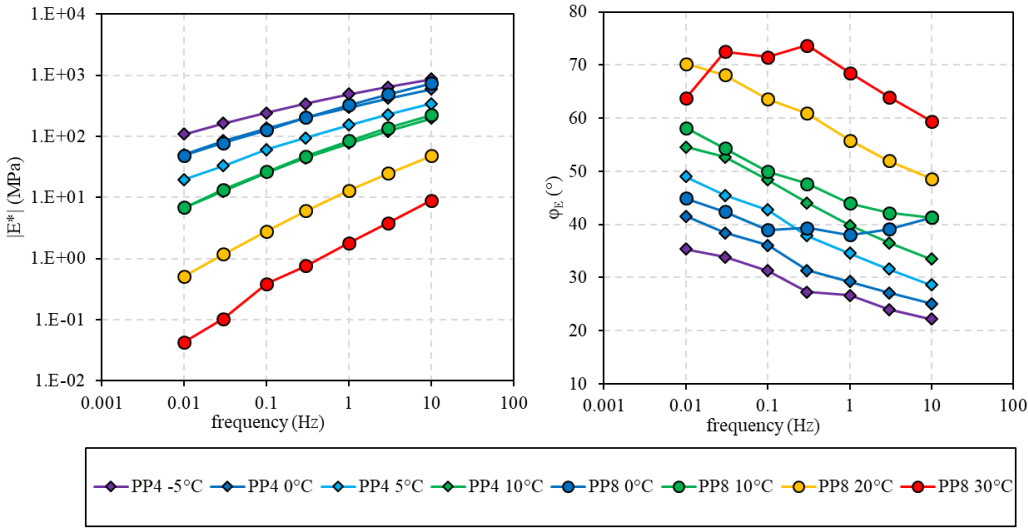


Figure 6.5 – Isothermal curves of B5070 bitumen axial complex modulus (left,  $E^*$ ) and phase angle (right,  $\phi_E$ ) at 5 mm sample height ( $AR=0.5$  and  $0.8$ ).

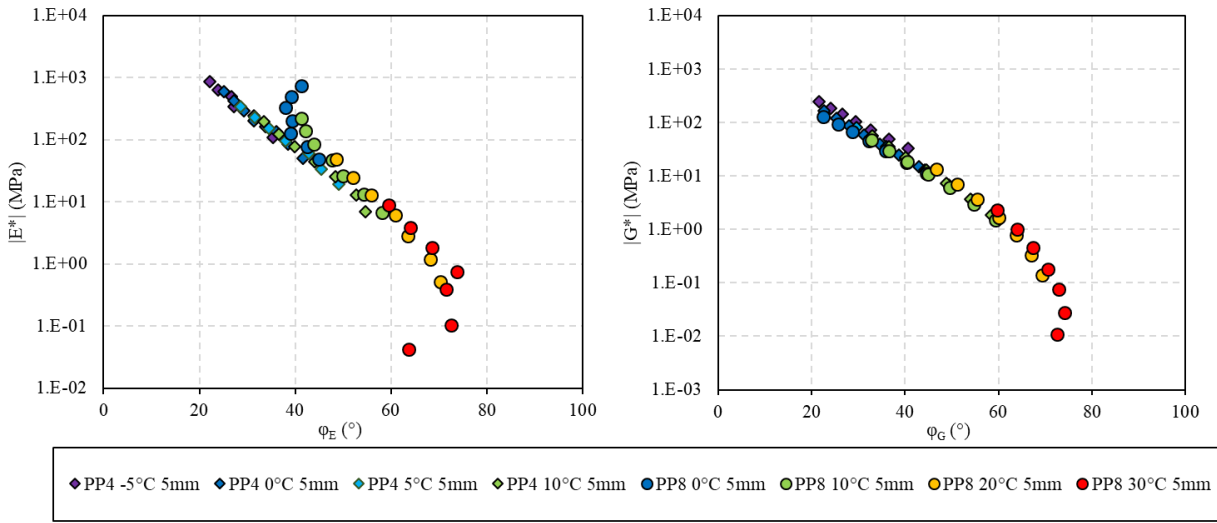


Figure 6.6 - Black diagram of B5070 bitumen axial (left,  $E^*$ ) and shear (right,  $G^*$ ) complex modulus at 5 mm sample height.

Following the above specimen height selection, Black diagrams of axial and shear complex moduli  $E^*$  and  $G^*$  (respectively) obtained at all temperatures (using both 4 mm and 8 mm spindle geometries) with a 5-mm sample thickness are plotted in Figure 6.6. As earlier

## 6.Campaign 3: Dynamic Shear Rheometer Determination of Axial $E^*$ and Shear $G^*$ Complex Moduli for Binder

mentioned, discrepancies are observed for  $E^*$  results at  $0^\circ\text{C}$  and  $10^\circ\text{C}$  obtained with the 8 mm geometry.

### 6.4 DSR Peltier assembly and axial motor assembly measured shear complex moduli

In order to conduct a comparison between the  $G^*$  measurements acquired using the DSR Peltier system at a specimen height of 1.75 mm and the data obtained at a height of 5 mm using the DSR axial motor assembly, the normalised Cole-Cole and Black diagrams of the  $G^*$  measurements are graphically represented in Figures 6.7.

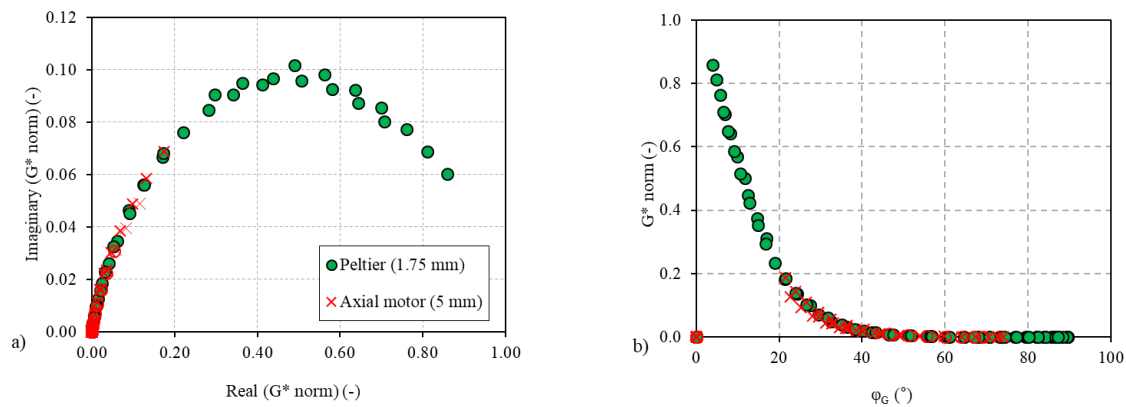


Figure 6.7 – Experimental measurements of B5070 bitumen normalised complex modulus  
a)  $G^*_{norm}$  in Cole-Cole plane, b)  $G^*_{norm}$  in Black space obtained using the two DSR assemblies at 1.75 mm and 5 mm specimen heights

The plots were expressed in both Cole-Cole and Black space to aid the visualisation of the data points at all test temperatures. Furthermore, the curves were normalised to eliminate the differences between  $G_{00}$  and  $G_0$  values. It was observed that the plots of both measuring devices overlapped quite well. This implies that a unique set of 2S2P1D model constants can be used to represent the linear viscoelastic behaviour of the bitumen measured in both devices.

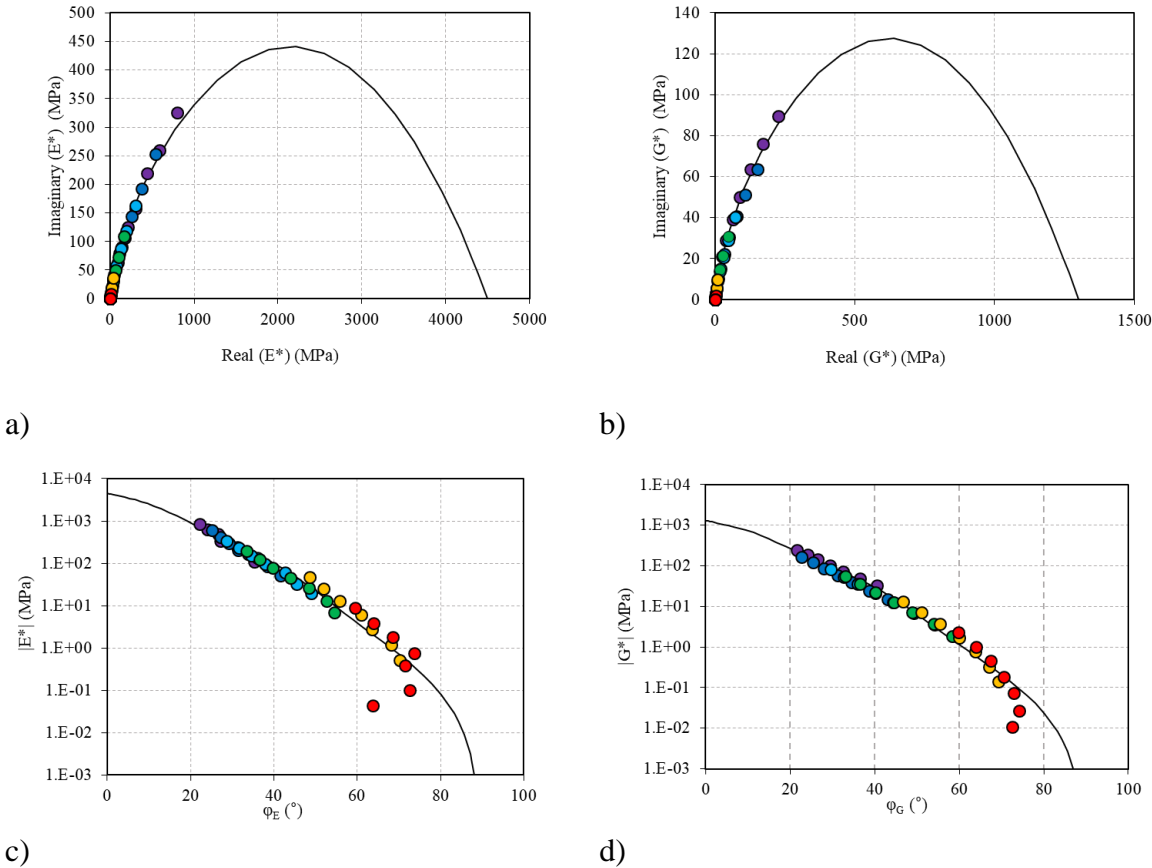
### 6.5 Rheological modelling of bitumen axial and shear complex modulus

Figure 6.8 shows the Cole-Cole plots (a-b), Black diagram (b-c), master curves of the norm and phase angle (e-f) and (g) plots of  $a_T$  versus the test temperatures of axial and shear complex moduli from tests on 5-mm thick specimens. The master curves were plotted at  $10^\circ\text{C}$  reference temperature using the calculated shift factors from WLF equation. The unique curves formed by the translation of the isothermal curves of norms and phase angles of axial and shear complex

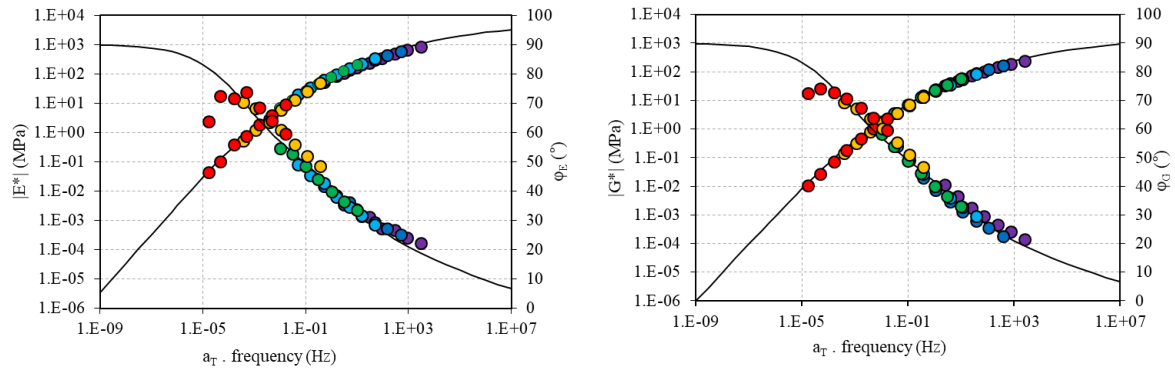
### 6.Campaign 3: Dynamic Shear Rheometer Determination of Axial $E^*$ and Shear $G^*$ Complex Moduli for Binder

modulus along the reduced frequency axis (Figures 6.8e-f) verifies the Time-Temperature Superposition Principle (TTSP) (François Olard et al., 2003). The WLF parameters  $C_1$  and  $C_2$  are reported in Table 6.1. The shift factors denoted as  $a_{TE}$  (axial) and  $a_{TG}$  (shear) are however found to be identical for both test modes.

Complex modulus experimental data in axial and shear test modes at 5 mm test gap were successfully fitted with 2S2P1D over the whole range of test temperatures and frequencies as shown in Figure 6.8. Although,  $E^*$  values at low temperatures were not well represented by the 2S2P1D on the Cole-Cole curve. This could be explained to be a result of an increased phase angle  $\varphi_E$  measured. Again, using identical set of 2S2P1D parameters, successful simulations of complex modulus data were achieved for the two test modes.

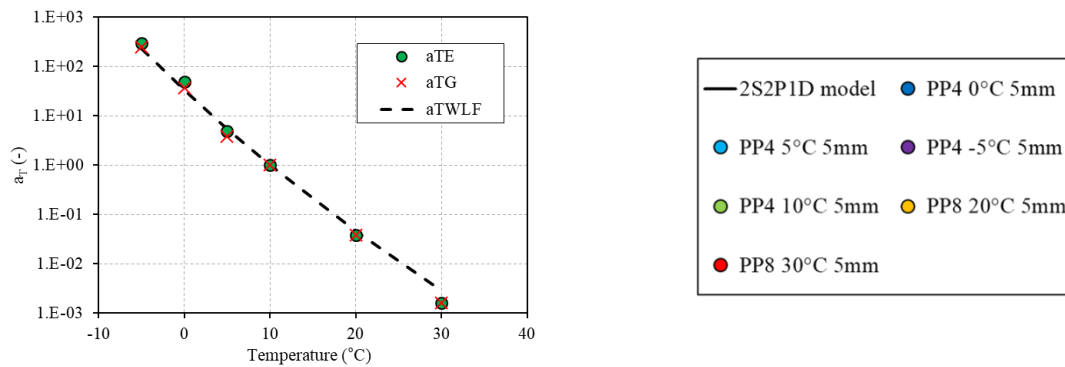


## 6.Campaign 3: Dynamic Shear Rheometer Determination of Axial $E^*$ and Shear $G^*$ Complex Moduli for Binder



e)

f)



g)

Figure 6.8 – 2S2P1D fitted B5070 bitumen axial complex modulus  $E^*$  and shear complex modulus  $G^*$  a-b) Cole-Cole curve; c-d) Black diagrams; e-f) master curves at  $T_{ref} = 10^\circ\text{C}$  and g) Experimental shift factors fitted with WLF equation at  $T_{ref} = 10^\circ\text{C}$ .

Table 6.1 - 2S2P1D and WLF parameters for tested binder at  $T_{ref} = 10^\circ\text{C}$

Binder	$E_{00}$ (MPa)	$E_0$ (MPa)	k	h	$\delta$	$\tau$ (s)	$\beta$	$C_1$ (-)	$C_2$ ( $^\circ\text{C}$ )
B5070	0	4500	0.24	0.59	5.00	0.0004	300	23	152
	$G_{00}$ (MPa)	$G_0$ (MPa)							
	0	1300	0.24	0.59	5.00	0.0004	300	23	151

The 2S2P1D parameters listed in Table 6.1 represents the characteristic viscoelastic evolution of the bitumen, therefore, it is expected that the viscoelastic behaviour does not change when loaded either in shear or tension-compression mode. The constants determined in shear testing mode are identical to those stated in Table 5.1 (see section 5.3) with the exception of  $\tau$ . The glassy modulus  $E_0$  value of 4500 MPa was found to be higher than 2000 MPa reported by

### 6.Campaign 3: Dynamic Shear Rheometer Determination of Axial $E^*$ and Shear $G^*$ Complex Moduli for Binder

(François Olard & Di Benedetto, 2003). Although, bitumen are considered elastic at low temperatures and the stiffness is considered to approach 5000 MPa (Anderson et al., 1994). However, the discrepancies between  $E_0$ ,  $E_{00}$  and  $G_0$ ,  $G_{00}$  can again be eliminated through the process of normalisation as depicted in Figure 6.9.

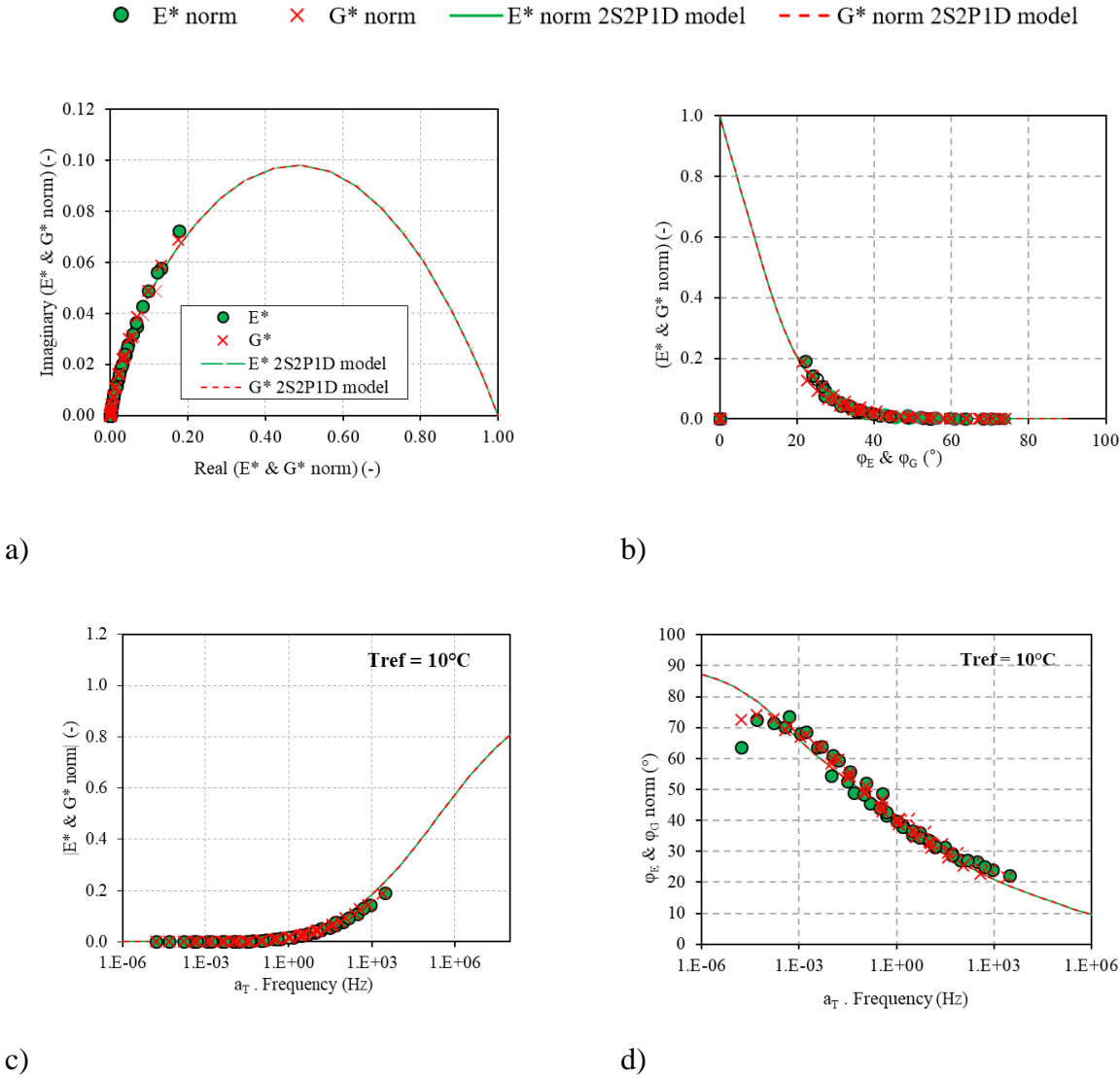


Figure 6.9 – Experimental results and fitted 2S2P1D curves of normalised complex modulus  
 a)  $E^*_{norm}$  and  $G^*_{norm}$  in Cole-Cole plane, b)  $E^*$  and  $G^*_{norm}$  in Black space, c)  $|E^*$  and  $G^*_{norm}|$  master curves at  $T_{ref} = 10^\circ C$ , d)  $\phi_E$  and  $\phi_{Gnorm}$  master curves at  $T_{ref} = 10^\circ C$

The normalised complex modulus in Cole-Cole plane, Black diagram, and master curves of norm and phase angle of complex modulus are shown in Figure 6.9. This normalised moduli are defined as

## 6.Campaign 3: Dynamic Shear Rheometer Determination of Axial $E^*$ and Shear $G^*$ Complex Moduli for Binder

---

$$G_{norm}^* = \frac{G^* - G_{00}}{G_0 - G_{00}} \quad (6.1)$$

$$E_{norm}^* = \frac{E^* - E_{00}}{E_0 - E_{00}} \quad (6.2)$$

Mangiafico et al. (2014) determined that the normalised curves of a mixture overlap with those of the corresponding binder. This is however expected to be applicable to bitumen tested in different modes (axial tension-compression or shear oscillation). All normalised curves of binders in both test modes (axial and shear) overlapped quite well across all tested temperatures and frequencies.

The 2S2P1D model has been effectively utilised to simulate the linear viscoelastic properties of bitumen in both shear and tension-compression test configurations. However, it is anticipated that the Poisson's ratio ( $\nu^*$ ) of bitumen can be computed by employing both the 2S2P1D model of  $E^*$  and  $G^*$ . Nevertheless, a notable issue arises when attempting to evaluate  $\nu^*$  using the shear and axial complex modulus values derived from the 2S2P1D model, as the values of  $\nu^*$  observed exceed 0.5. The 2S2P1D model was built to function independently in the prediction of complex moduli  $E^*$  and  $G^*$ . Hence the utilisation of the 2S2P1D is inadequate for obtaining an accurate estimation of the value of  $\nu^*$ .

As an example, an analysis could be done on the asymptotic values of  $E^*$  and  $G^*$ . The values of 4500 MPa and 1300 MPa were obtained for the glassy moduli of  $|E^*|$  and  $|G^*|$  (Table 6.1). However, assuming the classical hypotheses of isotropic behaviour and a real  $\nu$  equal to 0.5 as for an incompressible material,  $|E^*|$  is equal to  $3|G^*|$ . The values of glassy moduli obtained are not coherent with these assumptions since they would imply  $|\nu^*| > 0.5$ . Hence, a deeper analysis is needed, including refined 2S2P1D simulations and extended range of data for  $E^*$  and including the oedometric effect for axial test.

### 6.6 Conclusions on campaign 3

The third campaign of this thesis focused on determination of axial ( $E^*$ ) and shear ( $G^*$ ) complex modulus of an unmodified bitumen (B5070) with a DSR.



## 6.Campaign 3: Dynamic Shear Rheometer Determination of Axial $E^*$ and Shear $G^*$ Complex Moduli for Binder

---

The results of the experimental campaign confirm the possibility of linear viscoelastic characterization of a binder using a DSR in tension-compression at different temperatures and frequencies.

- Linear viscoelastic limit of binders can be determined by strain amplitude sweep test in tension-compression using a DSR. The axial strain amplitude limit of bitumen varies from 0.1% (1000  $\mu\text{m}/\text{m}$ ) to 7%.
- Adequate geometry selection to be used for DSR tests in axial mode is fundamental for an adequate rheological characterisation of binder behavior because of oedometric effect due to the aspect ratio of the sample.
- Time temperature superposition principle was verified for the tested bitumen for both axial and shear complex moduli.
- The normalized shear complex modulus  $G^*$  values obtained with the DSR Peltier assembly and the axial motor assembly overlap quite well.
- 2S2P1D model simulates well the linear viscoelastic properties of the binder over the ranges of temperature and frequencies tested in both shear oscillatory and tension-compression measurements. The same set of 2S2P1D constants and shift factors  $a_T$  was used to simulate both shear  $G^*$  and axial  $E^*$  complex moduli.
- The glassy modulus of bitumen  $E_0$  and  $G_0$  determined are 4.5  $\text{GPa}$  and 1.3  $\text{GPa}$  respectively.
- The normalized Cole-Cole and Black diagrams of axial and shear complex moduli plot superimpose quite well.
- The precise determination of bitumen Poisson's ratios is not possible when employing the combined 2S2P1D model of  $E^*$  and  $G^*$ .
- Finally, the results obtained are promising in view of developing an analysis method to determine the correct binder Poisson's ratio.

## 7. Campaign 4: 3D Linear Viscoelastic Characterisation and Modelling of Bitumen

---

### **7. Campaign 4: 3D Linear Viscoelastic Characterisation and Modelling of Bitumen**

#### **7.1 Objectives**

The linear viscoelastic properties of bituminous materials are important for road pavement design. The basic laboratory experiments given in the literature allow for the measurement of bitumen's complex moduli  $E^*$  (Young's modulus) or  $G^*$  (complex shear modulus). The stiffness of materials in one direction (1D) in space is characterised by  $E^*$  (complex Young's modulus) or  $G^*$  (complex shear modulus). Some tests have been designed to quantify the complicated Poisson's ratio  $\nu^*$  in order to expand the description of the linear viscoelastic behaviour of bitumen and mastics to the three-dimensional case (Hervé Di Benedetto et al., 2007). This test, however, is difficult to perform and necessitates a substantial quantity of bitumen.

The tension-compression test on bitumen using DSR was created in this thesis at the ENTPE to overcome these shortcomings and attempt to improve correlations between the behaviour of bitumen and asphalt mixes. The measurement of the axial  $E^*$  and shear  $G^*$  complex modulus of three different bitumen (B5070, B3550, PmB) and the determination of the complex Poisson's ratio coefficient  $\nu^*$  from the results of axial complex modulus and shear complex moduli tests is illustrated as the first objective of this Campaign. The second objective involves the finite element modelling of the tension-compression test and an attempt to correct the experimental axial complex modulus measurements by the determination of the correct Poisson's ratios.

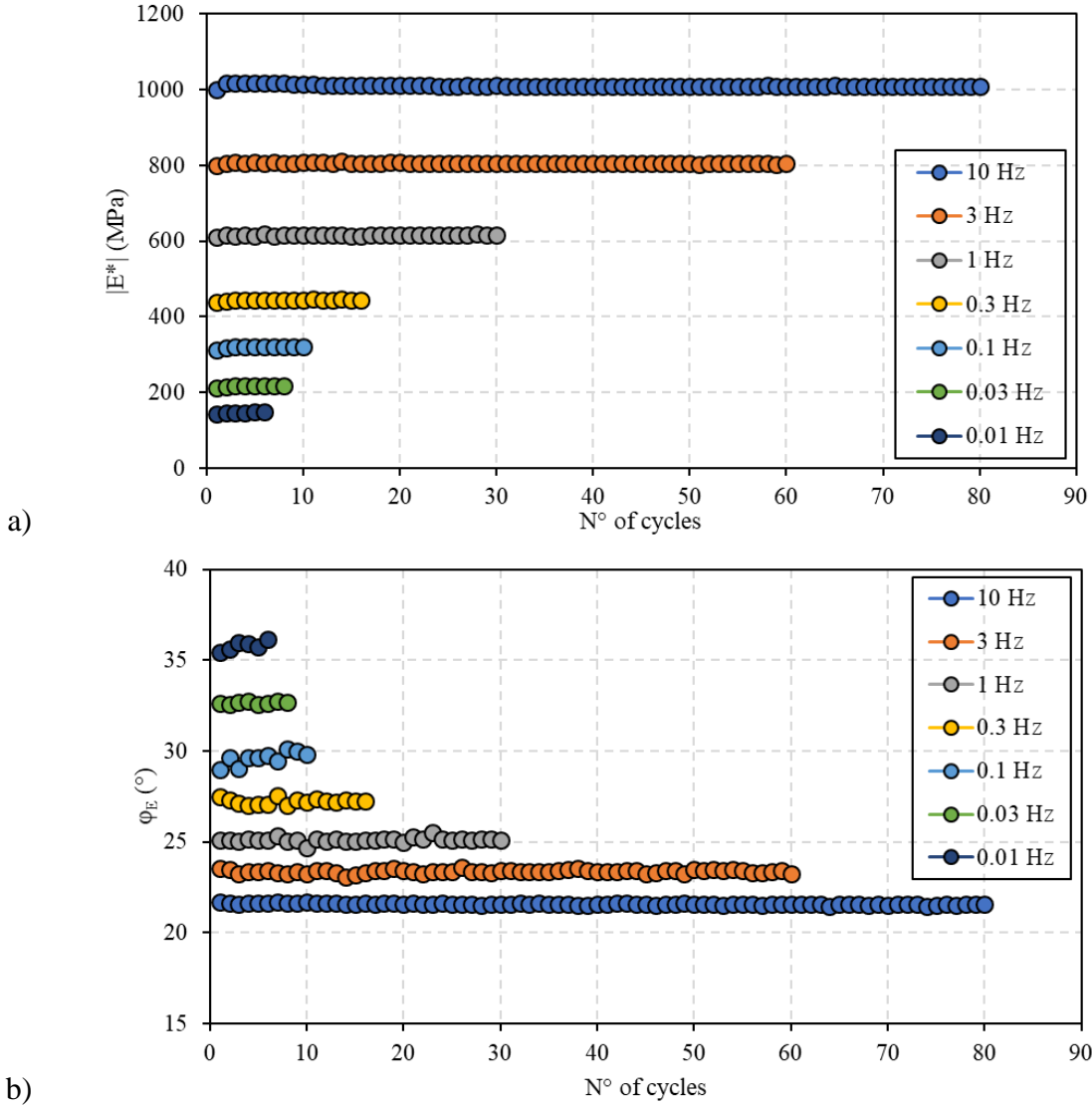
#### **7.2 Axial and shear complex modulus test on binders of 5 mm height**

Consequently, to the variations observed in the plots of the axial complex modulus  $E^*$  and phase angles versus number of cycles (see section 6.3), an attempt is made to improve on the accuracy of the signals measured. The irregularities of the modulus signals obtained in the previous campaign can be attributed to the sensitivity of the DSR. Therefore, in this Campaign, the imposed axial strain on B5070 bitumen was increased to 0.1%. This value is close to the LVE limit in axial strain of the test binder (see section 6.2). The axial amplitude strain sweep test results of two other bitumen (B3350 and PmB) are displayed in appendix (Figure C1). The axial strain sweep test on all the three test binders reached a strain limits above 0.1 %. However, an attempt to perform axial complex modulus test on B3550 and PmB binders at this imposed axial strain resulted in the failure of the test specimens at low temperatures. Therefore, test

# 7. Campaign 4: 3D Linear Viscoelastic Characterisation and Modelling of Bitumen

strain levels were maintained at a maximum of 0.07 %. The axial and shear complex modulus test procedures however remains unchanged.

Figure 7.1 shows the plots of cycle acquisitions used to determine the norm of the axial complex modulus and the respective phase angles at 0.1% imposed axial strain amplitude. The maximum difference measured on the norms of axial complex modulus at this strain rate amounts to 0.2% in axial complex modulus at 3 Hz frequency and 0.2° difference in phase angle at 0.1 Hz. The deviations are calculated as the maximum difference between the average measured absolute modulus value or phase angle of cycles considered at a frequency and an individual cycle measurement within the same frequency. The observed discrepancies are of a relatively minor magnitude and are unlikely to significantly affect the measurements of the modulus and phase angles. It is evident that the increase in axial strain translates to an increase in the data acquisition accuracy of the DSR linear motor.



## 7. Campaign 4: 3D Linear Viscoelastic Characterisation and Modelling of Bitumen

Figure 7.1 – B5070 axial complex modulus test results at  $-5^{\circ}\text{C}/0.1\%$  strain. a) Norm of complex modulus; and b) phase angle in function of number of cycles.

This is based on the comparison of the variations obtained in this campaign with a higher test strain (0.1%) and Campaign 3 with a low imposed axial strain (0.01%).

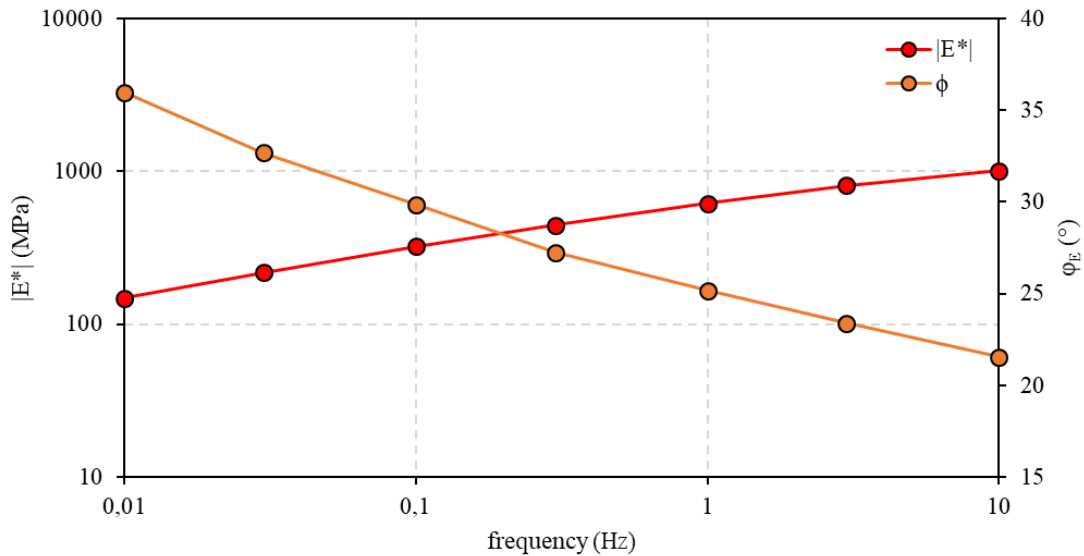


Figure 7.2 – Complex modulus and phase angle average values with respective deviations of B5070 bitumen at  $-5^{\circ}\text{C}/0.1\%$

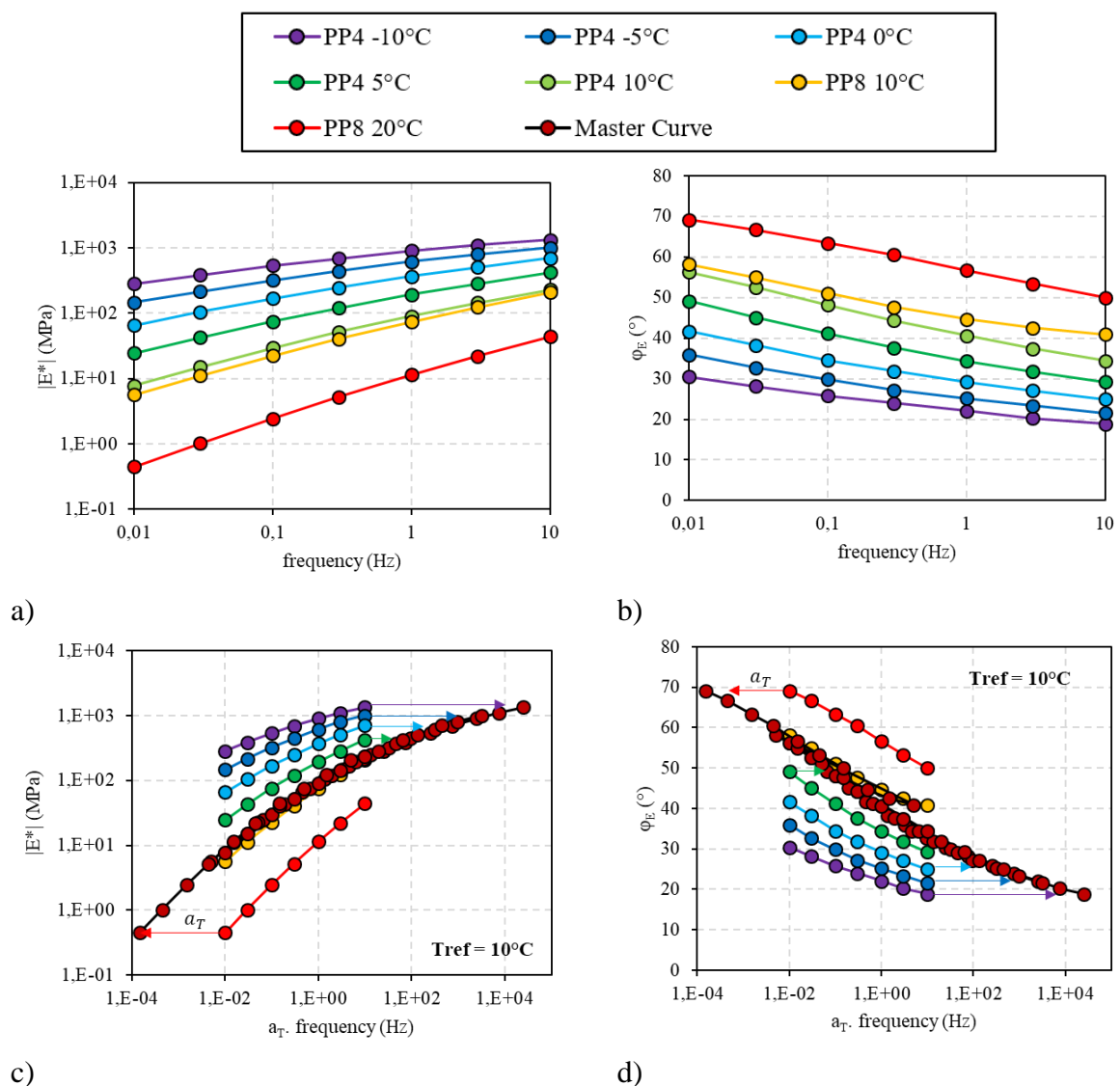
Figure 7.2 shows the average values of norms of axial complex modulus and corresponding phase angles as a function of test frequencies at 0.1% imposed strain amplitude. The error bars on the plots are however not visible due to the insignificance of the variations observed in the modulus and phase angle results at this test strain.

### 7.2.1 Time temperature superposition principle

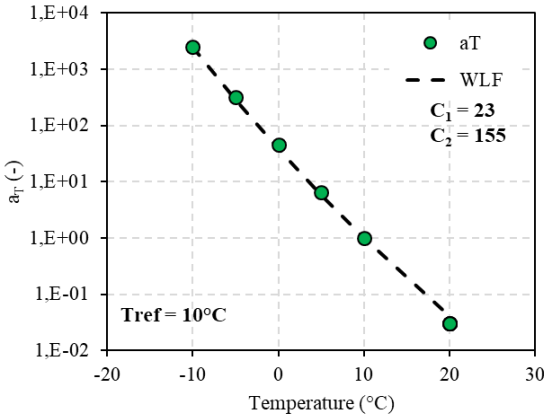
Figure 7.3a-b depicts the isotherm curves for the axial complex modulus of a B5070 bitumen. The complementary shear isotherm curves are shown in the appendix (Figure C2). Smoother isotherm curves of norms of axial complex modulus  $E^*$  and phase angles  $\phi_E$ , seen in this section translates to a better measurement achieved due to an increase in the imposed axial strain amplitude. However, measurements at  $10^{\circ}\text{C}$  with PP4 and PP8 are identical in terms of the axial complex modulus. The phase angles measured with PP8 are seen to diverge at 0.3 Hz to 10 Hz. Hence, measurements with PP4 are chosen for analysis due to the high axial and shear complex modulus values measured and a reduced, non-divergent phase angle. The shape of the isotherm curves demonstrates that the same complex modulus value can be obtained for a variety of

## 7. Campaign 4: 3D Linear Viscoelastic Characterisation and Modelling of Bitumen

temperature and frequency pairs. The complex modulus and phase angle master curve is plotted by translating the isotherms (axial and shear) along the horizontal axis by a reference factor  $a_T$ . At a reference temperature of 10°C, a distinct curve is formed. The time-temperature superposition principle (TTSP) is therefore verified. Furthermore, as seen in Figure 7.3e, the WLF equation accurately predicts the experimental shift factors  $a_T$ . The norms of axial complex modulus and phase angle isotherms curves of other test binders are further presented in the appendix (Figure C3-C4).



# 7. Campaign 4: 3D Linear Viscoelastic Characterisation and Modelling of Bitumen

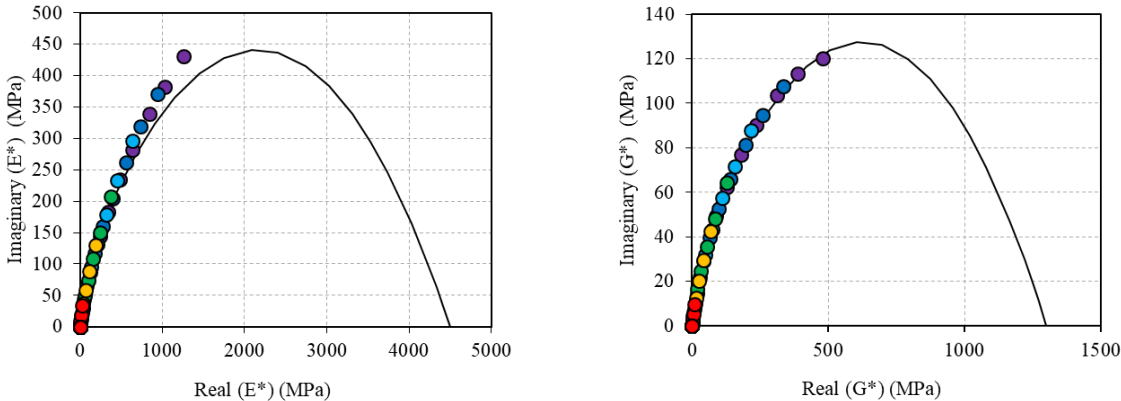


e)

Figure 7.3 – a) Norm of axial complex modulus isotherms; b) phase angle isotherms; c) Master curve of axial complex modulus and d) phase angle master curve e) experimental  $a_T$  WLF fit of B5070 bitumen at  $T_{ref} = 10^\circ\text{C}$  measured at 0.1% strain

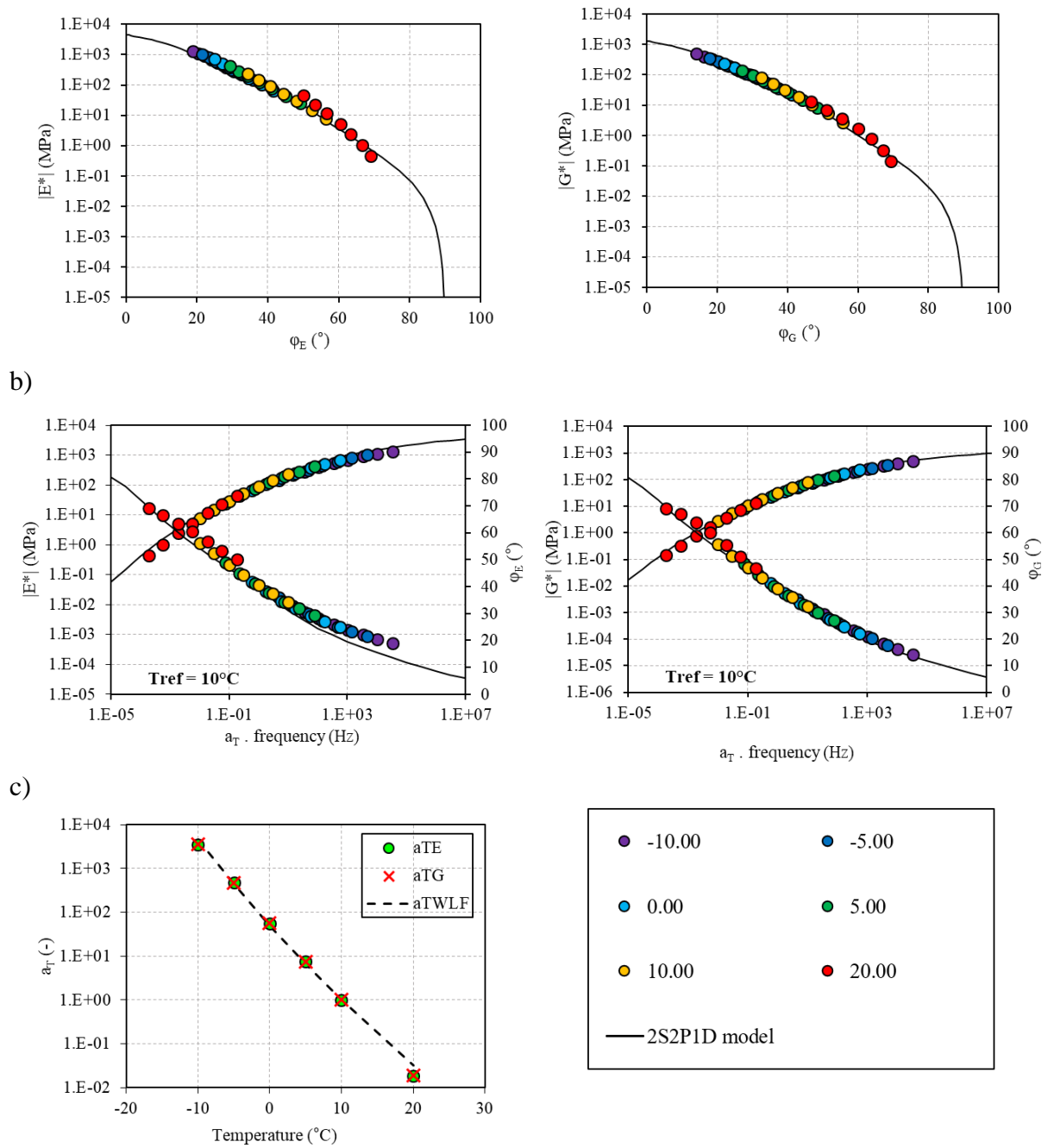
## 7.2.2 2S2P1D modelling of axial and shear complex modulus of binders

The 2S2P1D fitted axial and shear complex modulus test results on B5070 bitumen are presented in Figure 7.4 for brevity. The reader can refer to the appendix (Figures C4 and C5) for other bitumen. The 2S2P1D constants used to model the LVE behaviour of the bitumen alongside with the WLF parameters, are available in Table 7.1.



a)

## 7. Campaign 4: 3D Linear Viscoelastic Characterisation and Modelling of Bitumen



d) *Figure 7.4 – 2S2P1D fitted B5070 bitumen axial complex modulus  $E^*$  and shear complex modulus  $G^*$  at 5 mm test height a) Cole-Cole curve; b) Black diagrams; c) master curves at  $T_{ref} = 10^\circ\text{C}$  and d) Experimental shift factors fitted with WLF equation at  $T_{ref} = 10^\circ\text{C}$ .*

## 7. Campaign 4: 3D Linear Viscoelastic Characterisation and Modelling of Bitumen

Table 7.1 - 2S2P1D and WLF parameters for tested binders at  $T_{ref} = 10^{\circ}C$

Binder	$E_{00}$ (MPa)	$E_0$ (MPa)	$k$	$h$	$\delta$	$\tau$ (s)	$\beta$	$C_1$	$C_2$
<b>B5070</b>	0	4500	0.24	0.59	5.00	0.0008	330	24	151
	$G_{00}$ (MPa)	$G_0$ (MPa)							
	0	1300	0.24	0.59	5.00	0.0008	330	24	152
<b>B3550</b>	$E_{00}$ (MPa)	$E_0$ (MPa)							
	0	4200	0.25	0.60	3.40	0.0012	120	22	149
	$G_{00}$ (MPa)	$G_0$ (MPa)							
	0	1030	0.25	0.60	3.40	0.0026	120	22	151
<b>PmB</b>	$E_{00}$ (MPa)	$E_0$ (MPa)							
	0.04	4300	0.27	0.56	6.30	0.0015	700	27	169
	$G_{00}$ (MPa)	$G_0$ (MPa)							
	0.015	920	0.22	0.53	4.50	0.0015	900	26	164

The two unmodified bitumen validated the TTSP as described above in Section 7.2. Furthermore to this, polymer modified binders are evidenced to verify the TTSP at temperatures below  $10^{\circ}C$  (François Olard & Di Benedetto, 2003). Therefore, the PmB is said to verify the partial time temperature superposition principle (PTTSP).

The PmB is a modification of B5070, therefore the reduction in phase angles measured at mid temperature of the PmB is attributed to the cross linking of the polymer chains. The figures of PmB can be seen in the appendix C7

The WLF equation equally provided a satisfying model of shift factors. The axial complex modulus and shear complex modulus shift factors, WLF constants ( $C_1$  and  $C_2$ ) are near identical for each bitumen. This suggests that both test modes share identical time and temperature equivalency within the LVE domain. The 2S2P1D model fitted well the experimental results measured in shear oscillation. It is important to note that, these constants were also utilised to fit experimental results measured with the Peltier assembly in the previous Campaign (Chapter 5). However, higher shear glassy moduli ( $G_0$ ) were recorded for the unmodified bitumen in Table 7.1. This could be as a result of geometry variations in the test samples. The sample geometry variation was however associated with the different upper and lower plate sizes utilised for the test which leads to an inefficient trimming procedure. Again, an increase in  $G_0$  can be associated with the binder thermal history as the axial complex modulus  $E^*$  protocol is



## 7. Campaign 4: 3D Linear Viscoelastic Characterisation and Modelling of Bitumen

completed prior to that of shear complex modulus  $G^*$ . Furthermore, different temperature regulation set-ups were adopted in the measurements.

The 2S2P1D model does not fit well the axial complex modulus  $E^*$  measurements as seen in Figure 7.4a on the Cole-Cole curve and Figure 7.4c, the phase angle master curve. Typically for all the bitumen tested, a higher phase angle was seen to be recorded at temperatures  $0^\circ\text{C}$  and below. Identical set of 2S2P1D constants ( $k, h, \tau, \delta$  and  $\beta$ ) were used to fit the shear and axial complex modulus measurements of unmodified bitumen however the constant  $\tau$  differed with bitumen B3550. The PmB displayed an opposite behaviour with a different set of 2S2P1D constants used to fit the axial complex modulus measurements.

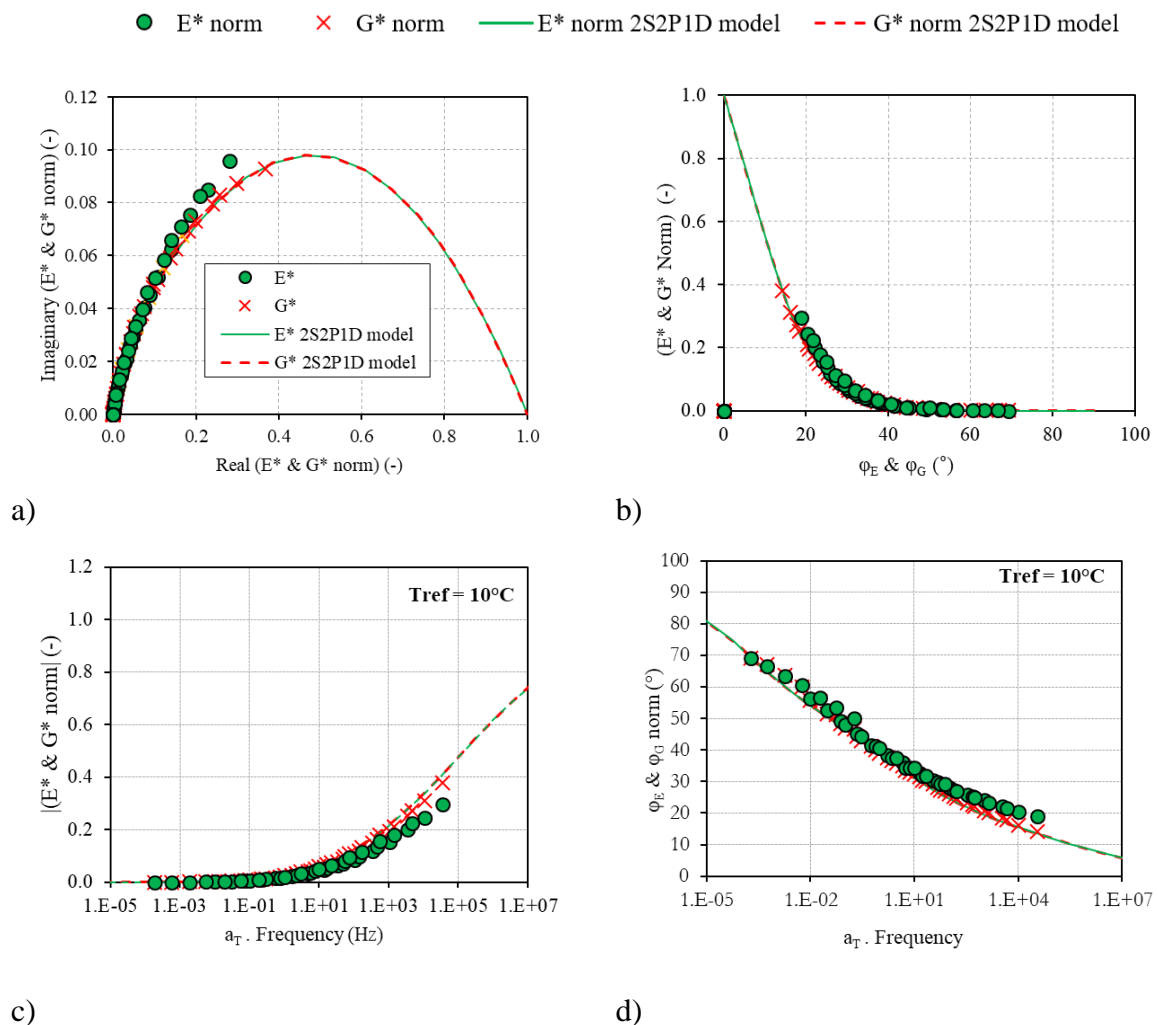


Figure 7.5 – Experimental results and fitted 2S2P1D curves of normalised complex modulus of B5070 bitumen a)  $E^*_{norm}$  and  $G^*_{norm}$  in Cole-Cole plane, b)  $E^*$  and  $G^*_{norm}$  in black space, c)  $|E^*$  and  $G^*_{norm}|$  master curves d)  $\phi_E$  and  $\phi_{Gnorm}$  master curves at  $T_{ref} = 10^\circ\text{C}$  and 0.1% axial strain

## 7. Campaign 4: 3D Linear Viscoelastic Characterisation and Modelling of Bitumen

---

As illustrated in Figure 7.5 for B5070 bitumen, both normalised axial and shear complex modulus Cole-Cole and Black space do not overlap due to the discrepancies observed earlier with measurements of  $E^*$  below  $5^\circ\text{C}$ . Similar differences were observed with other bitumen B3550 and PmB. (See appendix C5-C8).

The two unmodified bitumen, share identical static modulus ( $E_{00}, G_{00} = 0 \text{ MPa}$ ) whereas a low static modulus was recorded for the PmB due to the active polymer networks at high temperatures. This implies that the bitumen is considered purely viscous and newtonian at high temperatures. The glassy moduli of axial complex modulus ( $E_0 = 4200 \text{ MPa} \sim 4300 \text{ MPa}$ ) were significantly higher than their corresponding shear complex modulus ( $G_0 = 920 \text{ MPa} \sim 1300 \text{ MPa}$ ). The glassy modulus value of all test binders is higher than the values stated in the literatures  $E_0 = 2.1 \text{ GPa}$  (François Olard & Di Benedetto, 2003). This can be associated with an insufficient specimen height to diameter ratio. As a concluding remark, the increase in imposed strain of B5070 bitumen during axial complex modulus test improved only the cyclic signals. However, the unobservable influence on the LVE model accuracy can be attributed to the test being performed within the LVE domain. Within this domain, there exists variations of insignificant magnitude in viscoelastic responses (Babadopulos, 2017; Q. T. Nguyen et al., 2019) which are not visible in the respective viscoelastic plots.

### 7.3 Poisson's ratio determination

The axial and shear complex modulus of three different bitumen have been determined and the experimental results fitted to the 2S2P1D model. The Poisson's ratio  $\nu^*$  is determined indirectly from the experimental results as stated in Equations 2.81 and 2.82.

The variation of B5070 Poisson's ratio  $\nu^*$  in relation to frequency and temperature is shown in Figure 7.6. These results were obtained at 5 temperatures and 7 frequencies respectively. Poisson's ratios at  $20^\circ\text{C}$  are excluded as a result of incompressibility and further shown in the appendix (Figure C9). Bitumen Poisson's ratio values are generally supposed constant in literatures when no measurements were available. The values have been shown by (Hervé Di Benedetto et al., 2007) to reduce with an increase in frequency and temperature reduction. Although the evolution of Poisson's ratio shown in Figure 7.6 in terms of temperature and frequency is not in the direction expected, the values obtained with the B5070 bitumen ranged between 0.36 and 0.51. These values are well within those stated by (Hervé Di Benedetto et al., 2007). Furthermore, the phase angles show the obvious temperature and frequency dependence and the correct evolution. The phase angles ranged between  $-1^\circ$  and  $-18^\circ$ . These

# 7. Campaign 4: 3D Linear Viscoelastic Characterisation and Modelling of Bitumen

values of phase angles are negative which implied the axial deformation leads the radial deformation as stated by (Hervé Di Benedetto et al., 2007). However, they possess a wider range than the values reported by (Hervé Di Benedetto et al., 2007) utilizing the direct test method (see section 2.5.3).

Similar evolution patterns are also observed with B3550 and PmB bitumen detailed in the appendix, Figures C10a and C11a. Poisson’s ratio values of B3550 bitumen ranged from 0.39 to 0.64. The phase angles ranged between  $-18.43^\circ$  and  $-0.84^\circ$ . Considering the PmB, higher Poisson’s ratio values and phase angles were recorded, these ranged between 0.68 to 1.09 and  $-9.89^\circ$  and  $6.62^\circ$  respectively. These can be explained by the complex behaviour of the binder due to the modification. It is however expected to exhibit a behaviour similar to unmodified bitumen within the considered temperature ranges. Therefore, further experimental campaign is necessary to study the polymer modification influence on Poisson’s ratio values.

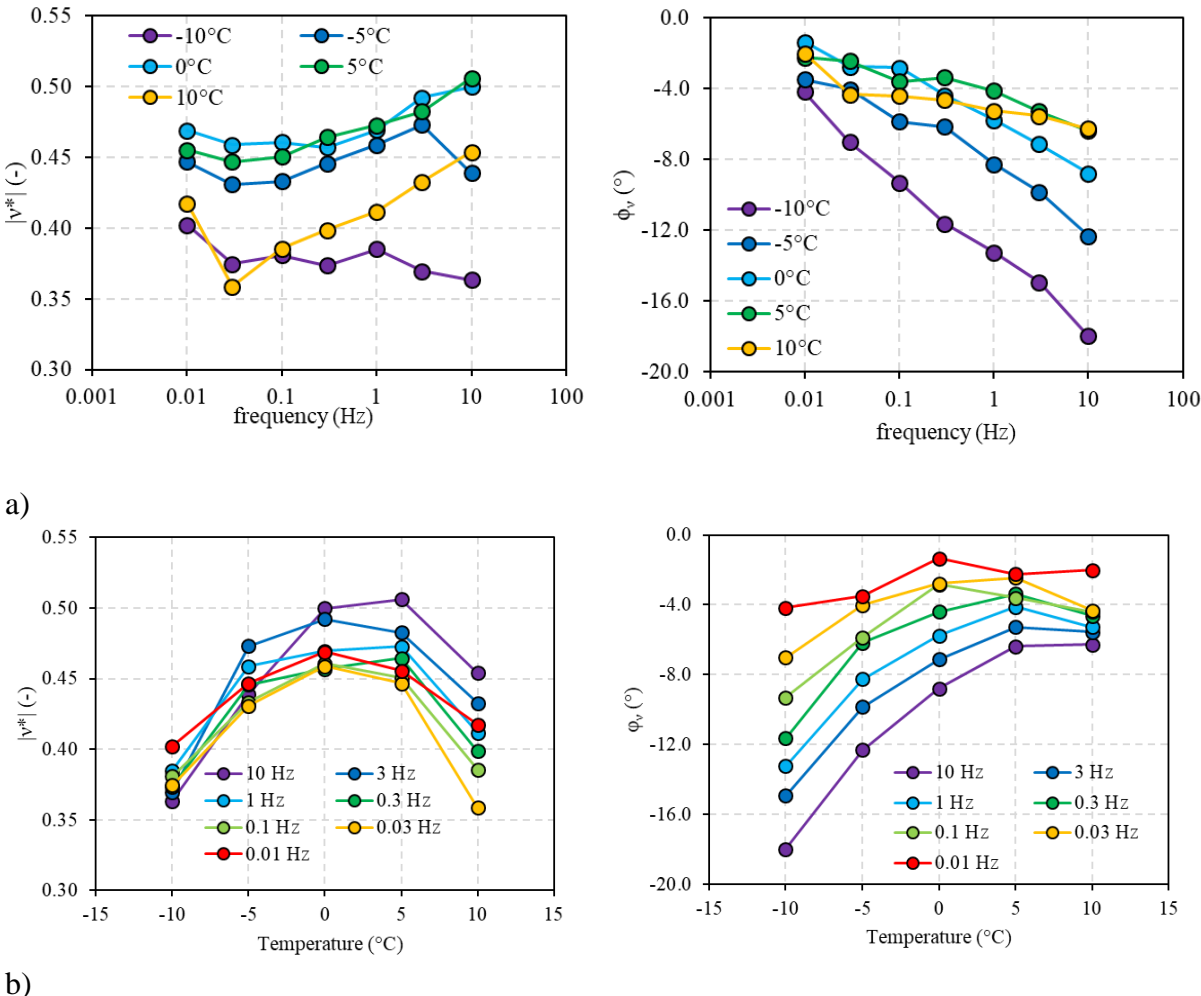


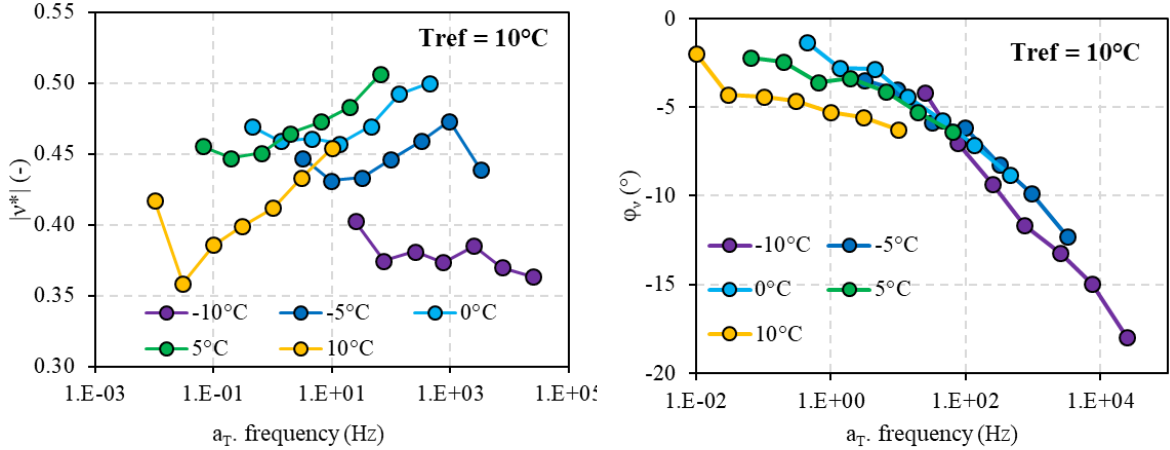
Figure 7.6 - Norm of complex Poisson’s ratio  $v^*$  and phase angle  $\phi_v$  of B5070 a) isotherms of experimental results; b) isochrones of experimental results

## 7. Campaign 4: 3D Linear Viscoelastic Characterisation and Modelling of Bitumen

Additionally, considering the isochronal evolution of bitumen Poisson’s ratio as shown in Figure 7.6b, the values of B5070 Poisson’s ratio and corresponding phase angles were observed to increase with temperature and peaked at 0°C. This evolution pattern was also observed with B3550 bitumen as shown in appendix Figure C10b. Similar tendencies have been reported by (Crowson & Arridge, 1979; Koppelman, 1959) where they demonstrated that a 1°C increase in experimental temperatures can have a significant impact on the Poisson’s ratio derived from two independently measured response functions. As previously noted, there is a distinct disparity in the evolution of the Poisson’s ratio between PmB bitumen and unmodified bitumen. This phenomenon is further illustrated by the isochronal plots depicted in Figure C11b (refer to the appendix). The values of Poisson’s ratio exhibited a decrease as the temperature increased. It is necessary to state that similar test conditions in the axial and shear complex modulus test must be maintained to improve Poisson’s ratio determination.

### 7.3.1 Time temperature dependence of Poisson’s ratio

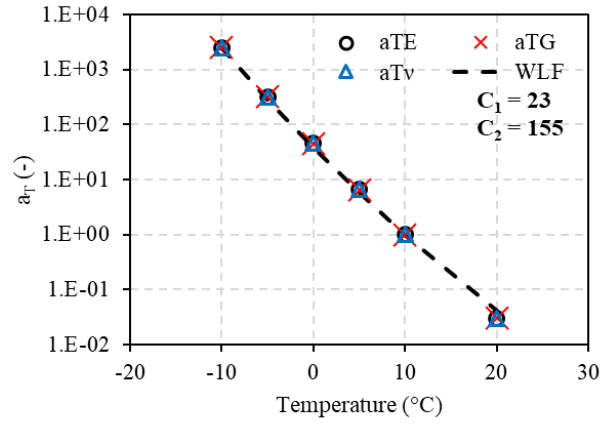
Similar translation method adopted in Figure 7.3 to form master curves of  $E^*$  and  $G^*$  were utilised. The shift factors  $a_T$  used to translate the isotherms of norms of  $E^*$  and  $G^*$  were adopted for Poisson’s ratio  $|v^*|$  and its corresponding phase angle  $\phi_v$  to form a unique curve (Master curve) at a reference temperature ( $T_{ref} = 10^\circ\text{C}$ ).



a)

b)

## 7. Campaign 4: 3D Linear Viscoelastic Characterisation and Modelling of Bitumen



c)

Figure 7.7 - The experimental results of the complex Poisson's ratio  $v^*$  of B5070 bitumen a) Master curve of norm of Poisson's ratio; b) Master curve of Phase angle of Poisson's ratio c) WLF fit of shift factors at  $T_{ref} = 10^\circ\text{C}$

The shift factor  $a_{TE}$  was directly used in the translation of Poisson's ratio isotherms, as it was not possible to directly determine  $a_{Tv}$ . Nevertheless, it is evident that a unique curve depicting the norm of Poisson's ratio cannot be achieved, but this is feasible for phase angles as shown in Figure 7.7. This verifies the time-temperature superposition principle.

### 7.3.2 2S2P1D Poisson's ratio determination

In this section, an attempt was made to determine Poisson's ratio of B5070 bitumen and its corresponding phase angle values from simulated 2S2P1D complex modulus values. The adopted corresponding equation is as follows:

$$v'_{2S2P1D}(\omega) = \frac{E_{2S2P1D}^*(\omega)}{2G_{2S2P1D}^*(\omega)} \cos(\varphi_{E2S2P1D} - \varphi_{G2S2P1D}) - 1 \quad (7.1)$$

$$v''_{2S2P1D}(\omega) = \frac{E_{2S2P1D}^*(\omega)}{2G_{2S2P1D}^*(\omega)} \sin(\varphi_{G2S2P1D} - \varphi_{E2S2P1D}) \quad (7.2)$$

Figure 7.8 illustrates the isothermal curves of 2S2P1D derived complex Poisson's ratio and phase angles of Poisson's ratio ( $\varphi_v$ ). The norm of Poisson's ratio and phase angles varied from 0.73 to 0.75 and from  $0^\circ$  to  $0.6^\circ$ . As earlier mentioned in the previous chapter (Campaign 3), the 2S2P1D model works properly when it is used to determine  $E^*$  and  $G^*$  independently, but when combined to determine  $v^*$ , it will not work. This is because Poisson's ratio ( $v^*$ ) has the same evolution as  $E^*$  or  $G^*$ .

## 7. Campaign 4: 3D Linear Viscoelastic Characterisation and Modelling of Bitumen

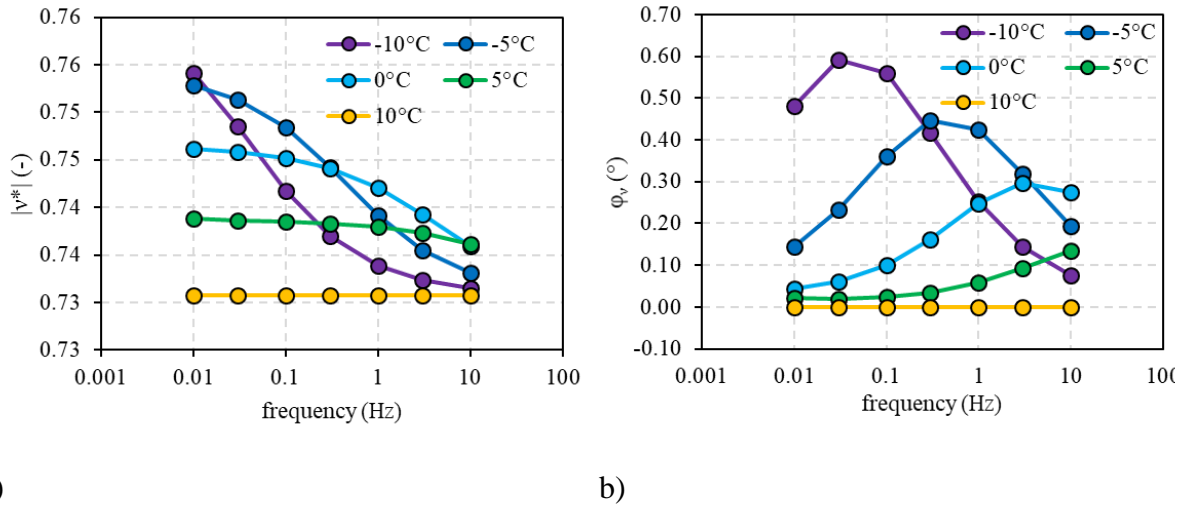


Figure 7.8 - The 2S2P1D simulated results of the complex Poisson's ratio  $v^*$  of B5070 bitumen a) norm of Poisson's ratio; b) Phase angle of Poisson's ratio

### 7.4 Finite element simulation of DSR axial complex modulus test

Axial and shear complex modulus test results have been modelled with 2S2P1D and, Poisson's ratio determined from experimental results. However, some backdrops such as the abnormally high glassy modulus and corresponding phase angles of axial complex modulus, Poisson's ratios value above 0.5 were identified. Therefore, it is pertinent to simulate the DSR axial complex modulus test making use of finite element methods to cross-reference the experimental results.

#### 7.4.1 Finite element model description

The simulation of a 2D axisymmetric bonded cylindrical bitumen sample compressed between two DSR steel plates was carried out in COMSOL. Varying bitumen aspect ratios, denoted by  $s$  were simulated. The dimension of the lower DSR plate was taken as the contact diameter of the bitumen sample (4 mm). An axisymmetric model with a fixed boundary condition (displacement = 0 along  $r$  and  $z$ ) was applied to the top part of the model, and a vertical displacement boundary condition imposed at the bottom to allow for the simulation of a tension-compression movement. Symmetrical boundary conditions were effective along the axis of the cylinder ( $r = 0$ ). The apparent simulated modulus of the binder was evaluated as:

$$E_{simul} = \frac{\sigma}{\epsilon} \quad (7.4)$$

## 7. Campaign 4: 3D Linear Viscoelastic Characterisation and Modelling of Bitumen

Where,  $\bar{\sigma}$  is the average axial stress and  $\bar{\epsilon}$  average axial strain calculated along the central cross section of the binder. The finite element model scheme is shown in Figure 7.9.

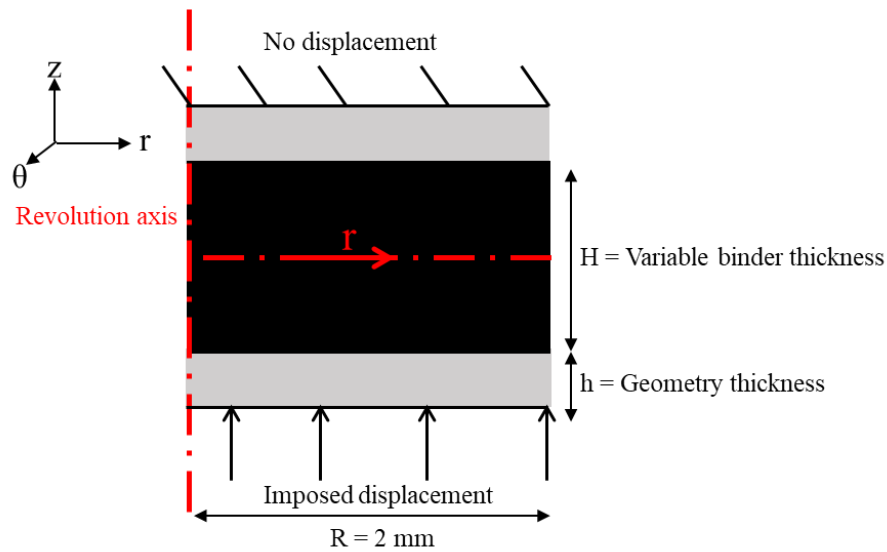


Figure 7.9 – Finite element model of the binder

The FE simulation was run for a linear elastic bitumen material. The materials involved are regarded as deformable bodies with properties listed as follows;

- Shear complex modulus of bitumen  $G_b = 1000 Pa$ , two values of Poisson's ratios  $\nu = 0.35$  and  $0.49995$  were selected to represent compressible and near incompressible conditions in solids. Young's modulus of bitumen at the respective Poisson's ratios are therefore given as  $E_b = 2700 Pa$  and  $3000 Pa$ .
- The steel plates have a modulus of  $E_{steel} = 2 \times 10^{11} Pa$  and Poisson's ratio  $\nu_{steel} = 0.3$
- The aspect ratios ( $s$ ) is defined herein as the ratio of the specimen radius to its height  $s(R/H) = 1.14, 0.67, 0.50$  and  $0.40$ . The stated aspect ratios correspond to the heights of the bitumen samples tested in Campaign 3. Furthermore, an aspect ratio of  $0.33$  that was not executed in the laboratory was included. The radial position is represented by  $r$  as shown in Figure 7.9.
- Quadrilateral mesh with maximum element size of  $0.296 mm$  was applied. 1770 degrees of freedom was solved for by imposing a displacement corresponding to  $0.01\%$  strain on the binder at every run.

## 7. Campaign 4: 3D Linear Viscoelastic Characterisation and Modelling of Bitumen

---

### 7.4.2 Analytical solutions of materials in compression

An analytical solution has been derived by (J. G. Williams & Gamonpilas, 2008) for compression of cylindrical materials between two rigid plates similar to the bitumen described above. The relationship between the apparent Young's modulus ( $E_{apparent}$ ) and true Young's modulus ( $E_{material}$ ) of the material is expressed as shown in Equation 7.5

$$\frac{E_{apparent}}{E_{material}} = \frac{1 + 3\nu \left( \frac{1-\nu}{1+\nu} \right) s^2}{1 + 3\nu(1-2\nu)s^2} \quad (7.5)$$

Where  $\nu$  is the Poisson's ratio of the material and  $s = \frac{a}{h}$ , the aspect ratio of the cylinder. For an incompressible material where  $\nu = 0.5$ , the relationship results in;

$$\frac{E_{apparent}}{E_{material}} = 1 + \frac{s^2}{2} \quad (7.6)$$

Equation 7.6 was also expressed as the constant volume solution for cylindrical discs loaded axially (Gent & Lindley, 1959). Furthermore, as  $s \rightarrow \infty$ , the oedometric modulus is expressed as;

$$\frac{E_{eodo}}{E_{material}} = \frac{1-\nu}{(1+\nu)(1-2\nu)} \quad (7.7)$$

where  $E_{eodo}$  represents the eodometric modulus.

### 7.4.3 Effect of Poisson's ratio on the apparent complex modulus

The simulated bitumen stiffness and the input stiffness are denoted by  $E_{apparent}$  and  $E_b$  respectively as shown in the Figure 7.10. This plot shows the variation of the stiffness against Poisson's ratio.  $E_{apparent}$  is derived from the following equation:

$$E_{apparent} = \frac{F/\pi R^2}{d/H} \quad (7.8)$$

Where vertical load F is obtained from the Integration of the stress component  $\sigma_{zz}$ , d is taken as the imposed global displacement which corresponds to 0.0001 mm, R is the radius of the bitumen sample and H is the height of the sample.



## 7. Campaign 4: 3D Linear Viscoelastic Characterisation and Modelling of Bitumen

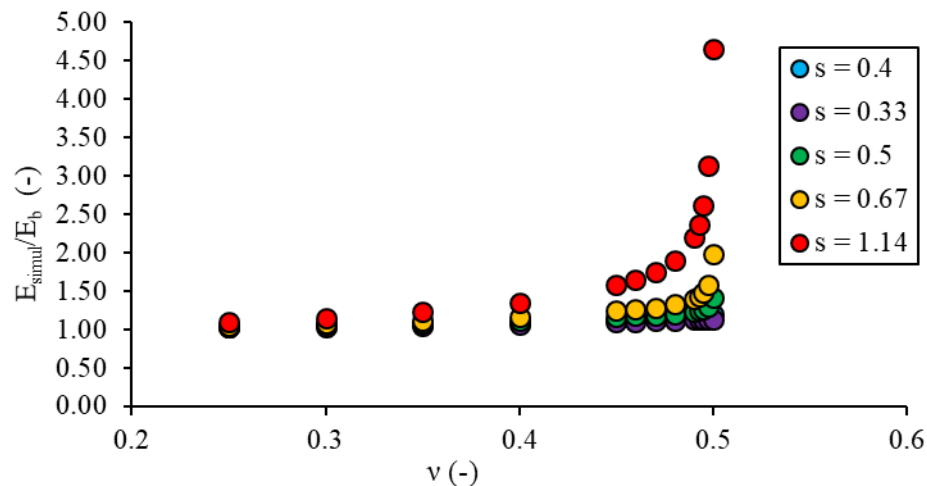


Figure 7.10 – Effect of Poisson’s ratio on the simulated binder stiffnesses at varying aspect ratios

It can be seen that there is a gradual increase in the estimated oedometric effect on  $E_{apparent}$  as the Poisson’s ratio tends to the value 0.5. Furthermore, this effect is reduced with a reduction in bitumen aspect ratio.

Figure 7.11 and 7.12 illustrates the plot of stresses existent in the centre part of tested bitumen samples with reference to the radial position  $r$ . The stresses are seen to decrease with reduction in aspect ratio of bitumen. Furthermore, stress homogeneity tends to be achieved with a reduction in aspect ratio. Bitumen is incompressible at high aspect ratios, this explains the rapid increase in stress ( $2.1 Pa$ ) at aspect ratio 1.14 shown in Figure 7.12a. This is further evidenced by a non-homogenous complementary high strain of  $1.5 \times 10^{-4}$  as shown in Figure 7.12b. It is important to reiterate that the maximum convenient test height with the 4 mm parallel plate in the DSR, corresponds to an aspect ratio of 0.4. It is indeed logical to perform axial complex modulus test at heights independent of stress influences. The average stress at  $s = 0.4$  and  $v = 0.35$  is however 7 % higher than the minimum stress at the ideal test height (Figure 7.11).

## 7. Campaign 4: 3D Linear Viscoelastic Characterisation and Modelling of Bitumen

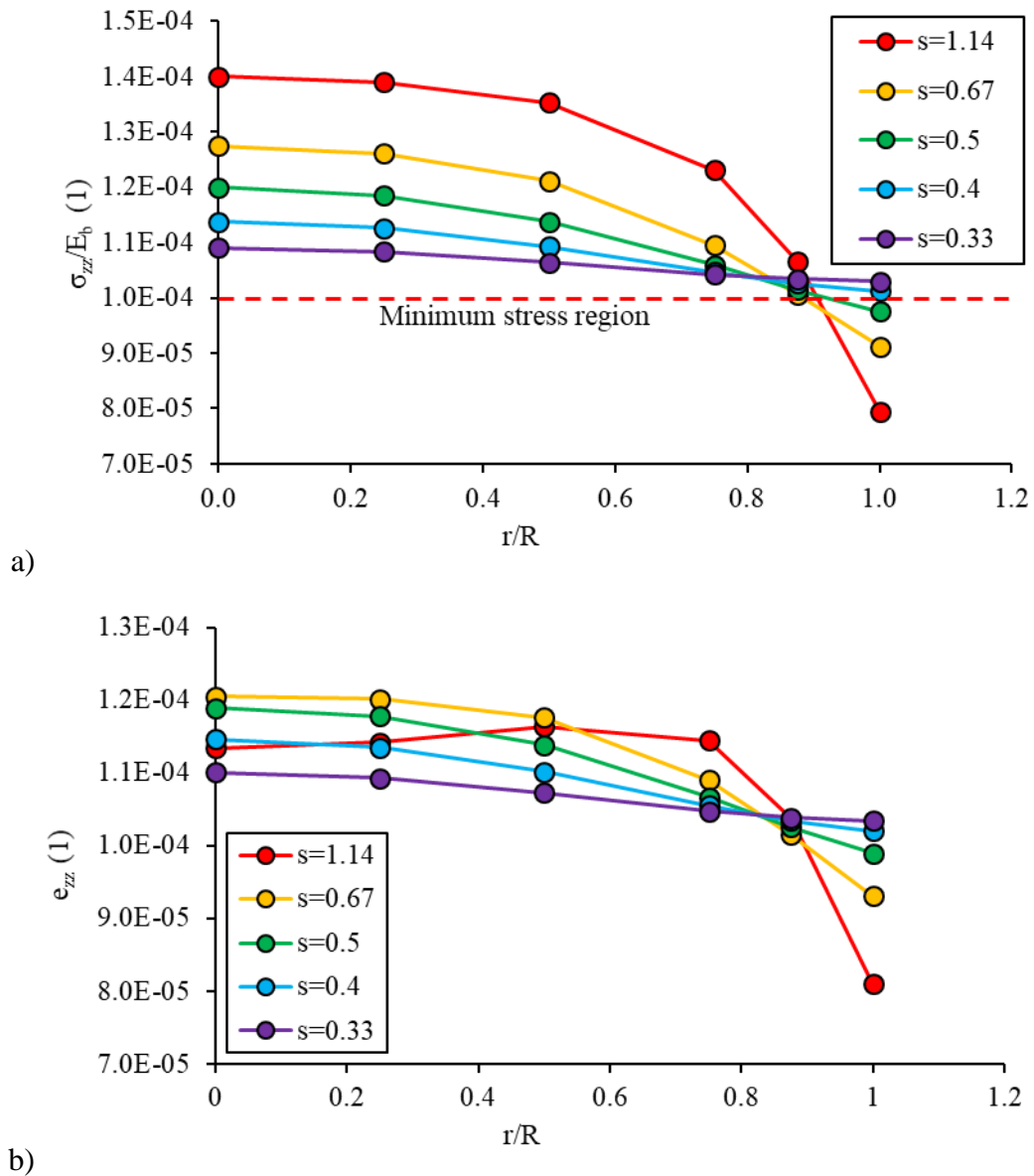


Figure 7.11 – Effect of aspect ratio ( $s$ ) on stress and strain distribution along the central axis ( $r$ ) of the bitumen at a constant Poisson's ratio ( $0.35$ )

# 7. Campaign 4: 3D Linear Viscoelastic Characterisation and Modelling of Bitumen

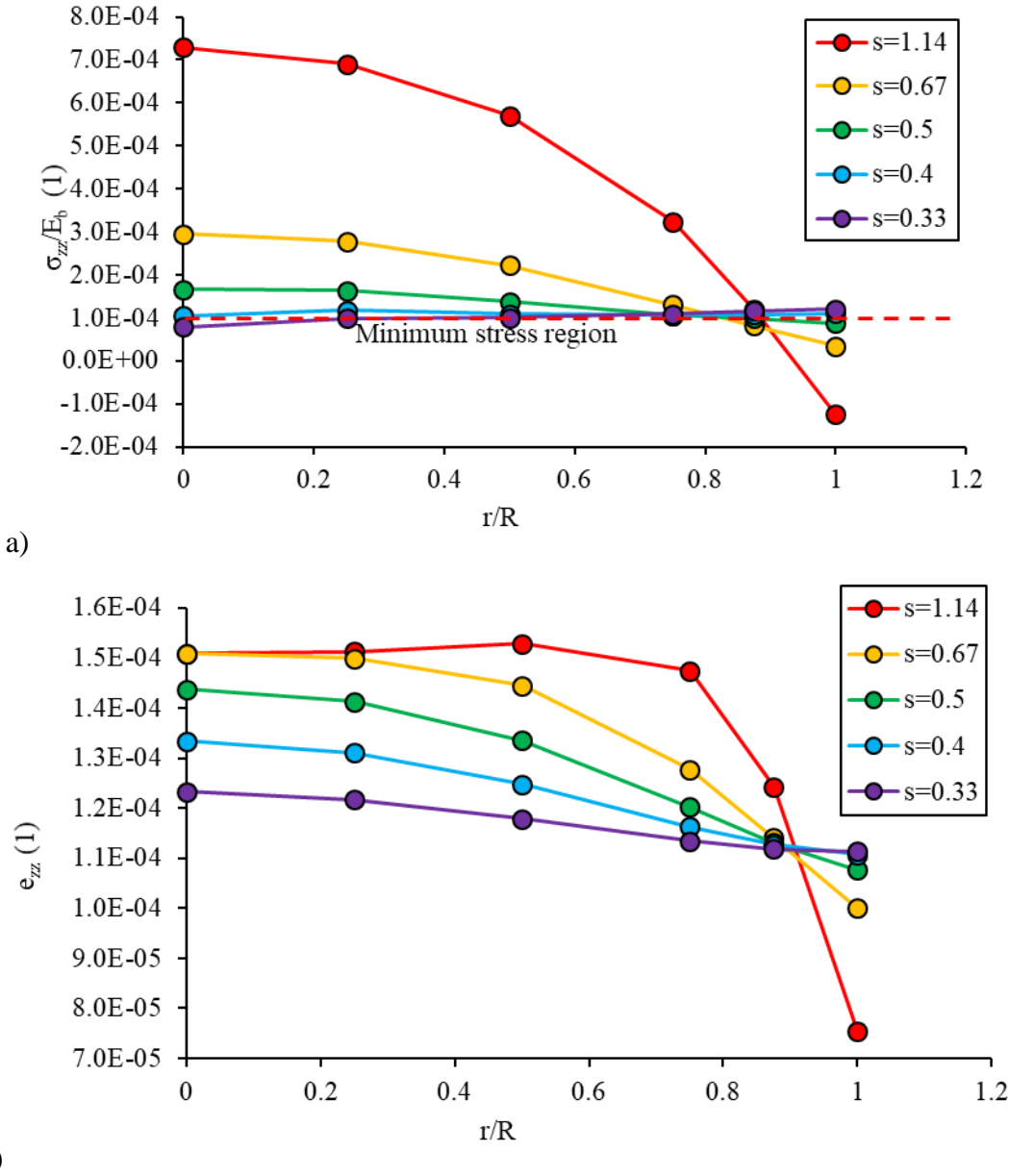


Figure 7.12 – Effect of aspect ratio ( $s$ ) on stress and strain distribution along the central axis ( $r$ ) of the bitumen at a constant Poisson’s ratio near oedometric condition (0.49995)

## 7.4.4 Stress and strain tensors within the bitumen finite element model

Figure 7.13 through Figure 7.16 show the results of stress and strain tensor terms  $zz$ ,  $rr$ ,  $\theta\theta$ , and  $rz$  in the central region around the bitumen sample with aspect ratio ( $s$ ) 0.4 and Poisson’s ratio 0.35. This aspect ratio is considered since it is the test sample geometry possible to be adapted for a near accurate measurement as seen in section 7.5.3.

## 7. Campaign 4: 3D Linear Viscoelastic Characterisation and Modelling of Bitumen

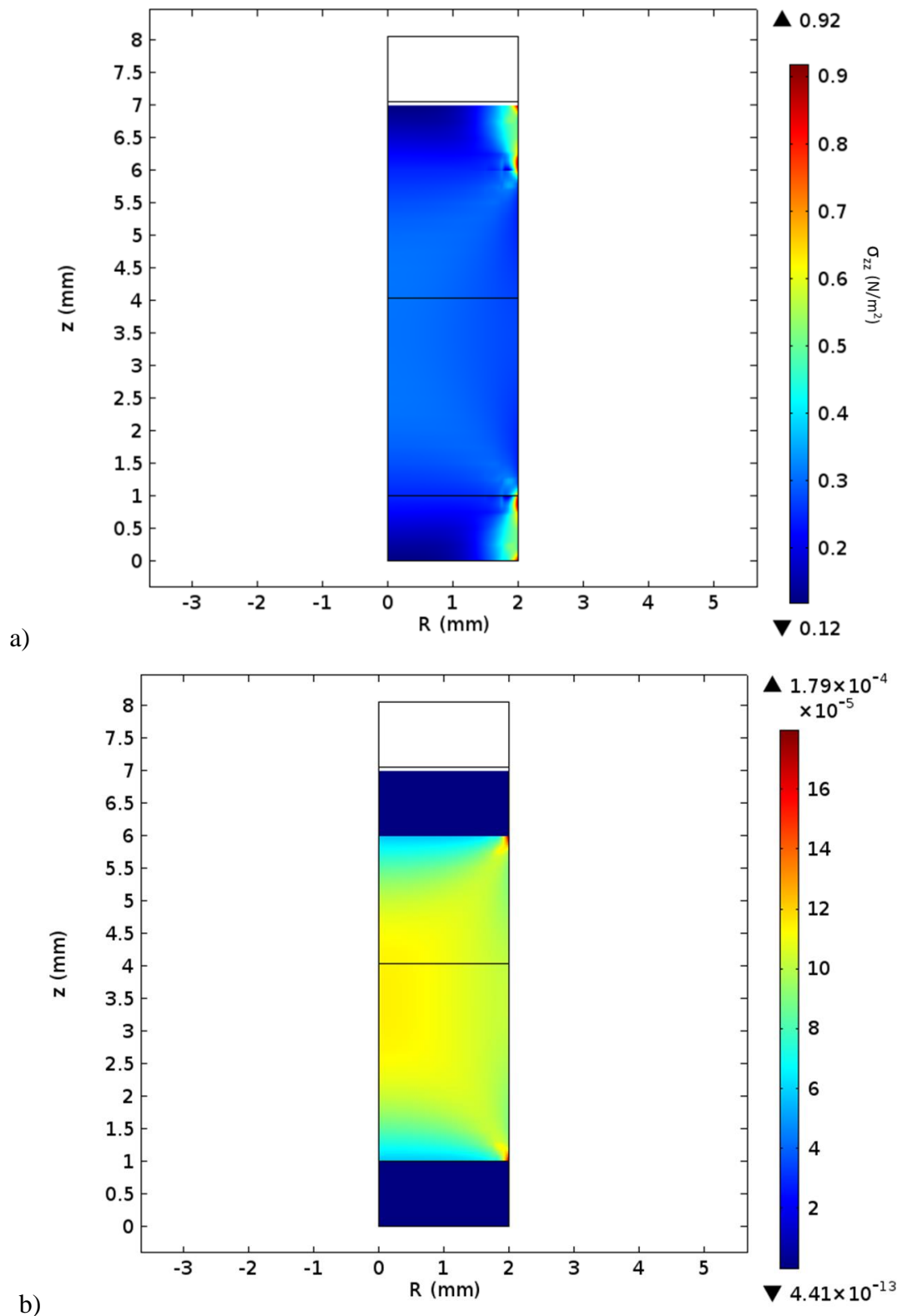
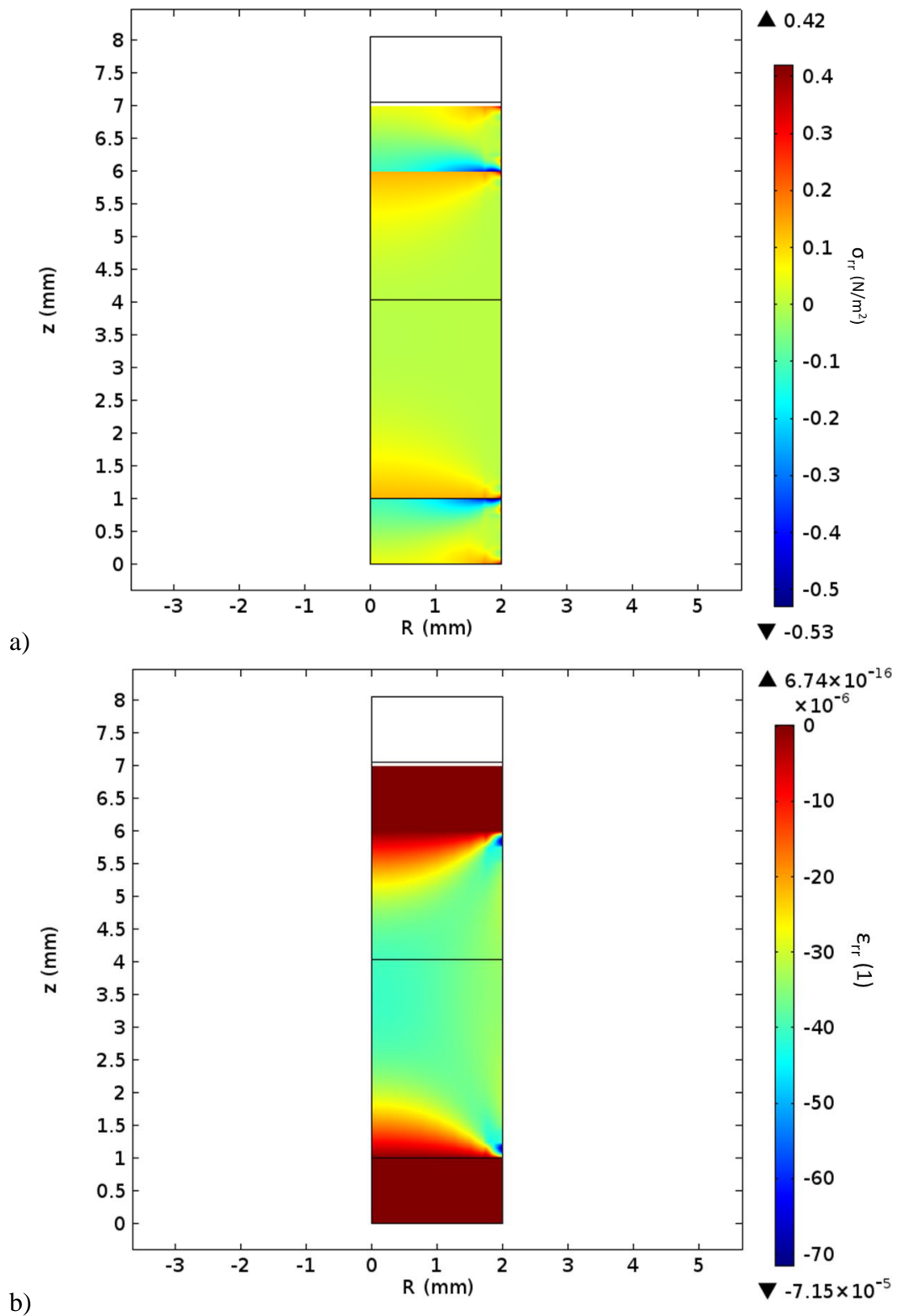


Figure 7.13 – The distribution of stress  $\sigma_{zz}$  and strain tensor  $\epsilon_{zz}$  in the bitumen's central region at 5 mm specimen height

## 7. Campaign 4: 3D Linear Viscoelastic Characterisation and Modelling of Bitumen



## 7. Campaign 4: 3D Linear Viscoelastic Characterisation and Modelling of Bitumen

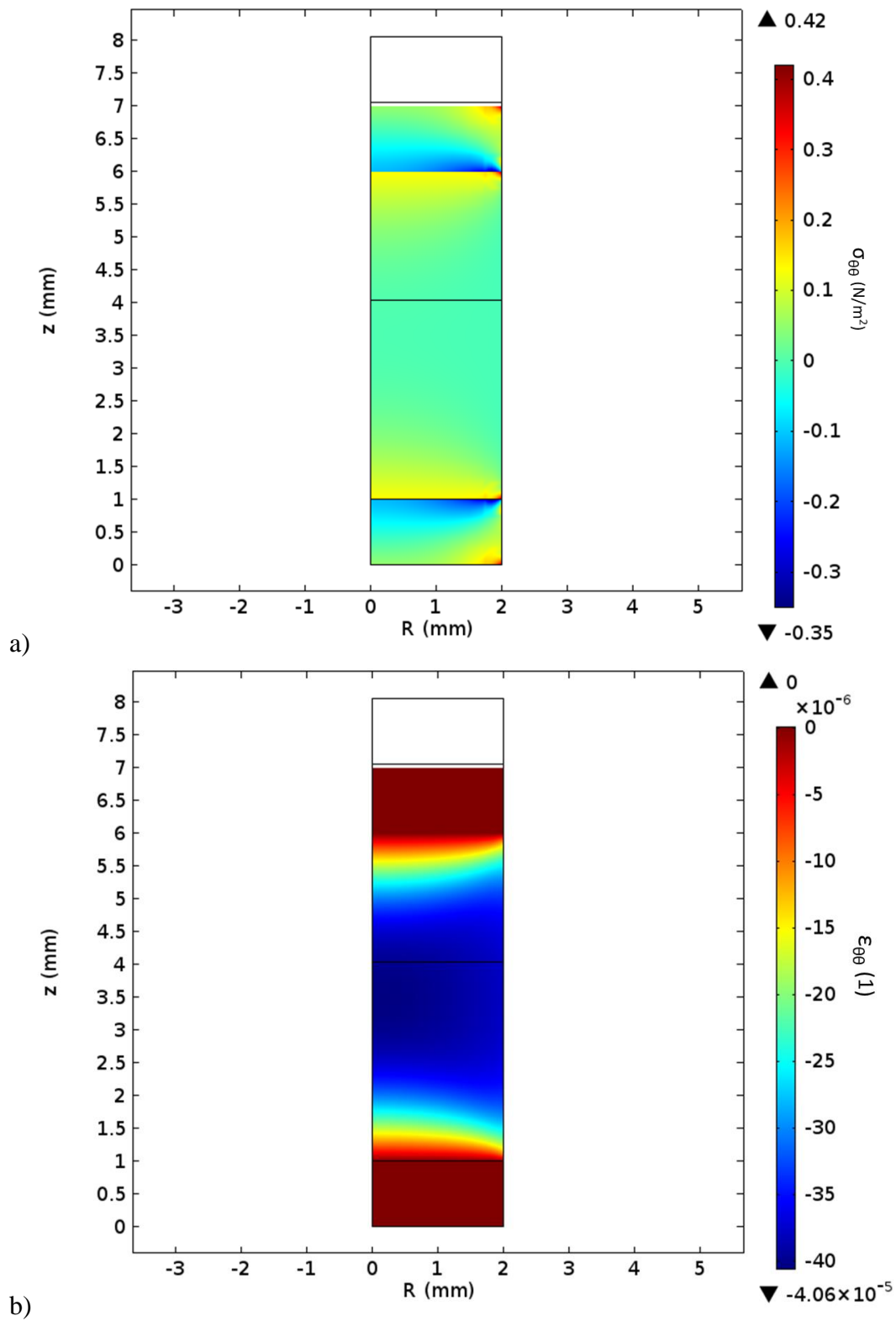


Figure 7.15 – The distribution of stress  $\sigma_{\theta\theta}$  and strain tensor  $\epsilon_{\theta\theta}$  in the bitumen's central region at 5 mm specimen height

## 7. Campaign 4: 3D Linear Viscoelastic Characterisation and Modelling of Bitumen

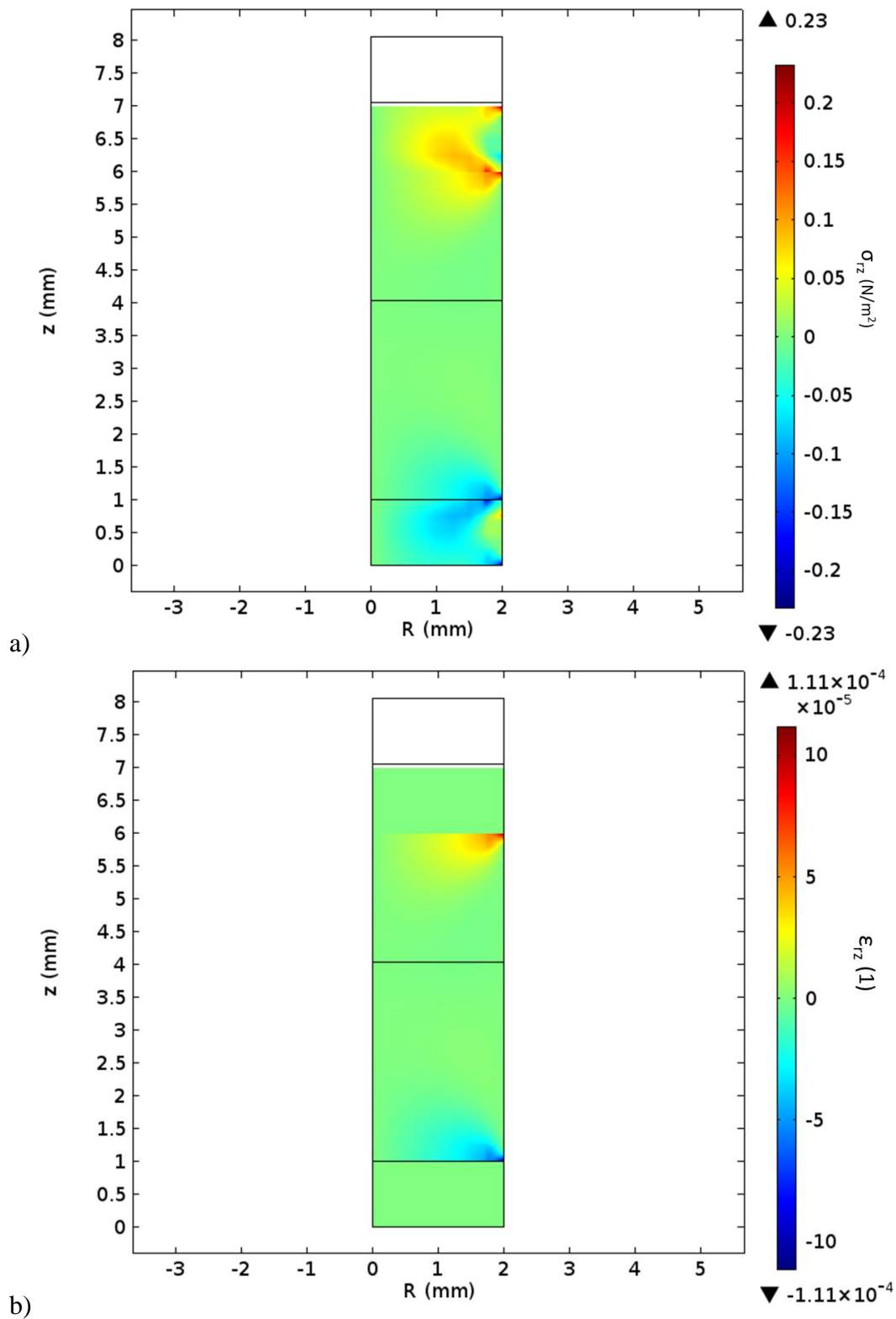


Figure 7.16 – The distribution of stress  $\sigma_{rz}$  and strain tensor  $\epsilon_{rz}$  in the bitumen's central region at 5 mm specimen height

As shown in Figure 7.13, the average axial stress  $\sigma_{zz}$  over the bitumen's horizontal central axis was 0.29 Pa. This value is however close to the analytic solution of 0.28 Pa calculated from

## 7. Campaign 4: 3D Linear Viscoelastic Characterisation and Modelling of Bitumen

---

Equation 7.5. Moreover, the average strain  $\epsilon_{zz}$  of  $1.07 \times 10^{-4}$  was close to the imposed strain. The test plates exerted a radial stress  $\sigma_{rr}$  (Figure 7.14) within the range of -0.4 to 0.1 Pa. However, these ranges are less than the axial stress (0.29 Pa). The upper limit (0.1 Pa) of the imposed radial stress exists at the plate-bitumen interface, indicating that the plates are responsible for the bitumen's radial stress. According to Figure 7.16b, the test plates imposed a null radial deformations. The ratio of the average axial stress  $\bar{\sigma}$ , to the average axial strain,  $\epsilon_{zz}$ , was 2871 Pa. As the test conditions approaches oedometric state, the analysis of the test becomes inaccurate.

The results demonstrated a homogeneous state of stress and strain for both bitumen and DSR steel plates, as well as the outer diameter of the steel plates in contact with the bitumen.

The stress and strain tensor terms in bitumen near oedometric state ( $\nu = 0.49995$ ) are shown in the appendix (Figures C12 – C15).

### 7.4.5 Bitumen stiffness influence on the simulated modulus

In this section, the variation of the simulated modulus along the radial section of the bitumen is examined. Figures 7.17 shows the plots of normalised stress against the radial positions at Poisson's ratios 0.35 and 0.49995 respectively. The range of bitumen modulus examined were selected to represent the typical values of stiffnesses tested using the 4 mm parallel plate geometry ( $1.3 \times 10^9 Pa$  corresponded to the glassy modulus of binders from Section 7.1). The curves of the stiffnesses considered overlap quite well. This is further indicative of the non-existence of induced radial stresses in the test plates as seen in Figure 7.15. There exists high variation in the stiffnesses observed near oedometric condition as seen in Figure 7.17b. However, as suggested by (Orozco, 2020), an increase in aspect ratio is required to obtain a homogenous stress distribution near oedometric state.



## 7. Campaign 4: 3D Linear Viscoelastic Characterisation and Modelling of Bitumen

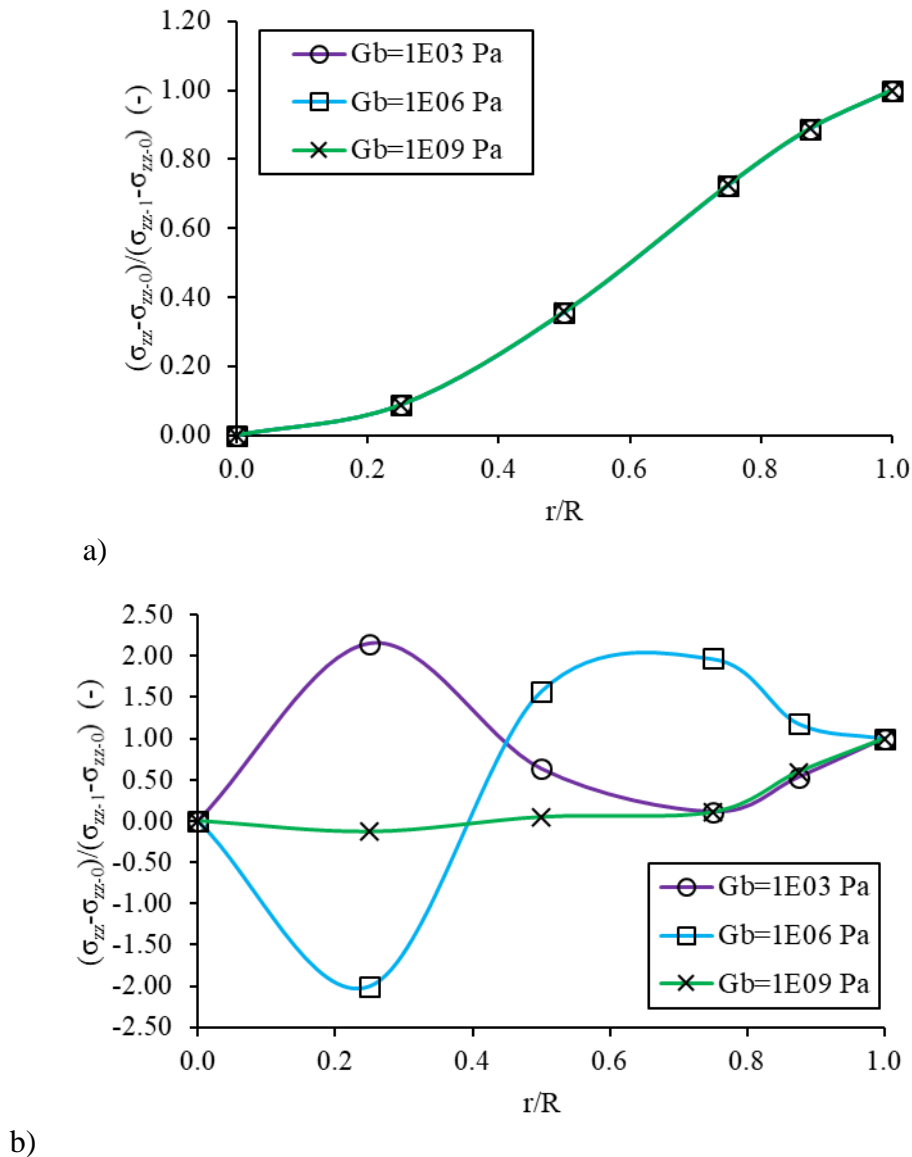


Figure 7.17 – Effect of bitumen stiffness on stress distribution along the axis of the bitumen at a constant Poisson's ratio a)0.35; b)0.49995

### 7.5 Correction method for measured DSR axial complex modulus

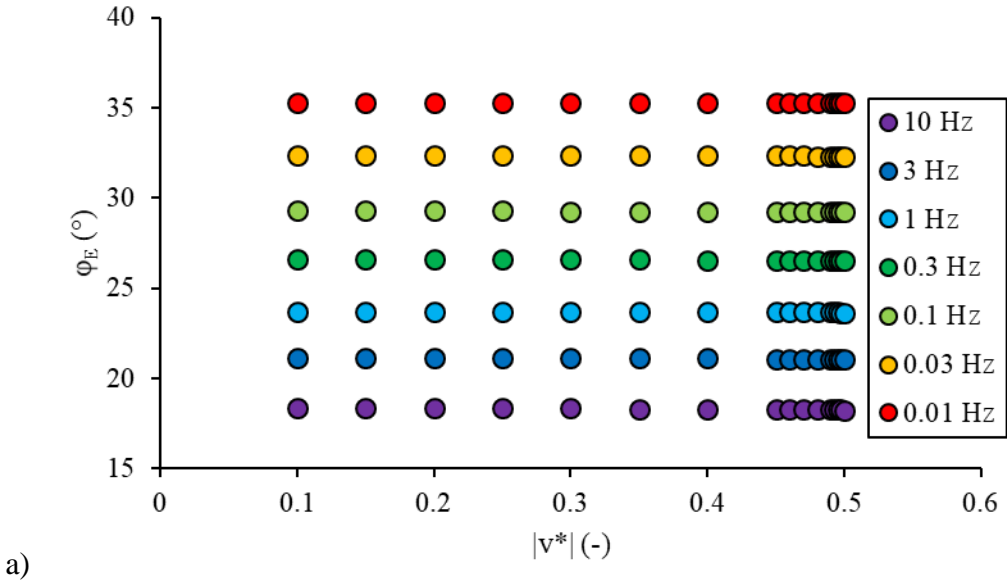
Finite element modelling of DSR axial complex modulus has been implemented. Stress and strain variations in binder samples with different aspect ratios has been examined.

Axial and shear complex modulus tests were performed using a DSR and Poisson's ratio calculated from experimental results. Poisson's ratio determined from indirect method of response measurements however, are often not in accordance with the values derived from direct measurements as seen in Section 7.3. It is therefore pertinent to correct the DSR measured axial complex modulus at any temperature and frequency pair, as the DSR shear complex modulus  $G^*$  values seem correct in order to determine the correct bitumen Poisson's ratio.

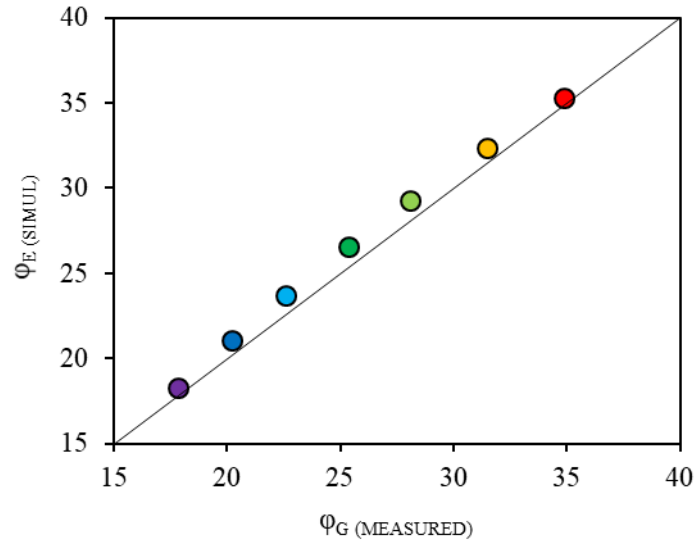
## 7. Campaign 4: 3D Linear Viscoelastic Characterisation and Modelling of Bitumen

It is important to state that the finite element model was isotropic linear elastic case and in frequency domain it is equivalent to isotropic linear viscoelastic in steady state. A FEM with an aspect ratio of 0.4 similar to the linear elastic model was created. To improve the performance and variability in terms of frequency and temperature, 2S2P1D model constants were utilised to optimise the FEM inputs. To avoid the increased stiffness seen with the glassy modulus  $G_0$  of bitumen, the 2S2P1D model constants derived in Chapter 5 were used. Here the glassy modulus  $G_0$  of B5070 bitumen was 1050 MPa. Frequency was in addition considered in simulation, which ranged from 0.01 Hz to 10 Hz as obtained in the complex modulus test. Although the linear elastic case could be considered since Poisson's ratio are to be determined in the low temperature range. However, it is equally important to have access to the phase angle of the simulated modulus of the bitumen.

The plot of the simulated phase angle against Poisson's ratio at  $-5^\circ\text{C}$  is shown in the Figure 7.18. It is clearly seen that the phase angle is independent of Poisson's ratio.



## 7. Campaign 4: 3D Linear Viscoelastic Characterisation and Modelling of Bitumen



b)

Figure 7.18 – Plots of a) Simulated phase angle at  $-5^{\circ}\text{C}$ ; b) measured phase angle  $\varphi_G$  and simulated phase angle  $\varphi_E$

Furthermore, there is a maximum of  $1.2^{\circ}$  difference between the simulated phase angle  $\varphi_E$  and input shear complex modulus phase angle  $\varphi_G$  at  $-5^{\circ}\text{C}/10\text{ Hz}$  as shown in Figure 7.18b.

As already seen from section 7.5.1 the oedometric effect depends on the value of  $\nu$ . Furthermore, in this context, it is presumed that the value of measured axial complex modulus is affected by these oedometric effect. Therefore, an attempt was made to determine the correct value of  $\nu$  in order to determine the right value of measured  $E^*$  ( $E_{measured}^*$ ). However, to effect this correction, the value of  $\nu$  is not known, therefore a method to determine the right value of  $\nu$  is explained as follows.

Firstly, the values of  $G^*$  obtained from shear complex modulus test is supposed correct. Then, 2S2P1D model calibrated on these data give the values of  $G^*$  ( $G_{2S2P1D}^*$ ) for any temperature and frequency. Therefore, the true value of  $E^*$  can be determined from equation 7.9 which is a function of  $\nu$

$$E_{true\ value}^* = 2G_{2S2P1D}^*(1 + \nu) \quad (7.9)$$

Where  $G_{2S2P1D}^*$  represents the shear complex modulus measured or taken from 2S2P1D model and  $\nu^*$  is taken as  $\nu$  (real number).

The ratio of the measured complex modulus ( $E_{measured}^*$ ) and  $E_{true\ value}^*$  in function of Poisson's ratio  $\nu$  yields a polynomial function as shown in the Figure 7.19

7. Campaign 4: 3D Linear Viscoelastic Characterisation and Modelling of Bitumen

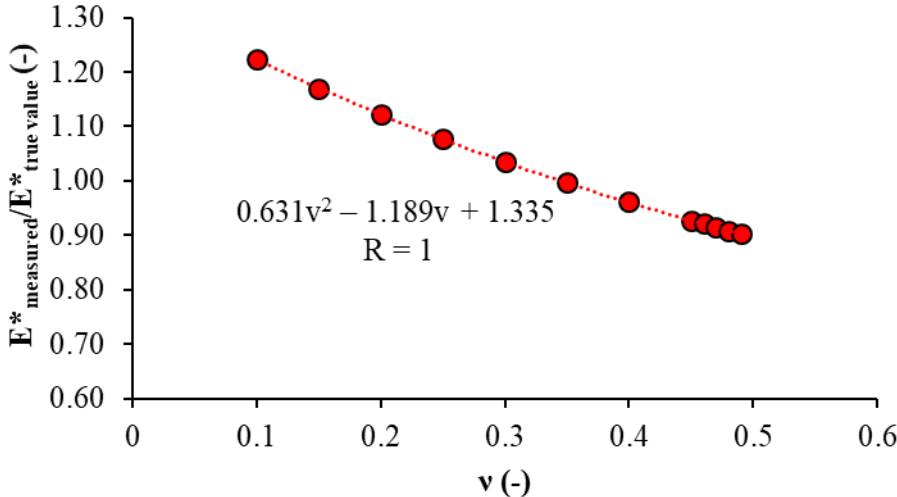


Figure 7.19 – Ratio of measured complex modulus and true material modulus as a function of Poisson’s ratio

Secondly, an FEM simulation of the apparent complex modulus denoted as  $E_{apparent}$  was performed using  $E_b$  as input. This simulation takes into account the oedometric effect and results depend on the Poisson’s ratio. Therefore, the ratio of the simulated apparent modulus ( $E_{apparent}$ ) and  $E_b$  in function of  $v$  yields a second order polynomial shown in the Figure 7.20. This plot corresponds to Figure 7.10 at aspect ratio  $s = 0.4$ .

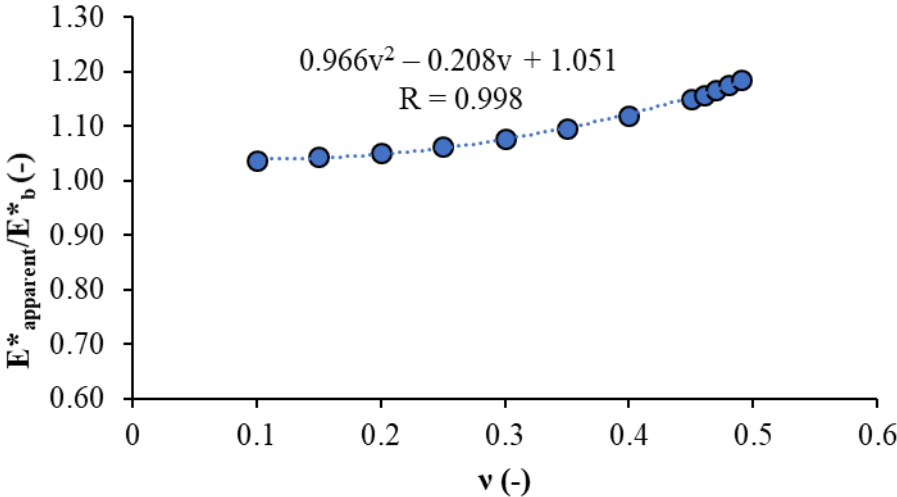


Figure 7.20 – Ratio of simulated apparent modulus and FEM input modulus as a function of Poisson’s ratio

### 7. Campaign 4: 3D Linear Viscoelastic Characterisation and Modelling of Bitumen

If the error in the  $E^*$  measurement is completely due to the oedometric effect, it is therefore assumed that similar effect occurs in the simulated complex modulus ( $E_{apparent}^*$ ). That means the  $\nu$  can be determined. This is the  $\nu$  needed to completely explain the error in the value of measured  $E^*$ . This can be achieved by equating both expressions as seen in equation 7.10. The solution of the resultant polynomial is then determined. The true value of  $E^*$  is therefore obtained.

$$\frac{E_{apparent}^*}{E_b^*} = \frac{E_{measured}^*}{E_{true\ value}^*} \tag{7.10}$$

As an example, the Poisson’s ratio of B5070 bitumen at  $-5^\circ\text{C}/10\text{ Hz}$  is determined as shown in Figure 7.21. Poisson’s ratio of 0.27 was determined. This value was used to calculate the correct value of axial complex modulus (948.6 MPa) using the expression in Equation 7.9 at this temperature and frequency pair. The corresponding phase angle of  $18^\circ$  is determined from Figure 7.18a at Poisson’s ratio of 0.27.

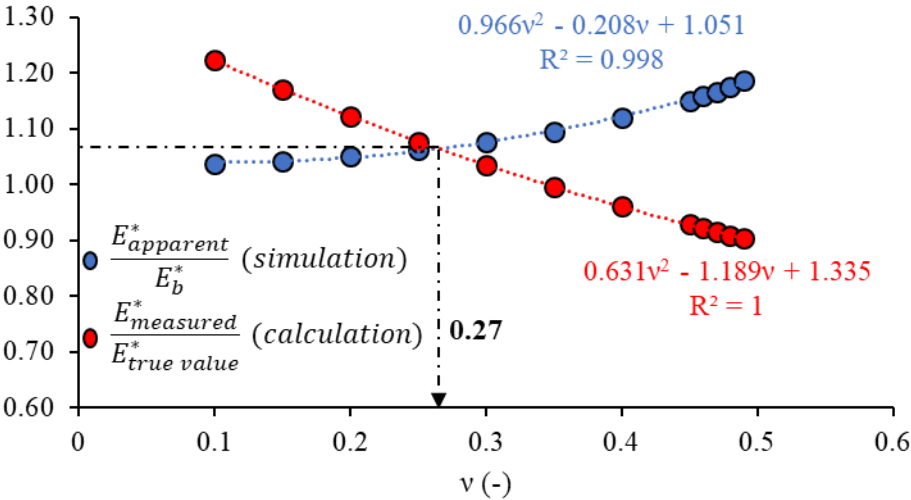


Figure 7.21 – B5070 bitumen Poisson’s ratio determination at  $-5^\circ\text{C}/10\text{ Hz}$  in order to correct the complex modulus ( $E_{measured}^*$ ) and obtain ( $E_{true\ value}^*$ )

These methods have been applied to determine the true values of the measured axial complex modulus at all temperatures and frequencies tested.

The comparison between the measured and corrected norms of axial complex modulus and phase angles are shown in Figure 7.22. A 12% maximum difference was observed with the measured and corrected modulus. Additionally, it was observed that a higher phase angle was

## 7. Campaign 4: 3D Linear Viscoelastic Characterisation and Modelling of Bitumen

measured by the DSR across all temperatures and frequencies. The phase angle value difference increased with a reduction in temperature as depicted in Figure 7.23b. This difference averaged  $1^\circ$  from  $10^\circ\text{C}$  to  $0^\circ\text{C}$  and increased to a maximum of  $5.5^\circ$  at  $-10^\circ\text{C}/10\text{ Hz}$ . This wide discrepancy in measured phase angle can only be attributed to the flaws of the DSR. Currently, there is no access to the raw measurement values either through the software interface or by observation through a connected oscilloscope to verify the true measurements.

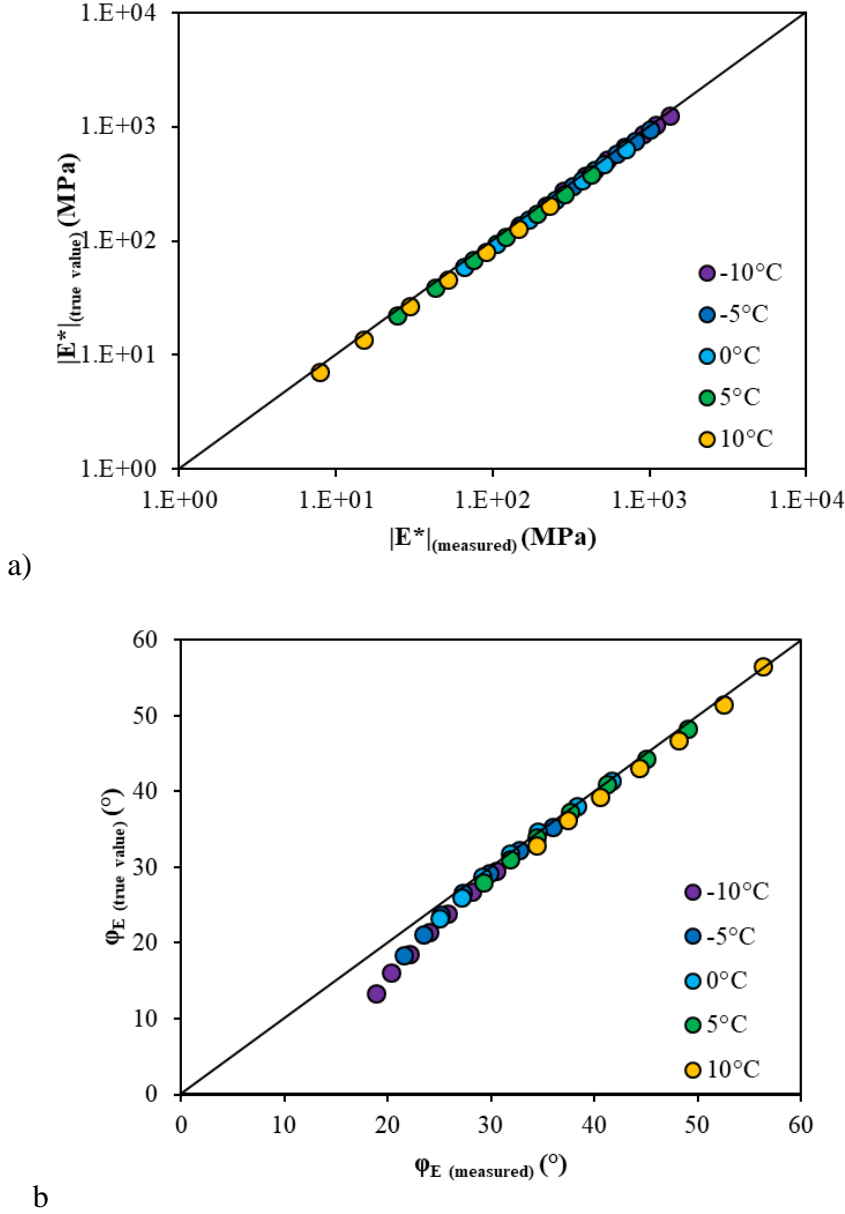


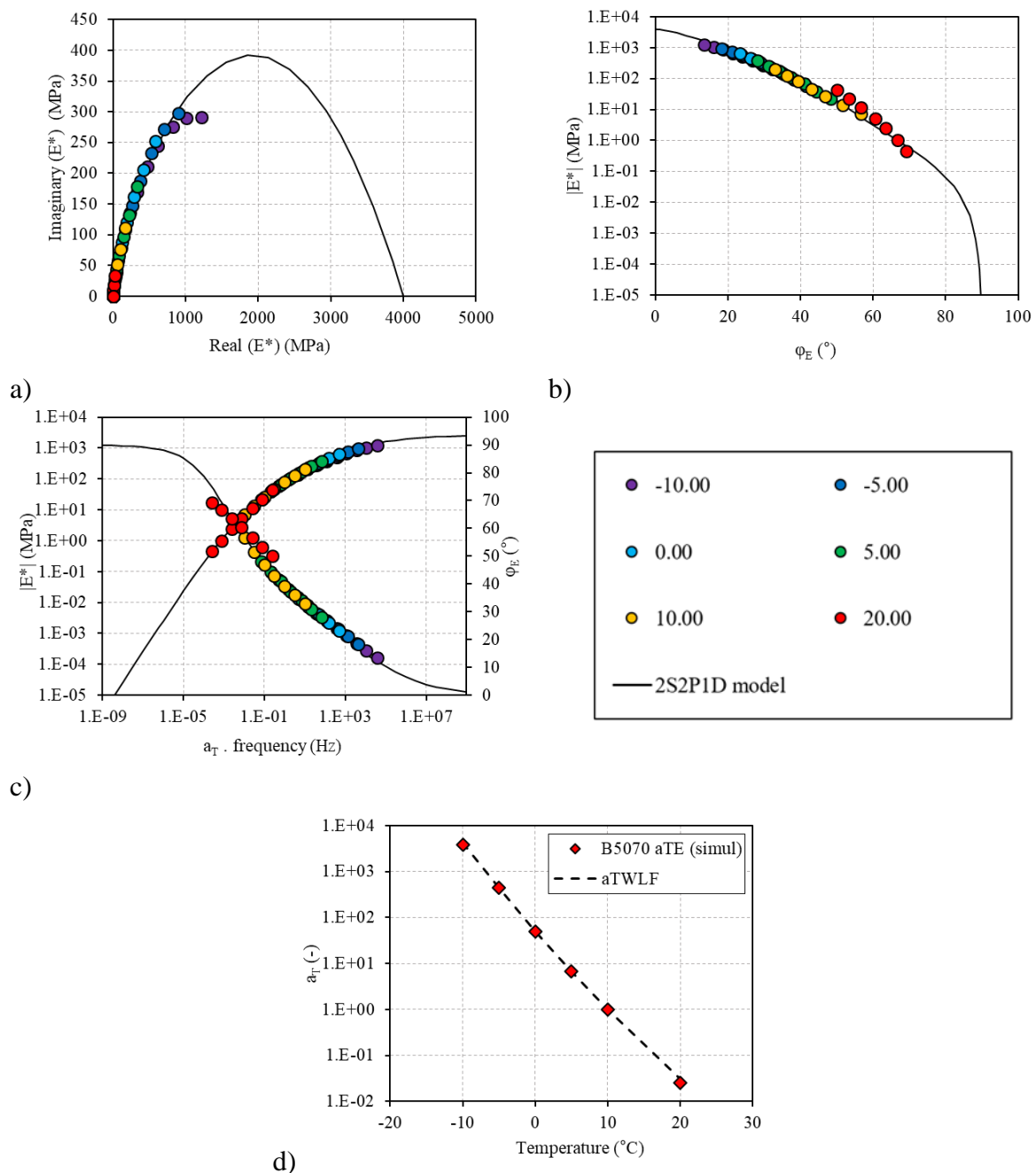
Figure 7.22 – Comparison between measured and simulated a) norm of axial complex modulus b) phase angles.

Figure 7.23 shows the Cole-Cole plot, Black diagrams, master curves of FEM corrected axial complex modulus experimental results fitted with 2S2P1D model of B5070 bitumen. The

## 7. Campaign 4: 3D Linear Viscoelastic Characterisation and Modelling of Bitumen

2S2P1D constants are displayed in Table 7.2a including the WLF parameters at 10°C reference temperature. The corresponding plots of B3550 bitumen is illustrated in appendix C16 and C17.

Overall, the 2S2P1D fit quite well the corrected moduli for both bitumen. The model constants are identical to the values obtained prior to correction with the exception of the glassy modulus  $E_0$  which equalled 3.9 *GPa* and 2.85 *GPa* for B5070 and B3550 respectively. Assuming a constant Poisson's ratio of 0.5, the corresponding shear glassy modulus  $G_0$  equals 1300 *MPa* and 933 *MPa* respectively. This of course is identical to the  $G_0$  value obtained in Table 7.1 for B5070 bitumen. Although both are in the range of 1 *GPa* as stated in the literatures.



## 7. Campaign 4: 3D Linear Viscoelastic Characterisation and Modelling of Bitumen

Figure 7.23 – 2S2P1D fitted B5070 bitumen FEM axial complex modulus  $E^*$  a) Cole-Cole curve; b) Black diagrams; c) master curves and d) shift factors fitted with WLF equation at  $T_{ref} = 10^\circ C$ .

Once,  $E_{true\ value}^*$  was obtained from  $E_{measured}^*$ , it is possible to obtain  $\nu^*$  with  $G_{2S2P1D}^*$  from the following equation:

$$\nu^* = \frac{E_{true\ value}^*}{2G_{2S2P1D}^*} - 1 \quad (7.12)$$

The phase angles of Poisson's ratio were derived from the real and imaginary part relationships stated in Equations 7.13 and 7.14.

$$\nu'_{simul}(\omega) = \frac{E_{true\ value}^*(\omega)}{2G_{2S2P1D}^*(\omega)} \cos(\varphi_{E_{true\ value}^*} - \varphi_{G_{2S2P1D}^*}) - 1 \quad (7.13)$$

$$\nu''_{simul}(\omega) = \frac{E_{true\ value}^*(\omega)}{2G_{2S2P1D}^*(\omega)} \sin(\varphi_{G_{2S2P1D}^*} - \varphi_{E_{true\ value}^*}) \quad (7.14)$$

Where  $E_{true\ value}^*$  represents the corrected measured axial complex modulus values,

$G_{2S2P1D}^*$  represents the measured shear complex modulus or obtained from 2S2P1D

$\varphi_{E_{true\ value}^*}$  represents the phase angle that corresponds to  $E_{true\ value}^*$  and;

$\varphi_{G_{2S2P1D}^*}$  represents the phase angle that corresponds to  $G_{2S2P1D}^*$

The isotherm plots of norms of simulated complex Poisson's ratio and the corresponding phase angles of B5070 bitumen are shown in Figure 7.24a. The corresponding fitted master curves of the Poisson's ratio are equally shown in Figure 7.24b. A gentle reduction in complex Poisson's ratio values with frequency is observed. The phase angles equally decreased with frequency as expected. The Poisson's ratio values ranged between 0.16 at low temperature/high frequency to 0.46 at high temperature/low frequency. The phase angles ranged between  $-4.6$  to  $0^\circ$ . These values however agree with those stated in the literatures as seen in (Hervé Di Benedetto et al., 2007).

The 2S2P1D constants are listed in Table 7.2b. The identical shift factors used to represent the LVE characteristics of the unmodified bitumen in axial and shear loading modes are also illustrated by the overlap of the corrected normalised axial complex modulus Cole-Cole, Black



## 7. Campaign 4: 3D Linear Viscoelastic Characterisation and Modelling of Bitumen

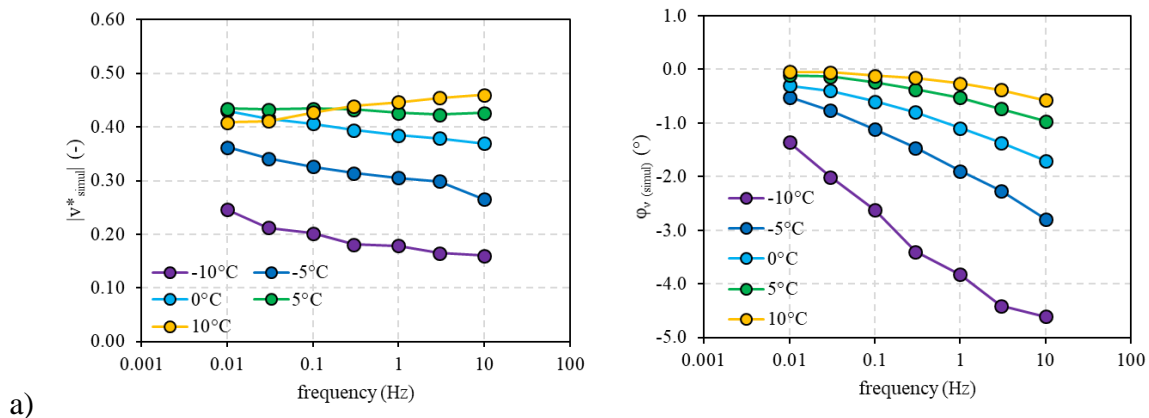
diagram curves with that of the normalised shear complex modulus ones as seen in the Figure 7.25 (B5070) and as displayed in the appendix Figure C18 (B3550).

In general, the model fits quite well the phase angles and a good tendency are observed on the plots of the complex Poisson's ratio for both bitumen considered. As stated earlier, it is impossible to form a unique master curve of norms of Poisson's ratio and the corresponding phase angles with an identical shift factor.

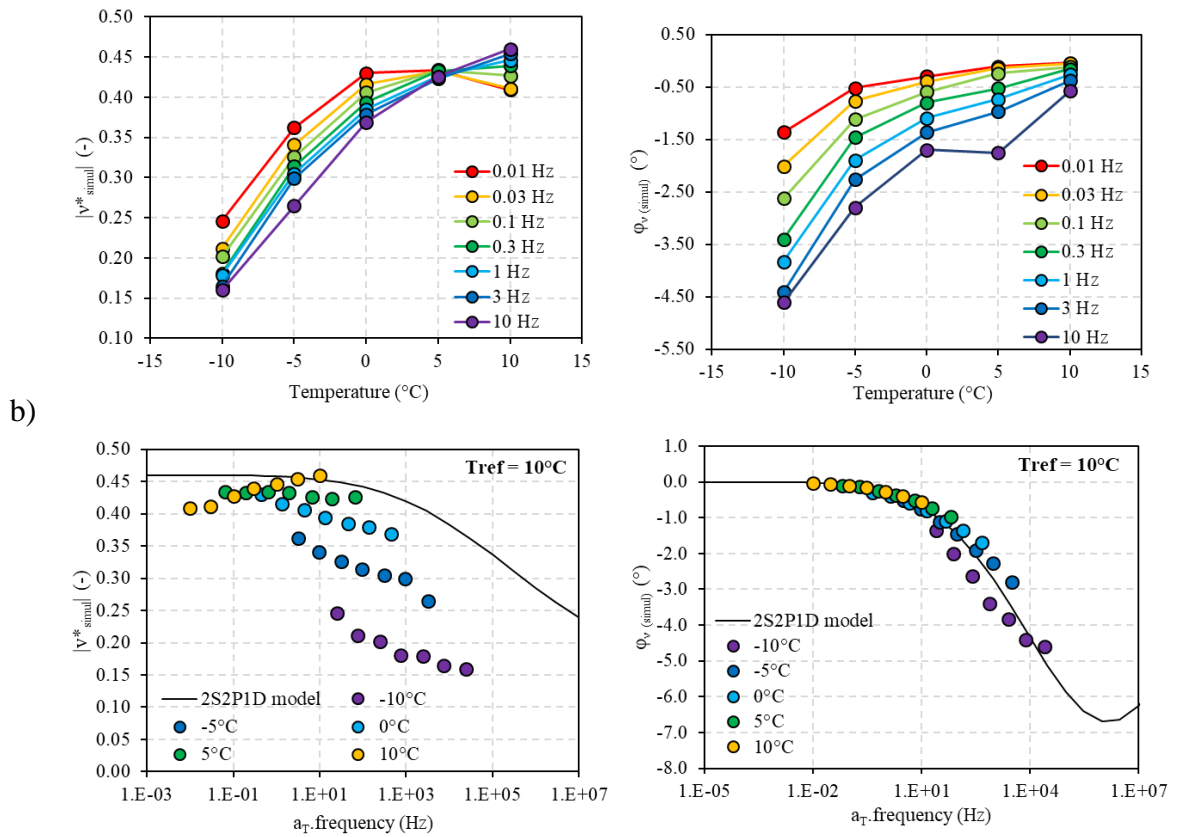
Table 7.2 - 2S2P1D constants and WLF parameters at  $T_{ref} = 10^{\circ}\text{C}$  for B5070 and B3550 bitumen FEM corrected axial complex moduli

Binder	$E_{00}$ (MPa)	$E_0$ (MPa)	$k$	$h$	$\delta$	$\tau$ (s)	$\beta$	$C_1$	$C_2$
B5070	0	3900	0.24	0.59	5.00	0.0008	330	22	151
B3550	$E_{00}$ (MPa)	$E_0$ (MPa)							
a)	0	2850	0.25	0.60	3.40	0.0026	120	22	140

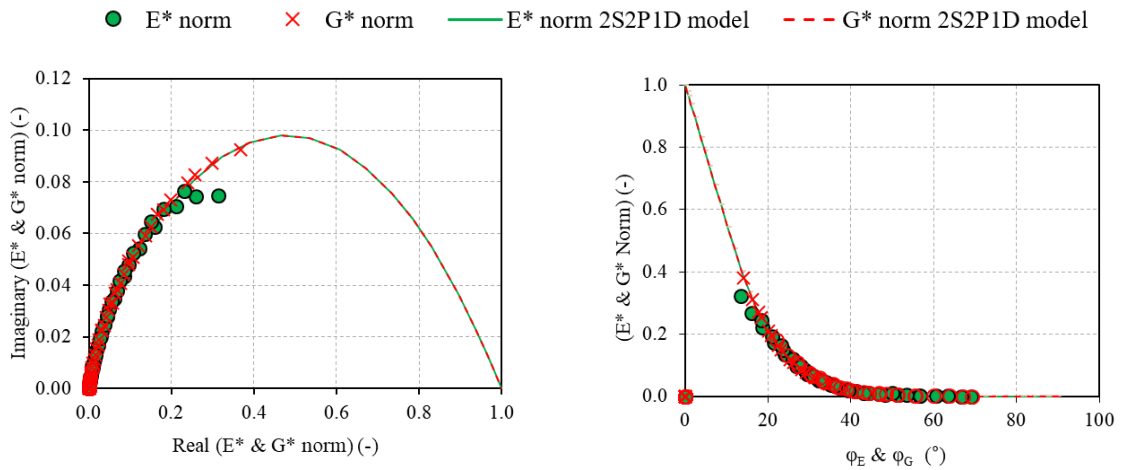
Binder	$\nu_{00}$ (-)	$\nu_0$ (-)	$\gamma_{Ev}$	$\tau_\nu$ (s)
B5070	0.46	0.16	5.00	0.0001
b) B3550	0.42	0.32	1.20	0.001



## 7. Campaign 4: 3D Linear Viscoelastic Characterisation and Modelling of Bitumen



c) *Figure 7.24 – Norms and phase angles of simulated B5070 bitumen Poisson's ratio a) isotherms b) isochrones; c) 2S2P1D fitted master curves at  $T_{ref} = 10^\circ\text{C}$ .*



a)

b)

# 7. Campaign 4: 3D Linear Viscoelastic Characterisation and Modelling of Bitumen

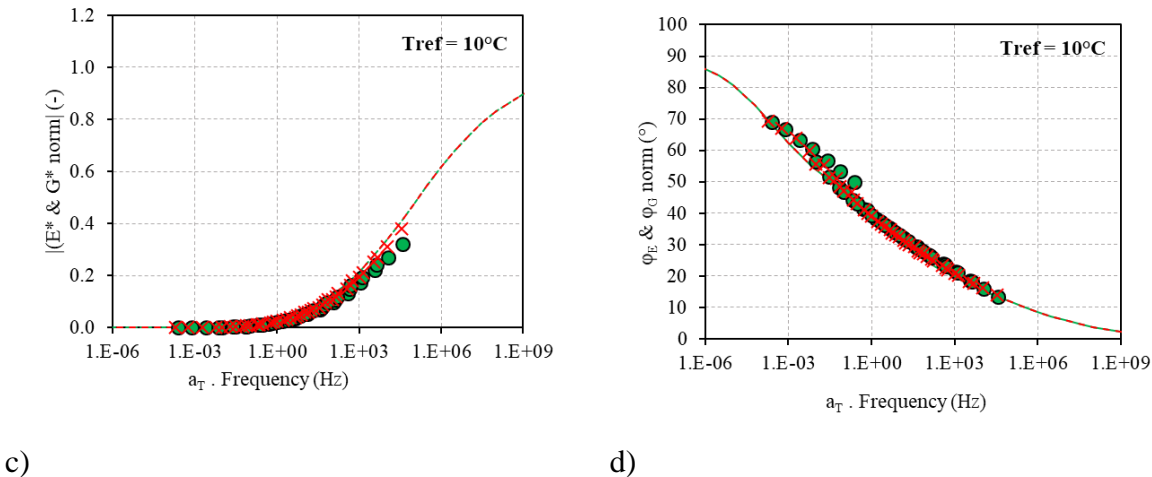


Figure 7.25 – Corrected experimental results and fitted 2S2P1D curves of normalised complex modulus of B5070 bitumen measured at 0.1% axial strain a)  $E^*_{norm}$  and  $G^*_{norm}$  in Cole-Cole plane, b)  $E^*$  and  $G^*_{norm}$  in black space, c)  $|E^*$  and  $G^*_{norm}|$  master curves d)  $\phi_E$  and  $\phi_{Gnorm}$  master curves at  $T_{ref} = 10^\circ C$

It is pertinent to state that, this correction methods are only applicable to unmodified bitumen. This can be attributed to the fact that the correction factor required exceeds the maximum range for this aspect ratio. The polymer modified bitumen correction curves converged at few temperature and frequency pairs. An example of such frequency and temperature at which it seemed possible to determine Poisson’s ratio of PmB was  $-5^\circ C/0.1$  Hz. This is shown in the Figure 7.26. However, the temperature and frequency pairs at which the curves converged indicated a Poisson’s ratio of 0.5 and above.

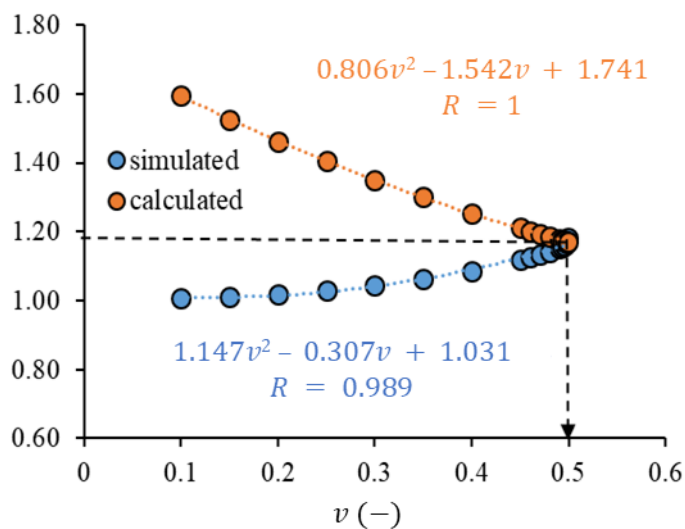


Figure 7.26 – PmB bitumen Poisson’s ratio determination at  $-5^\circ C/0.1$  Hz.

## 7. Campaign 4: 3D Linear Viscoelastic Characterisation and Modelling of Bitumen

---

Furthermore, the phase angles derived from the FEM appeared higher than measured and experimentally obtainable values. The complex polymer chains resulting from bitumen modification appear challenging for the FEM software to simulate.

### 7.6 Conclusions of Campaign 4

This fourth campaign focused on the 3D linear viscoelastic characterization and modelling of three different bitumen with a DSR. The test was performed in line with the procedures stated in campaign 3. The test temperatures ranged from  $-10^{\circ}\text{C}$  to  $30^{\circ}\text{C}$ .

- Tests performed below  $-10^{\circ}\text{C}$  resulted in the cracking of test samples due to their glassy nature at these temperatures. Furthermore, due to the size of the test sample, a limited axial force can be applied to maintain its form.
- The axial complex modulus and phase angle signals greatly improved with strain magnitude.
- The experimental results were successfully fitted with 2S2P1D rheological model. A maximum glassy modulus  $E_0$  of  $4500\text{ MPa}$  and  $G_0$   $1300\text{ MPa}$  were recorded for the test binders.
- There were differences between  $G_0$  values obtained with the Peltier setup and Convention oven setup. This was attributed to the use of different temperature regulation equipment, bitumen thermal history and inaccuracy in trimming due to the size difference between upper and lower plate. Furthermore, high axial complex modulus phase angles were measured at low temperatures.
- Identical 2S2P1D constants were used to fit each unmodified bitumen in axial and shear test mode. This varied for modified bitumen. Furthermore, there exist discrepancies between the normalised axial and shear complex modulus measurements at low temperatures.
- Bitumen Poisson's ratio determined from experimental measurements were found to possess wider ranges than that specified in the literature. The phase angles were negative and reduced with frequency. These values expressed in terms of temperature, peaked at  $0^{\circ}\text{C}$ .
- Modified bitumen calculated Poisson's ratio values are higher than 0.5.
- Identical shift factors were used to create master curves of Poisson's ratio phase angles and complex modulus master curves. Poisson's ratio verified the Time temperature superposition principle (TTSP).

## 7. Campaign 4: 3D Linear Viscoelastic Characterisation and Modelling of Bitumen

---

- The combination of  $E^*$  and  $G^*$  2S2P1D model cannot be used to determine the Poisson's ratios of bitumen.
- Homogeneity of stress distribution along the axis of the binder increased with a reduction in aspect ratio. Overall, stress and strain distributions are near homogenous along the axis of the binder at 0.4 aspect ratio.
- The average stress observed at 5 mm test height (0.4 aspect ratio) was 7% higher than the stress expected at the test gap at which the modulus measured is independent of the test gap. Also, the stress calculated by the analytical solution is identical to the simulated stress.
- The corrected axial complex modulus ( $E^*$ ) and Poisson's ratio ( $\nu^*$ ) fitted with 2S2P1D resulted in glassy modulus  $E_0$  of bitumen that ranged between 2.85 GPa and 3.9 GPa.
- Poisson's ratio values ranged between 0.16 and 0.46 and the phase angles varied between -4.6 to 0.
- The normalized axial  $E^*$  (corrected) and shear  $G^*$  (measured) complex modulus measurements of unmodified bitumen overlapped quite well.
- Experimental axial complex modulus and phase angles were found to be higher than the simulated values.
- The complex modulus correction method introduced in this thesis functions solely for unmodified binders. Therefore, unmodified bitumen Poisson's ratio can be determined using a combination of DSR measurements and finite element analysis.

## 8. Conclusions and Perspectives

This thesis investigated the three-dimensional linear viscoelastic characterization of bitumen, focusing on the characterization of bitumen using a dynamic shear rheometer. The scope of the study was limited to four distinct campaigns, each with its own set of objectives and conclusions. The initial two campaigns served as a foundation for the final two campaigns. The summaries are listed beneath.

Campaign 1 was primarily concerned with the shear oscillatory linear viscoelastic limit of binders. A DSR was used to determine the LVE limit of binders across a wide range of temperatures and frequencies. Introduced is a method for quantifying the physical hardening influence on the LVE limit at low temperatures. The time-temperature superposition principle of bitumen LVE was demonstrated, and then a 2S2P1D rheological model was fitted to the data. Following are the conclusions derived from the campaign:

- Physical hardening effect on shear complex modulus  $G^*$  appears to be temperature and time dependent.
- Physical hardening effect on the LVE limit was quantified based on the regression on stiffness and found to be non-negligible in the determination of LVE limits of binders at low temperatures. This can increase the LVE limit of a binder.
- DSR determined binder LVE limits were found to verify the time temperature superposition principle.
- 2S2P1D simulated well the LVE limit of binders across the range of tested temperatures and frequencies.
- Linearity strain criterion for bitumen varies from 0.2% to 10,000%.

The focus of the second campaign was the linear viscoelastic characterization of binders in shear. The linear viscoelastic properties of two unmodified bitumens and one polymer-modified bitumen (PmB) were examined. The LVE behaviour was characterised by a complex shear modulus test conducted at temperatures varying from  $-30^{\circ}\text{C}$  to  $70^{\circ}\text{C}$  and frequency ranges of 10 Hz to 0.01 Hz. Following are the conclusions derived from the campaign:

- Torque limitations encountered during the LVE characterisation of bitumen at low temperatures with 8 mm parallel plate can be overcome by the use of 4 mm parallel plate.

- It is important to switch of the AGC function of the DSR to prevent sample breakage at low temperatures while using Peltier and hood assembly.
- Time-Temperature-Superposition Principle (TTSP) and Partial Time Temperature Superposition Principle (PTTSP) were verified by the two unmodified binders and modified binder respectively.
- Unmodified bitumen shift factors deviated from the WLF law beyond  $-20^{\circ}\text{C}$ . However, the shift factors were successfully fitted with the modified Kaelble equation.
- The 2S2P1D model was well fitted to two unmodified binder complex modulus test results. Except for the PmB at low equivalent frequencies (high temperatures/low frequencies), the obtained simulations are satisfactory.

A DSR equipped with two motors (upper and lower) was employed in Campaign 3 to determine the axial ( $E^*$ ) and shear ( $G^*$ ) complex modulus of an unmodified bitumen. The bitumen was subjected to an axial strain amplitude sweep test. A complex modulus test in tension-compression followed by shear on bitumen samples with various test gaps was used to characterise the LVE behaviour. The campaign resulted in the following conclusions:

- DSR can be used to determine the linear viscoelastic limit of binders through a strain amplitude sweep test in tension-compression. The axial strain amplitude limit of bitumen varies from 0.1% (1000  $\mu\text{m}/\text{m}$ ) to 7%.
- Due to the oedometric effect caused by the aspect ratio of the sample, selecting the proper geometry for DSR experiments in axial mode was essential for accurately characterising the rheological behaviour of the binder.
- The time-temperature superposition principle was validated for both the axial and shear complex moduli of the tested bitumen.
- The linear viscoelastic properties of the binder were accurately simulated by the 2S2P1D model over the temperature and frequency ranges evaluated in shear oscillatory and tension-compression measurements. Furthermore, both shear  $G^*$  and axial  $E^*$  complex moduli were simulated with the same set of 2S2P1D constants and shift factors  $a_T$ .

In Campaign 4, three-dimensional linear viscoelastic characterisation and modelling of binders were performed. The influence of increment in axial strain amplitude on the measured axial complex modulus was examined. TTSP verification of binders were examined. Complex modulus test in tension-compression and shear were used to characterise the LVE properties of

binders. The results of the test on binders were fitted with 2S2P1D model. Poisson's ratio was determined from the experimental result and also the 2S2P1D simulated results. The axial complex modulus test was simulated in linear elastic conditions with numerical finite element method. A finite element parametric study with varying bitumen properties ( $E$ ,  $\nu$ ) and test binder aspect ratio (ratio of diameter to thickness) was done to provide axial modulus for different binder aspect ratios. Finally, the axial complex modulus test was again simulated in linear viscoelastic conditions followed by a parametric study in the frequency domain. A method to correct the experimental axial complex modulus was introduced and bitumen Poisson's ratios determined. The main conclusions of Campaign 4 were drawn as follows:

- The axial complex modulus and phase angle signals improved significantly as strain magnitude increased.
- The axial and shear complex modulus of the tested bitumen were able to validate the time-temperature superposition principle and partial time-temperature superposition principle. In axial and shear testing conditions, the temperature shift factors for each bitumen samples were comparable.
- The 2S2P1D rheological model was effectively fitted to the experimental data. Identical 2S2P1D constants were used to fit each unmodified bitumen in axial and shear test modes, and all binder WLF constants were quasi identical.
- Master curves of Poisson's ratio phase angle and complex modulus were created by employing identical shift factors. The Poisson ratio verified the TTSP.
- At an aspect ratio of 0.4 (5 mm test gap), the stress and strain distributions are near homogeneous along the axis of the binder.
- Bitumen Poisson's ratio determined varied between 0.16 at low temperature/high frequency and 0.46 at high temperature/low frequency. Phase angles varied between -4.6 to 0°.
- Glassy modulus  $E_0$  determined for all unmodified bitumen after correction varied between 2.8 *GPa* to 3.9 *GPa*. The introduced correction method is only applicable to unmodified bitumen.



**Perspectives**

- The quantification of physical hardening during low temperature strain amplitude sweep test has been demonstrated with unmodified binders. It is equally necessary to repeat this procedure for a modified bitumen
- As there appears to be no reduction in linearity limits for low penetration grade bitumen when compared to higher penetration grade bitumen, additional strain sweep tests on similar grades of bitumen are required to reaffirm the assumption of bitumen penetration grade linearity independence.
- Potential strategies for improving the values of  $G_0$  include conducting experiments on materials manufactured in a mould, employing plates of identical diameters in both the upper and lower plates of the DSR, and evaluating samples that are devoid of any bulge.
- To further validate the functionality of this Poisson's ratio determination and axial complex modulus correction method, further test on other types of bitumen is necessary. It could aid in enhancing the veracity of the relationship between  $E^*$  and  $G^*$  of modified and unmodified binders.

**References**

- Abhijith, K., & Kumar, P. (2020). Quantifying particulate matter reduction and their deposition on the leaves of green infrastructure. *Environmental Pollution*, 265, 114884. doi:<https://doi.org/10.1016/j.envpol.2020.114884>
- Airey, G., Rahimzadeh, B., & Collop, A. (2003). Linear viscoelastic performance of asphaltic materials. *Road Materials and Pavement Design*, 4(3), 269-292. doi:<https://doi.org/10.1080/14680629.2003.9689949>
- Airey, G. D. (1997). *Rheological characteristics of polymer modified and aged bitumens*. University of Nottingham Nottingham, UK,
- Airey, G. D. (2002a). Rheological evaluation of ethylene vinyl acetate polymer modified bitumens. *Construction and Building Materials*, 16(8), 473-487. doi:[https://doi.org/10.1016/S0950-0618\(02\)00103-4](https://doi.org/10.1016/S0950-0618(02)00103-4)
- Airey, G. D. (2002b). Use of Black Diagrams to Identify Inconsistencies in Rheological Data. *Road Materials and Pavement Design*, 3(4), 403-424. doi:10.1080/14680629.2002.9689933
- Airey, G. D., & Rahimzadeh, B. (2004). Combined bituminous binder and mixture linear rheological properties. *Construction and Building Materials*, 18(7), 535-548. doi:<https://doi.org/10.1016/j.conbuildmat.2004.04.008>
- Airey, G. D., Rahimzadeh, B., & Collop, A. C. (2002). Linear viscoelastic limits of bituminous binders. *Asphalt Paving technology*, 71, 89-115.
- Airey, G. D., Rahimzadeh, B., & Collop, A. C. (2003). Viscoelastic linearity limits for bituminous materials. *Materials and Structures*, 36, 643-647. doi:<https://doi.org/10.1007/BF02479495>
- Airey, G. D., Rowe, G. M., Sias, J. E., Di Benedetto, H., Sauzeat, C., & Dave, E. V. (2021). Black Space Rheological Assessment of Asphalt Material Behavior. *Journal of Testing and Evaluation*, 50(2). doi:<https://doi.org/10.1520/JTE20210205>
- Anderson, D. A., Christensen, D. W., Bahia, H. U., Dongre, R., Sharma, M., Antle, C. E., & Button, J. J. S. H. R. P., National Research Council, Washington, DC. (1994). Binder characterization and evaluation, volume 3: Physical characterization.
- Anderson, D. A., Christensen, D. W., Roque, R., & Robyak, R. A. (1992). Rheological properties of polymer-modified emulsion residue. In *Polymer Modified Asphalt Binders*: ASTM International.
- Anderson, D. A., & Marasteanu, M. O. (1999). Physical hardening of asphalt binders relative to their glass transition temperatures. *Transportation Research Record*, 1661(1), 27-34. doi:<https://doi.org/10.3141/1661-05>
- Arabani, M., & Pedram, M. (2016). Laboratory investigation of rutting and fatigue in glassphalt containing waste plastic bottles. *Construction and Building Materials*, 116, 378-383. doi:<https://doi.org/10.1016/J.CONBUILDMAT.2016.04.105>
- Aschenbrener, T. (1995). *INVESTIGATION OF LOW TEMPERATURE THERMAL CRACKING IN HOT MIX ASPHALT. FINAL REPORT*. Retrieved from
- Babadopulos, L. (2017). *Phenomena occurring during cyclic loading and fatigue tests on bituminous materials: Identification and quantification*. Lyon,
- Baglieri, O., Dalmazzo, D., Barazia, M., Tabatabaee, H. A., & Bahia, H. U. (2012). Influence of Physical Hardening on the Low-Temperature Properties of Bitumen and Asphalt Mixtures. *Procedia - Social and Behavioral Sciences*, 53, 504-513. doi:<https://doi.org/10.1016/j.sbspro.2012.09.901>
- Bahia, H. U., & Anderson, D. A. (1993). Glass transition behavior and physical hardening of asphalt binders (with discussion). *Journal of The Association of Asphalt Paving Technologists*, 62.

## References

---

- Bahia, H. U., Hanson, D., Zeng, M., Zhai, H., Khatri, M., & Anderson, R. (2001). *Characterization of modified asphalt binders in superpave mix design*.
- Bari, J., & Witczak, M. W. (2005). Evaluation of the effect of lime modification on the dynamic modulus stiffness of hot-mix asphalt: use with the new mechanistic–empirical pavement design guide. *Transportation Research Record*, 1929(1), 10-19. doi:<https://doi.org/10.3141/1929-02>
- Bari, J., & Witczak, M. W. (2007). New predictive models for viscosity and complex shear modulus of asphalt binders: for use with mechanistic-empirical pavement design guide. *Transportation Research Record* 2001(1), 9-19.
- Bell, C. A. (1989). *Summary report on aging of asphalt-aggregate systems* (Vol. 89): Strategic Highway Research Program, National Research Council.
- Büchner, J., Wistuba, M., & Klüter, I. (2020). Asphalt Binder Testing using 4 mm parallel plate geometry of Dynamic Shear Rheometer: Interlaboratory Study including test results of 20 participating laboratories from Belgium, Czech Republic, Denmark, Finland, France, Germany, Italy, Lithuania, and Poland; Final Report.
- Büchner, J., Wistuba, M. P., Remmler, T., & Wang, D. (2019). On low temperature binder testing using DSR 4 mm geometry. *Materials and Structures*, 52, 1-11. doi:<https://doi.org/10.1617/s11527-019-1412-3>
- Cardona, D. A. R. (2016). *Characterisation of thermomechanical properties of bituminous mixtures used for railway infrastructures*. Université de Lyon,
- Cardone, F., Frigio, F., Ferrotti, G., & Canestrari, F. (2015). Influence of mineral fillers on the rheological response of polymer-modified bitumens and mastics. *Journal of traffic and transportation engineering*, 2(6), 373-381. doi:<https://doi.org/10.1016/J.JTTE.2015.06.003>
- Chavez, F., Marcobal, J., & Gallego, J. (2019). Laboratory evaluation of the mechanical properties of asphalt mixtures with rubber incorporated by the wet, dry, and semi-wet process. *Construction and Building Materials*, 205, 164-174. doi:<https://doi.org/10.1016/j.conbuildmat.2019.01.159>
- Chen, J., Huang, B., & Shu, X. (2013). Air-void distribution analysis of asphalt mixture using discrete element method. *Journal of Materials in Civil Engineering*, 25(10), 1375-1385. doi:<https://doi.org/10.1061/%28ASCE%29MT.1943-5533.0000661>
- Christensen, D. W., & Anderson, D. A. (1992). Interpretation of dynamic mechanical test data for paving grade asphalt cements (with discussion). *Journal of The Association of Asphalt Paving Technologists*, 61.
- Christensen, D. W., & Bonaquist, R. (2015). Improved Hirsch model for estimating the modulus of hot-mix asphalt. *Road Materials and Pavement Design*, 16(sup2), 254-274. doi:<https://doi.org/10.1080/14680629.2015.1077635>
- Christensen Jr, D., Pellinen, T., & Bonaquist, R. (2003). Hirsch model for estimating the modulus of asphalt concrete. *Journal of The Association of Asphalt Paving Technologists*, 72.
- Clopotel, C., Velasquez, R., & Bahia, H. (2012). Measuring physico-chemical interaction in mastics using glass transition. *Road Materials and Pavement Design*, 13(sup1), 304-320. doi:<https://doi.org/10.1080/14680629.2012.657095>
- Colorado Asphalt Pavement Association (2023). Retrieved from <https://www.co-asphalt.com/assets/docs/vma-justification.pdf>
- Coutinho, R. P., Babadopulos, L. F., Freire, R. A., Castelo Branco, V. T., & Soares, J. B. (2014). The use of stress sweep tests for asphalt mixtures nonlinear viscoelastic and fatigue damage responses identification. *Materials and Structures*, 47(5), 895-909. doi:<https://doi.org/10.1617/S11527-013-0101-X>

## References

---

- Crowson, R. J., & Arridge, R. G. (1979). Linear viscoelastic properties of epoxy resin polymers in dilatation and shear in the glass transition region: 2. Measurement of the glass transition temperature. *Polymer*, 20(6), 747-754. doi:<https://doi.org/10.1016/0032-3861%2879%2990250-7>
- Da Silva, L. S., de Camargo Forte, M. M., de Alencastro Vignol, L., & Cardozo, N. S. M. J. J. o. M. S. (2004). Study of rheological properties of pure and polymer-modified Brazilian asphalt binders. *Journal of Materials Science*, 39(2), 539-546. doi:<https://doi.org/10.1023/B%3AJMSC.0000011509.84156.3B>
- Dave, E. V., & Hoplin, C. (2015). Flexible pavement thermal cracking performance sensitivity to fracture energy variation of asphalt mixtures. *Road Materials and Pavement Design*, 16(sup1), 423-441. doi:10.1080/14680629.2015.1029697
- Delaporte, B. (2006). Etude de la rhéologie des mastics bitumineux à l'aide d'un rhéomètre à cisaillement annulaire. *Revue Européenne de Génie Civil*, 10(8), 999-999. doi:<https://doi.org/10.1080/17747120.2006.9692880>
- Delaporte, B., Di Benedetto, H., Chaverot, P., & Gauthier, G. (2009). Linear viscoelastic properties of bituminous materials including new products made with ultrafine particles. *Road Materials and Pavement Design*, 10(1), 7-38. doi:<https://doi.org/10.1080/14680629.2009.9690180>
- Delorme, J., & Wendling, L. (2007). LPC Bituminous Mixtures Design Guide, The RST Working Group. In: Design.
- Di Benedetto, H. (1998). *Modélisation: écart entre état des connaissances et applications*. Paper presented at the Journée LAVOC: Ecole Polytechnique Fédérale de Lausanne (EPFL). Septembre, Suisse.
- Di Benedetto, H., & Corté, J. (2005). *Matériaux routiers*. Paris: Hermes-Lavoisier.
- Di Benedetto, H., De La Roche, C., Baaj, H., Pronk, A., & Lundström, R. (2004). Fatigue of bituminous mixtures. *Materials and Structures*, 37(3), 202-216. doi:<https://doi.org/10.1007/BF02481620>
- Di Benedetto, H., Delaporte, B., & Sauzéat, C. (2007). Three-dimensional linear behavior of bituminous materials: experiments and modeling. *International Journal of Geomechanics*, 7(2), 149-157. doi:<https://doi.org/10.1061/%28ASCE%291532-3641%282007%297%3A2%28149%29>
- Di Benedetto, H., Gabet, T., Grenfell, J., Perraton, D., Sauzéat, C., & Bodin, D. (2013). Mechanical testing of bituminous mixtures. In *Advances in Interlaboratory Testing and Evaluation of Bituminous Materials* (pp. 143-256): Springer.
- Di Benedetto, H., Mondher, N., Sauzéat, C., & Olard, F. (2007). Three-dimensional thermo-viscoplastic behaviour of bituminous materials: the DBN model. *Road Materials and Pavement Design*, 8(2), 285-315. doi:<https://doi.org/10.1080/14680629.2007.9690076>
- Di Benedetto, H., Nguyen, Q. T., & Sauzéat, C. (2011). Nonlinearity, heating, fatigue and thixotropy during cyclic loading of asphalt mixtures. *Road Materials and Pavement Design*, 12(1), 129-158. doi:<https://doi.org/10.1080/14680629.2011.9690356>
- Di Benedetto, H., Olard, F., Sauzéat, C., & Delaporte, B. (2004). Linear viscoelastic behaviour of bituminous materials: From binders to mixes. *Road Materials and Pavement Design*, 5(sup1), 163-202. doi:<https://doi.org/10.1080/14680629.2004.9689992>
- Di Benedetto, H., Sauzéat, C., & Sohm, J. (2009). Stiffness of bituminous mixtures using ultrasonic wave propagation. *Road Materials and Pavement Design*, 10(4), 789-814. doi:<https://doi.org/10.1080/14680629.2009.9690227>
- Doubbaneh, E. (1995). *Comportement mécanique des enrobés bitumineux en «petites» et «moyennes» déformations*. Thèse de Doctorat, INSA de Lyon, 219 p., 1995.[In French],

## References

---

- Durrieu, F., Farcas, F., & Mouillet, V. (2007). The influence of UV aging of a Styrene/Butadiene/Styrene modified bitumen: Comparison between laboratory and on site aging. *Fuel*, 86(10), 1446-1451. doi:<https://doi.org/10.1016/j.fuel.2006.11.024>
- EN 12591:2009. (2009). Bitumen and bituminous binders. Specifications for paving grade bitumens
- EN 12593:2015. (2015). Bitumen and bituminous binders. Determination of the fraas breaking point
- EN 12697-46:2013d. (2013d). Bituminous Mixtures - Low Temperature Cracking and Properties by Uniaxial Tension Tests.
- EN 13043:2003-AC/ 2004 Aggregates for bituminous mixtures and surface treatments for roads, airfields and other trafficed areas
- EN 13924-1:2016. (2016). Bitumen and bituminous binders. Specification framework for special paving grade bitumen - Part 1 : hard paving grade bitumens
- EN 13924-2:2014. (2014). Bitumen and bituminous binders. Specification framework for special paving grade bitumen - Part 2 : multigrade paving grade bitumens
- EN 1426:2018. (2018). Bitumen and bituminous binders. Determination of needle penetration.
- EN 1427:2018. (2018). Bitumen and bituminous binders. Determination of the softening point. Ring and Ball method
- EN 14769 (2012). EN 14769: Bitumen and Bituminous Binders—Accelerated Long-Term Ageing Conditioning by a Pressure Ageing Vessel (PAV). In *European Committee for Standardization: Brussels, Belgium*.
- EN14770. (2012). Bitumen and bituminous binders—Determination of complex shear modulus and phase angle—Dynamic Shear Rheometer (DSR). In: European Committee for Standardization Brussels.
- EN, C. (2003). 12697-22. Bituminous mixtures. Test methods for hot mix asphalt. Part 22: Wheel tracking. In *Brussels: European Committee for Standardization*.
- EN, C. (2012). Bituminous mixtures—test methods for hot mix asphalt—Part 26: Stiffness. In *European committee for standardization Brussels*.
- Eringen, A. C. (1962). *Nonlinear theory of continuous media*: McGraw-Hill.
- Farrar, M., Sui, C., Salmans, S., & Qin, Q. (2015). Determining the low-temperature rheological properties of asphalt binder using a dynamic shear rheometer (DSR). *Report 4FP*, 8, 20.
- Feng, Z.-g., Wang, S.-j., Bian, H.-j., Guo, Q.-l., & Li, X.-j. (2016). FTIR and rheology analysis of aging on different ultraviolet absorber modified bitumens. *Construction and Building Materials*, 115, 48-53. doi:<https://doi.org/10.1016/j.conbuildmat.2016.04.040>
- Ferry, J. D. (1980). *Viscoelastic properties of polymers*: John Wiley & Sons.
- Forton, A., Di Benedetto, H., Mangiafico, S., Sauzéat, C., & Marc, P. (2019). Rheological properties of fresh and RAP bitumen blends with or without regenerating agent. *Bituminous Mixtures and Pavements VII*, 13-19. doi:<https://doi.org/10.1201/9781351063265-2>
- Freire, R. A. (2020). *Use of fiberglass geogrids to the reinforcement of bituminous mixtures layers*. Université de Lyon,
- Frolov, I. N., Bashkirceva, N. Y., Ziganshin, M. A., Okhotnikova, E. S., & Firsin, A. A. (2016). The steric hardening and structuring of paraffinic hydrocarbons in bitumen. *Petroleum Science and Technology*, 34(20), 1675-1680. doi:10.1080/10916466.2016.1221962
- Gayte, P., Di Benedetto, H., Sauzéat, C., & Nguyen, Q. T. (2016). Influence of transient effects for analysis of complex modulus tests on bituminous mixtures. *Road Materials and Pavement Design*, 17(2), 271-289.
- Gent, A., & Lindley, P. (1959). The compression of bonded rubber blocks. *Proceedings of the Institution of Mechanical Engineers*, 173(1), 111-122.



## References

---

- González, M. N. (2010). Rheology and engineering parameters of bitumen modified with polyolefins. *Elastomers and reactive polymers*.
- Graziani, A., Bocci, M., & Canestrari, F. (2014). Complex Poisson's ratio of bituminous mixtures: measurement and modeling. *Materials and Structures*, 47(7), 1131-1148. doi:<https://doi.org/10.1617/S11527-013-0117-2>
- Graziani, A., Di Benedetto, H., Perraton, D., Sauzeat, C., Hofko, B., Poulidakos, L., & Pouget, S. (2017). Recommendation of RILEM TC 237-SIB on complex Poisson's ratio characterization of bituminous mixtures. *Materials and Structures*, 50(2), 1-7. doi:<https://doi.org/10.1617/S11527-017-1008-8>
- Gražulytė, J., Soenen, H., Blom, J., Vaitkus, A., Židanavičiūtė, J., & Margaritis, A. (2021). Analysis of 4-mm DSR tests: calibration, sample preparation, and evaluation of repeatability and reproducibility. *Road Materials and Pavement Design*, 22(3), 557-571. doi:<https://doi.org/10.1080/14680629.2019.1634636>
- Gudmarsson, A., Ryden, N., Di Benedetto, H., & Sauzéat, C. (2015). Complex modulus and complex Poisson's ratio from cyclic and dynamic modal testing of asphalt concrete. *Construction and Building Materials*, 88, 20-31. doi:<https://doi.org/10.1016/J.CONBUILDMAT.2015.04.007>
- Gudmarsson, A., Ryden, N., Di Benedetto, H., Sauzéat, C., Tapsoba, N., & Birgisson, B. (2014). Comparing linear viscoelastic properties of asphalt concrete measured by laboratory seismic and tension-compression tests. *Journal of nondestructive evaluation*, 33(4), 571-582. doi:<https://doi.org/10.1007/S10921-014-0253-9>
- Hall, K. D., Dandu, S. K., & Gowda, G. V. (1996). Effect of specimen size on compaction and volumetric properties in gyratory compacted hot-mix asphalt concrete specimens. *Transportation Research Record*, 1545(1), 126-132.
- Heukelom, W., & Klomp, A. (1964). *Road design and dynamic loading*. Paper presented at the Assoc Asphalt Paving Technol Proc.
- Huet, C. (1963). *Study of the viscoelastic behaviour of bituminous mixes by method of impedance*. (Ph.D. Ph.D.). Paris.
- Hunter, R. N., Self, A., Read, J., & Hobson, E. (2015). *The shell bitumen handbook* (Vol. 514): Ice Publishing London, UK:.
- Islam, M. (2015). *Thermal fatigue damage of asphalt pavement*. (PhD). The University of New Mexico,
- Jasso, M., Hampl, R., Vacin, O., Bakos, D., Stastna, J., & Zanzotto, L. (2015). Rheology of conventional asphalt modified with SBS, Elvaloy and polyphosphoric acid. *Fuel Processing Technology*, 140, 172-179. doi:<https://doi.org/10.1016/J.FUPROC.2015.09.002>
- Kallas, B. F., Puzinauskas, V. P., & Krieger, H. (1962). Mineral fillers in asphalt paving mixtures. *Highway Research Board Bulletin*(329). Retrieved from <http://onlinepubs.trb.org/Onlinepubs/hrbulletin/329/329-002.pdf>
- Kassem, E., Grasley, Z. C., & Masad, E. (2013). Viscoelastic Poisson's ratio of asphalt mixtures. *International Journal of Geomechanics*, 13(2), 162-169. doi:<https://doi.org/10.1061/%28ASCE%29GM.1943-5622.0000199>
- Kassem, E., Masad, E., Lytton, R., & Chowdhury, A. (2011). Influence of Air Voids on Mechanical Properties of Asphalt Mixtures. *Road Materials and Pavement Design*, 12(3), 493-524. doi:10.1080/14680629.2011.9695258
- Kett, I. (1998). *Asphalt Materials and Mix Design Manual*: Noyes.
- Koppelman, J. (1959). Über den dynamischen Elastizitätsmodul von Polymethacrylsäuremethylester bei sehr tiefen Frequenzen. *Kolloid-Zeitschrift*, 164(1), 31-34. doi:<https://doi.org/10.1007/BF01512378>
- Lakes, R., & Lakes, R. S. (2009). *Viscoelastic materials*: Cambridge university press.

## References

---

- Laukkanen, O.-V., & Winter, H. H. (2018). The dynamic fragility and apparent activation energy of bitumens as expressed by a modified Kaelble equation. *Journal of Non-Crystalline Solids*, 499, 289-299. doi:<https://doi.org/10.1016/J.NONCRY SOL.2018.07.036>
- Laukkanen, O.-V., Winter, H. H., & Soenen, H. (2015). Rheological analysis of the low-temperature dynamics of bitumens. *Annual Transactions of the Nordic Rheology Society*, 23, 23-26. Retrieved from <https://nrs.blob.core.windows.net/pdfs/nrspdf-e3537aba-c230-48b1-8603-15e87b61a58c.pdf>
- Laukkanen, O.-V., Winter, H. H., Soenen, H., & Seppälä, J. (2016). Rheological analysis of bitumen as a complex glass-forming liquid and comparison with some simple glass-forming liquids. *Annu Trans Nord Rheol Soc*, 24, 17-21. doi:<https://nrs.blob.core.windows.net/pdfs/nrspdf-6950b0a3-4bf2-41ba-830c-4db789801574.pdf>
- Laukkanen, O.-V., Winter, H. H., Soenen, H., & Seppälä, J. (2018). An empirical constitutive model for complex glass-forming liquids using bitumen as a model material. *Rheologica Acta*, 57, 57-70. doi:<https://doi.org/10.1007/s00397-017-1056-6>
- Leandro, R. P., Vasconcelos, K. L., & Bernucci, L. L. B. (2017). Evaluation of the laboratory compaction method on the air voids and the mechanical behavior of hot mix asphalt. *Construction and Building Materials*, 156, 424-434. doi:<https://doi.org/10.1016/J.CONBUILDMAT.2017.08.178>
- Lesueur, D. (2009). The colloidal structure of bitumen: Consequences on the rheology and on the mechanisms of bitumen modification. *Advances in colloid and interface science*, 145(1-2), 42-82. doi:<https://doi.org/10.1016/j.cis.2008.08.011>
- Lesueur, D., & Little, D. N. (1999). Effect of hydrated lime on rheology, fracture, and aging of bitumen. *Transportation Research Record*, 1661(1), 93-105. doi:<https://doi.org/10.3141/1661-14>
- Lira, B., Jelagin, D., & Birgisson, B. (2013). Gradation-based framework for asphalt mixture. *Materials and Structures*, 46(8), 1401-1414. doi:<https://doi.org/10.1617/S11527-012-9982-3>
- Little, D. N., & Petersen, J. C. (2005). Unique effects of hydrated lime filler on the performance-related properties of asphalt cements: Physical and chemical interactions revisited. *Journal of Materials in Civil Engineering*, 17(2), 207-218. doi:<https://doi.org/10.1061/%28ASCE%290899-1561%282005%2917%3A2%28207%29>
- Lu, X., & Isacsson, U. (2000). Laboratory study on the low temperature physical hardening of conventional and polymer modified bitumens. *Construction and Building Materials*, 14(2), 79-88. doi:<https://doi.org/10.1016/S0950-0618%2800%2900012-X>
- Lu, X., & Isacsson, U. (2002). Effect of ageing on bitumen chemistry and rheology. *Construction and Building Materials*, 16(1), 15-22. doi:[https://doi.org/10.1016/S0950-0618\(01\)00033-2](https://doi.org/10.1016/S0950-0618(01)00033-2)
- Lu, X., Isacsson, U., & Ekblad, J. (2003). Influence of polymer modification on low temperature behaviour of bituminous binders and mixtures. *Materials and Structures*, 36, 652-656. doi:<https://doi.org/10.1007/BF02479497>
- Lu, X., Uhlback, P., & Soenen, H. (2017). Investigation of bitumen low temperature properties using a dynamic shear rheometer with 4mm parallel plates. *International Journal of Pavement Research and Technology*, 10(1), 15-22. doi:<https://doi.org/10.1016/j.ijprt.2016.08.010>
- Mahmoudi, Y., Mangiafico, S., Sauzéat, C., Di Benedetto, H., Pouget, S., & Faure, J.-P. (2021). Tridimensional linear viscoelastic properties of bituminous mixtures produced with

## References

---

- crumb rubber added by dry process. *Road Materials and Pavement Design*, 22(9), 2086-2096. doi:<https://doi.org/10.1080/14680629.2020.1737566>
- Mallick, R. B. (1999). Use of Superpave gyratory compactor to characterize hot-mix asphalt. *Transportation Research Record*, 1681(1), 86-96. doi:<https://doi.org/10.3141/1681-11>
- Malvern, L. E. (1969). *Introduction to the Mechanics of a Continuous Medium*.
- Mangiafico, S. (2014). *Linear viscoelastic properties and fatigue of bituminous mixtures produced with Reclaimed Asphalt Pavement and corresponding binder blends*. (PhD). ENTPE, Lyon.
- Marasteanu, M., & Anderson, D. (1999). *Improved model for bitumen rheological characterization*. Paper presented at the Eurobitume workshop on performance related properties for bituminous binders.
- Masad, E., Muhunthan, B., Shashidhar, N., & Harman, T. (1999). Internal structure characterization of asphalt concrete using image analysis. *Journal of computing in civil engineering*, 13(2), 88-95. doi:<https://doi.org/10.1061/%28ASCE%290887-3801%281999%2913%3A2%2888%29>
- Masson, J., & Polomark, G. (2001). Bitumen microstructure by modulated differential scanning calorimetry. *Thermochimica acta*, 374(2), 105-114.
- Masson, J., Polomark, G., & Collins, P. (2002). Time-dependent microstructure of bitumen and its fractions by modulated differential scanning calorimetry. *Energy & Fuels*, 16(2), 470-476.
- Mastrofini, D., & Scarsella, M. (2000). The application of rheology to the evaluation of bitumen ageing. *Fuel*, 79(9), 1005-1015. doi:<https://doi.org/10.1016/S0016-2361%2899%2900244-6>
- Mauduit, C., Hammoum, F., Piau, J.-M., Mauduit, V., Ludwig, S., & Hamon, D. (2010). Quantifying expansion effects induced by Freeze-Thaw cycles in partially water saturated bituminous mix: Laboratory Experiments. *Road Materials and Pavement Design*, 11(sup1), 443-457. doi:<https://doi.org/10.3166/rmpd.11hs.443-457>
- McKenna, G. B. (2012). Physical Aging in Glasses and Composites. In K. V. Pochiraju, G. P. Tandon, & G. A. Schoeppner (Eds.), *Long-Term Durability of Polymeric Matrix Composites* (pp. 237-309). Boston, MA: Springer US.
- Miró, R., Martínez, A. H., Pérez-Jiménez, F. E., Botella, R., & Álvarez, A. (2017). Effect of filler nature and content on the bituminous mastic behaviour under cyclic loads. *Construction and Building Materials*, 132, 33-42. doi:<https://doi.org/10.1016/J.CONBUILDMAT.2016.11.114>
- Mounier, D., Di Benedetto, H., & Sauzéat, C. (2012). Determination of bituminous mixtures linear properties using ultrasonic wave propagation. *Construction and Building Materials*, 36, 638-647. doi:<https://doi.org/10.1016/j.conbuildmat.2012.04.136>
- Neifar, M., & Di Benedetto, H. (2001). Thermo-viscoplastic law for bituminous mixes. *Road Materials and Pavement Design*, 2(1), 71-95. doi:10.1080/14680629.2001.9689894
- Nguyen, H. (2010). *Comportement cyclique aux déformations permanentes des enrobés bitumineux*. Ph. D. thesis, ENTPE, University of Lyon (in French),
- Nguyen, H. M., Pouget, S., Di Benedetto, H., & Sauzéat, C. (2009). Time-temperature superposition principle for bituminous mixtures. *European Journal of Environmental and Civil Engineering*, 13(9), 1095-1107. doi:10.1080/19648189.2009.9693176
- Nguyen, Q. T., Di Benedetto, H., & Sauzéat, C. (2015). Linear and nonlinear viscoelastic behaviour of bituminous mixtures. *Materials and Structures*, 48(7), 2339-2351. doi:<https://doi.org/10.1617/S11527-014-0316-5>
- Nguyen, Q. T., Di Benedetto, H., Sauzéat, C., & Tapsoba, N. (2013). Time temperature superposition principle validation for bituminous mixes in the linear and nonlinear



## References

---

- domains. *Journal of Materials in Civil Engineering*, 25(9), 1181-1188. doi:<https://doi.org/10.1061/%28ASCE%29MT.1943-5533.0000658>
- Nguyen, Q. T., Nguyen, M. L., Benedetto, H. D., Sauzeat, C., Chailleux, E., & Hoang, T. T. N. (2019). Nonlinearity of bituminous materials for small amplitude cyclic loadings. *Road Materials and Pavement Design*, 20(7), 1571-1585. doi:<https://doi.org/10.1080/14680629.2018.1465452>
- O'Flaherty, C. A. (2001). *Highways*: CRC Press.
- Olard, F. (2012). GB5 mix design: high-performance and cost-effective asphalt concretes by use of gap-graded curves and SBS modified bitumens. *Road Materials and Pavement Design*, 13(sup1), 234-259. doi:<https://doi.org/10.1080/14680629.2012.657074>
- Olard, F., & Di Benedetto, H. (2003). General "2S2P1D" model and relation between the linear viscoelastic behaviours of bituminous binders and mixes. *Road Materials and Pavement Design*, 4(2), 185-224. doi:<https://doi.org/10.1080/14680629.2003.9689946>
- Olard, F., Di Benedetto, H., Dony, A., & Vaniscote, J.-C. (2005). Properties of bituminous mixtures at low temperatures and relations with binder characteristics. *Materials and Structures*, 38(1), 121-126. doi:<https://doi.org/10.1007/BF02480584>
- Olard, F., Di Benedetto, H., Eckmann, B., & Triquigneaux, J.-P. (2003). Linear viscoelastic properties of bituminous binders and mixtures at low and intermediate temperatures. *Road Materials and Pavement Design*, 4(1), 77-107. doi:<https://doi.org/10.1080/14680629.2003.9689941>
- Orozco, G. (2020). *Relationship between thermomechanical performances of bituminous binders and mixtures with focus on binder-aggregate adhesion*. (PhD). University of Lyon ENTPE,
- Perraton, D., Di Benedetto, H., Sauzéat, C., Hofko, B., Graziani, A., Nguyen, Q. T., . . . Grenfell, J. (2016). 3Dim experimental investigation of linear viscoelastic properties of bituminous mixtures. *Materials and Structures*, 49(11), 4813-4829. doi:10.1617/s11527-016-0827-3
- Petersen, J., Robertson, R., Branthaver, J., Harnsberger, P., Duvall, J., Kim, S., . . . Bahia, H. J. R. N. S.-A.-., Strategic Highway Research Program, National Research Council, Washington, DC. (1994). Binder characterization and evaluation: Volume 1.
- Petersen, J. C. (1989). A thin film accelerated aging test for evaluating asphalt oxidative aging. *Asphalt Paving Technol.*, 58, 220-237. Retrieved from <https://www.scopus.com/inward/record.uri?eid=2-s2.0-0012849570&partnerID=40&md5=d60c534d8f33d754deac67a2bf2abcb3>
- Petersen, J. C. (2009). A review of the fundamentals of asphalt oxidation: chemical, physicochemical, physical property, and durability relationships. *Transportation research circular*(E-C140). doi:<https://doi.org/10.17226/23002>
- Pham, N. H., Sauzéat, C., Di Benedetto, H., González-León, J.-A., Barreto, G., Nicolai, A., & Jakubowski, M. (2015). Reclaimed asphalt pavement and additives' influence on 3D linear behaviour of warm mix asphalts. *Road Materials and Pavement Design*, 16(3), 569-591. doi:10.1080/14680629.2015.1021108
- Phan, C. V., Di Benedetto, H., Sauzéat, C., & Lesueur, D. (2016, 2016/). *Influence of Hydrated Lime on Linear Viscoelastic Properties of Bituminous Mixtures*. Paper presented at the 8th RILEM International Symposium on Testing and Characterization of Sustainable and Innovative Bituminous Materials, Dordrecht.
- Picado-Santos, L. G., Capitão, S. D., & Neves, J. M. C. (2020). Crumb rubber asphalt mixtures: A literature review. *Construction and Building Materials*, 247, 118577. doi:<https://doi.org/10.1016/j.conbuildmat.2020.118577>
- Pouget, S. (2011). *Influence des propriétés élastiques ou viscoélastiques des revêtements sur le comportement des ponts à dalle orthotrope*. (254).

## References

---

- Pouget, S., Sauzéat, C., Di Benedetto, H., & Olard, F. (2010). From the Behavior of Constituent Materials to the Calculation and Design of Orthotropic Bridge Structures. *Road Materials and Pavement Design*, 11(sup1), 111-144. doi:10.1080/14680629.2010.9690329
- Ramirez Cardona, D. A., Pouget, S., Di Benedetto, H., & Olard, F. (2015). Viscoelastic behaviour characterization of a gap-graded asphalt mixture with SBS polymer modified bitumen. *Materials Research*, 18, 373-381. doi:<https://doi.org/10.1590/1516-1439.332214>
- Riccardi, C., Falchetto, A. C., Losa, M., & Leandri, P. (2017). Estimation of the SHStS transformation parameter based on volumetric composition. *Construction and Building Materials*, 157, 244-252. doi:<https://doi.org/10.1016/J.CONBUILDMAT.2017.09.083>
- Rowe, G., Sharrock, M., Bouldin, M., & Dongre, R. (2001). Advanced Technique to Develop Asphalt Master Curves from the Bending Beam Rheometer. *Petroleum and Coal*, 43(1), 54-59.
- Rowe, G. M., & Sharrock, M. J. (2011). Alternate shift factor relationship for describing temperature dependency of viscoelastic behavior of asphalt materials. *Transportation Research Record*, 2207(1), 125-135. doi:<https://doi.org/10.3141/2207-16>
- Santagata, E., Baglieri, O., Dalmazzo, D., & Tsantilis, L. (2016). *Experimental investigation on the combined effects of physical hardening and chemical ageing on low temperature properties of bituminous binders*. Paper presented at the 8th RILEM International symposium on testing and characterization of sustainable and innovative bituminous materials.
- Sayegh, G. (1965). *Variation des modules de quelques bitumes purs et enrobés bitumineux*. (Ph.D. Ph.D.). University of Paris,
- Standardization, E. C. f. (2003). 12697-22. Bituminous mixtures. Test methods for hot mix asphalt. Part 22: Wheel tracking. In.
- Stastna, J., Zanzotto, L., & Vacin, O. (2003). Viscosity function in polymer-modified asphalts. *Journal of colloid and interface science*, 259(1), 200-207. doi:<https://doi.org/10.1016/S0021-9797%2802%2900197-2>
- Struik, L. C. E. (1977). *Physical aging in amorphous polymers and other materials*. Citeseer, Retrieved from <http://citeseerx.ist.psu.edu/viewdoc/download?doi=10.1.1.899.1753&rep=rep1&type=pdf>
- Subhy, A. (2017). Advanced analytical techniques in fatigue and rutting related characterisations of modified bitumen: Literature review. *Construction and Building Materials*, 156, 28-45. doi:<https://doi.org/10.1016/J.CONBUILDMAT.2017.08.147>
- T342, A. (2011). Standard method of test for determining dynamic modulus of hot mix asphalt (HMA). In: American Association of State Highway and Transportation Officials ....
- Tabatabaee, H. A., Velasquez, R., & Bahia, H. U. (2012). Predicting low temperature physical hardening in asphalt binders. *Construction and Building Materials*, 34, 162-169. doi:<https://doi.org/10.1016/J.CONBUILDMAT.2012.02.039>
- Tan, X., He, Y., Zhang, M., & Zhang, J. (2023). Research on low temperature properties and physical hardening effect of asphalt components. *Case Studies in Construction Materials*, 19, e02484. doi:<https://doi.org/10.1016/j.cscm.2023.e02484>
- Tapsoba, N. (2012). *Comportement des enrobés bitumineux à base de matériaux recyclés et / ou fabriqués à température réduite*. (PhD). University of Lyon., ENTPE.
- Tashman, L., Masad, E., D'Angelo, J., Bukowski, J., & Harman, T. (2002). X-ray Tomography to Characterize Air Void Distribution in Superpave Gyrotory Compacted Specimens. *International Journal of Pavement Engineering*, 3(1), 19-28. doi:10.1080/10298430290029902a

## References

---

- Tauste, R., Moreno-Navarro, F., Sol-Sánchez, M., & Rubio-Gámez, M. (2018). Understanding the bitumen ageing phenomenon: A review. *Construction and Building Materials*, *192*, 593-609. doi:<https://doi.org/10.1016/J.CONBUILDMAT.2018.10.169>
- Test, O. (2010). Determining the rheological properties of asphalt binder using a dynamic shear rheometer (DSR). In *Washington, DC*.
- Thurston, R., & Knowles, E. (1941). Asphalt and its constituents. Oxidation at Service Temperatures. *Industrial & Engineering Chemistry*, *33*(3), 320-324. doi:<https://doi.org/10.1021/IE50375A010>
- Thyagarajan, S., Tashman, L., Masad, E., & Bayomy, F. (2010). The heterogeneity and mechanical response of hot mix asphalt laboratory specimens. *International Journal of Pavement Engineering*, *11*(2), 107-121. doi:<https://doi.org/10.1080/10298430902730521>
- Tschoegl, N. W. (1989). Energy storage and dissipation in a linear viscoelastic material. In *The Phenomenological Theory of Linear Viscoelastic Behavior* (pp. 443-488): Springer.
- Tschoegl, N. W., Knauss, W. G., & Emri, I. (2002). Poisson's ratio in linear viscoelasticity—A critical review. *Mechanics of Time-Dependent Materials*, *6*(1), 3-51. doi:<https://doi.org/10.1023/A%3A1014411503170>
- Turnbull, D., & Cohen, M. H. (1961). Free-volume model of the amorphous phase: glass transition. *The Journal of chemical physics*, *34*(1), 120-125.
- Turner, T. F., & Branthaver, J. F. (1997). DSC studies of asphalts and asphalt components. *Asphalt science and technology*, 59-101.
- Ugé, P., Gest, G., Gravois, A., & Bonnaure, F. (1977). Nouvelle méthode de calcul du module complexe des mélanges bitumineux. *ULL LIAISON LAB PONTS CHAUSS(SPEC V)*.
- Underwood, B. S., & Kim, Y. R. (2011). Experimental investigation into the multiscale behaviour of asphalt concrete. *International Journal of Pavement Engineering*, *12*(4), 357-370. doi:<https://doi.org/10.1080/10298436.2011.574136>
- Walubita, L. F., Jamison, B., & Alvarez, A. E. (2012). Air void characterisation of HMA gyratory laboratory-moulded samples and field cores using X-ray computed tomography (X-ray CT). *Journal of the South African Institution of Civil Engineering= Joernaal van die Suid-Afrikaanse Instituut van Siviele Ingenieurswese*, *54*(1), 22-31. doi:<http://www.scielo.org.za/pdf/jsaice/v54n1/03.pdf>
- Wang, D., Cannone Falchetto, A., Riccardi, C., Westerhoff, J., & Wistuba, M. P. (2021). Investigation on the effect of physical hardening and aging temperature on low-temperature rheological properties of asphalt binder. *Road Materials and Pavement Design*, *22*(5), 1117-1139. doi:10.1080/14680629.2019.1665089
- Wang, H., Al-Qadi, I. L., Faheem, A. F., Bahia, H. U., Yang, S.-H., & Reinke, G. H. (2011). Effect of mineral filler characteristics on asphalt mastic and mixture rutting potential. *Transportation Research Record*, *2208*(1), 33-39. doi:<https://doi.org/10.3141/2208-05>
- Wang, T., Wang, J., Hou, X., & Xiao, F. (2021). Effects of SARA fractions on low temperature properties of asphalt binders. *Road Materials and Pavement Design*, *22*(3), 539-556. doi:10.1080/14680629.2019.1628803
- Williams, J. G., & Gamonpilas, C. (2008). Using the simple compression test to determine Young's modulus, Poisson's ratio and the Coulomb friction coefficient. *International Journal of Solids and Structures*, *45*(16), 4448-4459. doi:<https://doi.org/10.1016/j.ijsolstr.2008.03.023>
- Williams, M. L., Landel, R. F., & Ferry, J. D. (1955). The temperature dependence of relaxation mechanisms in amorphous polymers and other glass-forming liquids. *Journal of the American Chemical Society*, *77*(14), 3701-3707. doi:<https://doi.org/10.1021/JA01619A008>

## References

---

- Witczak, M., & Fonseca, O. (1996). Revised predictive model for dynamic (complex) modulus of asphalt mixtures. *Transportation Research Record*, 1540(1), 15-23. doi:<https://doi.org/10.1177/0361198196154000103>
- Yusoff Md., N. I. (2012). *Modelling the linear viscoelastic rheological properties of bituminous binders*. (PhD PhD). University of Nottingham, Retrieved from [http://eprints.nottingham.ac.uk/12582/1/Nur\\_Izzi\\_Md.\\_Yusoff.pdf](http://eprints.nottingham.ac.uk/12582/1/Nur_Izzi_Md._Yusoff.pdf) Access from the University of Nottingham repository: database.
- Yusoff, N. I. M., Chailleux, E., & Airey, G. D. (2011). A comparative study of the influence of shift factor equations on master curve construction. *International Journal of Pavement Research and Technology*, 4(6), 324. doi:<https://doi.org/10.6135/IJPR.TORG.TW%2F2011.4%286%29.324>
- Yusoff, N. I. M., Shaw, M. T., & Airey, G. D. (2011). Modelling the linear viscoelastic rheological properties of bituminous binders. *Construction and Building Materials*, 25(5), 2171-2189. doi:<https://doi.org/10.1016/J.CONBUILDMAT.2010.11.086>
- Zaidullin, I. M., Petrova, L. M., Yakubov, M. R., & Borisov, D. N. (2013). Variation of the composition of asphaltenes in the course of bitumen aging in the presence of antioxidants. *Russian Journal of Applied Chemistry*, 86(7), 1070-1075. doi:10.1134/S1070427213070203
- Zaltuom, A. M. (2018). A review study of the effect of air voids on asphalt pavement life. doi:<https://doi.org/10.21467/PROCEEDINGS.4.29>
- Zeng, M., Bahia, H. U., Zhai, H., Anderson, M. R., & Turner, P. (2001). Rheological modeling of modified asphalt binders and mixtures (with discussion). *Journal of The Association of Asphalt Paving Technologists*, 70.
- Zeng, W., Wu, S., Wen, J., & Chen, Z. (2015). The temperature effects in aging index of asphalt during UV aging process. *Construction and Building Materials*, 93, 1125-1131. doi:<https://doi.org/10.1016/j.conbuildmat.2015.05.022>
- Zhu, J., Birgisson, B., & Kringos, N. (2014). Polymer modification of bitumen: Advances and challenges. *European Polymer Journal*, 54, 18-38. doi:<https://doi.org/10.1016/J.EURPOLYMJ.2014.02.005>
- Ziari, H., Farahani, H., Goli, A., & Sadeghpour Galooyak, S. (2014). The Investigation of the Impact of Carbon Nano Tube on Bitumen and HMA Performance. *Petroleum Science and Technology*, 32(17), 2102-2108. doi:10.1080/10916466.2013.763827
- Zupanick, M., & Baselice, V. (1997). Characterizing Asphalt Volatility. *Transportation Research Record*, 1586(1), 1-9. doi:10.3141/1586-01

## APPENDIX A – SHEAR OSCILLATORY LVE LIMIT TEST RESULTS

Table A1 - Components of physical hardening equation (4.1) in relation to strain amplitude test performed on B5070 bitumen at the frequency (a) 0.01 Hz and (b) 0.3 Hz

0.01 Hz					
T(°C)	$G_b$ (MPa)	$ G^* _{\gamma 0.001\%}$ (MPa)	$R^2$	$avg \phi$ (°)	Std $\phi$
-25	5.99	376.700	0.933	15.64	0.36
-20	5.10	199.100	0.691	20.85	0.79
-10	2.31	59.540	0.879	31.67	0.48
0	0.62	12.760	0.896	44.33	1.12
10	0.06	1.558	0.934	57.89	0.37
a) 20	0.004	0.121	0.911	69.05	0.12

0.3 Hz					
T(°C)	$G_b$ (MPa)	$ G^* _{\gamma 0.001\%}$ (MPa)	$R^2$	$avg \phi$ (°)	Std $\phi$
-25	8.89	572.900	0.736	9.23	0.14
b) -20	4.37	432.700	0.325	13.16	0.2
-10	2.48	181.500	0.814	22.25	0.18
0	1.06	48.480	0.95	33.34	0.16
10	0.33	10.200	0.957	47.31	0.12
20	0.02	1.497	0.977	60.44	0.06

Table A2- Components of physical hardening equation (4.3) in relation to strain amplitude test performed on B3550 bitumen at frequency (a) 0.01 Hz and (b) 0.3 Hz

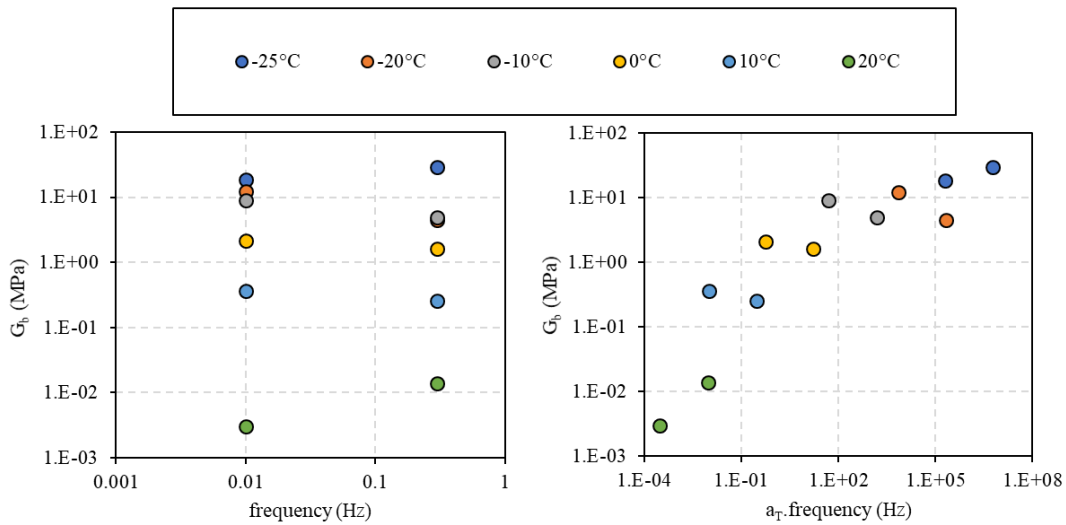
0.01 Hz					
T(°C)	$G_b$ (MPa)	$ G^* _{\gamma 0.01\%}$ (MPa)	$R^2$	$avg \phi$ (°)	Std $\phi$
-25	18.71	545.4	0.997	10.8	0.22
-20	12.42	370	0.941	15.89	0.28
a) -10	9.133	111.1	0.969	28.03	0.44

# Appendix

0	2.128	19.87	0.953	44.09	0.73
10	0.364	3.155	0.935	44.3	0.11
20	0.003	0.175	0.953	74.15	0.05

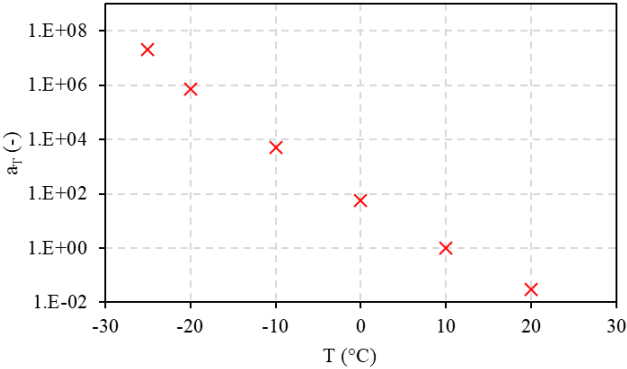
b)

0.3 Hz					
T(°C)	$G_b$ (MPa)	$ G^* _{\gamma 0.01\%}$ (MPa)	$R^2$	avg $\phi$ (°)	Std $\phi$
-25	29.59	697.4	0.884	6.07	0.05
-20	4.545	585.2	0.949	9.52	0.01
-10	4.961	266.7	0.881	18.13	0.04
0	1.606	86.62	0.962	30.41	0.07
10	0.256	21.15	0.655	44.3	0.11
20	0.014	2.389	0.974	60.64	0.01



a)

b)



c)

Figure A1 – (a) Isotherms; (b) Master curve and (c) temperature shift factors of B3550 bitumen LVE limit physical hardening constants ( $G_b$ ) at  $T_{ref} = 10^\circ\text{C}$

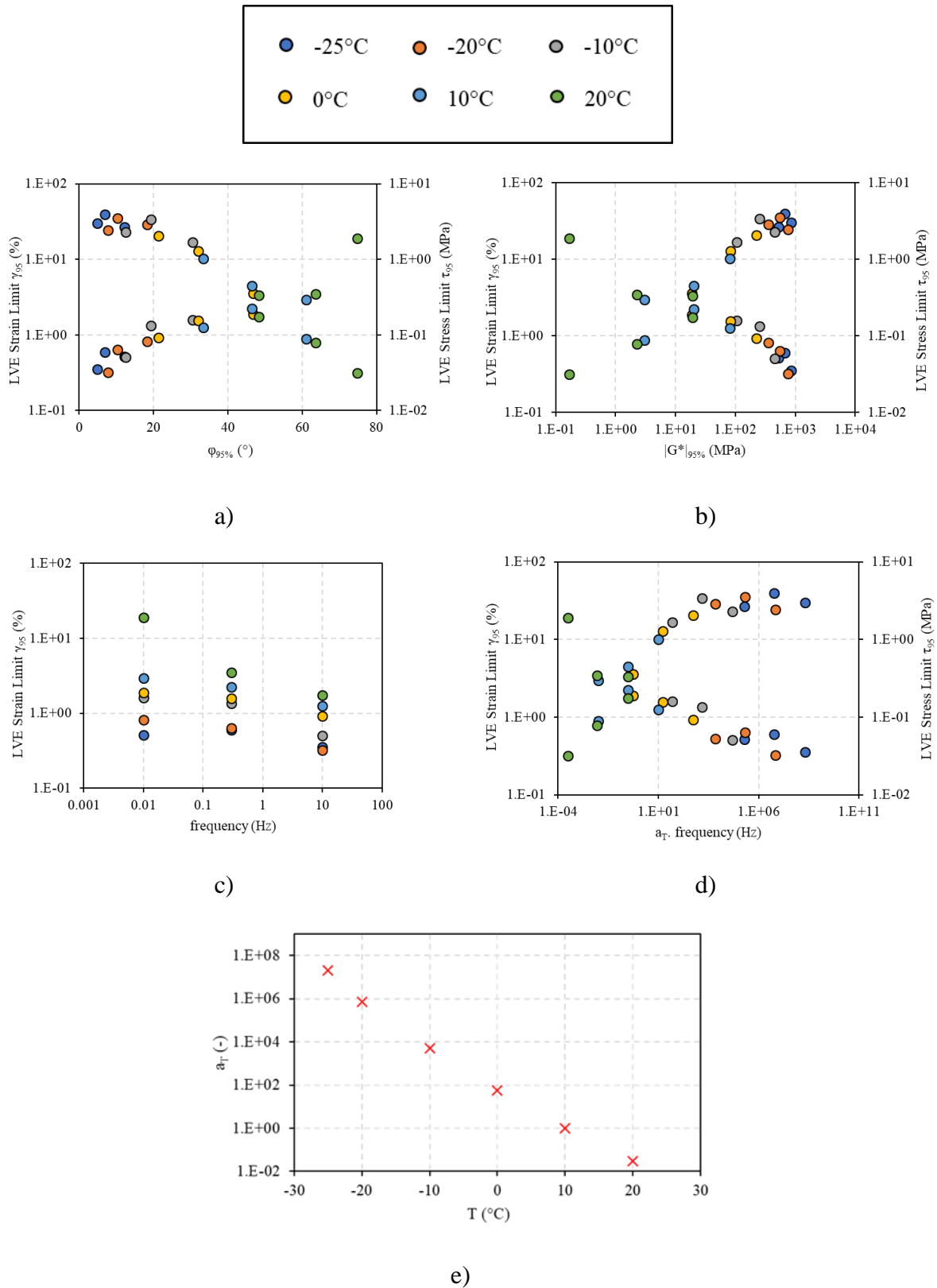


Figure A2 - Plots showing B3550 bitumen (a) Stress and strain limits as a function of phase angle  $\phi_{95\%}$  (b) stress and strain limits as a function of  $|G^*|_{95\%}$  (c) strain limit isotherms and (d) stress and strain limit master curve at  $T_{ref} = 10^\circ\text{C}$



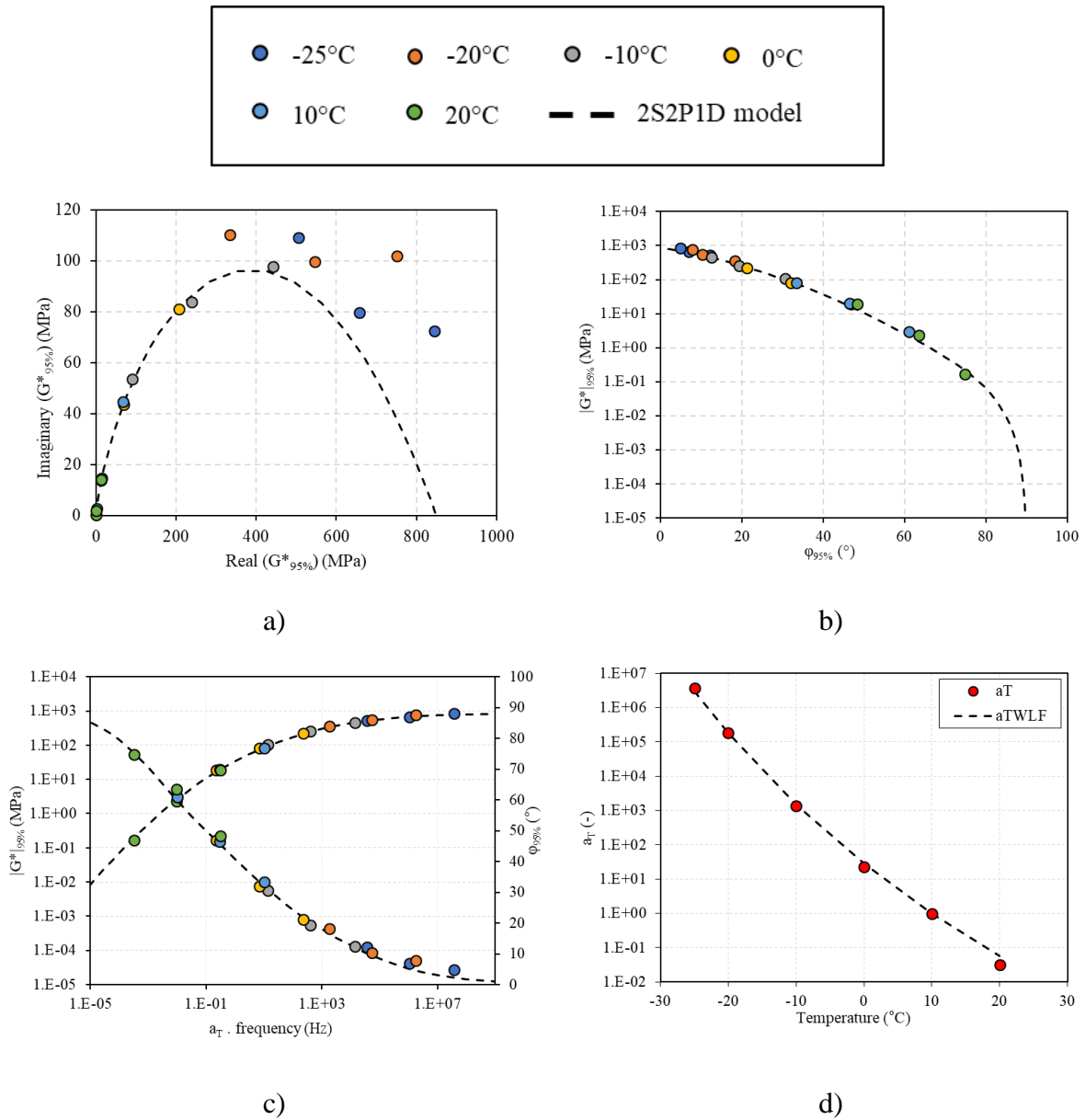
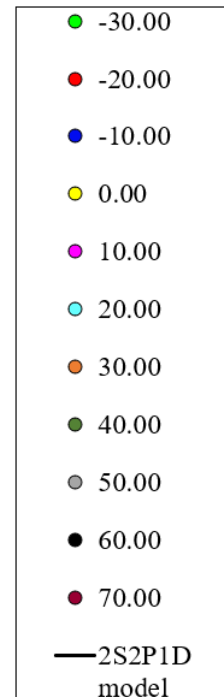
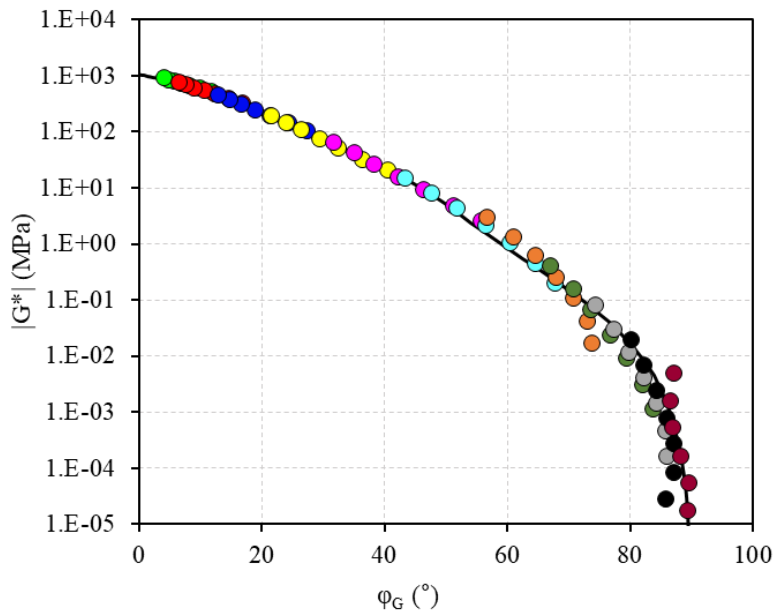
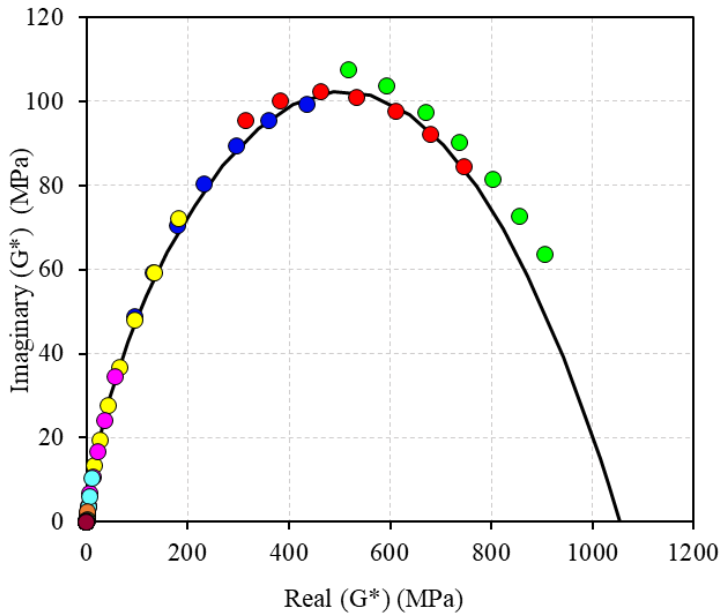


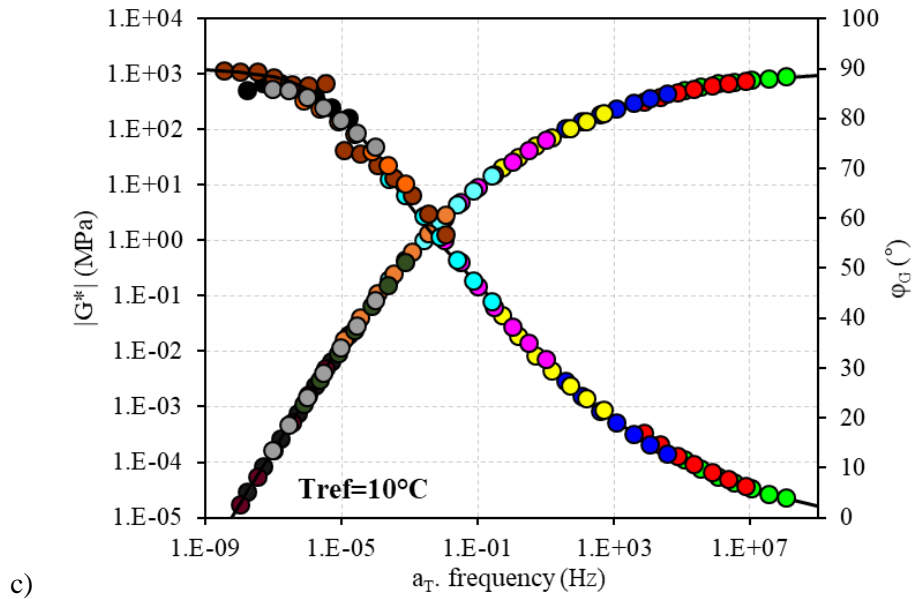
Figure A3 - B3550 bitumen (a) Cole-Cole diagram of  $|G^*|_{95\%}$  values (b) Black diagram of  $|G^*|_{95\%}$  and  $\phi_{95\%}$  values, corresponding to norm and phase angle of complex shear modulus at the LVE limit, for all tested frequencies and temperatures, for the tested bitumen. (c) Master curves of  $|G^*|_{95\%}$  and  $\phi_{95\%}$  values, corresponding to norm and phase angle of complex shear modulus at the LVE limit, and 2SP1D simulations. (d) Temperature shift factors and WLF fit used to build the master curves.

Table A3 – B3550 bitumen 2S2P1D model constants

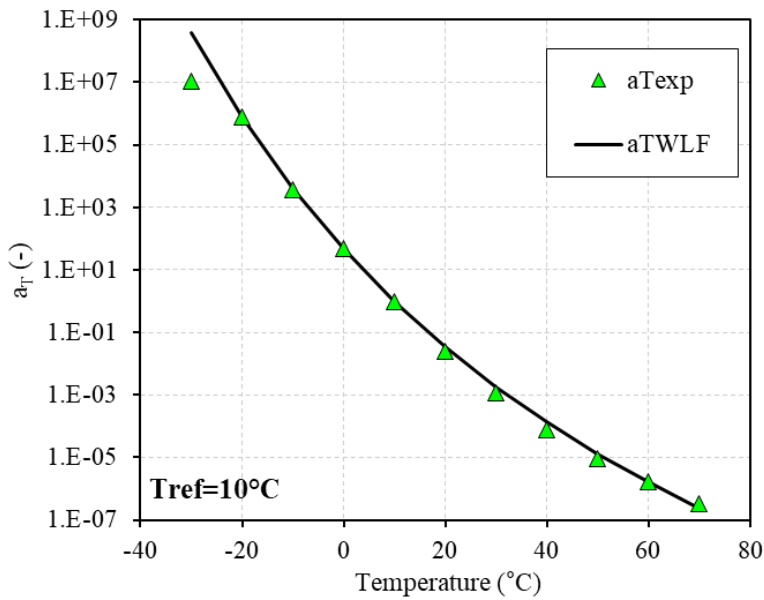
$G_{00}$ (MPa)	$G_0$ (MPa)	$k$	$h$	$\delta$	$\tau_{G95\%}$ (10°C)	$\beta$	$C_1$	$C_2$
0	850	0.27	0.60	3.40	2.0E-03	90	16.67	125.08

## APPENDIX B – DSR LINEAR VISCOELASTIC CHARACTERISATION OF BINDERS IN SHEAR TEST RESULTS



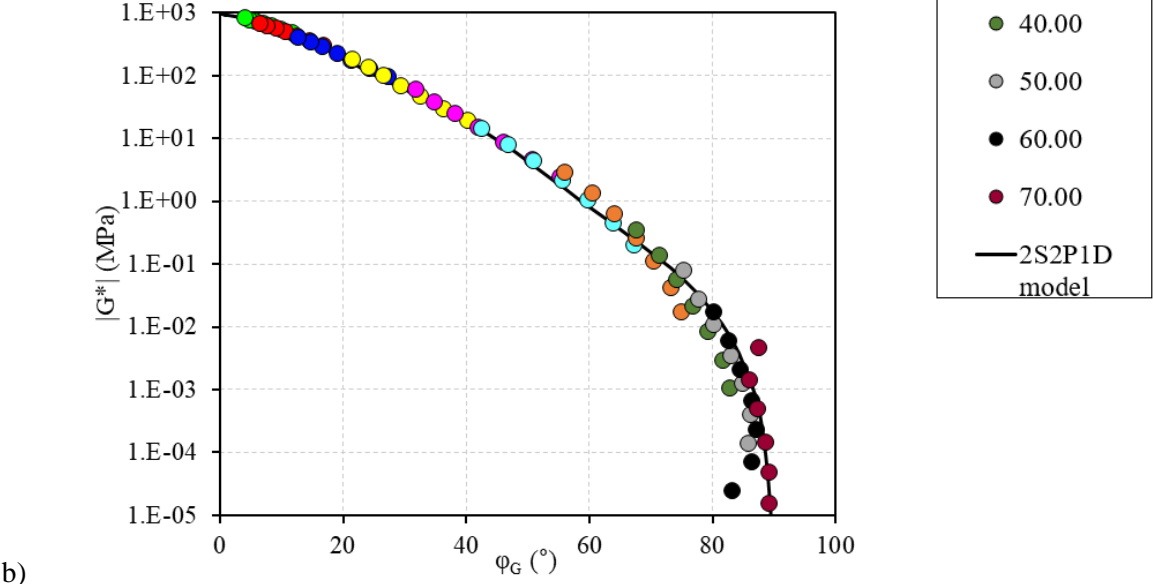
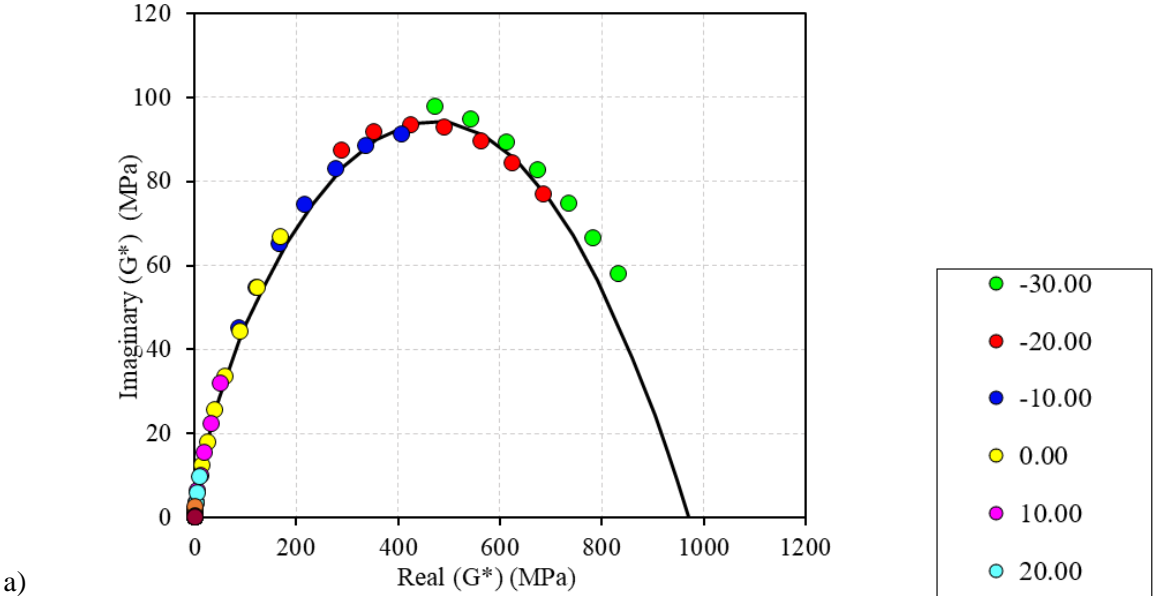


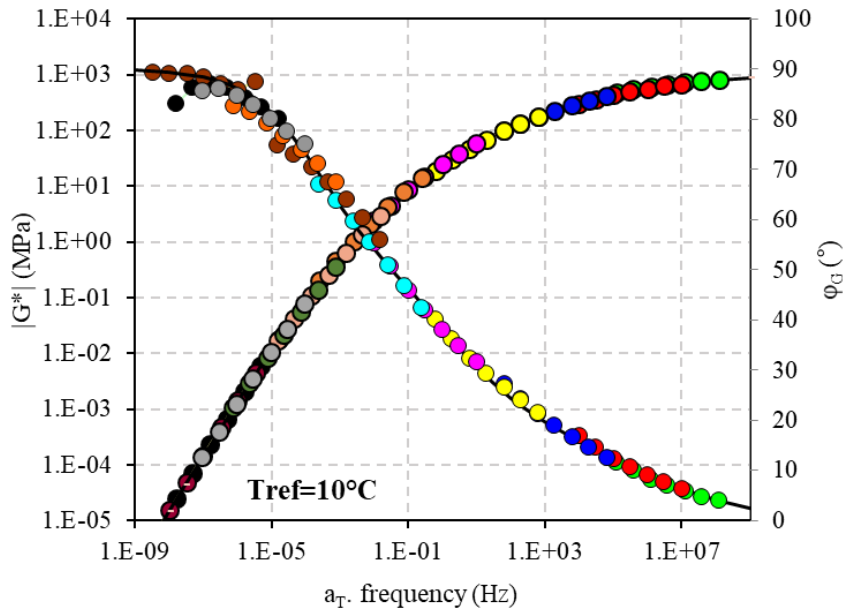
c)



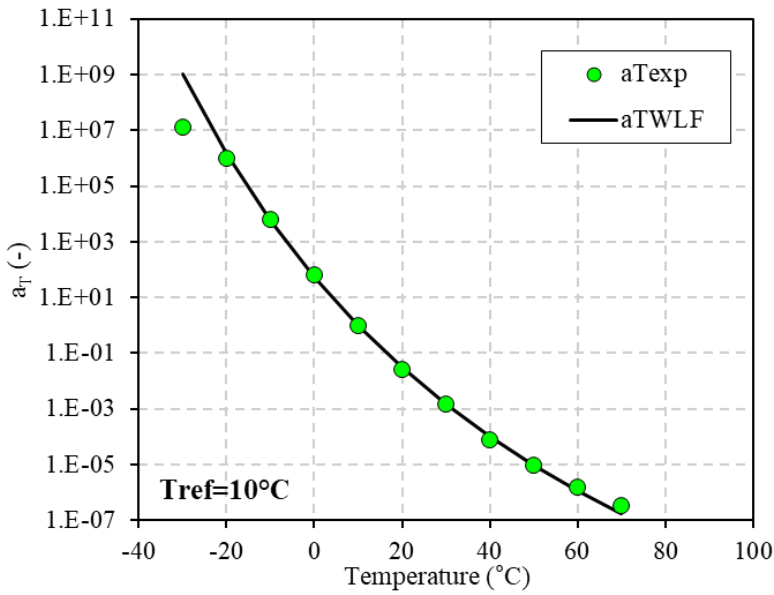
d)

Figure B1 – 2S2P1D fitted complex modulus test results for bitumen B5070-1: a) Cole-Cole plot; b) black diagram; c) master curves of norms of complex modulus and phase angle; d) WLF temperature shift factors at  $T_{ref} = 10^{\circ}\text{C}$



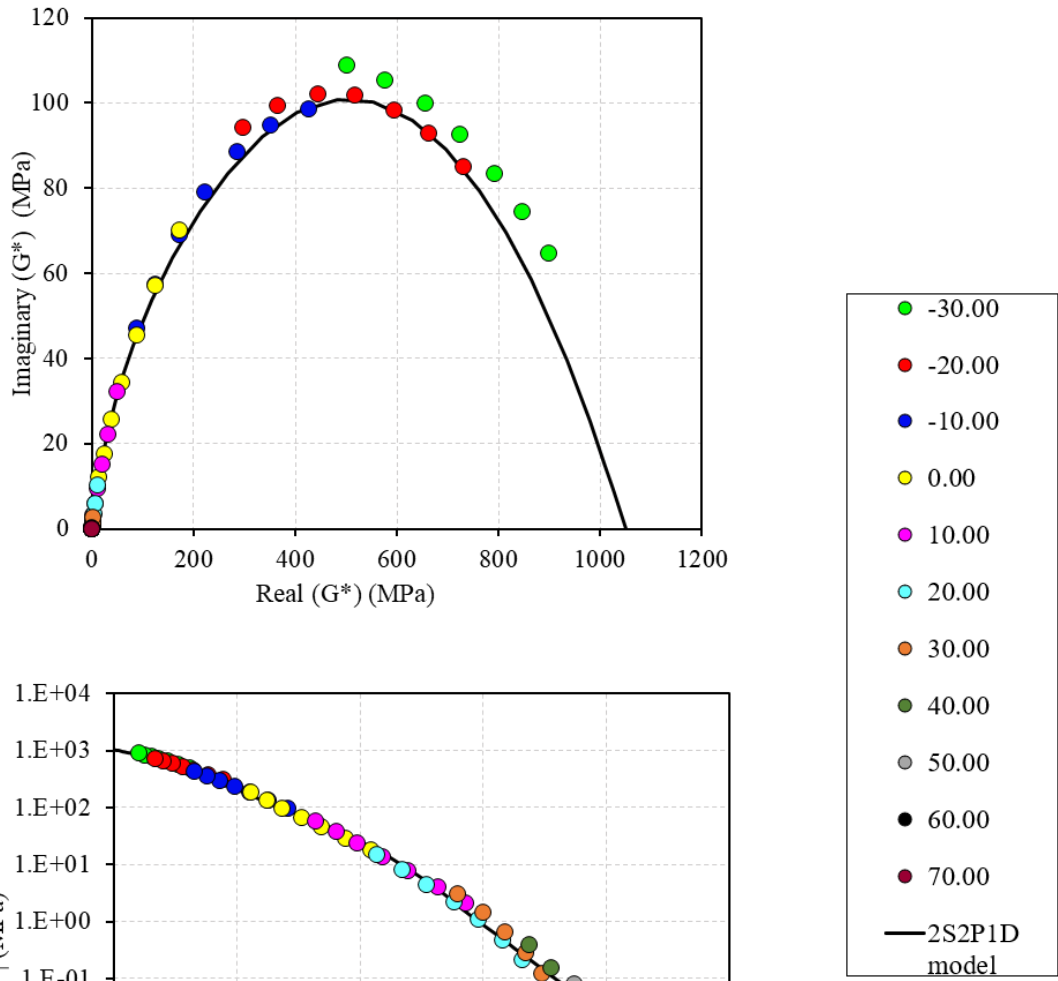


c)



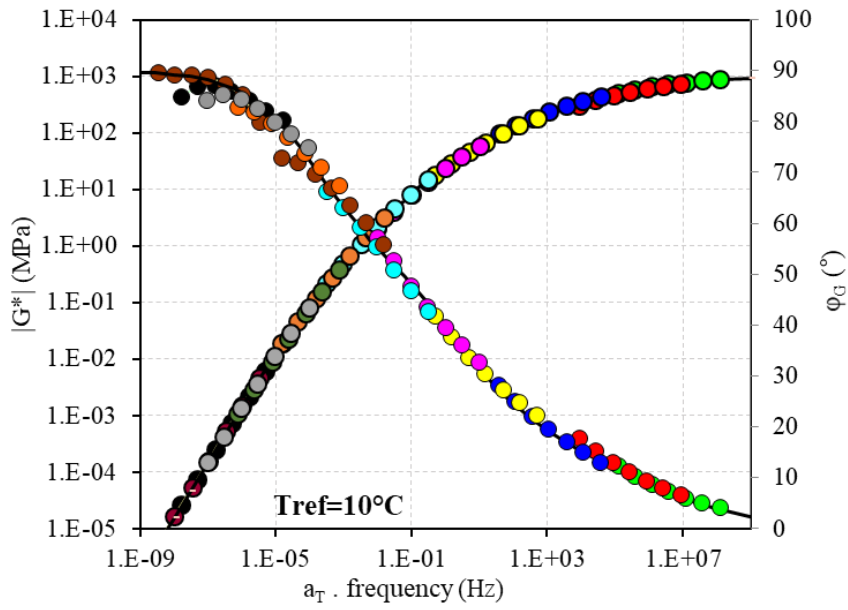
d)

Figure B2 – 2S2P1D fitted complex modulus test results for bitumen B5070-2: a) Cole-Cole plot; b) black diagram; c) master curves of norms of complex modulus and phase angle; d) WLF temperature shift factors at  $T_{ref} = 10^{\circ}\text{C}$

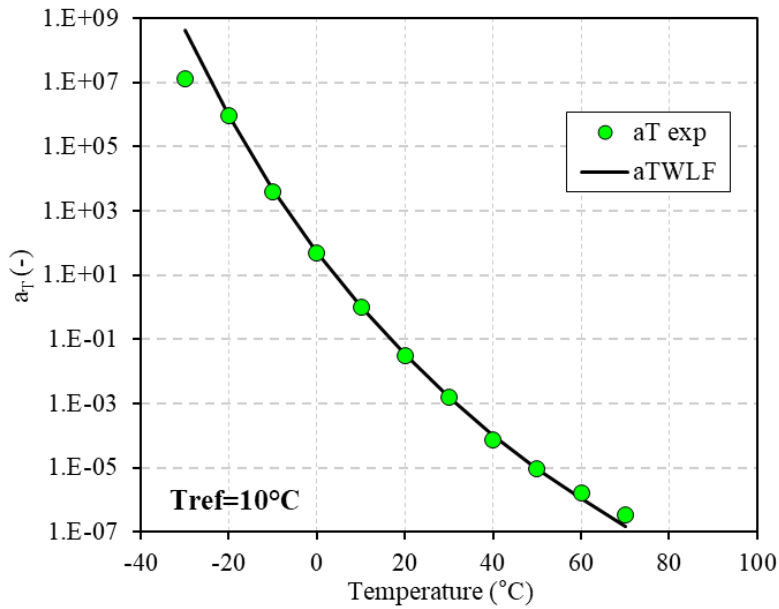


a)

b)

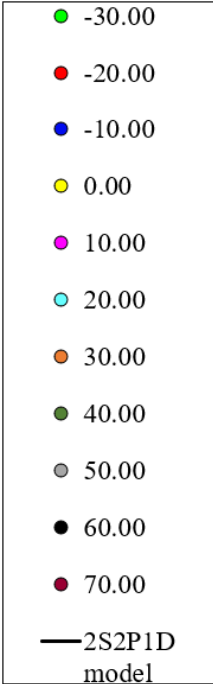
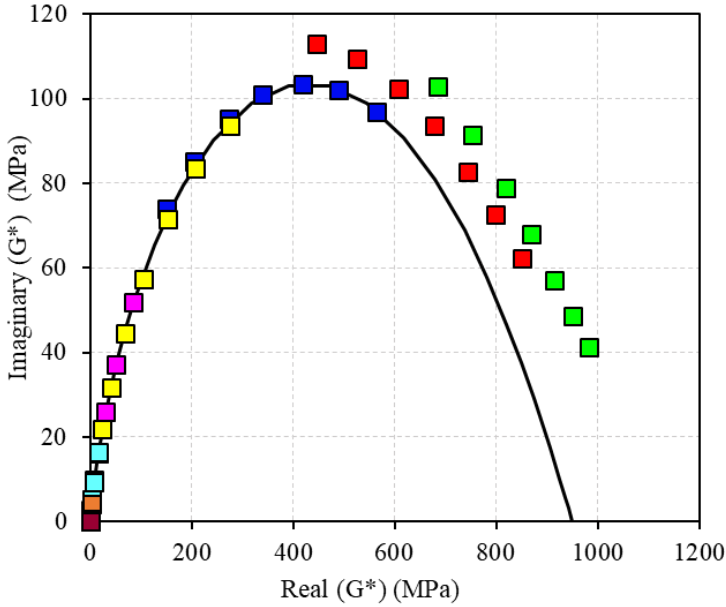


c)

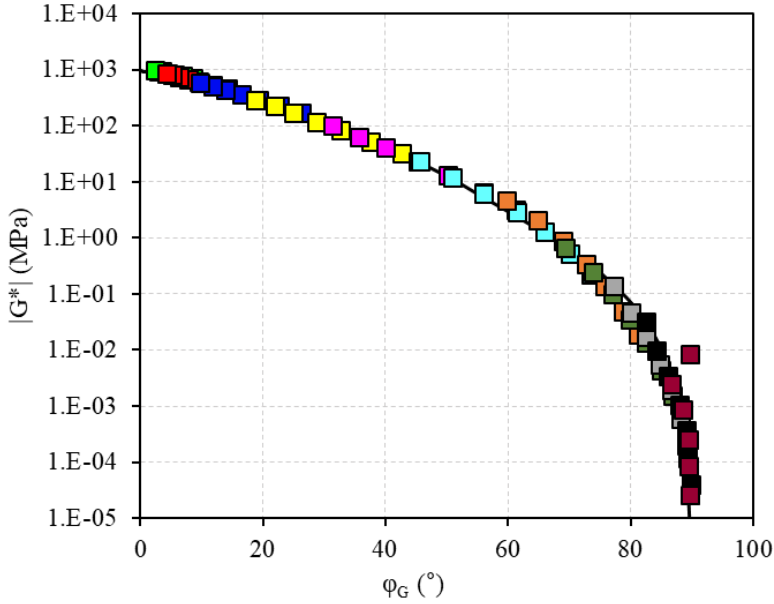


d)

Figure B3 – 2S2P1D fitted complex modulus test results for bitumen B5070-3: a) Cole-Cole plot; b) black diagram; c) master curves of norms of complex modulus and phase angle; d) WLF temperature shift factors at  $T_{ref} = 10^{\circ}C$

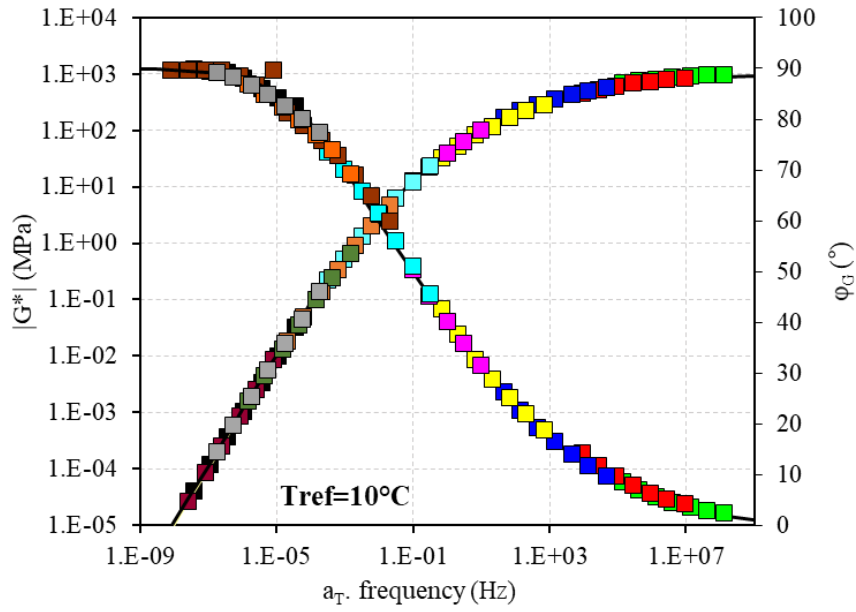


a)

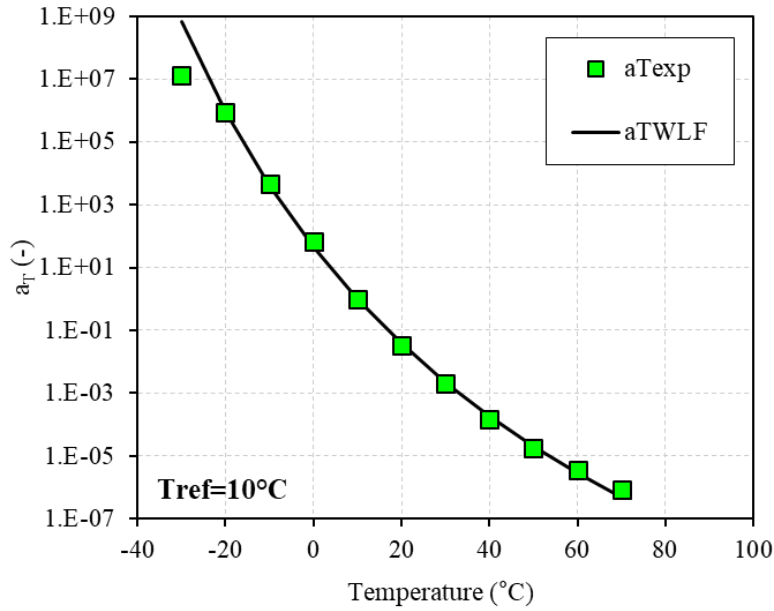


b)



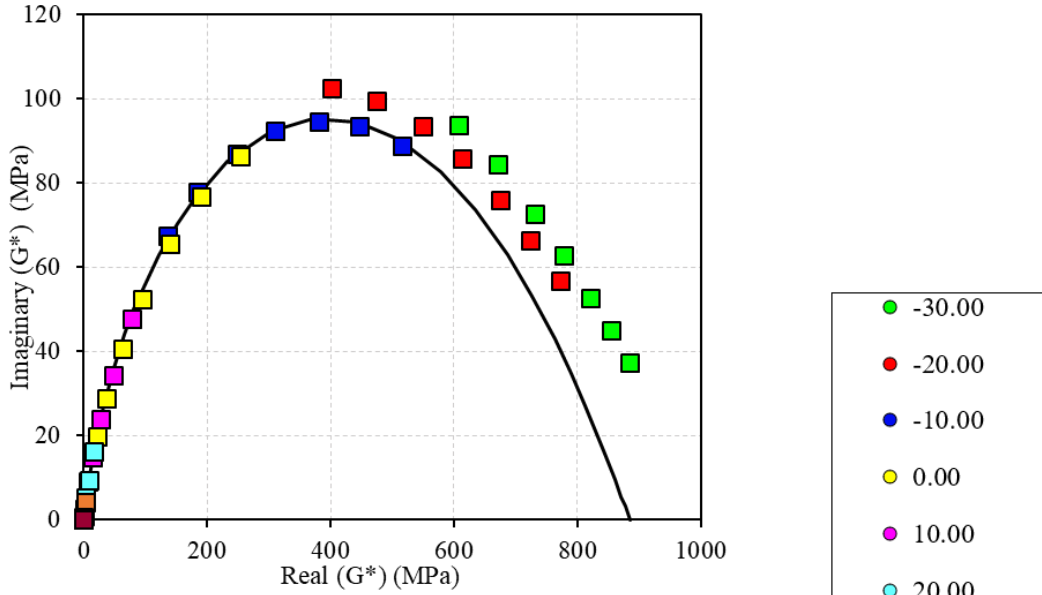


c)

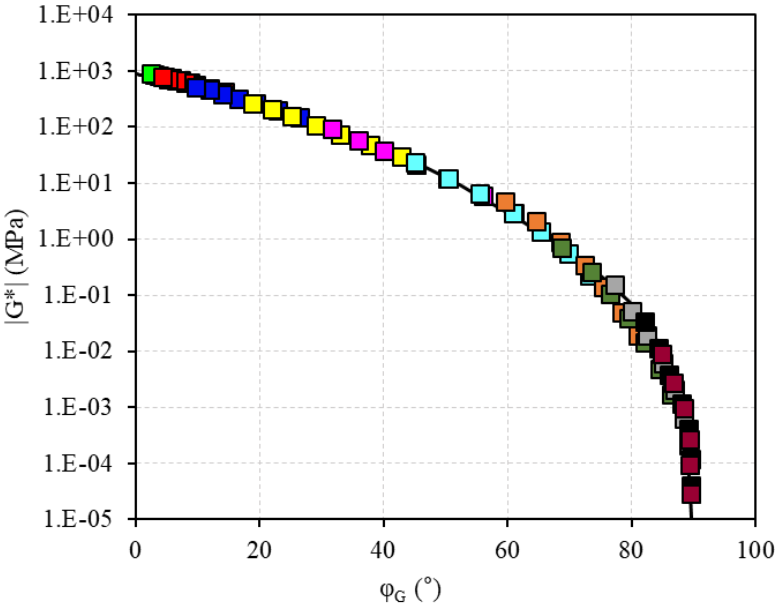


d)

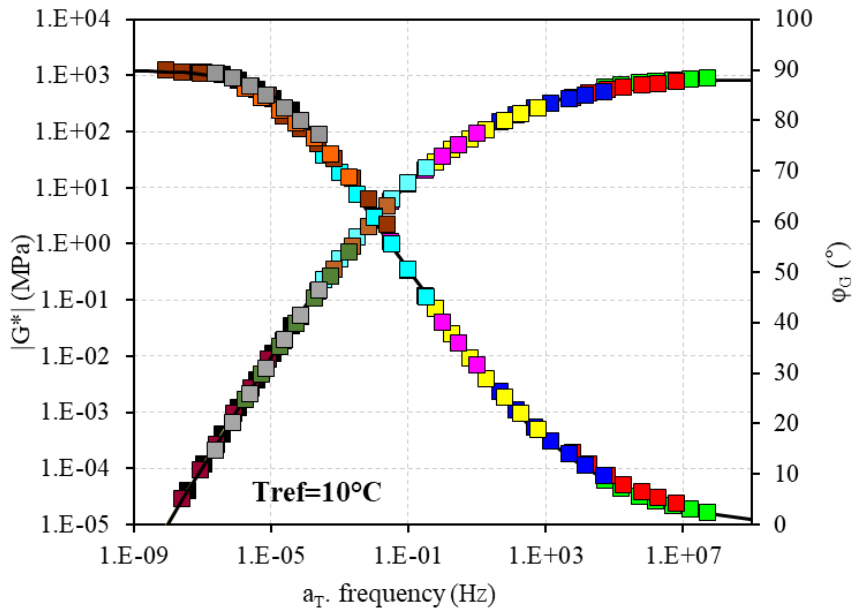
Figure B4 – 2S2PID fitted complex modulus test results for bitumen B3550-2: a) Cole-Cole plot; b) black diagram; c) master curves of norms of complex modulus and phase angle; d) WLF temperature shift factors at  $T_{ref} = 10^{\circ}C$



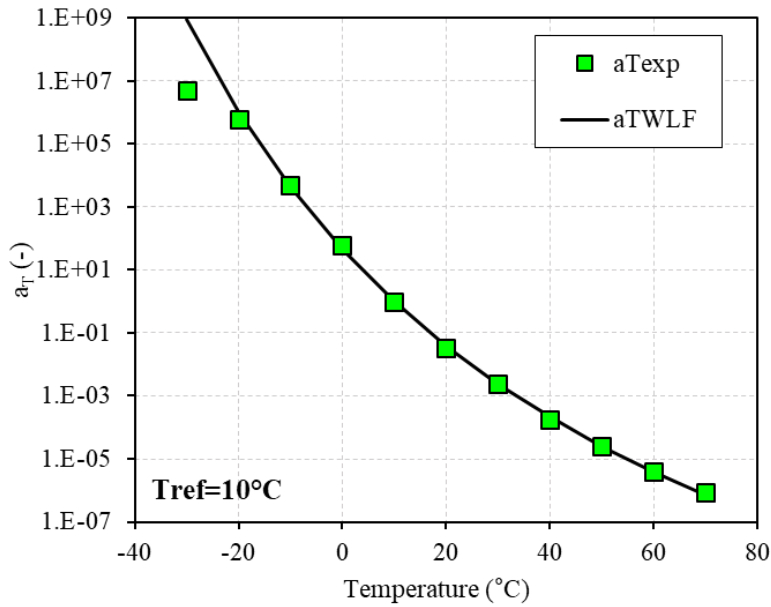
a)



b)

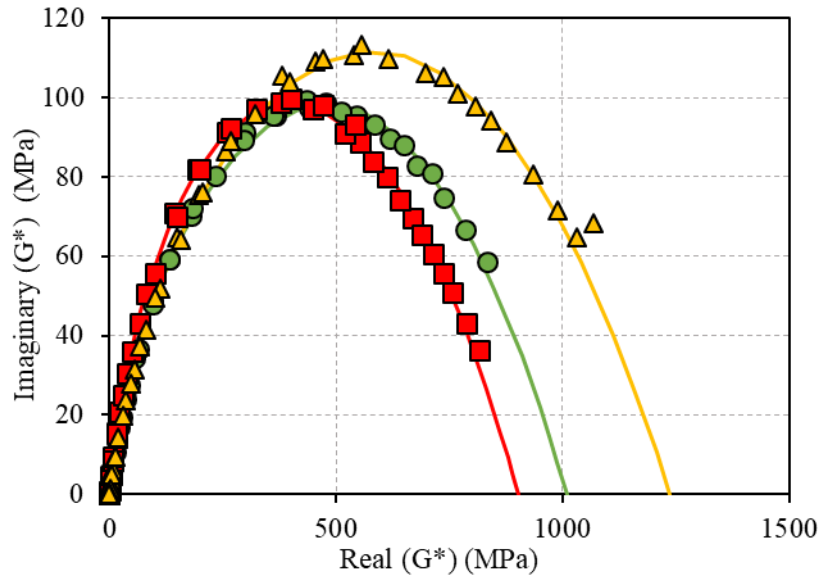
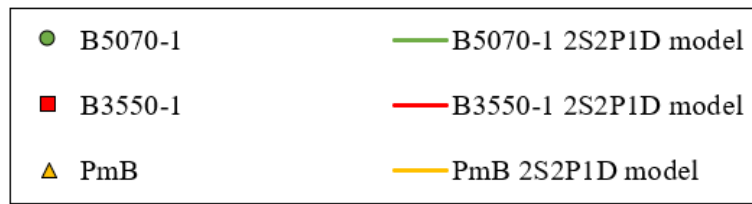


c)

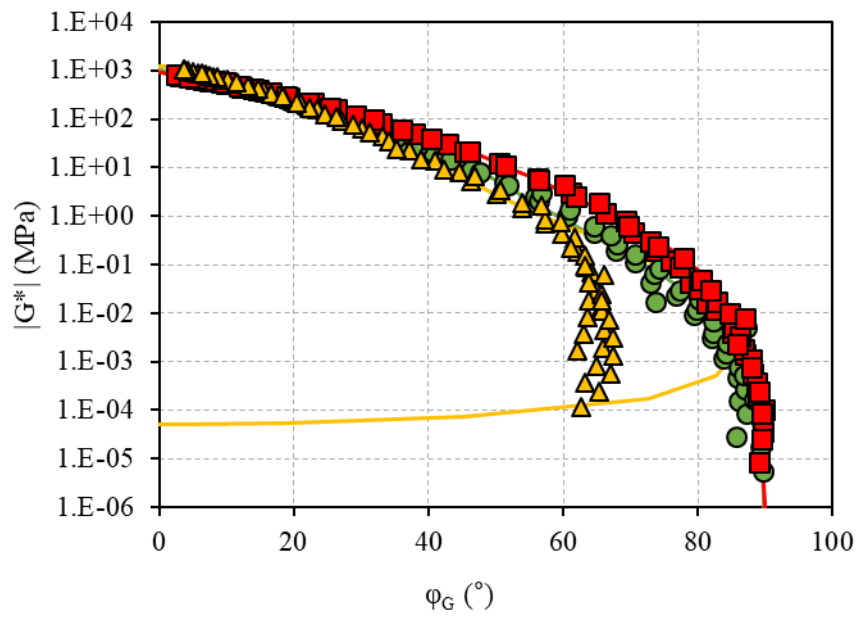


d)

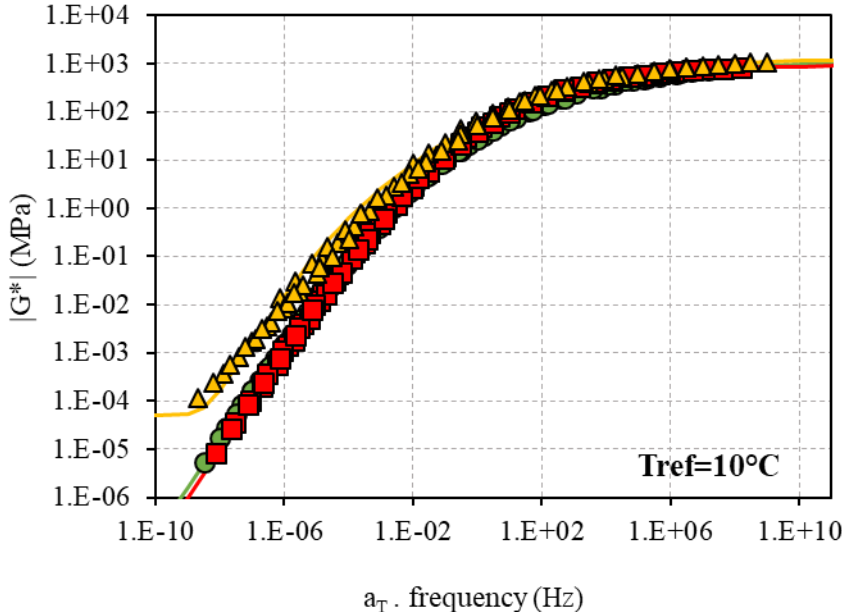
Figure B5 – 2S2P1D fitted complex modulus test results for bitumen B3550-3: a) Cole-Cole plot; b) black diagram; c) master curves of norms of complex modulus and phase angle; d) WLF temperature shift factors at  $T_{ref} = 10^{\circ}\text{C}$



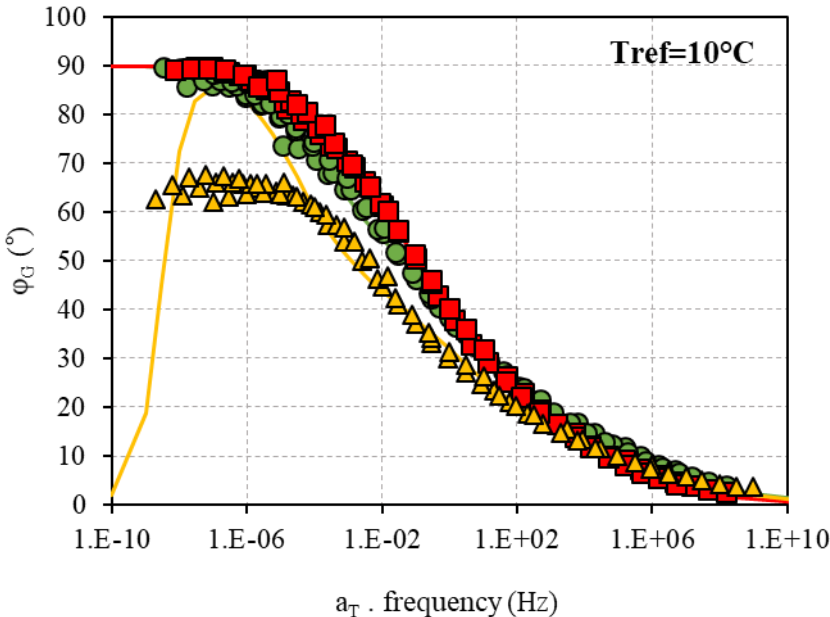
a)



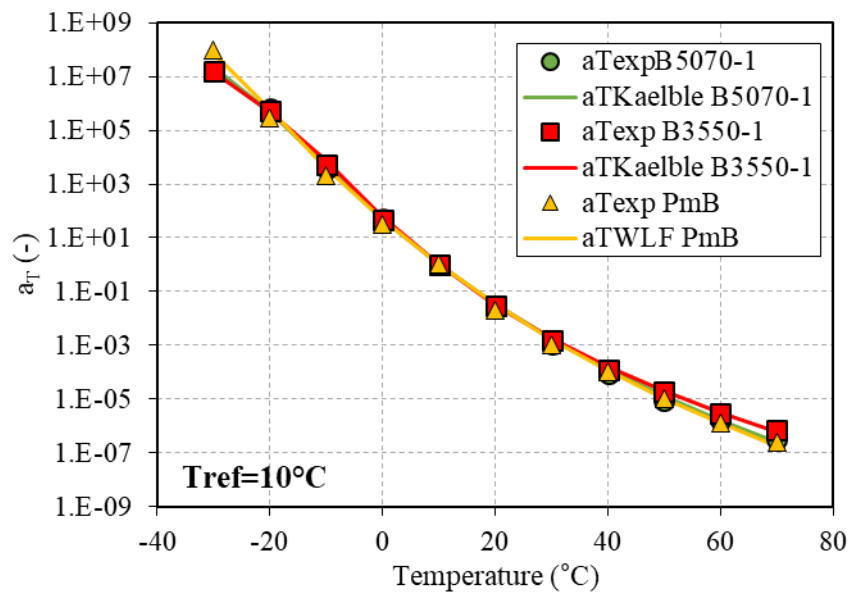
b)



c)



d)



e)

Figure B6 – Refitted 2S2P1D complex modulus test results for bitumen B5070-1, B3550-1 and PmB showing : a) Cole-Cole plot; b) black diagram; c) master curves of norms of complex modulus and phase angle; d) temperature shift factors at  $T_{ref} = 10^{\circ}\text{C}$

## APPENDIX C – 3D LINEAR VISCOELASTIC CHARACTERISATION AND MODELLING OF BITUMEN

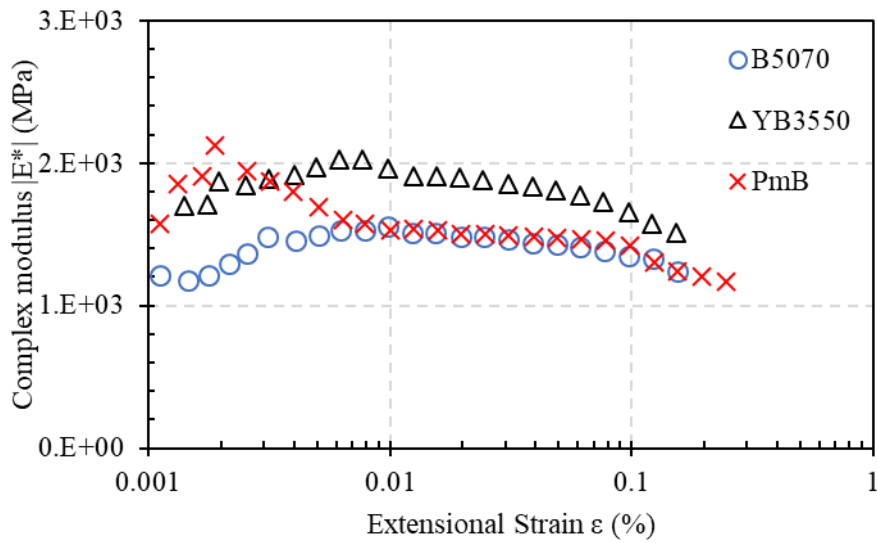
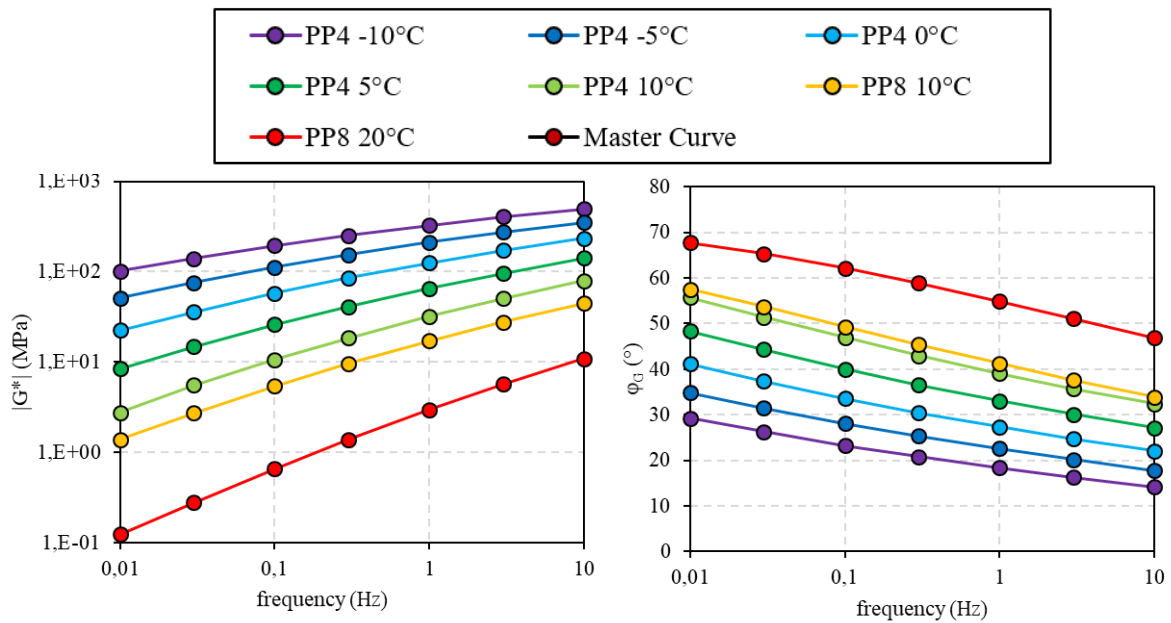
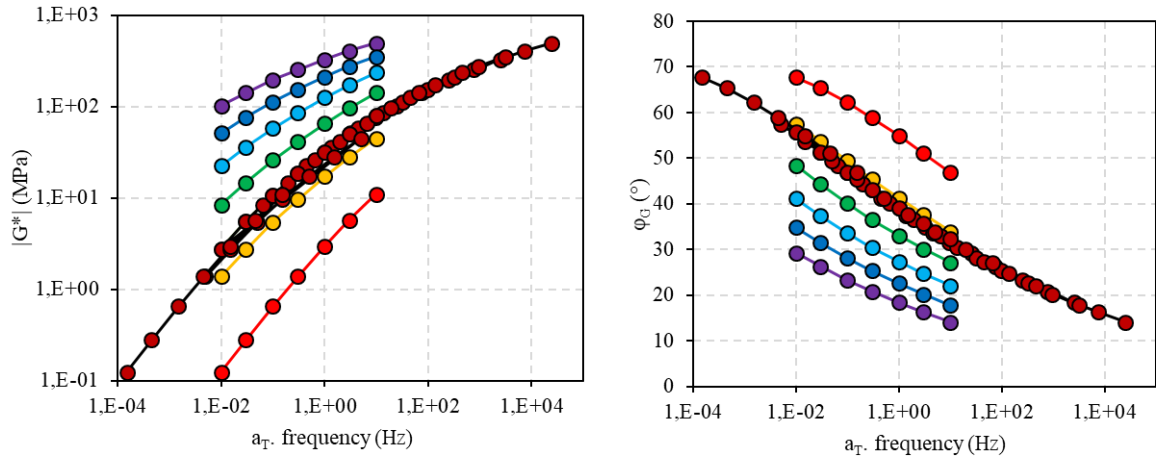


Figure C1 – a) Bitumen axial strain amplitude sweep test results at  $-10^{\circ}\text{C}/10\text{Hz}$

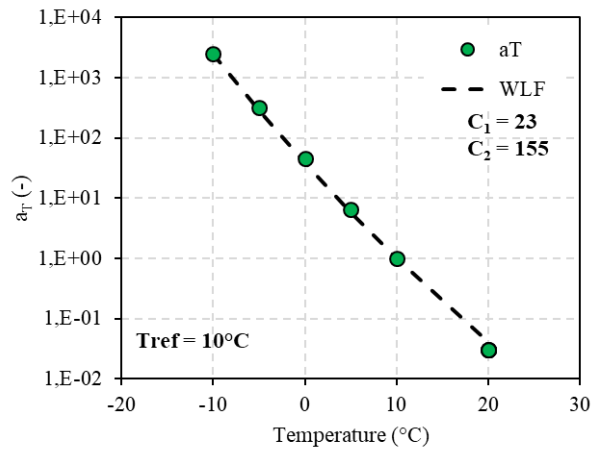


a)

b)



c)



d)

Figure C2 – a) Norm of shear complex modulus isotherms; b) phase angle isotherms; c) Master curve of shear complex modulus and d) phase angle master curve e) experimental  $a_T$  WLF fit of B5070 bitumen at  $T_{ref} = 10^\circ\text{C}$



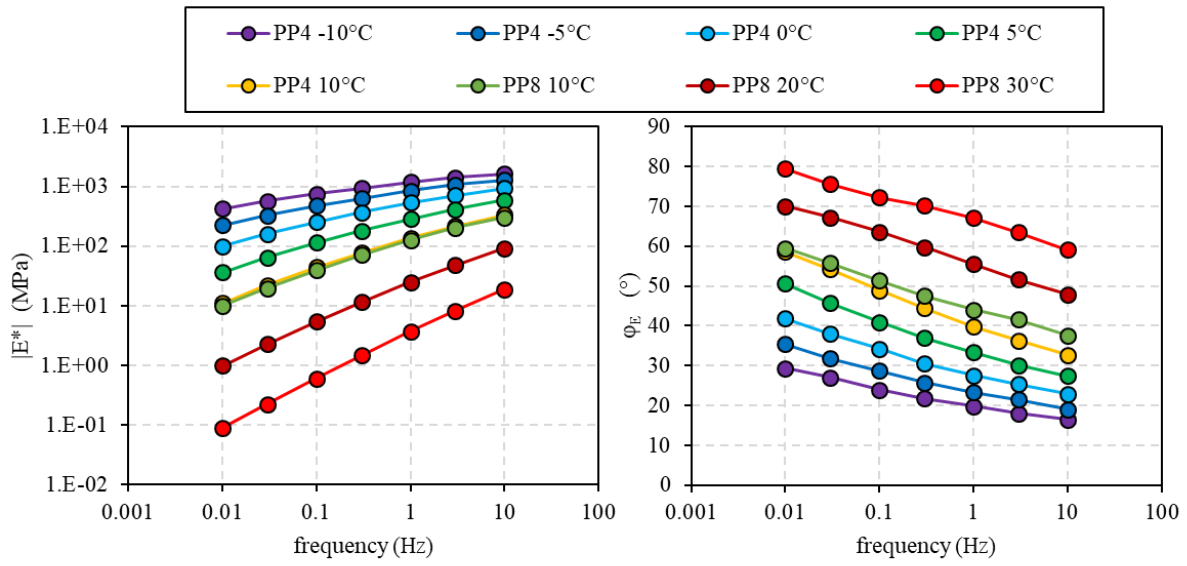


Figure C3 – a) Norm of axial complex modulus and phase angle isotherms of B3550 bitumen

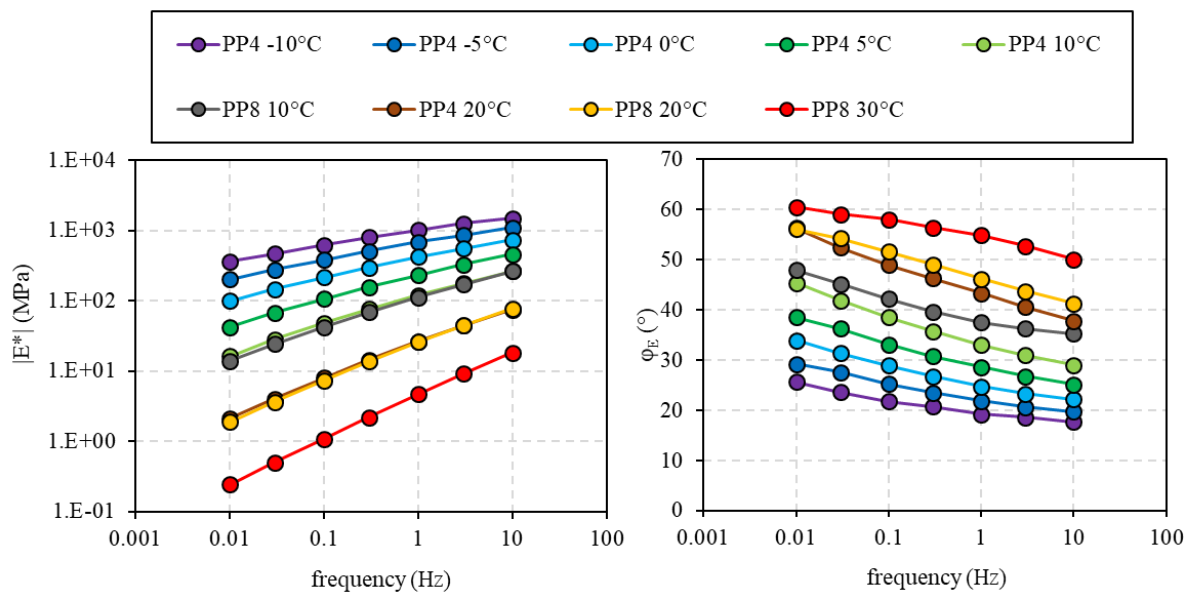
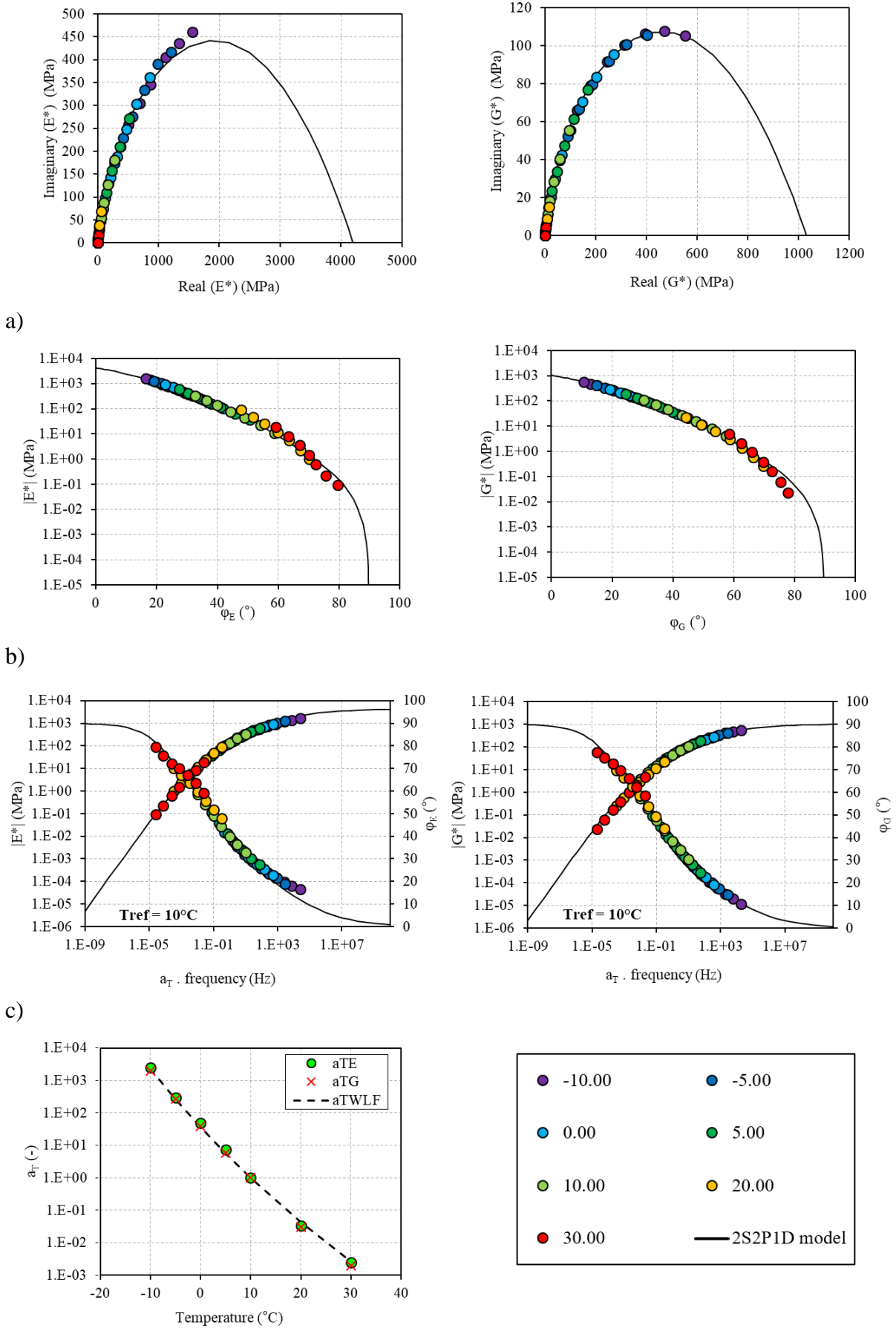


Figure C4 – a) Norm of axial complex modulus and phase angle isotherms of PmB



d)

Figure C5 – 2S2P1D fitted B3550 bitumen axial complex modulus  $E^*$  and shear complex modulus  $G^*$  a) Cole-Cole curve; b) Black diagrams; c) master curves at  $T_{ref} = 10^\circ\text{C}$  and d) Experimental shift factors fitted with WLF equation at  $T_{ref} = 10^\circ\text{C}$ .

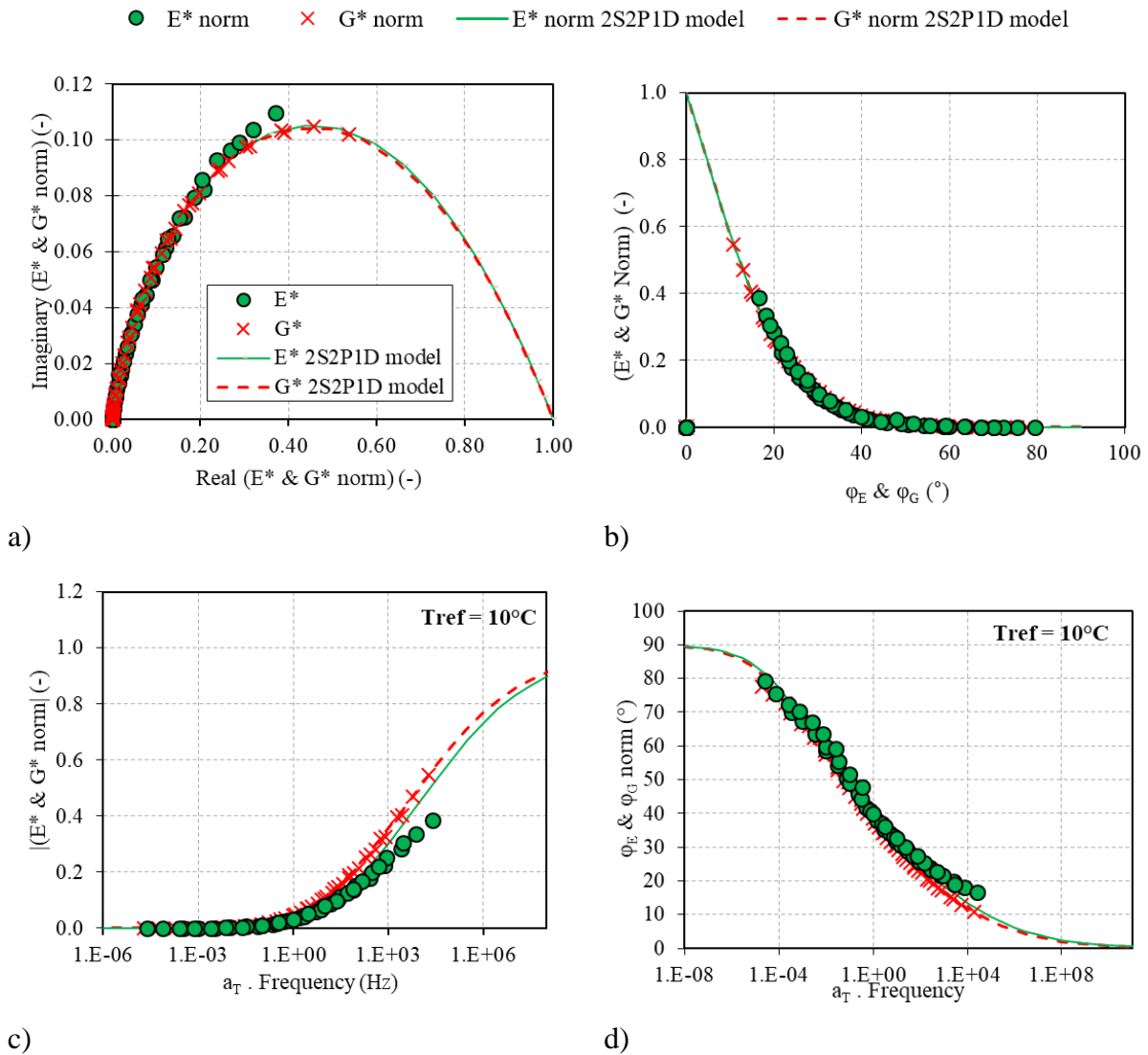
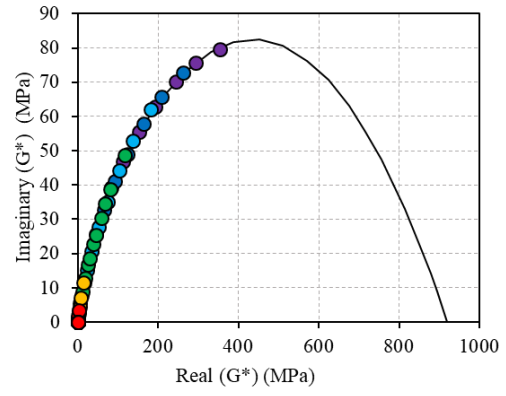
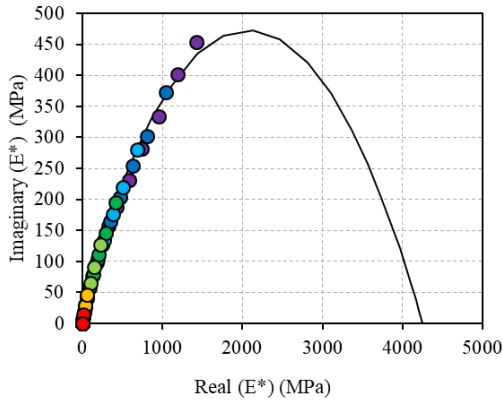
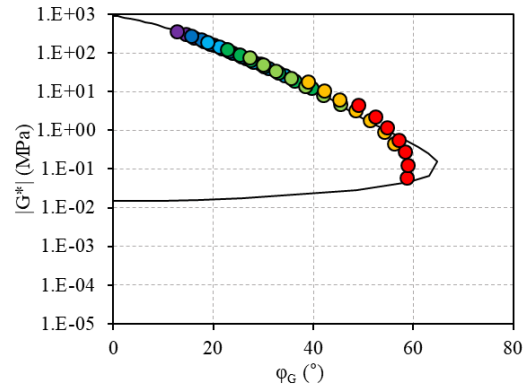
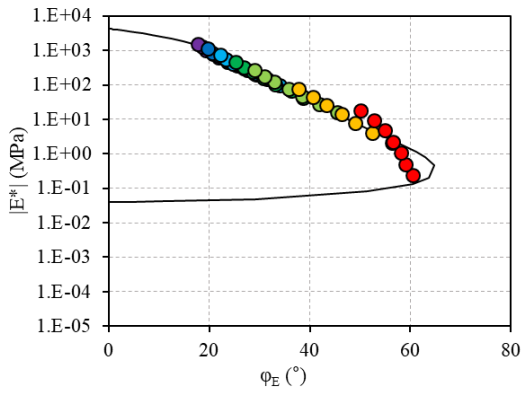


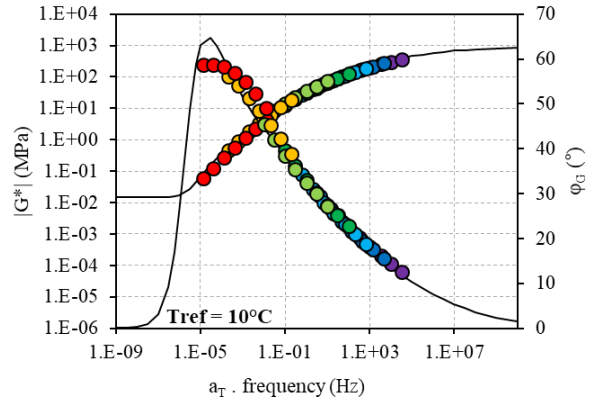
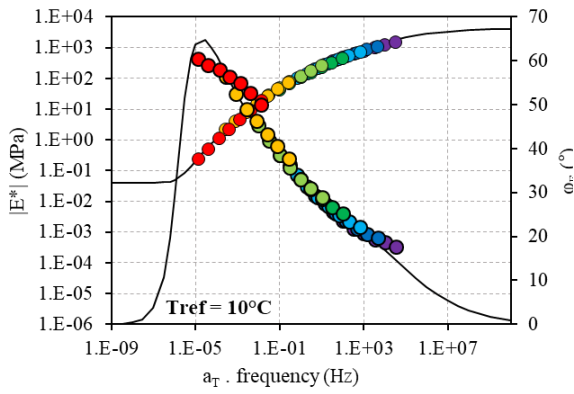
Figure C6 – Experimental results and fitted 2S2P1D curves of normalised complex modulus of B3550 a)  $E^*_{norm}$  and  $G^*_{norm}$  in Cole-Cole plane, b)  $E^*$  and  $G^*_{norm}$  in black space, c)  $|E^*$  and  $G^*_{norm}|$  master curves d)  $\phi_E$  and  $\phi_{Gnorm}$  master curves at  $T_{ref} = 10^\circ\text{C}$



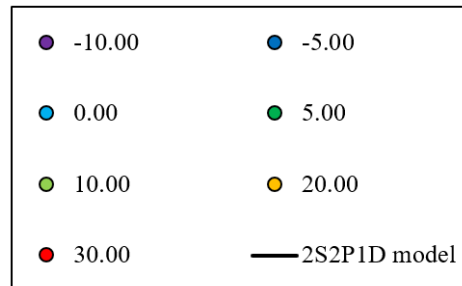
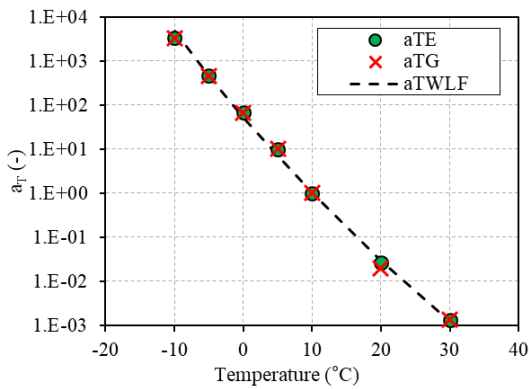
a)



b)



c)



d)

Figure C7 – 2S2P1D fitted PmB bitumen axial complex modulus  $E^*$  and shear complex modulus  $G^*$  a) Cole-Cole curve; b) Black diagrams; c) master curves at  $T_{ref} = 10^\circ\text{C}$  and d) Experimental shift factors fitted with WLF equation at  $T_{ref} = 10^\circ\text{C}$ .

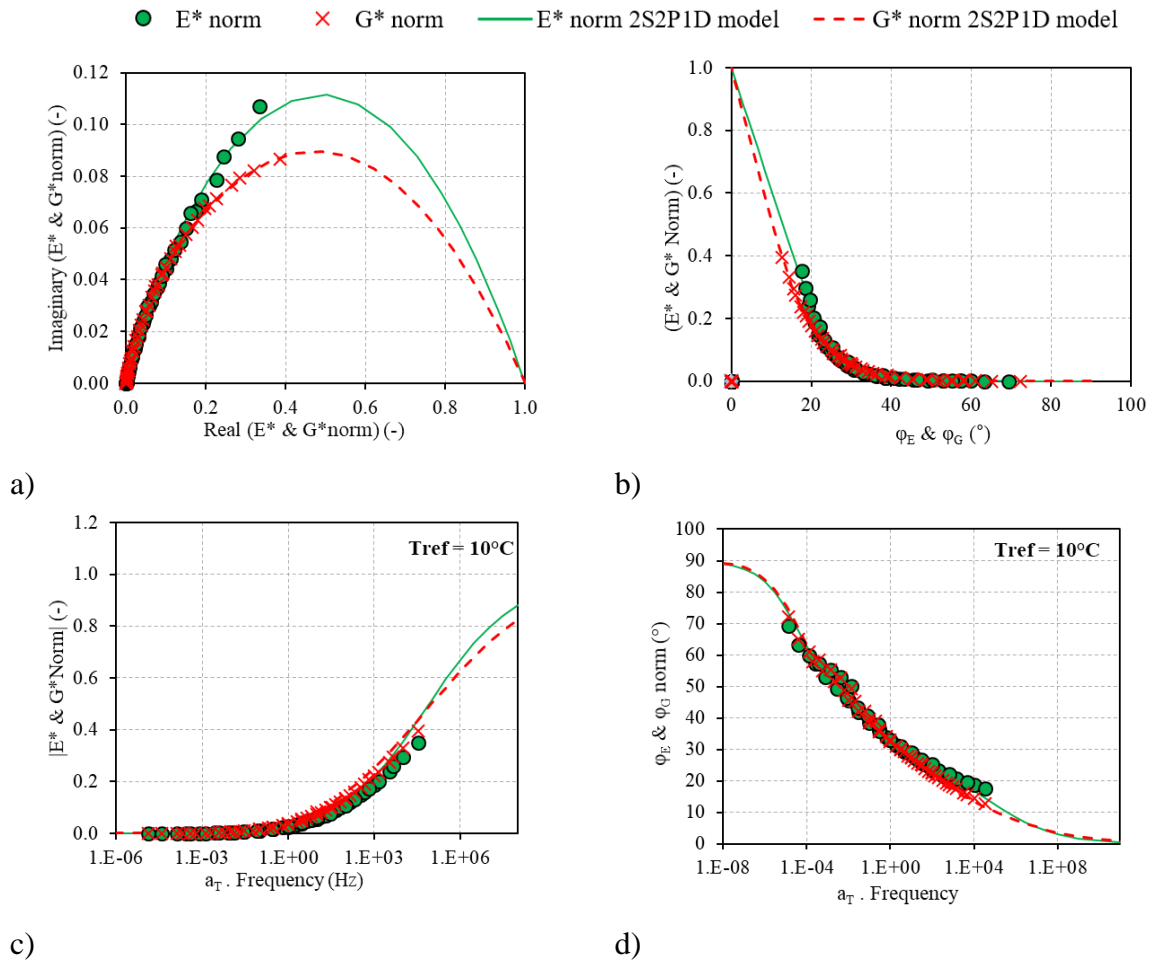
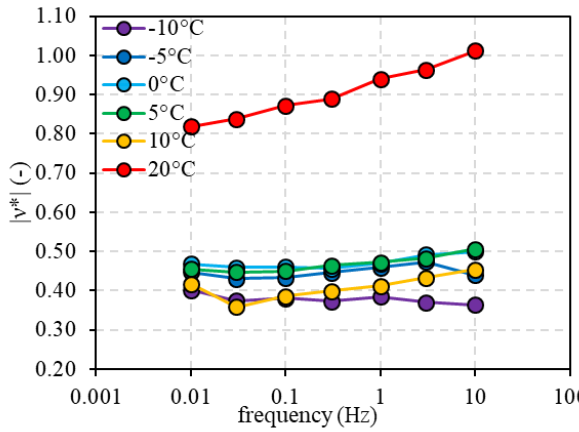
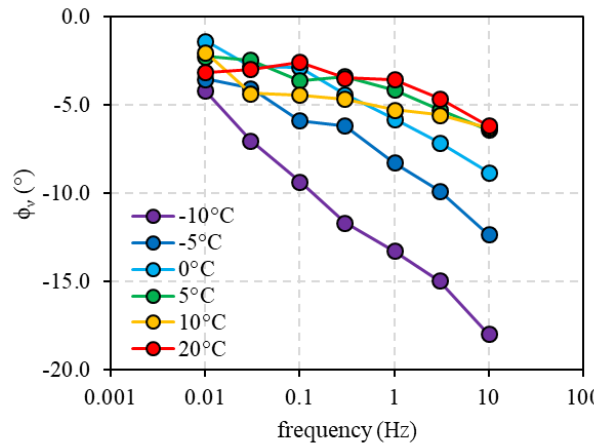


Figure C8 – Experimental results and fitted 2S2P1D curves of normalised complex modulus of PmB a)  $E^*_{norm}$  and  $G^*_{norm}$  in Cole-Cole plane, b)  $E^*$  and  $G^*_{norm}$  in black space, c)  $|E^*$  and  $G^*_{norm}|$  master curves d)  $\phi_E$  and  $\phi_{Gnorm}$  master curves at  $T_{ref} = 10^\circ\text{C}$

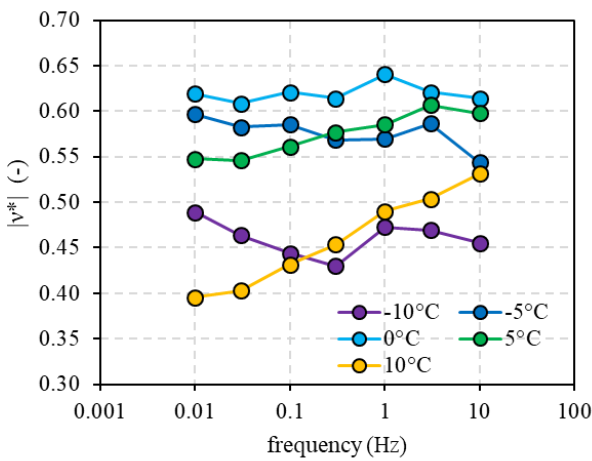


a)

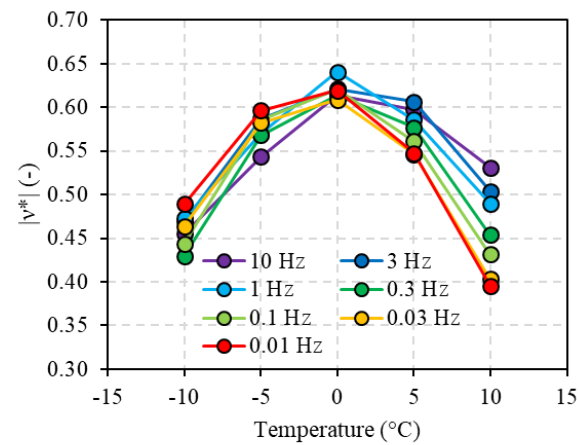
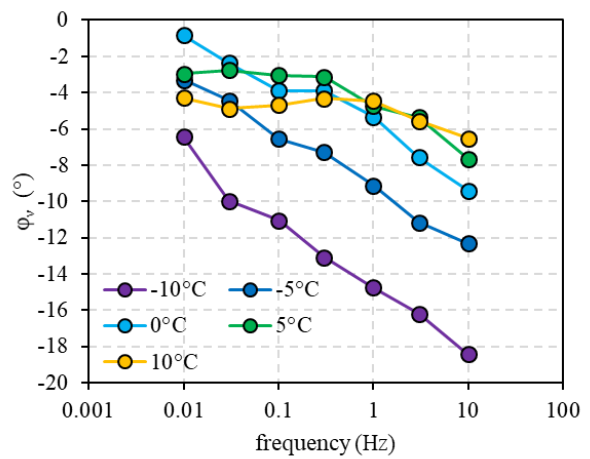


b)

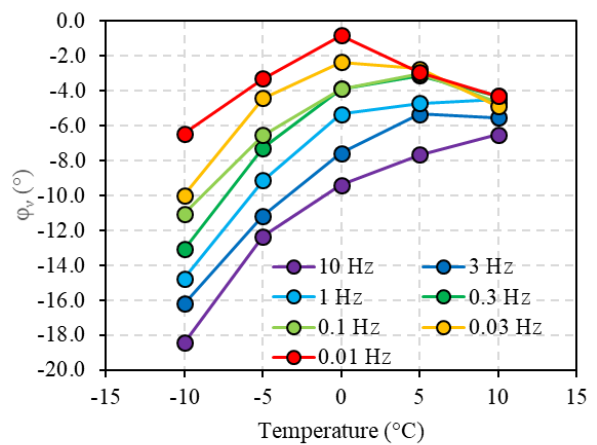
Figure C9 – The experimental results of the complex Poisson's ratio  $\nu^*$  of B5070 bitumen a) norm of Poisson's ratio; b) Phase angle of Poisson's ratio

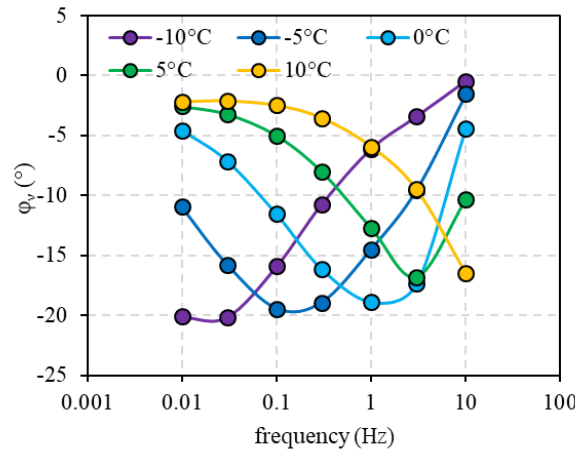
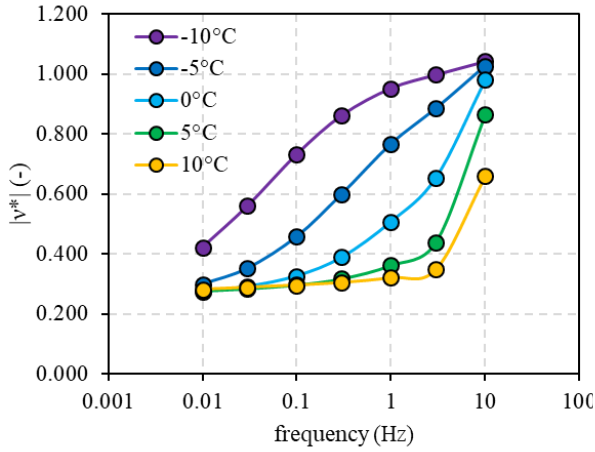


a)



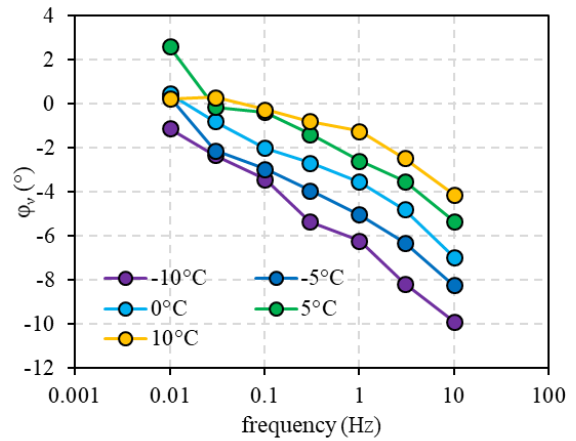
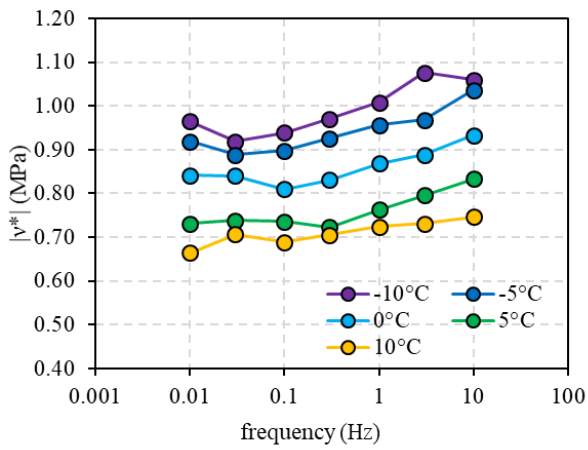
b)



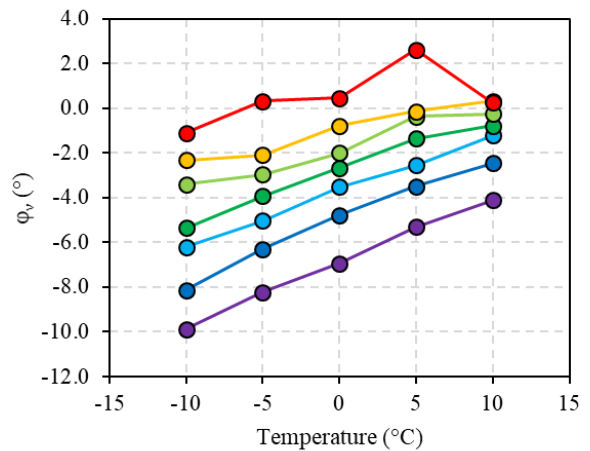
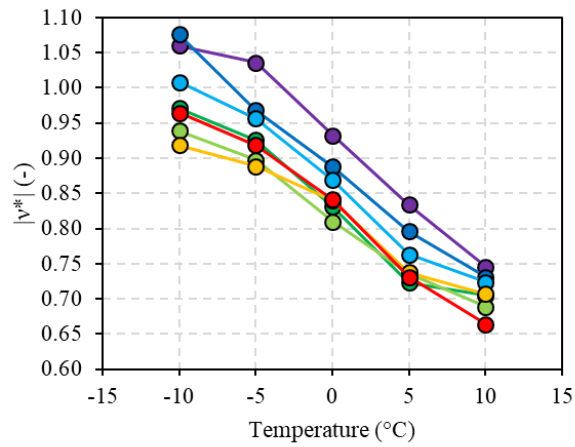


c)

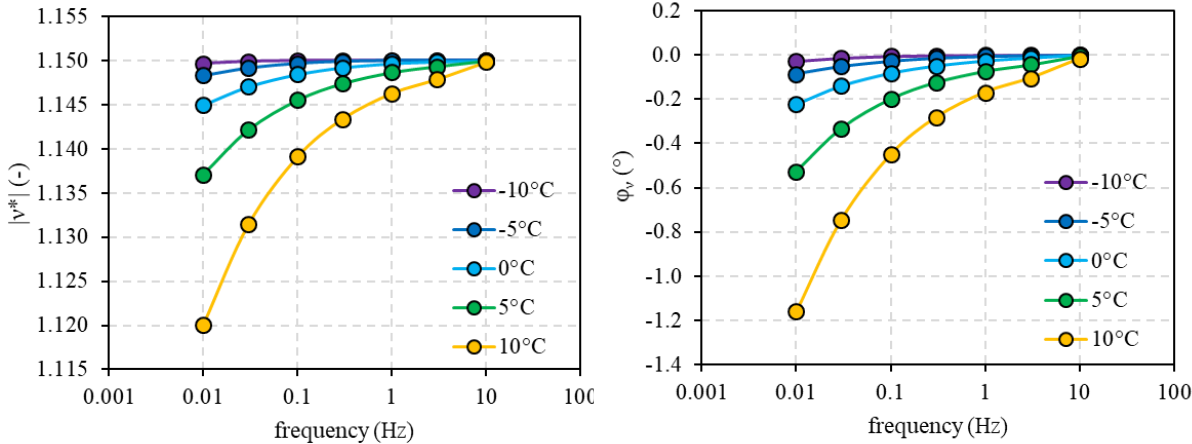
Figure C10 – Norm of complex Poisson's ratio  $v^*$  and phase angle  $\phi_v$  of B3550 a) isotherms of experimental results; b) isochrones of experimental results; c) 2S2PID simulated results



a)



b)



c)

Figure C11 – Norm of complex Poisson’s ratio  $v^*$  and phase angle  $\phi_v$  of PmB a) isotherms of experimental results; b) isochrones of experimental results; c) 2S2PID simulated results



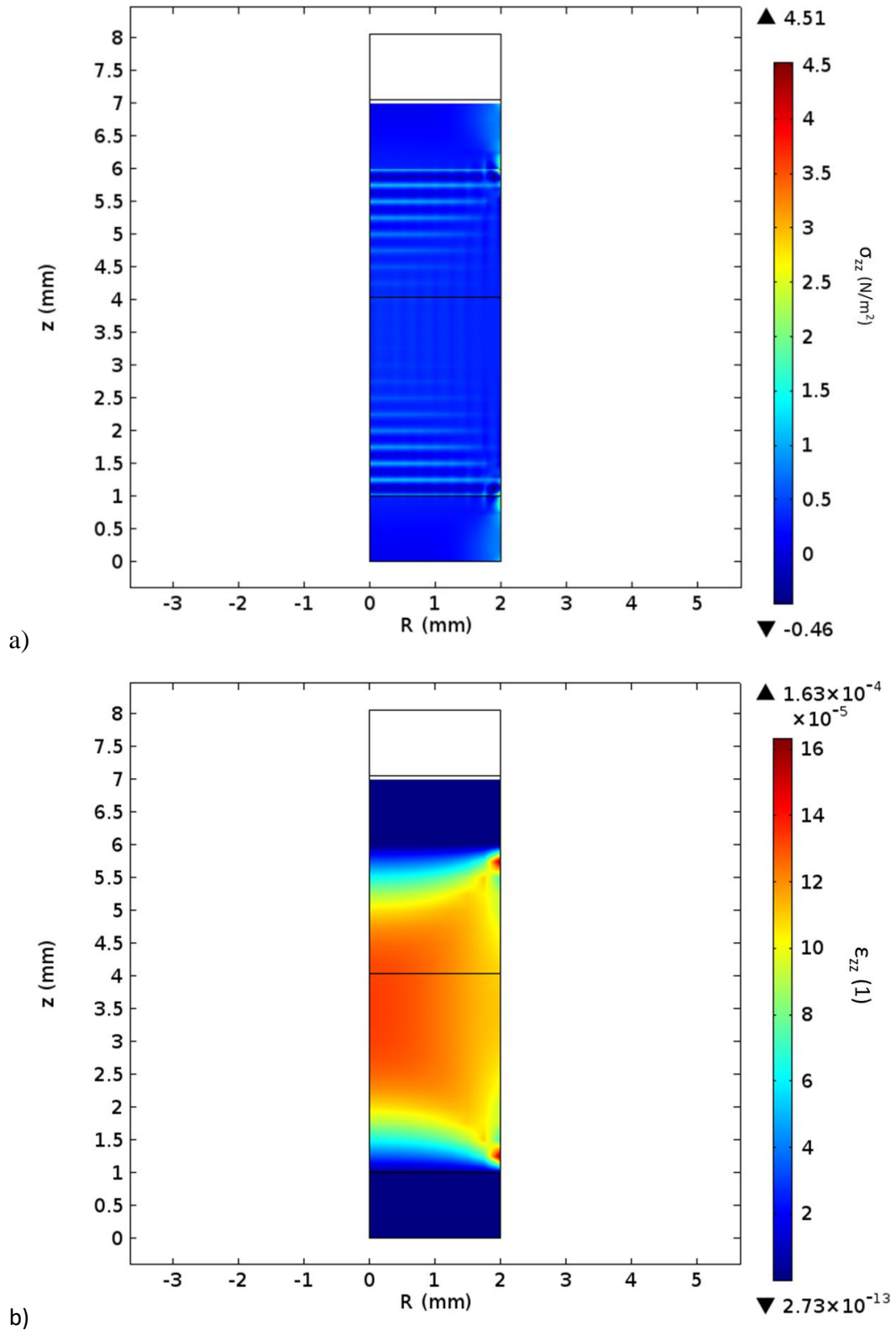


Figure C12 – The distribution of stress  $\sigma_{zz}$  and strain tensor  $\epsilon_{zz}$  in the bitumen's central region at 5 mm specimen height and  $\nu = 0.49995$

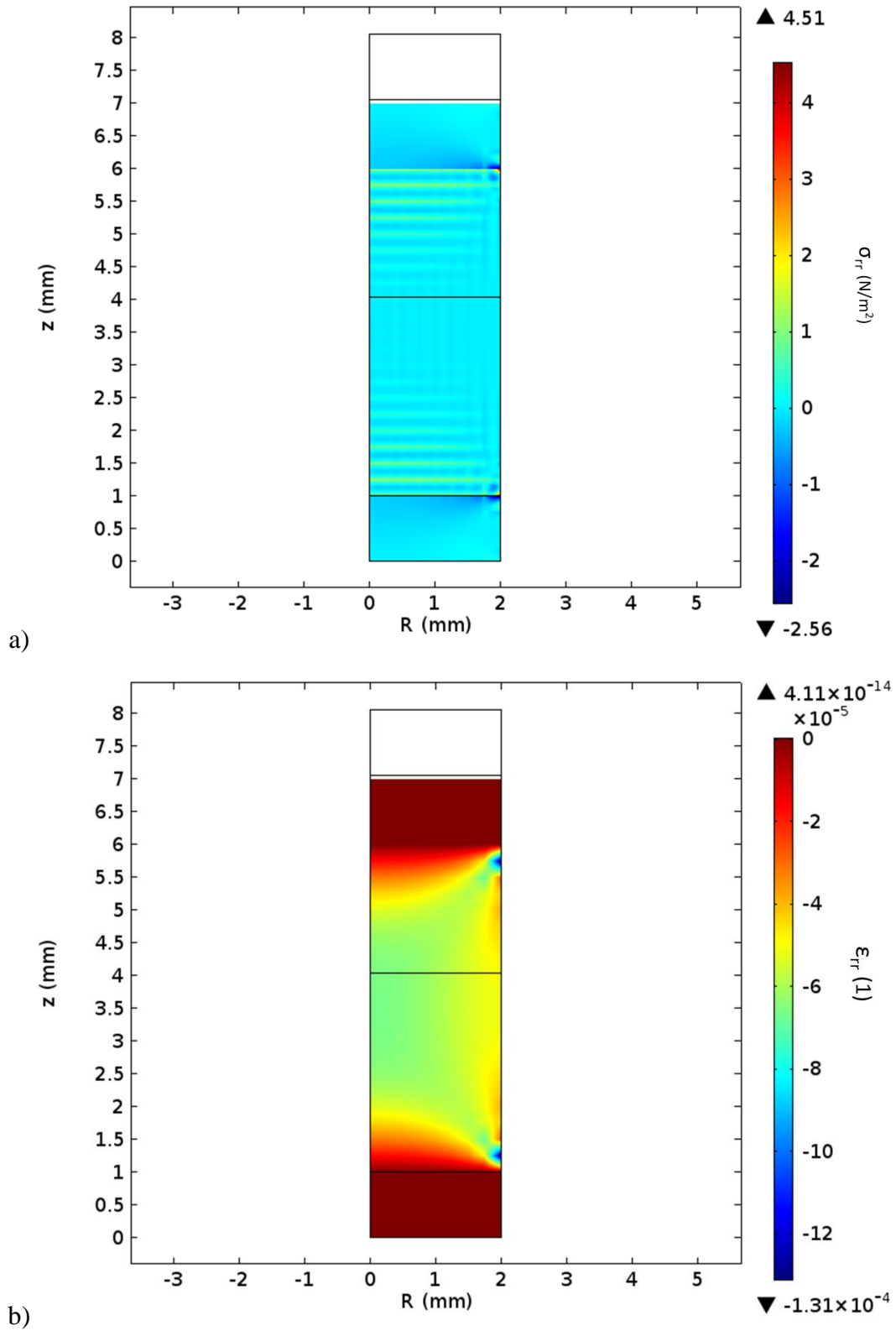


Figure C13 – The distribution of stress  $\sigma_{rr}$  and strain tensor  $\epsilon_{rr}$  in the bitumen's central region at 5 mm specimen height and  $\nu = 0.49995$

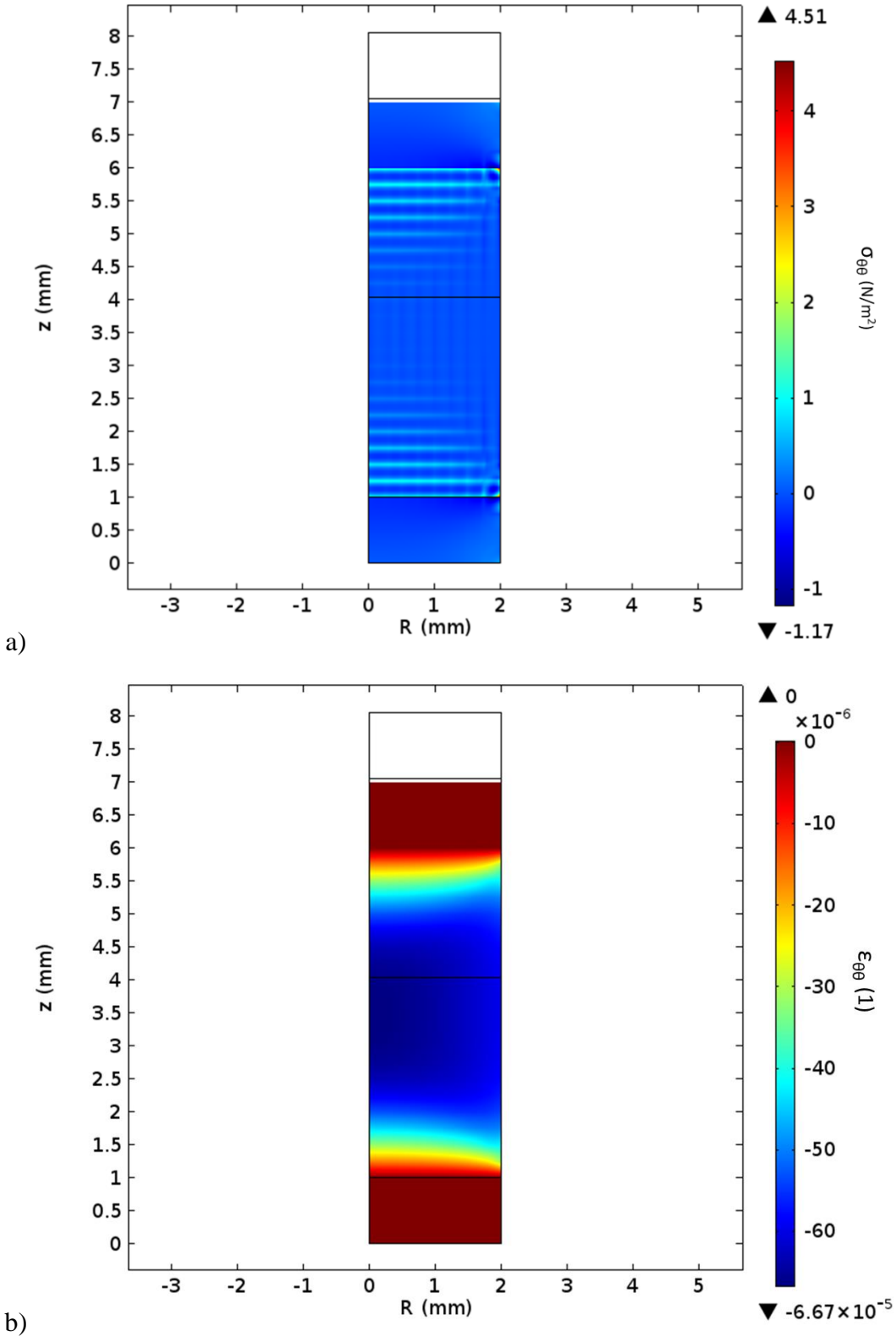


Figure C14 – The distribution of stress  $\sigma_{\theta\theta}$  and strain tensor  $\epsilon_{\theta\theta}$  in the bitumen's central region at 5 mm specimen height and  $\nu = 0.49995$

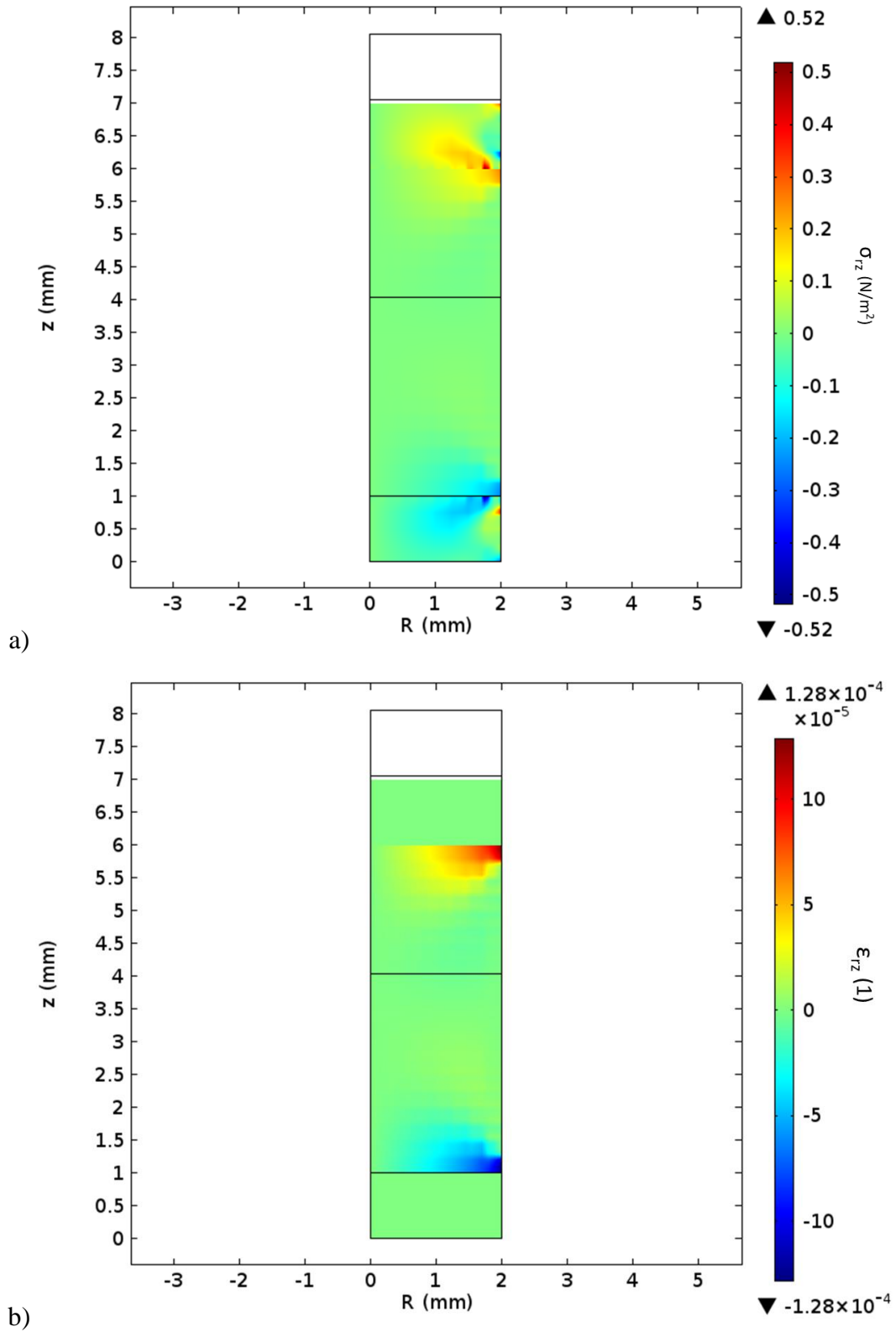


Figure C15 – The distribution of stress  $\sigma_{rz}$  and strain tensor  $\epsilon_{rz}$  in the bitumen's central region at 5 mm specimen height and  $\nu = 0.49995$

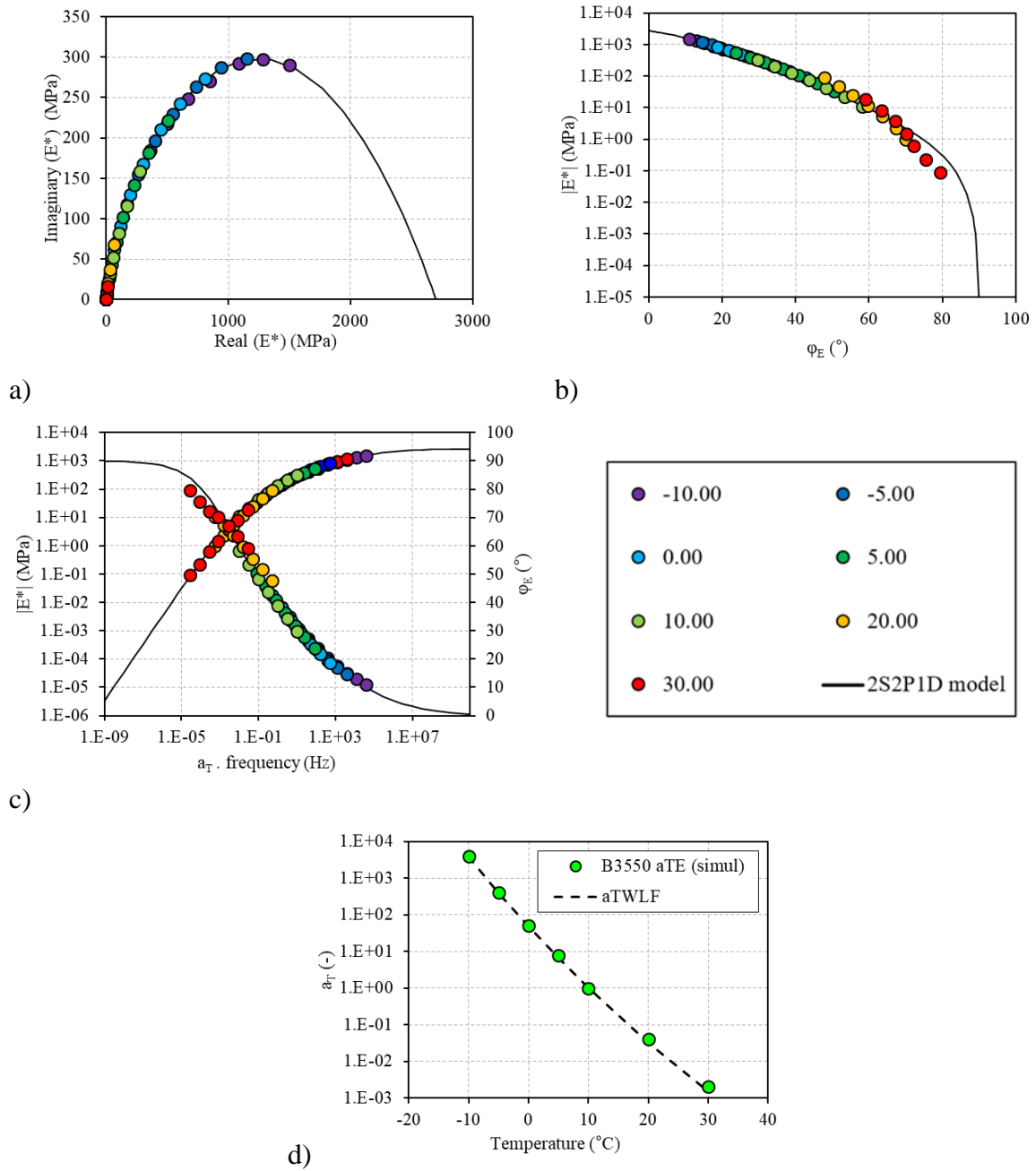


Figure C16 – 2S2P1D fitted B3550 bitumen FEM axial complex modulus  $E^*$  a) Cole-Cole curve; b) Black diagrams; c) master curves and d) shift factors fitted with WLF equation at  $T_{ref} = 10^\circ\text{C}$ .

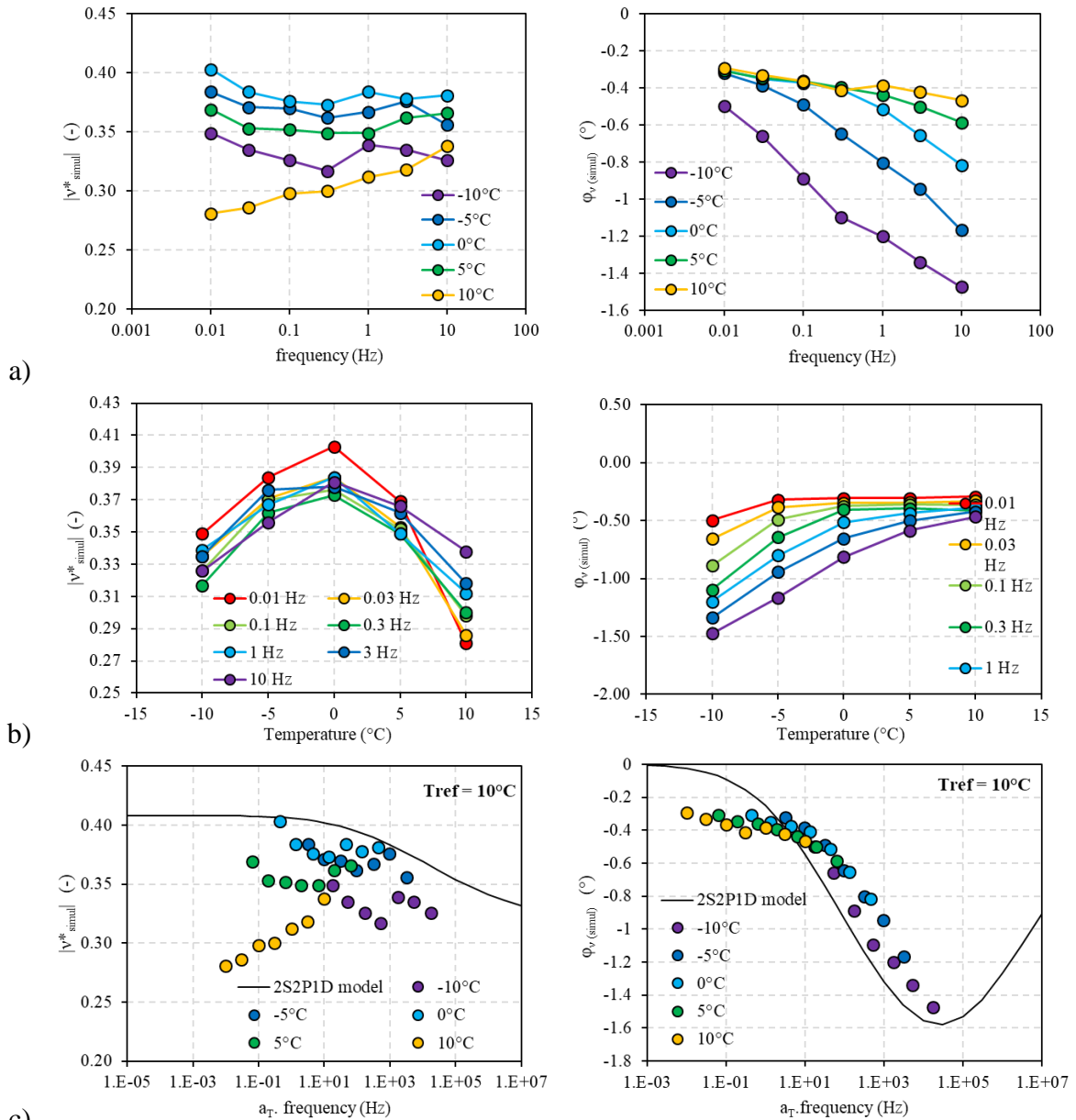
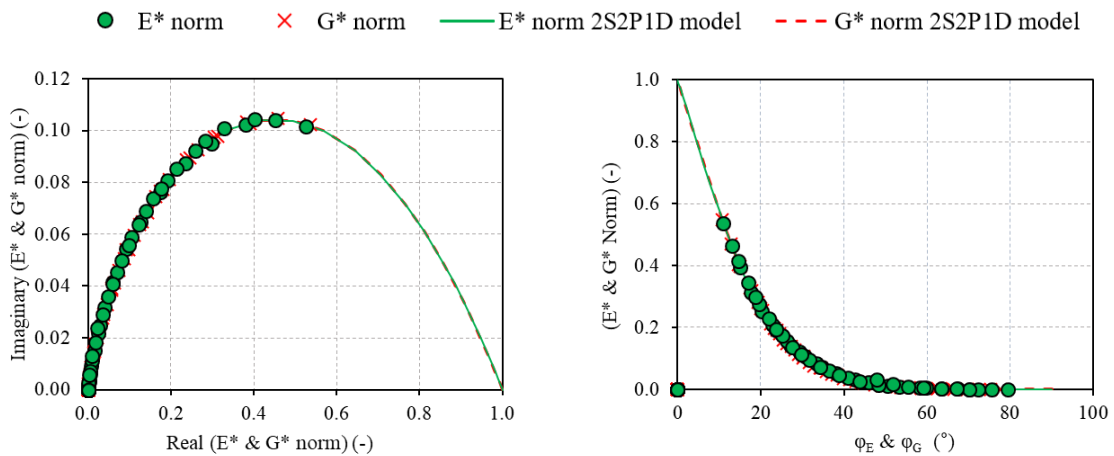


Figure C17 – Norms and phase angles of simulated B3550 bitumen Poisson's ratio a) isotherms; b) isochrones; c) 2S2P1D fitted master curves at  $T_{ref} = 10^{\circ}\text{C}$ .



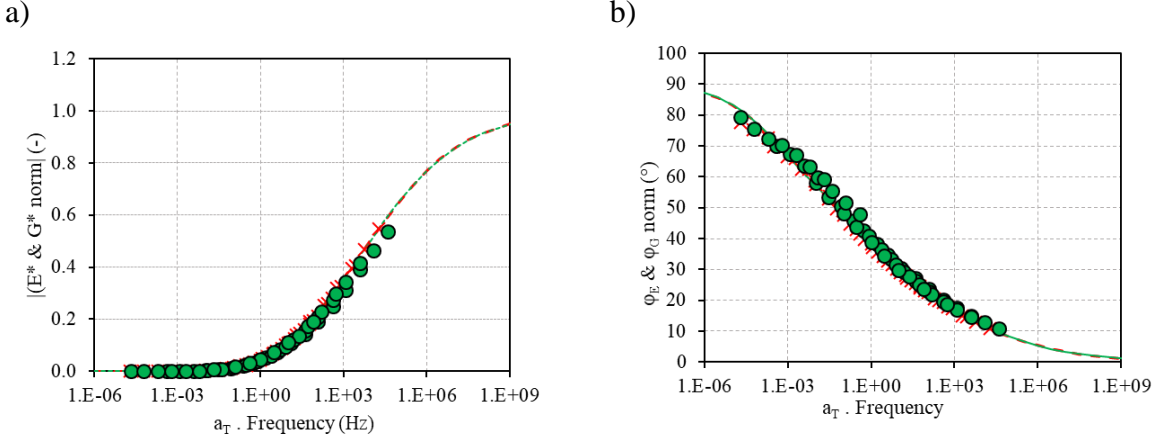


Figure C18 – Corrected experimental results and fitted 2S2P1D curves of normalised complex modulus of B3550 bitumen a)  $E^*_{norm}$  and  $G^*_{norm}$  in Cole-Cole plane, b)  $E^*$  and  $G^*_{norm}$  in black space, c)  $|E^*$  and  $G^*_{norm}|$  master curves d)  $\varphi_E$  and  $\varphi_{Gnorm}$  master curves at  $T_{ref} = 10^\circ C$